Understanding the interaction of wind farms and turbulent atmospheric boundary layer in a large eddy simulation framework: from periodic to LIDAR based data driven cases

by

Tanmoy Chatterjee

A Dissertation Presented in Partial Fulfillment
of the Requirements for the Degree
Doctor of Philosophy

Approved April 2018 by the
Graduate Supervisory Committee:

Yulia T. Peet, Chair
Ronald J. Adrian
Ronald J. Calhoun
Huei-Ping Huang
Mohamed Moustaoui

ARIZONA STATE UNIVERSITY

May 2018

ABSTRACT

This thesis focuses on an improved understanding of the dynamics at different length scales of wind farms in an atmospheric boundary layer (ABL) using a series of visualization studies and Fourier, wavelet based spectral analysis using high fidelity large eddy simulation (LES). For this purpose, a robust LES based neutral ABL model at very high Reynolds number has been developed using a high order spectral element method which has been validated against the previous literature. This ABL methodology has been used as a building block to drive large wind turbine arrays or wind farms residing inside the boundary layer as documented in the subsequent work. Studies conducted in the thesis involving massive periodic wind farms with neutral ABL have indicated towards the presence of large scale coherent structures that contribute to the power generated by the wind turbines via downdraft mechanisms which are also responsible for the modulation of near wall dynamics. This key idea about the modulation of large scales have seen a lot of promise in the application of flow past vertically staggered wind farms with turbines at different scales. Eventually, studies involving wind farms have been progressively evolved in a framework of inflow-outflow where the turbulent inflow is being fed from the precursor ABL using a spectral interpolation technique. This methodology has been used to enhance the understanding related to the multiscale physics of wind farm ABL interaction, where phenomenon like the growth of the inner layer, and wake impingement effects in the subsequent rows of wind turbines are important owing to the streamwise heterogeneity of the flow. Finally, the presence of realistic geophysical effects in the turbulent inflow have been investigated that influence the flow past the wind turbine arrays. Some of the geophysical effects that have been considered include the presence of the Coriolis forces as well as the temporal variation of mean wind magnitude and direction that might occur due to mesoscale dynamics. This study has been compared against

field experimental results which provides an important step towards understanding the capability of the mean data driven LES methodology in predicting realistic flow structures.

...to my daughter, Anika

ACKNOWLEDGMENTS

The work outlined in this dissertation could never have been possible without the constant help, support, and encouragement of several people whom I wish to acknowledge. First and foremost, I would like to express my sincere gratitude to my advisor, Dr. Yulia T. Peet for giving me an opportunity to work at the Integrative Simulations and Computational Fluid Lab at ASU, and for fostering a research environment that encouraged novel ideas, accommodated criticism. I am also extremely grateful to my committee members Dr. Ronald J. Calhoun, Dr. Ronald J. Adrian, Dr.Huei-Ping Huang and Dr. Mohamed Moustaoui for their valuable time. I would like to thank my previous colleagues, Dr. Brandon Merrill, Dr. Philip Sakievich and my current colleagues and friend Mr. Yiqin Xu and Mr. Daniel Coxe at lab with whom I have had the opportunity to work and discuss research problems and have enjoyed their company inside the lab. I would also like to express my sincere gratitude to my parents Tapan and Dalia Chatterjee, my parent-in-laws Paresh Nath and Ramala Roy, my wife Jinia, my sister-in-law Runia and my daughter Anika for the constant support. Finally, I would like to acknowledge U.S. National Science Foundation Grants NSF-CBET 13358568 grant and the compute hours at supercomputers Stampede, Gordon and Comet from XSEDE research allocations TG-ENG140005, TG-ENG150019 for supporting my work.

TABLE OF CONTENTS

CHAPTER Page

CHAPTER Page

CHAPTER Page

CHAPTER Page

LIST OF TABLES

Table Page

LIST OF FIGURES

Figure Page

Figure Page

Figure Page

Figure Page

Figure Page

Figure Page

Figure Page

Chapter 1

INTRODUCTION

Energy prices, supply uncertainties, and most importantly environmental concerns (air and water pollution in particular) are driving the United States to restructure the US power contribution that are derived from various sources and develop diverse sources of clean, renewable energy. The nation is working toward generating more energy from domestic resources – energy that can be cost-effective and replaced or "renewed" without contributing to climate change or major adverse environmental impacts. In this context, solar energy and particularly wind energy (which is our current focus) has been one of the rapidly emerging and developing fields of research as a cleaner as well as safer alternative to energy sources from fossil fuels, natural gas and even nuclear energy. United States has a very rich resource of wind, with a mean spead peaking up to $\sim 9\ m/s$ in central US (See Figure 1.1). This has led to a strong and rapid growth in the mid-1980s followed by a short-term plateau during the electricity restructuring period in the 1990s and then regaining momentum in 1999. Currently, the U.S. wind industry is growing rapidly (around $\sim 8\%$ of total electricity generation in US), stimulated by policy incentives like sustained production tax credits (PTCs), rising concerns about climate change, and renewable portfolio standards (RPS) in roughly 50% of the states. With such growth rates and advancement in electrical power distribution and transmission technology, the Department of Energy (DoE) has set up a target of "20% Wind Scenario", which aims at producing 20% of US Power from wind energy by the end of 2030. Under the "20% Wind Scenario", a cumulative total of 7,600 million metric tons of CO_2 emissions would be avoided by 2030, and more than 15,000 million metric tons of harmful CO_2 emissions would be avoided

through 2050. This would potentially also reduce cumulative water consumption in the electric sector by 8% (or 4 trillion gallons) from 2007 through 2030 – significantly reducing water consumption in the arid states of the interior West. In 2030, annual water consumption in the electric sector would be reduced by 17% (See Figure 1.4). With such targets and environmental incentives, the research scope of wind energy has expanded significantly over the last three decades, from a few KiloWatts being produced by single turbine to a hundreds of MegaWatts of power (See Figure 1.3) being produced by a large array of optimally placed wind turbines commonly referred to as "wind farm" (See Figure 1.2a, 1.2b).

In this context, we must mention that studying and optimizing the harvest of wind power using wind turbines is a challenging task and thus it requires careful analysis of various aspects of wind turbines, e.g., the design of rotor blades, choosing the appropriate size of rotor diameter, hub-height, location and spacing of the wind turbines as well as the wind farm location. Additional considerations for wind farm design also include the large scale variation of mean wind speed and direction with time due to geophysical effects. Figures 1.5, 1.5b with a typical example of a wind rose diagram and the probability distribution of wind speed magnitude illustrate a dominant wind direction and weibull distribution of speeds that might exist for typical wind flows in certain locations. While extensive amount of research has been performed in the field of wind turbines, there are several aspects which demand a profound understanding. Studies in this domain are necessary not only for rudimentary reasons but also for the control and optimization required in the power generation process.

The wind turbines usually reside in the atmospheric boundary layer which has a Reynolds number $\sim 10^{10}$. This very high Reynolds number creates a large separation of the length scales, starting from the large scale motions spanning for kilometers of length and affected by the topography, geophyiscal effects and boundary conditions,

to the smallest dissipative scales in the order of centimetres affected by a Kolomogorov cascade. Studies focusing on the interaction of wind turbines and atmospheric boundary layer are important in order to illustrate how the turbulence at relevant length scales of energy production is modulated. Understanding these multiscale dynamics is essential in order to optimize and control the power generated by the wind farms.

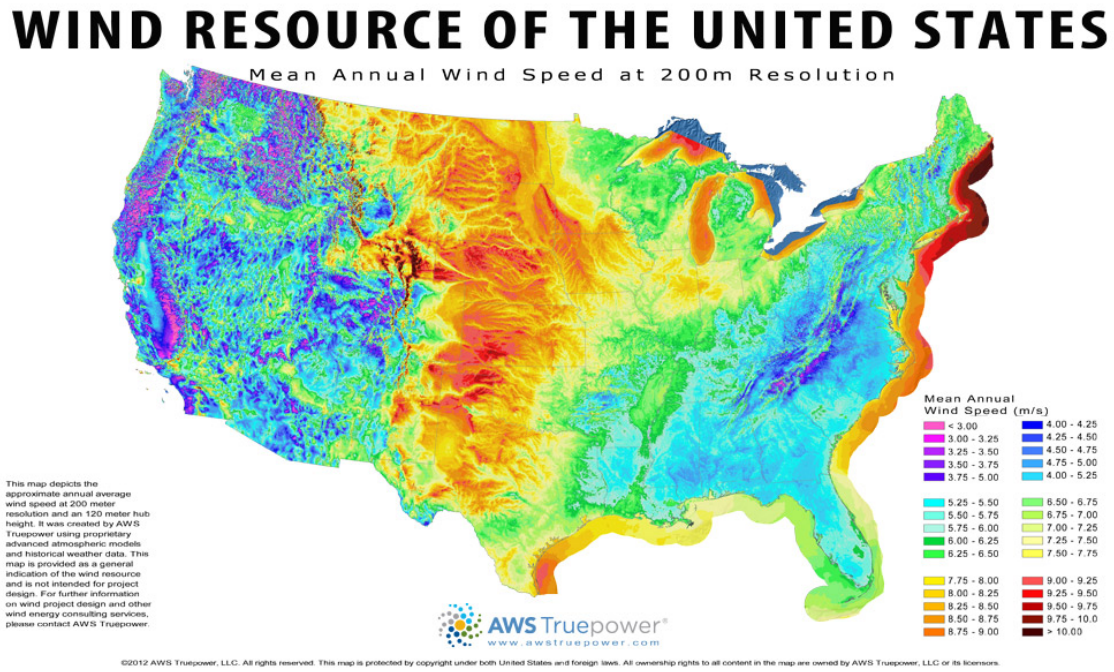

Figure 1.1: Mean annual wind speed in different states of US. Courtesy: AWS Truepower

source by:`https://www.awstruepower.com/`

From the numerical perspective, our current studies at very high Reynolds number atmospheric flow would call for very stringent mesh requirements to compute direct simulation (DNS) ($N_x \times N_y \times N_z \sim Re^{9/4}$) and hence would render the method computationally infeasible for ABL flows [1–3]. Large eddy simulation (LES) of wind turbine arrays is a promising technique with the potential of yielding a reliable data concerning the flow patterns as well as the energy output of turbines in a wind plant. An LES is justified for such calculations since it resolves the spatio-temporal evolu-

(a) (b)

Figure 1.2: (a) Offshore wind farm at Horn-Rev, Denmark depicting wind turbine wakes (b) A classical Onshore wind farm at Little Cheyne Court, UK.

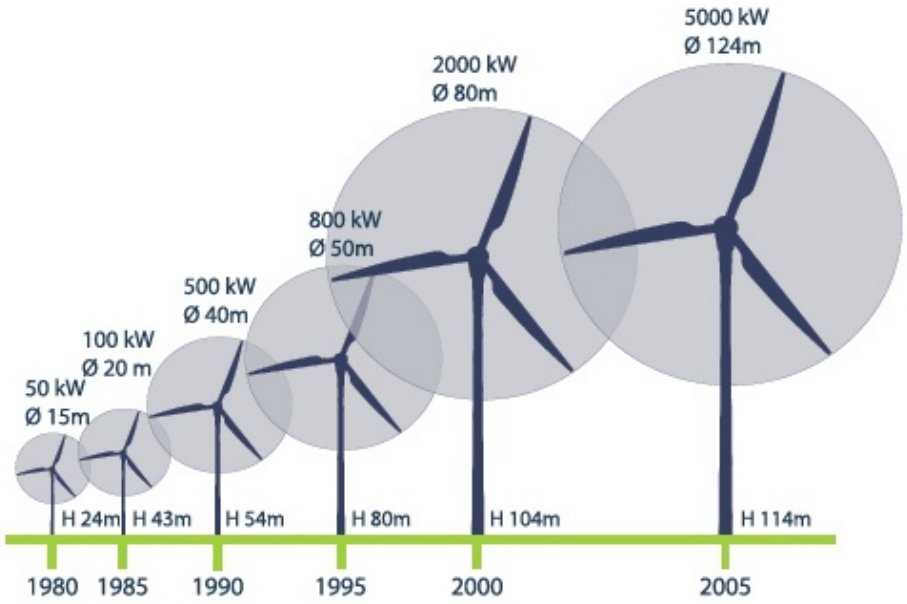

Figure 1.3: Growth trend in Wind Turbine Size used in wind farms from 1985 to 2005

tion of large scale flow structures faithfully, which are the dominant contributors to the energy generated by wind turbine. Several attempts at characterizing the performance of wind turbine arrays with LES have been undertaken [4–8] in the last decade.

Additionally, for more than two wind turbines as is the case in large wind farms, a fully resolved calculation of the wind turbine blades is practically infeasible. Reduced-

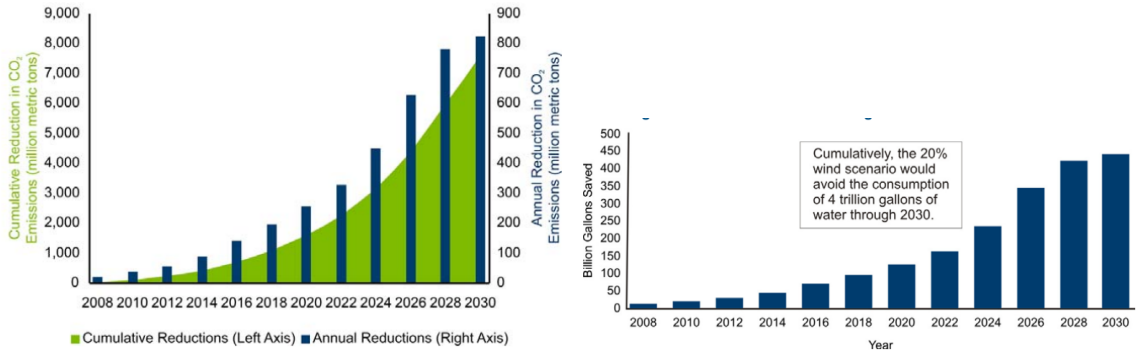

(a) (b)

Figure 1.4: Propose reduction of (a) CO_2 emission (b) Water capacity, projected till 2030 with the goal towards "20 % Wind Scenario"

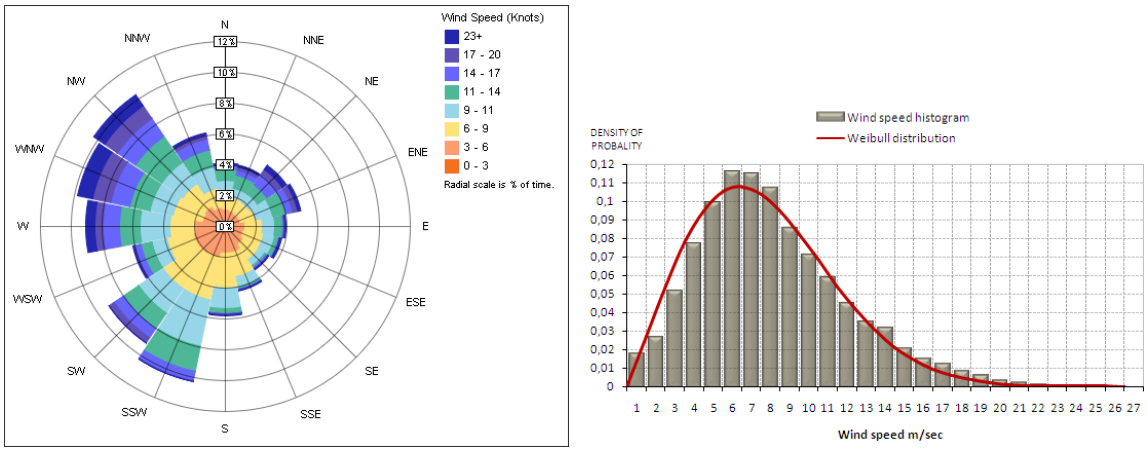

(a) (b)

Figure 1.5: (a) A typical wind rose depicting the dominant wind direction and magnitude (b) A typical wind speed probability density function illustrating trends of weibull distribution.

order aerodynamic models representing the effect of the rotating blades on the flow emerged and later evolved due to the computational bottleneck of fully-resolved calculations [4, 9–11]. Actuator line (AL) model is the state-of-art reduced order model that has been used in the recent literature [11, 12] and is also used in our current studies [13] in conjunction with LES of atmospheric boundary layer. It is important to note that most large scale wind farm simulations performed till date use fully developed wind turbine array boundary layer (WTABL) with periodic bound-

ary conditions [5, 14, 15] or precursor turbulent inflow condition [7, 16–18] and have focused on the velocity variations and power generation by the wind farms. Studies by [19–24] have also looked into the length scales of flow structures present in the wind turbine ABL interaction, that contribute to wind turbine power using various methods like visualization, temporal Fourier spectra, momentum and energy stream tubes and POD based methods. However, these studies involving the length scales have so far not focused on their spatial organization and coherence which are essential for understanding the modulation of large scale structures in atmospheric turbulence due to the presence of wind turbines. Understanding the organization in different length scale structures would elucidate more on the scales that contribute to wind turbine power.

The current thesis focuses on an improved understanding of the physics of the multiscale interaction of the wind turbine and ABL that contributes to turbine power and modulation of large scale structures. This study illustrates the fundamental mechanism in wind farms that results in the modulation of near wall turbulence and understand the dynamics behind the scaling laws of shape, structure of the organized eddies in wind farms. Our study retains its novelty in the focus and it is expected to elucidate more on the design efficiencies of wind turbine arrays from our understanding of length scales which are directly related to the optimization capabilities of power production and thrust generation in turbine blades.

1.1 Document Outline

This chapter (Chapter 1) is focused on providing the background motivation for the current work involving wind farms. Chapter 2 describes the numerical methodology in LES framework adopted for the current study with spectral element method.

In Chapter 3, we discuss the formulation, development and validation of the neutral atmospheric boundary layer model, in which the wind turbines reside and interact with. In this chapter, we address the question related to a better understanding of the numerical methods used in simulating neutral ABL, and their capability in capturing near-wall physics. It must be mentioned that Chapter 3 contains excerpts of the text from a work by the author and the PhD Committee Chair in Physics of Fluids. In Chapter 4, we begin by building our wind farm model based on a useful theoreticial conceptualization of wind turbine array boundary layer (WTABL). The numerical methodology in LES framework has been developed in a similar manner as discussed in Chapter 3. Our study reported in Chapter 4 adresses the questions related to the length scales that are responsible for power generation in wind farms and the modulation of near wall structures using spectral/Fourier analysis. Chapter 4 is taken from a work by the author and the PhD Committee Chair in Physical Review Fluids. The work in Chapter 5 stems from an idea proposed in the Conclusion in Chapter 4. This chapter studies wind farms containing turbines at different scales (diameter and hub height) in a WTABL framework. The work involves the investigation of the dynamics of the wind turbines at different scales and whether the small scale turbines has the potential to be benefitted in terms of power due to the modulation of large turbulent structures by the large scale turbines.

Chapter 6 directly builds on the shortcomings of the assumptions in WTABL framework as in Chapters 4, 5. The WTABL framework relies on horizontally periodic boundary conditions which enforces large-scale homogeneity in the horizontal direction, and only allows for small scale heterogeneity in between the turbines. This allows the model to develop streamwise heterogeneity that occurs due to phenomenon like the growth of the inner layer and the wake impingements in the subsequent rows of the turbines after the first row. In an effort to better understand the contribution

of multiscale dynamics that affect such finite scale interactions, we propose to utilize an inflow-outflow methodology in spectral element simulations of wind turbine arrays, with the inflow driven by a precursor ABL simulation using spectral interpolation technique. This inflow-outflow methodology ensures that the streamwise heterogeneity can be captured due to the presence of a finite size wind turbine array in the atmospheric boundary layer. Due to heterogeneity in the streamwise direction, advanced methods of analysis involving wavelet and Fourier-POD transforms have been utilized in the wind turbine array framework to improve our understanding of the turbulent interaction of wind turbines and ABL. Eventually, in Chapter 7, we build on the wind-turbine array study with inflow-outflow conditions to incorporate some of the features of realistic wind, e.g., time-varying mean wind speed and wind direction, which may be imparted from large scale geophysical effects. The realistic mean winds were fed from a cup and vane anemometer data at the Alpha Ventus wind farm in the North Sea collected by the environmental remote sensing group, Arizona State University headed by Dr. Ronald J. Calhoun. This chapter addresses the question related to the capability of LES models coupled with a mean wind information in capturing some structures of the realistic flow past the wind farms. Finally, Chapter 8 is dedicated to summarizing the major conclusions of the work and to the discussion of the potential future directions of the research.

1.2 Novel Contribution

This section outlines the major contributions that this work provides to the fields of science and engineering, and specifically the wind farm and atmospheric boundary layer community. A list of these contributions is provided below.

- Novel high-fidelity data have been collected for wind farm turbulence (highly resolved in the turbine rotor regions), .e.g., periodic wind farm cases in WTABL

framework, inflow-outflow cases with fully developed constant pressure driven neutral ABL inflow as well as inflow-outflow cases with the incoming flow to wind turbines involving field data driven neutral ABL. The data features an improved resolution in the turbine rotor area (streamwise and plane of the rotor) of wind farms, with resolved scales as fine as $5-10\%$ of the rotor diameter compared to the previous actuator line or actuator disc computation [5,7,24,25] adopted for wind farm studies with near turbine resolution of $\sim 10-50\%$ of the rotor diameter. Such highly resolved wind turbine rotor region captures the essential dynamics like helical vortices shed by the rotors and how they influence the atmospheric turbulence.

- Novel analysis techniques have been utilized including application of wavelet analysis and a Fourier POD decomposition to wind farm flows for understanding the large scale dynamics.

- Enhanced understanding of the structure of turbulence in wind farms via a series of visualization and spectral analysis have been achived which are documented specifically in an itemized form below.

  (i) Understanding the fundamental mechanism of the modulation of near wall attached eddies in the presence of downdraft mechanisms from mean kinetic energy(MKE) flux. We have also found that these mechanisms which lead to the growth of the integral length scale are also a function of the farm layout. In this context, we have proposed a theory corresponding to the scaling laws of attached eddies near wall and rotor region, and how it leads to the extented k^{-1} scaling in the wind farms. To the author's knowledge, the fundamental mechanisms found in the current work, has not been explored before. Additionally, identifying the coherence of the large scale

eddies, contributing to turbine power is novel, and it is confirmed for the first time, the prevalent contribution of scales larger than rotor diameter contributing to MKE flux by the direct computation of spatial spectrum of wind farms, documented in previous experimental observations using temporal data.

(*ii*) Comprehending the mechanisms involved in the heterogeneity of large scale structures in finite size wind farms, that are modulated in the inner layer and rotor region and responsible for turbine power. We have used wavelet intermittency function and spatial coherence involving wavelets in order to understand the spatial variability of the energy content and how "linearly correlated" and size of the large eddies at various streamwise locations are, due to the mechanisms like growth of the inner layer and wake impingement effects. To the author's knowledge, wavelet analysis of the spatial data in wind farm turbulence were conducted for the first time to gain an improved understanding of the spatial heterogeneity of large scales.

Chapter 2

NUMERICAL METHODS

2.1 Introduction

In the present chapter, we illustrate the numerical methods used for our study of wind farms in large eddy simulation (LES) framework. In particular, we have an open-source research code Nek5000 that solves a variational form of Navier-Stokes equation for all our numerical studies. Nek5000 is based on an exponentially accurate high-order spectral element discretization and is highly-scalable on massively-parallel computers [26]. Currently, the code supports a diverse range of fluid solver capabilities in incompressible and low Mach number fluid dynamics (more than 200 published scientific papers and more than 2000 researchers in community). Nek5000 is maintained through an svn and git repositories and is freely available for download through the svn checkout command, or github. The repository contains all the source files and subroutines, as well as auxiliary tools for pre/post processing and several benchmark examples.

2.2 Navier Stokes Equation

3D Navier-Stokes equation solving for velocity field $\boldsymbol{u}(\boldsymbol{x}, t)$, scalar pressure field $p(\boldsymbol{x}, t)$ with input volume force function $\boldsymbol{f}(\boldsymbol{x}, t)$ (momentum and continuity equations).

$$
\begin{aligned}
\frac{\partial \boldsymbol{u}}{\partial t} + \boldsymbol{u}.\nabla \boldsymbol{u} &= -\frac{1}{\rho}\nabla p + \nu \nabla^2 \boldsymbol{u} + \boldsymbol{f} \qquad \text{in} \quad \Omega \times (0,T), \\
\nabla.\boldsymbol{u} &= 0 \quad \text{in} \quad \Omega \times (0,T), \\
\boldsymbol{u}(\boldsymbol{x},0) &= \boldsymbol{u}^0(\boldsymbol{x}) \quad \text{for} \quad \boldsymbol{x} \in \Omega, \\
\mathcal{B}(\boldsymbol{u}_b) &= 0 \qquad\qquad \text{in} \quad \partial\Omega.
\end{aligned} \tag{2.1}
$$

Here, $\Omega \subset \mathbb{R}^3$ is the three-dimensional domain in Equation (A.1), $\boldsymbol{u}^0(\boldsymbol{x})$ represents the initial condition of the PDE and $\partial\Omega$ represents the external surface of Ω on which the boundary conditions $\boldsymbol{u}_b$ are defined.

In the computational domain, the 3D incompressible Navier-Stokes equations along with boundary conditions are solved in weak formulation using exponentially accurate higher order spectral element methods [27], [28], [29] (Refer to Appendix A.1 for details).

In spectral element method Nek5000, the weak formulation of the equations is carried out by weighted residual technique (orthogonal projection of the residual of the equations), or more specifically by Galerkin projection method [29], [30] cast using the concept of inner products in functional spaces.

Usually, in weighted residual technique the discrete inner products are carried out using summation on the quadrature nodes defined as the roots of the orthogonal polynomials from the solutions of the Sturm-Liouville problem [31], with the corresponding quadrature weights.

It must be mentioned, that a consistent approach of using spectral element discretization involves using polynomial orders of pressure interpolants (basis functions) usually two orders lower than the velocity interpolants, known as the $\mathbb{P}_N - \mathbb{P}_{N-2}$ approach. This is done to essentially remove the spurious modes of pressure along the lines of finite volume approach [28,30]. Using orthogonal interpolating polynomi-

als (Legendre polynomials) as basis functions on $N+1$ quadrature nodes as defined above ensures that the numerical integration is exact for polynomials of degree up to $2N+1$. (For details of quadrature nodes, qudrature weights see Appendix A.1.2, for Legendre polynomial see Appendix A.1.1, A.1.2)

In spectral element methods [27], [30], [29], the decomposition of the computational domain consists of subdividing $\bar{\Omega} = \Omega \cup \partial\,\Omega$ into E non-overlapping adjacent rectilinear elements such that $\bar{\Omega} = \cup_{e=1}^{E} \Omega_e$. Each Ω_e is the image of a reference subdomain under a mapping $\boldsymbol{x}^e(\boldsymbol{r}) \in \Omega_e \rightarrow \boldsymbol{r} \in \hat{\Omega}$, with a well defined inverse $\boldsymbol{r}^e(\boldsymbol{x}) \in \hat{\Omega} \rightarrow \boldsymbol{x} \in \Omega_e$, where the 3D reference subdomain is $\hat{\Omega} = [-1,1]^3$. Scalar functions within each local element Ω_e are represented as N^{th} order tensor product polynomials on a reference subdomain $\hat{\Omega}$. With such decomposition, a convenient choice of the functional spaces of velocity and pressure fields as discussed before, are commonly known as $\mathbb{P}_N - \mathbb{P}_{N-2}$ formulation (Refer to Equation(A.9) in Appendix A.1). In 3D, velocity function in the spectral element method in the element can be expressed as follows

$$u(r_1, r_2, r_3)|_{\hat{\Omega}} = \sum_{i=0}^{N_x} \sum_{j=0}^{N_y} \sum_{k=0}^{N_z} u^e_{ijk} \pi_{N_x,i}(r_1) \pi_{N_y,j}(r_2) \pi_{N_z,k}(r_3), \quad r_1, r_2, r_3 \in [-1,1]^3, \tag{2.2}$$

where, $\pi_{N_x,i}(r_1)$, $\pi_{N_y,j}(r_2)$, $\pi_{N_z,k}(r_3)$ are the Lagrange polynomial based interpolant of degree N_x, N_y and N_z. Identically the pressure function in SEM in the local element, with $\pi^p_{N,j}(\zeta) \in \mathbb{P}_{N-2}(\zeta)$ can be given as

$$p(r_1, r_2, r_3)|_{\hat{\Omega}} = \sum_{i=1}^{N_x-1} \sum_{j=1}^{N_y-1} \sum_{k=1}^{N_z-1} p^e_{ijk} \pi^p_{N_x,i}(r_1) \pi^p_{N_y,j}(r_2) \pi^p_{N_z,k}(r_3), \quad r_1, r_2, r_3 \in [-1,1]^3 \tag{2.3}$$

(See Equations(A.18, **??**) in Appendix A.1.2 for details abount Lagrange interpolants). It must be understood that due to the invertible mapping between Ω_e and $\hat{\Omega}$ there exists a one-to-one correspondence between the nodal values of $u(x,y,z)|_{\Omega_e}$, $p(x,y,z)|_{\Omega_e}$

and reference subdomain values $u(r_1, r_2, r_3)|_{\hat{\Omega}}$, $p(r_1, r_2, r_3)|_{\hat{\Omega}}$ and the coefficients u^e_{ijk}, p^e_{ijk} are the local nodal values of $u|_{\Omega_e}$, $p|_{\Omega_e}$ respectively in the nodal-based formulation. The local to global mapping of data is carried out using a boolean connectivity matrix that preserves inter element continuity.

The differential operators in the current SEM formulation have been carried out using efficient implementation of tensor products(Refer to [32], [33], [30] and for details). The block matrices formed by Kronecker/tensor products (Appendix A.3) are advantageous since various important matrix operations required in SEM like matrix inversion, affine transformation for differentiation, eigenvalue calculations can be obtained by using these linear algebra operators on much smaller matrices than the global matrices [32], [30]. Hence, tensor products are computationally very efficient in terms of parallel scalability when used in fast 2D/ 3D Poisson solvers, filtering and other linear operators in the current SEM methodology [34].

The time discretization of Navier-Stokes solver in the current spectral element code Nek5000 [35] involves k^{th} order backward difference/extrapolation scheme (BDF/EXT) where $k = 2$ or 3 (See [30] for details.). The code is fully dealiased using 3/2 rule [36, 37], the velocity is solved using preconditioned conjugate gradient (CG) method and the pressure solver uses iterative generalized mean residual solver (GMRES) method in Krylov subspace.

2.3 Large Eddy Simulation

For the mathematical formalism of LES we use the tensorial notation of the Navier-Stokes equation. In 3D, the tensorial notation of NS equation can be given by

$$\frac{\partial u_i}{\partial t} + u_j \frac{\partial u_i}{\partial x_j} = -\frac{1}{\rho}\frac{\partial p}{\partial x_i} + F_i + \nu \frac{\partial^2 u_i}{\partial x_j \partial x_j} \tag{2.4}$$

For very large Re there is a large separation between the largest integral scales and smallest dissipative (Kolomogorov) scales of motion. The large eddy simulation thus aims at capturing the spatio-temporal evolution of large scales of motion while modelling the relatively smaller scales also known as the subgrid scales of motion. Please note, that for simulations involving wind turbine arrays the forcing function F_i used is the actuator line model [12], the details of which are discussed in Section 2.4

The dynamical equation of the largest scales of motion can be obtained by applying a low-pass filtering to the Navier-Stokes equation.

For any scalar field $\phi(\boldsymbol{x}, t)$ the filtering in physical space can be represented as a convolution product. The resolved part $\widetilde{\phi}(\boldsymbol{x}, t)$ can be written as

$$\widetilde{\phi}(\boldsymbol{x}, t) = \iint_{\Omega} \phi(\boldsymbol{\xi}, t') G(\boldsymbol{x} - \boldsymbol{\xi}, t - t') \mathrm{d}t' \mathrm{d}^3\xi \tag{2.5}$$

with the convolution kernel G being the characteristic of the filter used and Δ and τ_c are cutoff scales in space and time associated with the kernel. Even though the filtering performed in large eddy simulation is mostly spatial in nature, it imposes and inherent temporal cut-off scale as well [38].

The filtered NS equations can be given as

$$\begin{aligned} &\frac{\partial \widetilde{u}_i}{\partial t} + \widetilde{u}_j \frac{\partial \widetilde{u}_i}{\partial x_j} + \frac{1}{\rho}\frac{\partial \widetilde{p^*}}{\partial x_i} - \widetilde{F}_i - \nu \frac{\partial^2 \widetilde{u}_i}{\partial x_j \partial x_j} = -\frac{\partial \tau_{ij}^{SGS}}{\partial x_j} \\ &-\int_{\partial\Omega} G(\boldsymbol{x} - \boldsymbol{\xi}) [p(\boldsymbol{\xi}) - \nu \left(\frac{\partial u_i}{\partial x_j}(\boldsymbol{\xi}) + \frac{\partial u_j}{\partial x_i}(\boldsymbol{\xi}) \right)] n_j \mathrm{d}S \end{aligned} \tag{2.6}$$

$$\frac{\partial \widetilde{u}_i}{\partial x_j} = -\int_{\partial\Omega} G\left(\boldsymbol{x} - \boldsymbol{\xi}\right) u_j n_j(\boldsymbol{\xi}) \mathrm{d}S = 0 \tag{2.7}$$

where the "tilde" represents the low-pass filtered variable and $\widetilde{u}_i$ is the instantaneous filtered velocity field in the i^{th} direction. The terms in the RHS of the Equations(2.6, 2.7) are direct consequence of *integration by parts & Gauss Divergence Theorem* and can be attributed as boundary commutation errors (For detailed derivation, see [39]). In this respect, we would like to point out that x is the streamwise direction, y is the spanwise direction and z is the wall-normal direction of flow.

Usually the filter chosen in the practise of LES is a linear operator and satisfies some fundamental properties like conservation of constants, principle of linear superposition and commutation with other linear operators like differentiation. Consequently, the non-linear convective term is the only term in the NS equation that gives rise to commutation error in the interior of the flow domain Ω (The boundary commutation errors are neglected for the time-being).

$$\frac{\partial \widetilde{u}_i}{\partial t} + \widetilde{u}_j \frac{\partial \widetilde{u}_i}{\partial x_j} = -\frac{1}{\rho}\frac{\partial \widetilde{p^*}}{\partial x_i} + \frac{\partial \tau_{ij}^{SGS}}{\partial x_j} + \widetilde{F}_i + \nu \frac{\partial^2 \widetilde{u}_i}{\partial x_j \partial x_j} \tag{2.8}$$

The modification to the original Navier-Stokes equations thus comes with an additional subgrid stress tensor $\tau_{ij}^{SGS}(u_i, u_j)$ which arises due to the filtering of the non-linear term , which is given by

$$\tau_{ij}^{SGS} = \widetilde{u}_i \widetilde{u}_j - \widetilde{u_i u_j}. \tag{2.9}$$

The modified pressure in the filtered equation can be given as

$$\widetilde{p^*} = \widetilde{p} + \frac{1}{2}\rho \widetilde{u_i}^2 \tag{2.10}$$

The interior closure problem of LES thus relies on developing a realistic model of $\tau_{ij}^{SGS}(u_i, u_j)$ by using a function $S_\tau(\widetilde{u}_i, \widetilde{u}_j)$. It is quite straightforward to visualize that the transfer of subgrid energy from the large to small scales of motion can be

given as $-\tau_{ij}^{SGS}(u_i, u_j)S_{ij}$ which manifests that the effects on smaller scales of motion rely on the subgrid stress model.

Some of the fundamental properties of $\tau_{ij}^{SGS}(u_i, u_j)$ that potentially needs to be seen in the closure $S_\tau(\widetilde{u}_i, \widetilde{u}_j)$ are enumerated below.

- τ_{ij}^{SGS} is translation and rotation invariant
- τ_{ij}^{SGS} is symmetric and reflective: $\tau_{ij} = \tau_{ji}$; $\tau_{ij}(-u_i, -u_j) = \tau_{ij}(u_i, u_j)$
- $\tau_{ij}^{SGS}$is realizable: $\tau_{ij}^{SGS}(u_i, u_j)\xi_i\xi_j \geq 0, \quad \forall \xi \in \mathbb{R}^3$
- Finite turbulent kinetic energy and $||\tau_{ij}^{SGS}(u_i, u_j) - S_\tau(\widetilde{u}_i, \widetilde{u}_j)|| \ \leq C(u_i)\Delta^\alpha$ for some $\alpha \geq 0$
- τ_{ij}^{SGS} is essentially dispersive and **not dissipative** in nature

However, for astronomically high Reynolds number flows as in neutral ABL, optimally dissipative SGS closure schemes have been used to correctly predict the physics of the inner and outer layer phenomenon.

2.3.1 Large Eddy Simulation: Subgrid Scale Modelling

The spatially filtered 3D Navier-Stokes equations for large eddy simulation of neutral ABL flows can be obtained by incorporating a convolution integral filter on the original Navier-Stokes equations

$$\frac{\partial \widetilde{\mathbf{u}}}{\partial t} + \widetilde{\mathbf{u}}\nabla\widetilde{\mathbf{u}} + \frac{1}{\rho}\nabla\widetilde{p^*} - \widetilde{\mathbf{F}} - \nu\nabla^2\widetilde{\mathbf{u}} = -\nabla \cdot \boldsymbol{\tau}^{SGS}(\widetilde{\mathbf{u}}, \widetilde{\mathbf{u}}) \tag{2.11}$$

The subgrid stress (SGS) tensor in Equation (2.11), $\boldsymbol{\tau}^{SGS}(\widetilde{\mathbf{u}}, \widetilde{\mathbf{u}}) = \widetilde{\mathbf{u}\mathbf{u}^T} - \widetilde{\mathbf{u}}\widetilde{\mathbf{u}}^T$ arising from the non-commutativity of filtering with the nonlinear advection term, is modelled

using a Smagorinsky type eddy viscosity closure

$$\boldsymbol{\tau}^{SGS} - \frac{1}{3} tr(\boldsymbol{\tau}^{SGS})\mathbb{I} = -2\nu_t \nabla^s \widetilde{\mathbf{u}}, \tag{2.12}$$

where $\nabla^s \widetilde{\mathbf{u}} = \frac{1}{2}(\nabla \widetilde{\mathbf{u}} + \nabla \widetilde{\mathbf{u}}^T)$ is the filtered stain rate, and $\mathbb{I}$ is the identity tensor. In classical Smagorinsky model, the eddy viscosity is given by

$$\nu_t = (l_f)^2 |\nabla^s \widetilde{\mathbf{u}}|, \tag{2.13}$$

where $|\nabla^s \widetilde{\mathbf{u}}| = (2\nabla^s \widetilde{\mathbf{u}} : \nabla^s \widetilde{\mathbf{u}})^{1/2}$. The filter length scale l_f is assumed to be proportional to the grid filter width (cutoff scale) Δ, $l_f = C_s \Delta$, and C_s is the non dimensional Smagorinsky coefficient. According to 40, l_f can also be interpreted as the mixing length of the subgrid scale eddies (l_f is usually less than Δ justifying the name "subgrid scale"). The grid filter width here is calculated as $\Delta = (\Delta x \Delta y \Delta z)^{1/3}$ [41], where $\Delta x, \Delta y, \Delta z$ are taken at the GLL nodes as the weighted averages of the node distances (analogous to a central difference scheme) at the element interior and one sided difference at the element boundaries. For high Reynolds number turbulent ABL flow, we use near wall algebraic wall damping function by Mason and Thompson (1992) [42],

$$\frac{1}{l_f^n} = \frac{1}{(C_0 \Delta)^n} + \left\{ \frac{1}{\kappa(z + z_0)} \right\}^n, \tag{2.14}$$

or, written directly in terms of the Smagorinsky coefficient,

$$\frac{1}{C_s^n} = \frac{1}{C_0^n} + \left\{ \frac{\Delta}{\kappa(z + z_0)} \right\}^n. \tag{2.15}$$

Equation (2.14) essentially represents an ad-hoc blending function with parameters C_0, n, such that the filter length scale saturates at $l_f(z) \sim C_0 \Delta$ at the outer layer while retrieving Prandtl's mixing length $l_f(z) \sim \kappa(z + z_0)$ as we approach the wall. While C_0 controls the asymptotic value of $l_f(z)$, n controls the shape or the growth rate of $l_f(z)$ in the inner layer as we will see later. Here κ is the Von-Karman constant and $z_0 \ll H$ is the aerodynamic roughness length of the bottom "wall", H is the boundary layer thickness.

2.3.2 Model Assumptions: Boundary Conditions

In this section, we discuss the boundary conditions used in the LES framework. We begin with neutral atmospheric boundary layer (ABL) where the turbulence is generated from the shear in the flow over rough wall terrain. Our present model uses x as the streamwise direction, y as the spanwise direction and z as the wall normal direction in a cartesian framework. The mean streamwise velocity profile of ABL in the surface layer (roughly $10 \sim 20\%$ of boundary layer) [43–46] can be given as

$$\bar{U}(z) = \frac{u_\tau}{\kappa} \ln \frac{z}{z_0} + \frac{u_\tau}{\kappa} \psi_m(\frac{z}{L_M}), \quad z \gg z_0 \tag{2.16}$$

where, u_τ is the friction velocity scale, z_0 is the aerodynamic roughness length and $\kappa = 0.4$ is the Von Karman constant, ψ_m is a non dimensional momentum stability function and L_M is stability length scale by Monin and Obukhov. [43,47]. For neutral ABL, $L_M \to \infty$ and hence the mean velocity profile is essentially logarithmic in nature in the surface layer [47] with $\psi_m \to 0$.

The boundary layer (BL) thickness for flat plate type of turbulent flows can be usually expressed as $\delta/x \sim Re_x^{-p}$, where p is very close to 1 ($p = 0.8$ for turbulent flow over smooth flat plate) [48]. Consequently, the streamwise growth of the turbulent BL, could be expressed as $d\delta/dx \sim Re_x^{-(1+p)}$. Since $Re_x \approx 10^8 - 10^{12}$ for ABL flows, the growth of the turbulent BL $d\delta/dx \approx 0$ rendering periodic boundary condition in the homogeneous streamwise direction feasible. The spanwise boundary conditions are periodic since it is consistent with the physics of the flow. The top boundary condition is a stress free lid similar to the flat plate flow, i.e., $d\tilde{u}_x/dz = d\tilde{u}_y/dz = \tilde{u}_z = 0$. For extremely high Re ABL flows, the viscous sublayer $\delta_\nu/\delta \sim O(Re_\tau^{-1}) \approx 0$, and the aerodynamic roughness $z_0 \gg \delta_\nu$ ($\delta_\nu = \nu/u_\tau$, δ ABL thickness). Since the viscous layer cannot be resolved in such simulations, the use of shear-stress boundary conditions as near-wall modelling LES becomes imperative. Consequently, the bottom rough wall

model for ABL has been developed from the log-law of the wall coupled with Monin-Obukhov similarity theory [47] and near wall shear stress model of Schumann [49] and was further used by Businger et al. [43], Moeng [50] and Stoll and Porté-Agel [51]. At the bottom surface, we use a wall stress boundary condition without having to resolve the rough wall [52], relating the wall stress vector to the in-plane horizontal velocity vector $\widetilde{\boldsymbol{u}_h}$ at the first half-node from the wall using the standard Monin-Obukhov similarity law [47] along with no-penetration conditions of large eddies, $\widetilde{w} = 0$,

$$\frac{1}{\rho}\boldsymbol{\tau}_s = -\kappa^2 \frac{\widehat{\widetilde{\boldsymbol{u}}}_{h,\frac{\Delta z}{2}}(x,y,t)|\ \widehat{\widetilde{\boldsymbol{u}}}_{h,\frac{\Delta z}{2}}|(x,y,t)}{\log(\frac{z}{z_0})\Big|^2_{\frac{\Delta z}{2}}}, \tag{2.17}$$

where $|\ \widehat{\widetilde{\boldsymbol{u}}}_{h,\frac{\Delta z}{2}}| = \sqrt{\widehat{\widetilde{u}}^2_{\frac{\Delta z}{2}} + \widehat{\widetilde{v}}^2_{\frac{\Delta z}{2}}}$ and $\widehat{\widetilde{\boldsymbol{u}}}_{h,\frac{\Delta z}{2}} = \widehat{\widetilde{u}}_{\frac{\Delta z}{2}}\vec{e_x} + \widehat{\widetilde{v}}_{\frac{\Delta z}{2}}\vec{e_y}$ ($\vec{e_x}, \vec{e_y}$ are unit vectors in the x, y direction). The "hat" represents additional explicit filtering carried out in the modal space by attenuating $k_c = 4$, highest Legendre polynomial modes of the spectral element model (please, refer to Appendix A.4 for the description of the explicit filtering method). This explicit filtering is done along the lines of [53, 54] to control the log-layer mismatch and to bound the wall shear stress. For collocated spectral element methods $\widehat{\widetilde{u}}_{\frac{\Delta z}{2}}$, $\widehat{\widetilde{v}}_{\frac{\Delta z}{2}}$ are calculated as an interpolation at half wall node $\Delta z/2$ i.e., between $\widehat{\widetilde{u}}(x,y,0,t)$ and $\widehat{\widetilde{u}}(x,y,z=\Delta z,t)$ (and similar procedure for $\widehat{\widetilde{v}}$). The aerodynamic roughness is $z_0 = 10^{-4}H$ which corresponds to the previous literature [44, 54]. An existing literature on near wall modelling [41, 44, 49, 50, 54–56] have generally used vertically staggered finite-difference schemes when using stress boundary conditions for rough wall models with $\Delta z/2$ being a physical grid distance of the horizontal velocities away from the wall. The present paper incorporates a new methodology for rough wall modeling using collocated spectral element method, which is reflected in Equation (2.17). Our spectral element model for shear stress developed using weak formulation is physically consistent, where the wall model essentially

acts as a momentum flux closure scheme. The element level filtering and the weak formulation of shear stress are discussed in the subsequent sections A.4, A.5.

2.4 Actuator Line Model for Wind Turbines

In the subsequent sections we describe the numerical methodologies used specific to the modelling of 3 bladed wind turbines and the computational domain used in wind farms. In the actuator line model, the local lift ($L_{i,k}$) and drag ($D_{i,k}$) forces experienced by each discrete blade element i of each turbine k are calculated as

$$\begin{aligned} L_{i,k} &= \frac{1}{2} C_l(\alpha_{i,k})\, \rho\, V_{rel,i,k}^2\, c_{i,k}\, w_{d,k}, \\ D_{i,k} &= \frac{1}{2} C_d(\alpha_{i,k})\, \rho\, V_{rel,i,k}^2\, c_{i,k}\, w_{d,k}, \end{aligned} \tag{2.18}$$

where $c_{i,k}$ is the chord length of the corresponding airfoil at each blade element location i of the turbine k, and $w_{d,k}$ is the width of the actuator line elements, which is kept constant at each actuator line and thus only varies between the turbines and not the blade element locations. $V_{rel,i,k}$ is the local velocity magnitude relative to the rotating blade element and is computed from the velocity triangle for the rotating blade (see also Figure 2.2) as

$$V_{rel,i,k,} = \sqrt{u_{i,k}^2 + (\Omega_k\, r_{i,k} - v_{\theta,i,k})^2)}. \tag{2.19}$$

Here, Ω_k is the rotor rotational speed of the turbine k, $u_{i,k}$ and $v_{\theta,i,k}$ are the local velocity components in the axial direction (perpendicular to the plane of rotation), and in circumferential direction (in the plane of rotation) obtained from Large Eddy Simulations, and $r_{i,k}$ is the radial coordinate of each blade element. The local angle of attack $\alpha_{i,k}$ is computed as $\alpha_{i,k} = \phi_{i,k} - \gamma_{i,k}$, where $\phi_{i,k}$ is the angle between the radial velocity and the rotor plane at each blade element,

$$\phi_{i,k} = \tan^{-1}\big(\frac{u_{i,k}}{\Omega_k\, r_{i,k} - v_{\theta,i,k}}\big). \tag{2.20}$$

The total reaction force from all the actuator line elements of all the turbines experienced by the fluid is distributed smoothly across the mesh points and is given as a forcing function in the Navier-Stokes equations

$$\widetilde{\mathbf{F}}_{AL}(x,\, y,\, z,\, t) = -\sum_{k=1}^{N_t} \sum_{i=1}^{N_b \times N_a} \left(L_{i,k}\vec{e}_{L,i,k} + D_{i,k}\vec{e}_{D,i,k}\right) \eta_\epsilon(|\vec{r} - \vec{r}_{i,k}|), \tag{2.21}$$

$\vec{r} = (x, y, z)$, where $\eta_\epsilon(d)$ is a Gaussian function in the form of $\eta_\epsilon(d) = 1/\epsilon^3\pi^{3/2} \exp\left[-\left(d/\epsilon\right)^2\right]$. $\vec{e}_{L,i,k}$, $\vec{e}_{D,i,k}$ are the local unit vectors for the lift and drag coefficients at the i^{th} blade panel of the k^{th} turbine. The summation in the forces is over all N_t turbines in the farm and all $N_b \times N_a$ actuator line elements per turbine, where N_b is the number of blades, and N_a is the number of actuator line elements per turbine blade. The value $\epsilon = 2\, w_d$ is used in the current study as suggested in [7, 12] for optimum results.

The azimuthal forces on wind turbine blade elements can be calculated as (See Figure 2.2 for reference),

$$F_{\theta,i,k} = L_{i,k} \sin\phi_{i,k} - D_{i,k} \sin\phi_{i,k}, \;\; \phi_{i,k} = \alpha_{i,k} + \gamma_{i,k}, \tag{2.22}$$

which can be utilized for the computation of the aerodynamic torque for each turbine as $T_k = \sum_{i=1}^{N_b \times N_a} r_{i,k} F_{\theta,i,k} \Delta r_{i,k}$ and the power

$$P_k = T_k \times \Omega_k. \tag{2.23}$$

2.5 Outflow Boundary Conditions of Wind Turbine Array

The boundary conditions for the rectangular domain of wind turbine array are very similar to the ABL domain (spanwise periodic, symmetry at the top and shear stress at the bottom "wall"), except for the streamwise direction where we choose to use a

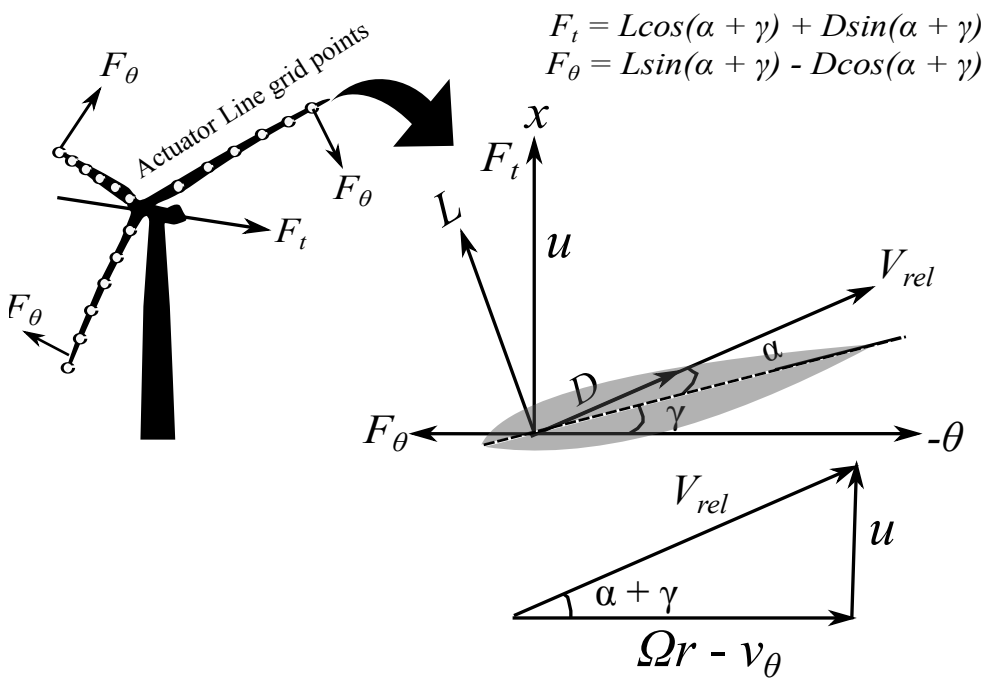

Figure 2.1: Actuator line forces obtained at different grid points (not to scale) of the turbine blades. V_{rel} obtained from the velocity triangle. F_t and F_θ are the axial thrust and rotational forces on the turbine blades due to aerodynamic lift (L) and drag (D) forces. θ: azimuthal direction, in the plane of the rotor motion. Ω: angular velocity of the rotor, r: radial distance in the blade from the center of the rotor. v_θ: azimuthal velocity of the rotor. Subscripts i, k for the local variables are omitted for clarity.

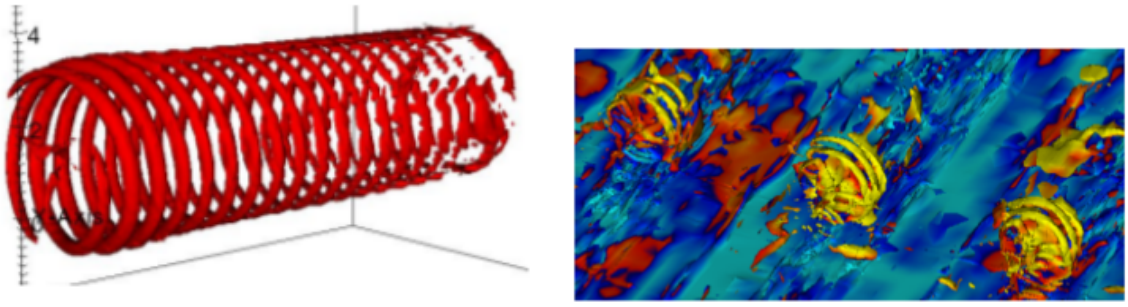

(a) (b)

Figure 2.2: (a) Helical vortices in a single turbine, observed in a uniform inflow $Re = 2 \times 10^4$ [13]. (b) Helical vortices observed in a wind turbine array [57] near the turbine rotor. Background of neutral ABL turbulence, $Re = 10^{10}$.

realistic inflow-outflow condition. The inflow condition is turbulent in nature and to maintain a realistic spatio-temporal coherence the inlow is being fed from a seperate

precursor ABL simulation. The choice of outflow boundary conditions in our spectral element code requires a careful analysis. Invoking Equation B.4 (See Appendix B.9 for more mathematical details) we see that the simplest choice of natural "do nothing" boundary condition at the outflow would be

$$(-p + \frac{1}{Re}\nabla \cdot \mathbf{u}) \cdot \mathbf{n} = 0 \quad \text{on} \quad \Gamma \tag{2.24}$$

However implementing such boundary conditions at high Reynolds number triggers amplification of outgoing large eddy structures at the outflow resulting in reflection and instability. To circumvent this problem we have used sponging by extending the domain with coarse elements and adding sufficient amount of artificial viscosity near the outflow region ensuring required dampening of the eddies before they go to the outflow boundary. However, sudden change in viscosity in the interface of physical and extended domain can be dangerous giving rise to spurious reflective waves which can potentially trigger instability. Consequently, we have extended the idea of carefully-designed non reflective sponging layer using simple Smagorinsky type viscosity in the sponge layer which restricts the indiscriminate growth of viscosity in that region. In the sponge-layer, $\nu = \nu_m + \nu_{sl}$, with ν_m being the molecular viscosity where $\nu_{sl} = (C_{sl}\Delta)^2|\widetilde{S}|$, with $|\widetilde{S}| = \sqrt{2\widetilde{S}_{ij}\widetilde{S}_{ij}}$. Δ is metric of grid spacing scale which is similar to that in LES Smagorinsky model [58]. In our spectral element model C_{sl} is designed to grow quadratically in the form $C_{sl} = b(x - x_0)^2$, with $b = 0.25$ and x_0 is the end of the streamwise extent of physical domain. The natural boundary condition with a non-reflective sponge layer is seen to stabilize eddies at the outflow. Additionally, we also plan to present the results from stabilized natural boundary conditions by Dong et. al [59] which can be given as

$$-p \cdot \mathbf{n} + \frac{1}{Re}\nabla \mathbf{u} \cdot \mathbf{n} - \frac{1}{2}|\mathbf{u}|^2\Theta(\mathbf{n}, \mathbf{u}) = 0 \quad \text{on} \quad \Gamma \tag{2.25}$$

where

$$\Theta(\mathbf{n}, \mathbf{u}) = \left(1 - \frac{\tanh(\mathbf{n} \cdot \mathbf{u})}{U\delta}\right)$$

is smooth Heaviside step function to remove sudden discontinuity of the outflow fluxes with $U,\ \delta$ being some chosen velocity and length scale in the flow and $\mathbf{n}$ is the unit normal vector at the outflow boundary. This boundary condition has been tested to stabilize energy of the system $1/2||\mathbf{u}||^2_{L_2(\Omega)}$ (projecting NS equation with $\mathbf{u}$) compared to a simple natural boundary condition [34] (See Equation 2.24).

Chapter 3

NEUTRAL ATMOSPHERIC BOUNDARY LAYER

3.1 Introduction

Accurate prediction of the turbulent transport phenomenon of momentum and the dynamics of wall bounded shear flows as in ABL require that various important spatio temporal scales of motion are captured efficiently within the flow. Understanding the dynamics of ABL at multiple length scales in the inner and outer layer becomes completely essential since the wind turbines live mostly in the inner layer of ABL. At present, the state-of-art computational resources allow us to perform direct numerical simulation (DNS) of wall bounded flows (mostly canonical in nature) with fine grid sizes resolving a span of length scales starting from the integral down to the smallest Kolomogorov scales at moderately high Reynolds numbers (Re) which serves as a "gold standard " [1] for numerical benchmark. With very high Reynolds number ($Re \sim O(10^8 - 10^{12})$) flows, as seen in an atmospheric surface layer, the scale separation increases and hence these cases are still beyond the reach of direct simulations in terms of computational resources (computational cost $N_x \times N_y \times N_z \sim O(Re^{2.7})$ [3]). The fidelity of the numerical simulations for very high Reynolds number flows, e.g. atmospheric boundary layer (ABL) with $Re \sim 10^8 - 10^{12}$ rely on the design of Large Eddy Simulations (LES) [38,39] with a capability of resolving only scales of a certain order Δ (related to a grid size or a filter size) while modelling the remaining scales smaller than Δ. For high $Re_\tau = u_\tau H/\nu$ (H is the boundary layer (BL) thickness, u_τ, skin friction velocity, and ν, the kinematic viscosity) rough-wall turbulent shear flows as in ABL, the grid requirements prohibit the resolution of viscosity dominated inner

layer $\delta_\nu = \nu/u_\tau$ and the scales associated with the aerodynamic roughness $z_0 \ll H$ at the bottom wall. Consequently, shear stress boundary conditions invoking Monin-Obukov similarity theory [47] instead of no-slip at the bottom wall has been used as a near wall model (cost independent of Re_τ) to emulate the law of the wall (LOTW) in atmospheric boundary layers.

In the near wall modeling LES framework, the dynamics of the smallest Kolomogorov or even the viscous dominated inner layer scales cannot be resolved, limited by the size of the computational grid. The smallest physical velocity and length scales that can be captured correspond to the attached eddies in the inertial layer ($\sim u_\tau$ for velocity scale and $\sim \kappa(z + z_0)$ for length scale that corresponds to a log layer, with $\kappa \approx 0.41$ being the Von-Karman constant and z being the normal distance from the wall [60]). These length scales are dominant compared to δ_ν and z_0 far away from the viscous wall effects. Apart from the physical length scales, there are additional scales that are generated as an artefact of the subgrid scale closure in an LES model and from the numerical grid in certain low order discretizations [61]. Although, both dissipative [44, 58, 62, 63] and dispersive [64, 65] subgrid scale closure models have been used in the past, dissipative type of subgrid closures (based on Smagorinsky model) have gained immense popularity in the last two decades in the simulation of atmospheric flows [50, 66–68], owing to its inherent stabilizing properties in high Re simulations while generating reasonably consistent physics in the flow, even without the energy backscatter [40, 42]. In particular for a dissipative LES model, a wall-damped standard Smagorinsky model [42] is being used in our current simulations as a less computationally expensive alternative to some other proposed models, such as turbulent kinetic energy (TKE) two equation model [69], equilibrium-based dynamic model [44], or adaptive Smagorinsky model [54]. For dissipative models , an artificial viscous sublayer due to LES dissipation in the grid will be formed near the wall

(see [38, 39] for more comprehensive discussion). The additional effects of filtering in the near-wall modelling would also impose an unphysical scale near the wall. It is thus the interaction of the physical and artificial length scales and the dominance of one over the other that gives rise to the near wall dynamics of the flow in numerical simulations [45].

The predominance of artificial length scales, especially in the near-wall region of high Re ABL flows have been long known to influence the statistics of the near wall region, e.g. the overshoot by $50 - 100\%$ of the normalized mean streamwise velocity gradient $\phi(z) = \kappa z/u_\tau \frac{dU}{dz}$ from the theoretical value of one (log law) in the lower 10% of the atmospheric boundary layer, commonly known as the problem of log-layer mismatch (LLM) [14, 42, 44–46, 67, 70, 71]. Sullivan et al. [67] pointed out that the neutral ABL models have worse results in terms of LLM compared to convective or stably stratified counterparts. LLM is usually attributed to a poor numerical accuracy (numerical dissipation and dispersion associated with insufficient grid resolution in discretization schemes) and inefficient SGS modelling. The elimination of LLM has been partially addressed in the previous literature. The related works include modifications to the design of the SGS model to incorporate decreasing integral length scales of the near-wall eddies [14, 42, 44, 53], explicit filtering in the wall closure model [53, 54, 72], and deconvolution type reconstruction techniques along with the Smagorinsky type dissipation [70]. More complicated techniques have also been proposed, including optimal control theory [73], designing high accuracy zones for the law of the wall [45], and blending functions in self-adaptive Smagorinsky models [54].

Unlike the previous engineered ways of eliminating the dominance of artificial length scales while addressing LLM, our choice of an efficient LES design for a rough wall-bounded flow (a canonical representation of a neutral ABL) is entirely based on the rudimentary knowledge of associated physical length scales of the turbulent near

wall eddies that are affected due to a nonlinear dissipative SGS and near wall stress models. A fundamental perception of such length scales acts as a better guidance to control the LES dissipation in a simplified way such that the effect of physical scales can be retrieved in the current study. While the phenomenon of the log-layer mismatch in the mean streamwise velocity gradient, or a relatively less known secondary peak generation in streamwise velocity variance seen in experiments are indeed manifestations of the dominance of *artificial length scales* in the flow [74, 75], an incorrect physics behind it cannot be properly analyzed in a coordinate framework in a physical space (x, y, z). Rather, these deficiencies are easier to visualize in a framework where the multiple length scales can be decoupled, since the nonlinearity in the LES model would incur different levels of detriment at different scales of motion. The presence of periodic boundary conditions in the streamwise and spanwise directions in the computation of neutral ABL flows (consistent with the physics due to homogeneity), conveniently allows us to conceive the definition of length scales in a proper way by studying important metrics in turbulence like kinetic energy and shear stress spectra in the wavenumber space [74, 76–78]. For example, the inverse of streamwise and spanwise wavenumbers (k_x, k_y), or the wavelengths $\lambda_{x,y} \sim 2\pi/k_{x,y}$, give an estimate of the length scales of turbulence corresponding to a specified turbulent kinetic energy and a shear stress in the spectra. However, to model the effects of the dynamics of the near wall coherent structures which scale with the wall normal distance z from the wall (e.g. attached eddies [60, 79]), the eddy viscosity of the SGS model must be decreased towards the wall to reflect the contribution of smaller integral scales of the near wall eddies. That would allow λ_x, λ_y and their scaling laws to be varying with z. The approaches presently proposed in the literature to dynamically control the eddy viscosity near the wall in the neutral ABL simulations, such as scale dependent dynamic Smagorinsky [44, 53] or scale adaptive Smagorinsky [54] models,

are expensive due to a calculation of eddy viscosity dynamically at every timestep and also due to a stringent time stepping requriement for stability compared to their static counterparts. To circumvent this problem, in the current simulation, we resort to a relatively inexpensive method of standard Smagorinsky with Mason and Thompson wall damping [42] for decreasing the eddy viscosity as we move towards the wall. In our current computations we use an exponentially accurate spectral element discretization in all directions that provides minimum dissipation and dispersion errors asymptotically [80, 81]. The previous literature have shown an importance of minimally-dissipative numerical schemes for Large Eddy Simulations [44, 82–84]. In this regard, the spectral element method can be considered a robust framework for analyzing the performance of the LES models, since the length scales involved in the current simulation correspond only to the physical length scales limited by the grid size and the artificial length scales due to the LES approximations.

In the current chapter, we investigate the effect of artificial length scales on neutral ABL (as incurred by the SGS and the near wall LES models), try to understand the nature of the *incorrect physical mechanisms* in the near-wall region that occur due to such scales and, finally, suggest how to choose the LES model parameters in a spectral element framework that can reduce the effect of artificial length scales and replicate the effect of true physical length scales in the flow with reasonable accuracy. Most importantly, our current study also provides a design rubric for standard Smagorinsky SGS closures in a spectral element method based on the least alteration of the true physics observed with these models. Furthermore, the multiscale spectral analysis with different subgrid models provides a basic understanding of the physics of the inner and outer-layer eddies of the neutral ABL and relates their similarities to the eddies found in high Re channel flows and turbulent boundary layers [74–78]. All the results in our current simulation have been compared against LES results from previ-

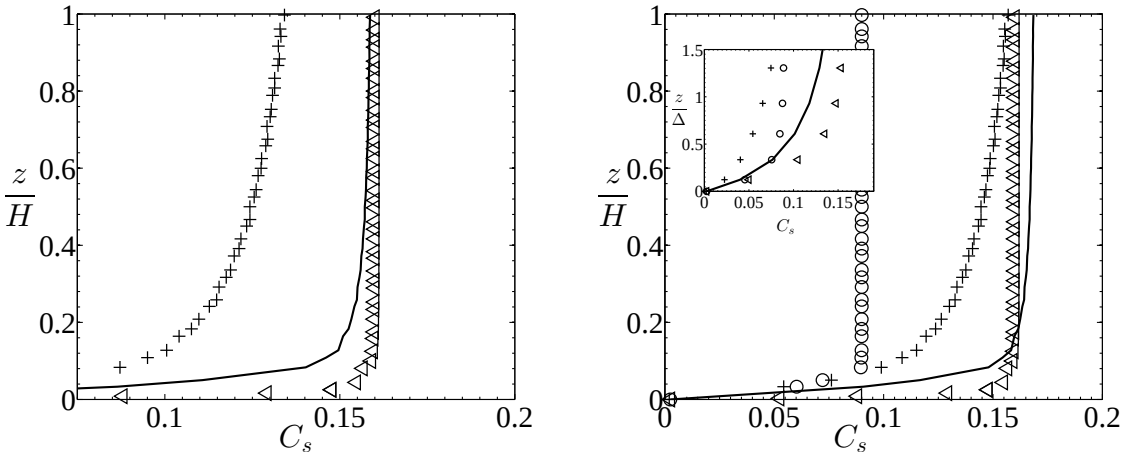

Figure 3.1: Smagorinsky coefficient C_s vs z/H for the current SEM grid ($30\times20\times24$ elements). (a) $C_0 = 0.16$ (fixed) $n = 0.5, 1, 2$. $\triangleleft$, $n = 2$; $-$, $n = 1$; $+$, $n = 0.5$. (b)$\triangleleft$, $C_0 = 0.16, n = 2$; $-$, $C_0 = 0.17, n = 1$; $+$, $C_0 = 0.19, n = 0.5$; $\circ$, $C_0 = 0.09, n = 2$; Inset: variation of C_s vs z/Δ, zoomed-in. $\kappa = 0.41$, von Karman constant; $z_0 = 10^{-4}H$, aerodynamic roughness length.

ous literature [44,53] or rigorous analytical results of turbulence statistics and spectra corroborated with the moderately high-Reynolds number DNS data [76, 77, 85].

3.1.1 Choice of LES Parameters

In order to analyze the subgrid-scale model given by Eqs. (2.12)–(2.15), we plot the dependence of the Smagorinsky coefficient C_s from Eq. (2.15) on the vertical distance z in Figure 3.1. The purpose of our analysis is to choose the appropriate values of the subgrid-scale model parameters C_0 and n to use in spectral-element methods in high-Reynolds number simulations of a neutral atmospheric boundary layer. Large Eddy Simulations in a continuous Galerkin based SEM with Smagorinsky-type models are not extensive in the community [86, 87] and even though some recent studies by Lodato and coworkers [88, 89] have explored moderate Reynolds number LES in a

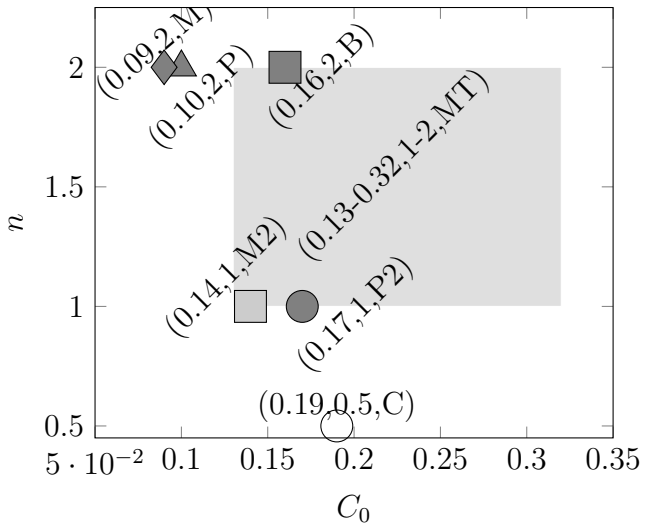

Figure 3.2: Values of $\{C_0, n\}$ tuple used in the past literature in a parametric space for wall-damped Smagorinsky model. MT (gray rectangular patch) – Mason and Thompson (1992) [42]; P,$P2$ – Porte-Agél et al. (2000) [44]; B – Bou-Zeid et al. (2005) [53]; M, – Meyers et al. [72]; $M2$ – Wu and Meyers (2013) [46]. C is the $\{C_0, n\}$ parameter tuple recommended for the standard wall-damped Smagorinsky model with SEM. $\{C_0, n\}$ corresponding to B,C,M and $P2$ are used in current simulations.

discontinuous flux based SEM framework, we don't know of any attempts to use these methods in the context of very high Reynolds numbers and atmospheric boundary layer flows. As discussed earlier, the value of C_0 controls the asymptotic value of the Smagorinsky coefficient C_s away from the wall. In order to understand the influence of the parameter n, the values of C_s for a fixed value of $C_0 = 0.16$ and different values of $n = 0.5, 1, 2$ are plotted in Figure 3.1a. Note that this plot is grid-dependent (as Δ is grid-dependent), and the Figure 3.1 is plotted for the baseline SEM grid ($30 \times 20 \times 24$ elements) used in the current simulations. We see that although the slope of C_s in the limit of $z \to z_{wall}$ does not depend on n which can also be understood from a previously discussed near-wall scaling of $l_f(z) \sim \kappa(z + z_0)$, the value of n controls the growth of C_s in the inner layer and, specifically, lower values of n result in a slower growth of C_s and a longer vertical distance it takes for C_s to saturate to its asymptotic value of C_0. This slow growth introduces a physically-relevant dependence of C_s on

z/Δ in the inner layer that results in correct near-wall dynamics and represents consistent trends of filter scales with grid-refinement. It is thus understandable that, in order to provide comparable dissipation length scales in the outer region, higher values of C_0 are usually used with lower values of n: $C_0|_{n=0.5} > C_0|_{n=1} > C_0|_{n=2}$. This is indeed reflected in the choice of parameters C_0 and n reported in the previous literature [5,42,44,53,72] and summarized here in a parametric form in Figure 3.2. The dependence of C_s versus z for the current choice of parameters is shown in Figure 3.1b. In addition to standard values of $n = 1, 2$, we also propose to explore a lower value of $n = 0.5$ ($\{C_0, n\} = \{0.19, 0.5\}$) than reported in the previous literature, which corresponds to a slower growth of C_s in the inner layer and provides a better control of near-wall dissipation length scales. We will show in Section 6.3 that this model indeed performs remarkably well in the SEM LES of atmospheric boundary layer flows and captures physically consistent near wall and outer layer eddies. Interesting to note that the slower inner growth of C_s corresponding to $C_0 = 0.19, n = 0.5$ is similar to the dynamic models of Porté-Agel [44]. In addition, we also consider an extremely low value of $C_0 = 0.09$ with $n = 2$ similar to [72] in our simulations and show that attempts to control the near-wall dissipation by lowering the value of C_0 without changing the near-wall growth of C_s (determined by n) results in an unphysical turbulence in the current spectral-element method.

Considering also the variation in the filtering parameter k_c in the near-wall model as discussed in Section 2.3.2, Table 3.1 summarizes the list of cases investigated in the current chapter involving a parametrically varying wall-damped Smagorinsky model. It must be noted that both the Smagorinsky length scale l_f as well as the cut-off modes k_c in near-wall model, incorporate artificial length scales into our flow simulations. Our purpose is to analyze the behavior of the numerical models in presence of these artificial length scales from the perspective of physics and develop

a *robust* and *physically consistent* ABL model in the context of spectral elements.

Case	k_c/N	$\{C_0,\ n\}$
$C_0^{16} n^2 k_c^{2/7}$ (I)	2/7	$\{0.16, 2\}$
$C_0^{16} n^2 k_c^{4/7}$ (IIa)	4/7	$\{0.16, 2\}$
$C_0^{9} n^2 k_c^{4/7}$ (IIb)	4/7	$\{0.09, 2\}$
$C_0^{16} n^2 k_c^{6/7}$ (III)	6/7	$\{0.16, 2\}$
$C_0^{17} n^1 k_c^{2/7}$ (IV)	2/7	$\{0.17, 1\}$
$C_0^{17} n^1 k_c^{4/7}$ (V)	4/7	$\{0.17, 1\}$
$C_0^{17} n^1 k_c^{6/7}$ (VI)	6/7	$\{0.17, 1\}$
$C_0^{19} n^{05} k_c^{2/7}$ (VII)	2/7	$\{0.19, 0.5\}$
$C_0^{19} n^{05} k_c^{4/7}$ (VIII)	4/7	$\{0.19, 0.5\}$
$C_0^{19} n^{05} k_c^{6/7}$ (IX)	6/7	$\{0.19, 0.5\}$

Table 3.1: Suite of LES cases for the neutral ABL flow involving parametric variation. k_c is the number of modes of cut-off filter per element in explicit filtering of the NWM (see Appendix A.4) and N is the order of Lagrange-Legendre polynomial in each element. $\{C_0,\ n\}$ are the tuning parameters of the wall-damped Smagorinsky SGS model.

3.1.2 Computational Domain

$N_x^e \times N_y^e \times N_z^e$	N_{xyz}	Δ_x/Δ_z	Δ_x/Δ_y	$\Delta z/z_0$
$30 \times 20 \times 24$	5.02×10^6	5.0265	1.33	27

Table 3.2: The baseline grid parameters for LES of atmospheric boundary layer

The computational domain is taken to be $2\pi H \times \pi H \times H$ as in [54], with $Re = U_\infty H/\nu = 10^{10}$, where U_∞ is the streamwise velocity outside of the boundary layer. The size of the computational domain ensures a sufficient decay of the streamwise

auto-correlation length scale necessary to make periodic boundary conditions consistent [1,90,91], and is also able to capture the appropriate scaling laws of the attached eddies [60, 79] as reported in the previous DNS literature [76, 77]. The discretization parameters of the computational domain are presented in Table 3.2. N_i^e represents the number of elements in the i^{th} direction and N_{xyz} is the global number of grid points used in the computation. Also, $\Delta_x/\Delta_z,\ \Delta_x/\Delta_y$ are the aspect ratios of the spectral elements, where $\Delta_x,\ \Delta_y,\ \Delta_z$ are the sizes of the spectral elements in the respective directions. We use 7^{th} order Lagrange-Legendre polynomials as the basis functions resulting in 8^3 collocation nodes per element. All the analysis involving the statistics and spectra in the later sections are carried out for the baseline grid in Table 3.2. However the LES simulations have also been tested for five other coarsened or refined grids for the *grid sensitivity* analysis in order to support the robustness of the wall modelled LES. The detailed results of the grid sensitivity can be found in Appendix C.

The minimum grid point wall-normal distance is $\Delta z/z_0 \gtrapprox 20$, manifesting that the first grid node does not resolve the geometric roughness and lies in the log-law of the wall, consistent with wall modeling conceptualizations [54]. All the grids designed for the current ABL are refined beyond the critical grid resolution required for an accurate representation of the mean streamwise velocity statistics, as discussed by Brasseur and Wei [45]. The three parameters identified by [45] (hereby referred to as BW parameters) used for designing a high-accuracy zone (HAZ), are (a) N_δ, the vertical grid resolution in the domain, (b) $\mathfrak{R}$, the ratio of the turbulent shear-stress to the total stress in the first grid point from the wall, and (c) R_{LES}, i.e., the Reynolds number based on the SGS eddy viscosity. According to Brasseur and Wei [45], these three parameters need to be greater than some critical value to be in HAZ. For brevity, we show the BW parameters for the different Smagorinsky based

SGS models in Figure 3.3 only for the baseline grid. However, the conclusions can be generalized for all the grids from Table C.1 in Appendix C. The vertical resolution in spectral elements ensures that N_δ is well above the critical value $N_\delta^* \sim 45 - 50$. The other two parameters, $\mathfrak{R}$ and R_{LES}, are SGS model dependent, and are only above their critical values indicating the appropriate accuracy of the model, for Cases VII-IX ($C_0^{19} n^{05} k_c^{2/7}, C_0^{19} n^{05} k_c^{4/7}, C_0^{19} n^{05} k_c^{6/7}$). For collecting statistics presented in the manuscript, the statistical stationarity of the neutral ABL simulations was first ensured after $\sim 45 T_e$, where $T_e = 2\pi H/U_\infty$ is the flow through time, upon which the temporal averaging of statistics and collection of instantaneous snapshots for spectral analysis have been carried out for 120 T_e time units.

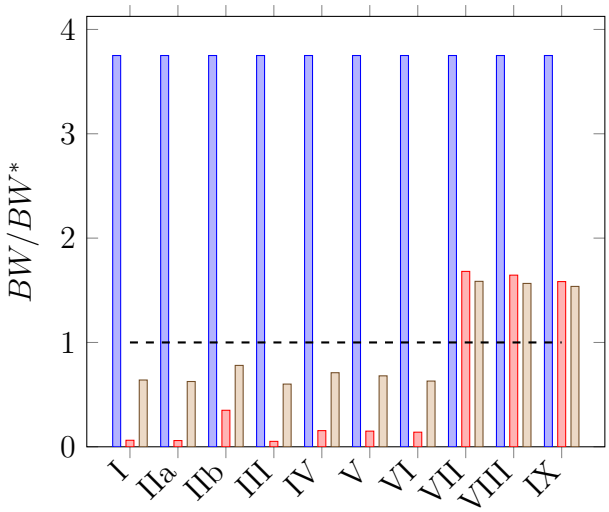

Figure 3.3: Three BW parameters [45] compared to their critical value $BW^* = \{N_\delta^*, \mathfrak{R}^*, R_{LES}^*\}$ plotted in a bar chart as BW/BW^* in our current wall-damped Smagorinsky model for baseline grid ($30 \times 20 \times 24$ elements). Blue (left): N_δ/N_δ^*; Red (middle): $\mathfrak{R}/\mathfrak{R}^*$, Brown (right): R_{LES}/R_{LES}^*. Black $--$ is the threshold $BW/BW^* = 1$ above which the results are considered in a high-accuracy zone [45]. Please, refer to Table 3.1 for Case numbering.

3.2 Results and Discussion

In this section, we provide a detailed comparison of the results involving the mean and turbulent statistics of our LES computations with the data from the previous literature [44, 53]. The results are further corroborated by a rigorous multi-dimensional spectral analysis which elucidates the flow physics in the inner and outer layer. Investigation of the results involving the statistics and the spectra of our LES computations helps us suggest an accurate and reliable LES-NWM model for spectral element computations, which can emulate the correct physics of the eddies in wall-bounded turbulence. The results have been further supported by grid sensitivity analysis (see Appendix C for details) which indicates that our conclusions are grid invariant and the statistics has a leading order effect from the wall model LES and not from the grid itself.

3.2.1 Law of the Wall: Mitigation of Log-Layer Mismatch

The theory of turbulent flows suggests that a well-defined region of a logarithmic dependence of the mean streamwise velocity on the vertical distance form the wall (log-law) persists due to a dominance of inertial scales in the inner layer corresponding to the lower 10% of the boundary layer, $z/H \sim 0.1$ [1]. The log-law can be compactly represented in terms of the non-dimensional streamwise velocity gradient, $\phi(z) = \kappa z/u_\tau dU/dz$, which attains a value of one in the log layer ($\phi(z) = \kappa z/u_\tau dU/dz$, $z/H \leq 0.1$) and deviates from one with $\phi(z) > 1,\ d\phi(z)/dz \neq 0$ beyond the inner layer depicting the so-called wake region (for more details of the logarithmic regime in high Re wall bounded turbulence, see, for example, a review by Smits et al. [75]). Figures 3.4a–3.4d show that except for Cases $C_0^{19}n^{05}k_c^{j/7}$ $j = 2, 4, 6$, all the current LES models develop strong deviations from the logarithmic trend of as much as 40-

60% at $z/H < 0.1$ known as *log-layer mismatch* (LLM). As was shown in Brasseur and Wei [45], these log-layer mismatches in LES are likely to occur due to the presence of an *artifial LES viscous sublayer*. Similar to physical log-law deviations due to the viscous sublayer in smooth-wall channel flows [90, 92], a numerical viscosity (i.e. due to a subgrid turbulent viscosity and other algorithmic additions to the dissipation) creates a numerical frictional layer that causes the overshoot. Interestingly, as the true viscous overshoot scales with the viscous units (ν/u_τ) showing the same location of the peak overshoot versus z^+ for different Reynolds numbers [90, 92], the LES overshoot scales with the "LES viscosity" (ν_{LES}/u_τ) showing the collapse of the velocity gradient curves in the inner layer if plotted with these z^+_{LES} units [45].

The manifestation of similar effects in our simulations with wall-damped Smagorinsky model are evident in Figure 3.4. We can see that decreasing C_0 to 0.09 from 0.16 with $n = 2$ fixed (Case $C_0^{16}n^2k_c^{4/7}$ vs $C_0^{09}n^2k_c^{4/7}$)) decreases the overall eddy viscosity in the LES computation, shifting the LLM peak from $z/H = 0.05$ to $z/H = 0.02$ towards the wall as seen in Figure 3.4c indicating the shorter extent of the LES eddy viscosity sublayer. The peaks of the log-layer mismatch in Figure 3.4 from our current SEM simulations are closer to the wall compared to the standard Smagorinsky model in the literature [44, 53, 54]. We point out that in Cases $C_0^{19}n^{05}k_c^{j/7}$ $j = 2, 4, 6$, the dissipation is low enough that the inertial scales $\sim \kappa z$ dominate over artificial viscous scales, which completely eliminates the formation of the artificial sublayer and hence LLM.

Effect of k_c in the Near Wall Model

The effect of explicit filtering in the near wall model is not very conspicuously observed in the near-wall region, $z/H < 0.1$, even though differences are visible in the far outer layer. Explicit filtering retains the large-scale near-wall velocity structures for the

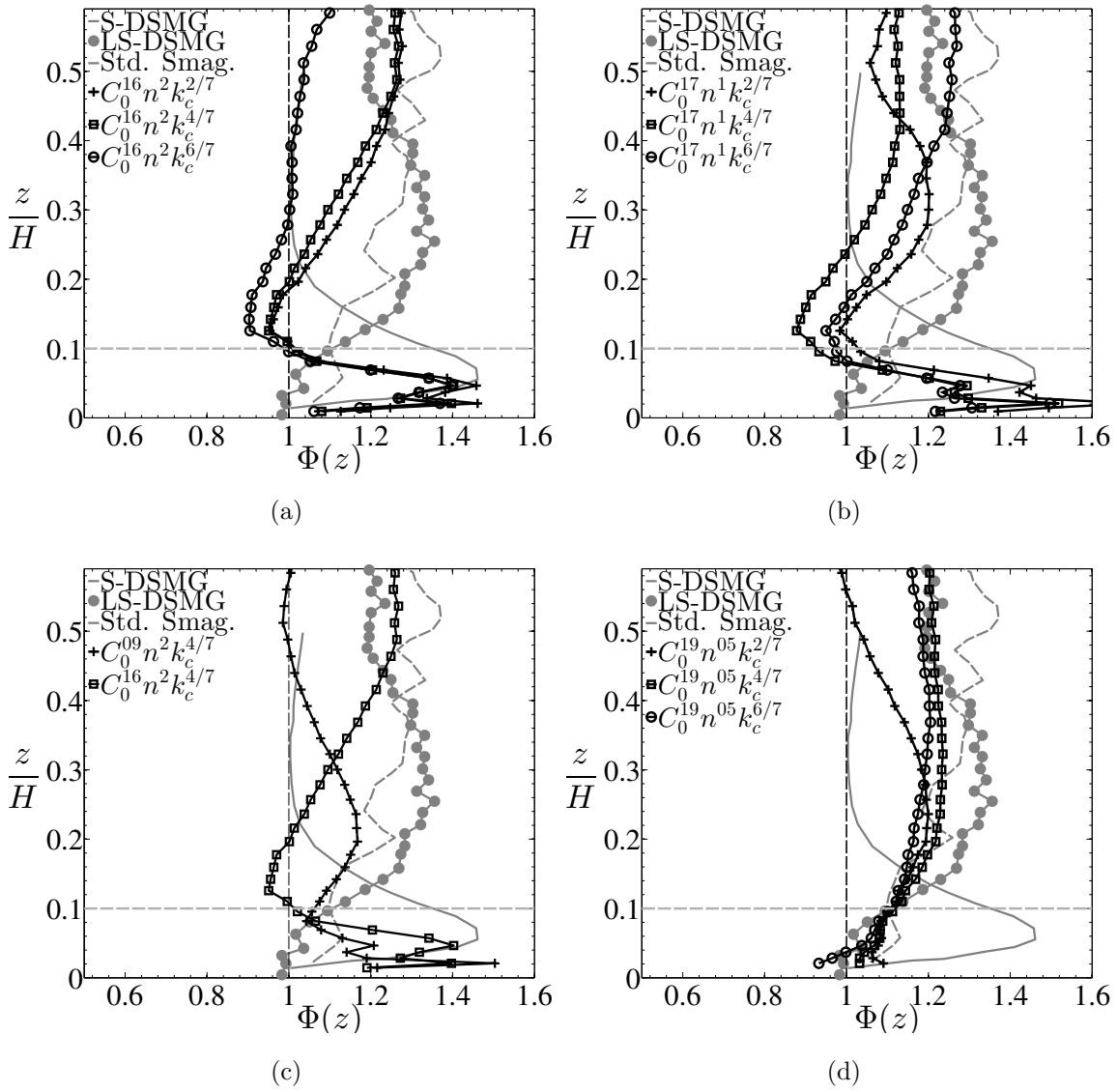

Figure 3.4: Temporally and horizontally averaged normalized mean streamwise velocity gradient $\Phi(z)$ vs z/H for SGS parameters (a) Cases $C_0^{16}n^2k_c^{j/7},\ j=2,4,6$ (b) Cases $C_0^{17}n^1k_c^{j/7},\ j=2,4,6$ (c) Cases $C_0^{\xi}n^2k_c^{4/7}, \xi=16,9$ (d) Cases $C_0^{19}n^{05}k_c^{j/7},\ j=2,4,6$. LS-DSMG: Lagrangian scale dependent dynamic Smagorinsky model, Bou-Zeid et al. [53]; Std. Smag. (Standard Smagorinsky), Bou-Zeid et al. [53]; S-DSMG: spatially averaged Scale dependent dynamic Smagorinsky model, Porté-Agel et al. [44]. The dashed-gray line is demarcation between the inner and outer layer.

model, while filtering out the smaller scales near the SGS limit. The fact that the log-law of the wall has its significant contribution from the larger scales of motion [75,85], is manifested in the slight reduction of log-layer mismatch, with increasing the cutoff modes in filtering k_c/N, from 2/7 to 4/7 (see Figure 3.6b, 3.6c). However excessive filtering on horizontal velocity, especially in models where artificial viscous layer is not formed (Cases $C_0^{19}n^2k_c^{j/7}$ $j = 2, 4, 6$), can contribute to the underdissipative negative log-layer mismatch as in Figure 3.6b for $k_c = 6/7$. However, further studies of this effect are needed to form a more complete description.

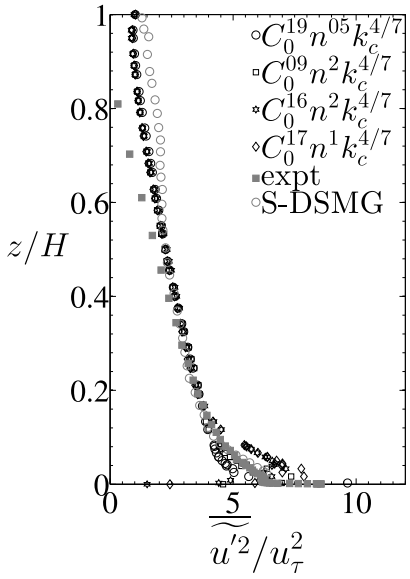

Figure 3.5: Horizontally averaged resolved streamwise variance $\widetilde{u'^2}$ normalized with u_τ^2 for different Smagorinsky based SGS models $C_0^{16}n^2k_c^{4/7}$, $C_0^{17}n^1k_c^{4/7}$, $C_0^{09}n^2k_c^{4/7}$ and $C_0^{19}n^{05}k_c^{4/7}$ compared against scale-dependant dynamic Smagosinky (S-DSMG) [44] and wind tunnel experiment [74].

3.2.2 Reynolds Stresses

For completeness of the discussion, we present the results of the second order moments before moving on to the discussion of the spectral analysis in the subsequent section. A comparison of the streamwise variance for the different model parameters

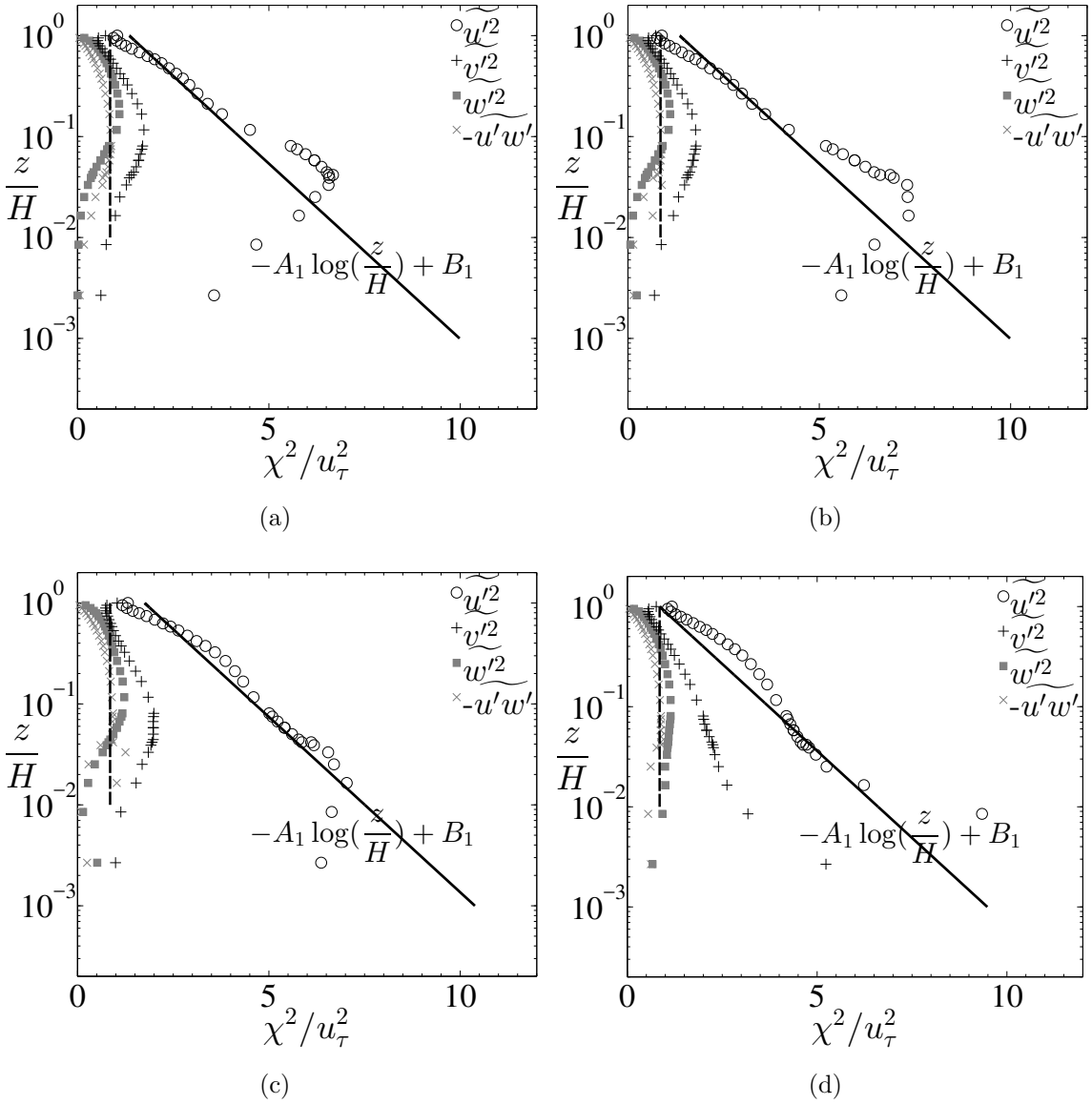

Figure 3.6: Variation of horizontally averaged resolved second order moments $\chi^2 = \widetilde{u'^2}, \widetilde{v'^2}, \widetilde{w'^2}, -\widetilde{u'w'}$ with z/H for different models (a) Case $C_0^{16} n^2 k_c^{4/7}$ (b) Case $C_0^{17} n^1 k_c^{4/7}$ (c) Case $C_0^{09} n^2 k_c^{4/7}$ (d) Case $C_0^{19} n^{05} k_c^{4/7}$. Solid black line: log-trend of streamwise variance, $A_1 = 1.25$ is the slope of the logarithmic trend [14, 79]. Dashed black line: flat trend of kinematic shear-stress – equilibrium layer.

of the wall-damped Smagorinsky model with previously published numerical simulations [44] and laboratory scale experiments [74] can be found in Figure 3.5. To better understand the near-wall analytical scalings of the variances, Figure 3.6 shows some of the resolved second order moments or Reynolds stresses for various parametric cases of Smagorinsky based LES model in logarithmic plot. Perry et al. [79, 93] performed a detailed analysis of the overlap regions in the spectra of $\overline{\widetilde{u}'^2}, \overline{\widetilde{v}'^2}, \overline{\widetilde{w}'^2}, -\widetilde{\overline{u'w'}}$ for wall-bounded turbulence, through the theory of an *equilibrium layer* supported by their hot-wire experiments. They found the evidence of a logarithmic trend in the streamwise and spanwise variance profiles, as well as a flat trend (independence on z) in the wall normal variance and in the kinematic shear stress in the near wall region $z/H < 0.1$. Such logarithmic trends of streamwise variance (observed only in $C_0^{09} n^2 k_c^{4/7}$, $C_0^{19} n^{05} k_c^{4/7}$) were also documented in later experiments of wall bounded turbulence using hot wires [74] and in the LES computations of rough wall ABL [14]. In our computations, it is only for the case $C_0^{19} n^{05} k_c^{4/7}$ that we observe *correct* logarithmic trends of streamwise *and* spanwise variances, as well as flat trends of wall normal variance and kinematic shear stress in the near wall region $z/H \sim 10^{-2} - 10^{-1}$ (see Figure 3.6d). Interestingly, a similar effect of an artificial secondary peak generation in streamwise variance is also observed in some experiments [74, 75] due to the presence of *artificial length scale* effects in hot wire probes.

3.2.3 Effect of Length Scales: Spectral Analysis

The spectral analysis of wall-bounded turbulence illustrates a clear picture of the dynamics of turbulent eddies (see the review by Jiménez (2012) [85]) responsible for the specific mean and turbulent statistics as discussed in Sections 3.2.1, 3.2.2 above.

In a statistical sense, the near-wall dynamics of high Re turbulence is made up of a hierarchy of self-similar coherent active wall normal motions, bearing Reynolds

stresses [60, 78, 79, 93–95] whose length scales, $\lambda_x \sim O(z)$, and the velocity scales, $\sim O(u_\tau)$. Apart from these eddies, also present are the quasi-inviscid, anisotropic and horizontal inactive eddies with $\lambda_x \gg O(z)$, "attached" in the sense of Townsend [60]. These inactive motions at distance z from the wall, can also be thought of as being "active" at wall distances $z_\lambda \gg z$, where z_λ is the vertical wall distance of the order of the length scale of *inactive motions* [85]. Larger coherent flow organizations in wall-bounded turbulence, e.g., large scale motions (LSM $\sim 3H$) and very large-scale motions (VLSM, $\gg 3H$), carying almost 50% of the kinetic energy and Reynold's stresses are beyond the scope of this paper, mainly due to a shorter computational domain, and hence are not discussed here (for more details on LSM's & VLSM's, please see [75, 78, 95–97]).

Figure 3.9a, 3.10a illustrates the grayscale temporal snapshots of the velocity magnitude at the inner and outer layer for Case $C_0^{19} n^{05} k_c^{4/7}$. While near-wall streaks representative of the attached inactive motions can be seen at the inner layer, the outer layer structures are mostly large scale bulges lacking such anisotropic streak features. Further in Figures 3.9, the instantaneous streamwise u and w velocities at two different times have been documented in the xz plane at $y = \pi H/2$ (middle of the spanwise extent). They indicate ramp like structures in the u velocity [98] and fine-scale vertical velocity updrafts and downdrafts To complement them, Figures 3.10 shows the temporal snapshots of streamwise u velocity contours and in-plane v, w velocity vectors at plane $x = \pi H$ (middle of the streamwise extent) have also been documented. These snapshots indicate the presence of circulations, representative of the streamwise vortices and downdrafts from the outer-layer, which hints towards the fact, that the inner and outer layer dynamics are not decoupled, rather the outer layer motions strongly affects the inner layer.

Strong analytical and experimental evidence of two distinct "overlap" regions

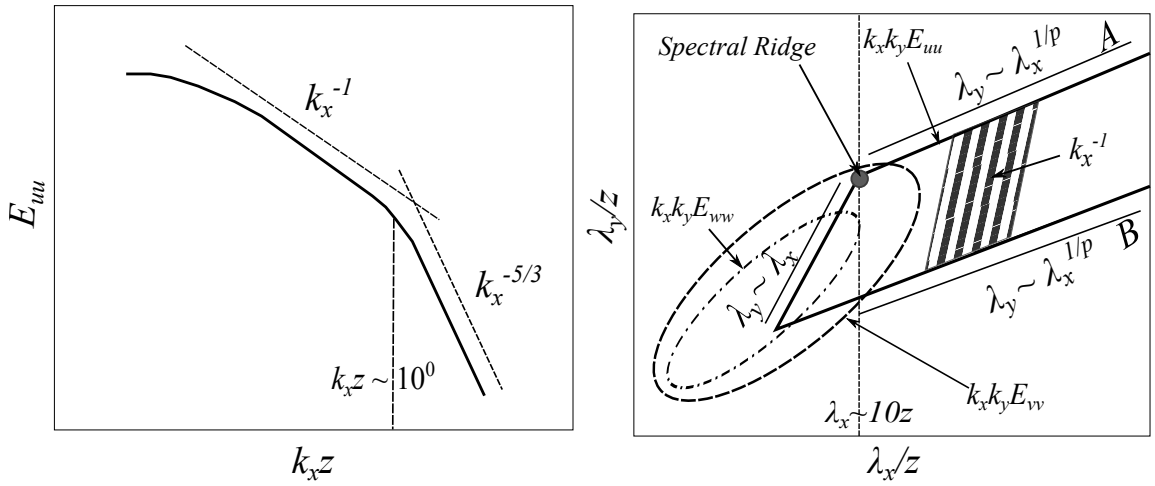

(a) (b)

Figure 3.7: (a) A schematic of a near-wall 1D u spectra, depicting the scaling laws and indicating the regions of k_x^{-1} & $k_x^{-5/3}$ scaling (b) A schematic of near-wall 2D premultiplied u, v, w energy spectra, with the linear $\lambda_y \sim \lambda_x$ and the power law $\lambda_y \sim \lambda_x^{1/p}$ scaling shown for u spectra. Both 1D and 2D spectra are representative of the near-wall phenomenon. Spectral Ridge corresponds to a change of scaling from linear to a power-law.

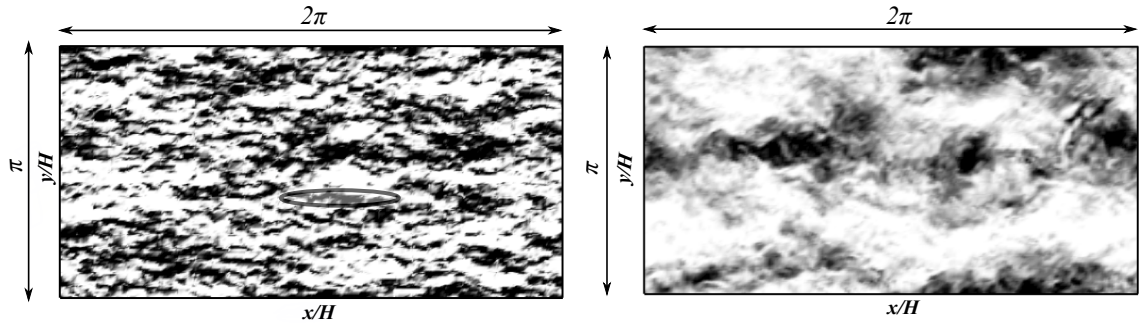

(a) (b)

Figure 3.8: Time-snapshot of velocity magnitude $\sqrt{u^2+v^2+w^2}$, normalized by U_∞ at xy plane for Case $C_0^{19} n^{05} k_c^{4/7}$. (a) Inner layer, $z/H = 0.025$. Black patch: $0.7U_\infty$; White patch: $0.5U_\infty$ (b) Outer layer, $z/H = 0.875$. Black patch: U_∞; White patch: $1.2U_\infty$. Encircled region in (a): low velocity streaky flow, $\lambda_x \sim 16z$.

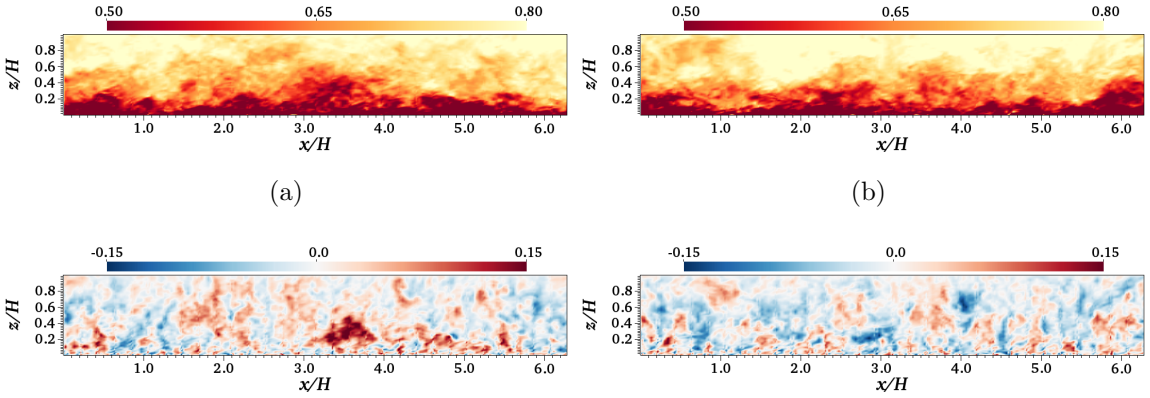

Figure 3.9: Time-snapshot of (a),(b) streamwise u and (c),(d) wall normal w velocity normalized by U_∞ at xz plane ($y = \pi H/2$) for Case $C_0^{19} n^{05} k_c^{4/7}$. Snapshots T_e times apart.

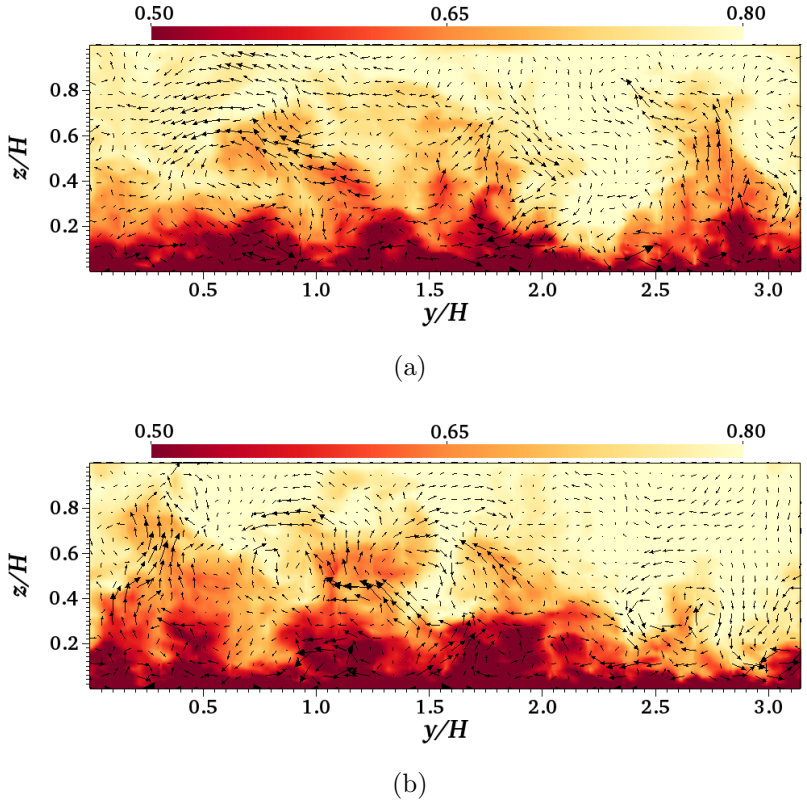

Figure 3.10: Temporal snapshot streamwise u contour and inplane v, w velocity vector normalized by U_∞ at yz plane ($x = \pi H$) for Case $C_0^{19} n^{05} k_c^{4/7}$. Snapshots $2T_e$ times apart.

in the spectra of streamwise and spanwise turbulent intensities $\overline{u'^2}, \overline{v'^2}$ and single "overlap" of Kolmogorov scaling for wall-normal turbulence intensity $\overline{w'^2}$ have been found at very high Reynolds number wall-bounded flows [79, 93, 99]. The overlap between the integral and the *attached eddy* length scales gives rise to the k_x^{-1} scaling in streamwise energy spectra while the overlap between the *attached eddy* and viscous / Kolmogorov scales gives rise to the Kolmogorov $k_x^{-5/3}$ law of the cascade [1,79], with k_x being the streamwise wave number (see the schematic in Figure 3.7a). Despite some debate on the existence of the k_x^{-1} spectra [77, 100, 101], hot wire experiments by [74, 102–104] have shown that for moderately high Re wall-bounded turbulence, a decade of range in the inverse law spectra can be observed in the near wall regime, at around $z/H \lesssim 0.01 - 0.02$. Additionally, the data from the previous literature also indicates a consistent region of $k_x^{-1/2}$ scaling at larger scales, or smaller wavenumbers $k_x z$, before the "well-documented" k_x^{-1} region, at high Re atmospheric surface layer experiments [105–108] and neutral atmospheric boundary layer simulations [44, 72]. Although this region was not explicitly discussed in the previous literature, we find a strong evidence of this scaling predicted by our best-performing SGS model, $\{C_0, n\} = \{0.19, 0.5\}$, and present some additional results in support of this.

A more supportive picture can be obtained in the two-dimensional spectra scenario for example, looking at a 2D energy spectrum premultiplied by wavenumbers k_x, k_y, as in the schematic of Figure 3.7b. A self-similar linear-scaling $\lambda_y \sim \lambda_x$ exists for length scales $\lambda_x \lesssim 10z$, which corresponds to the *active wall-normal motions*. These motions are three dimensional motions, due to the presence of vertical energy (E_{ww}) spectra. The regime of larger length scales, $\lambda_x \gtrsim 10z$ ($k_x z \sim 10^0$), where the power-law scaling is present, corresponds to the *attached inactive motions*, which are mainly horizontal motions, as seen from the long-wavelength cut-off of vertical energy, E_{ww} spectra. (For more details of "**active and inactive motions**" see Ref. 60, 107, 109, 110).

The basis of this power-law behaviour $\lambda_y \sim (\lambda_x)^{1/p}$ has been discussed in details in [76,77] and is mainly attributed to the effects of long-time dispersion of flow structures in background turbulence. While $p = 3$ scaling occurs at low-speed regions of the near wall streaks, dominated by shear, the $p = 2$ scaling is more generic, and is not only formed at high-speed regions of the near wall streaks, dominated by a uniform momentum, but also due to the dissipation in the outer layer. Figure 3.8a shows the near-wall streaky flow, which has completely different flow structures than the outer layer in Figure 3.8b, the latter being populated by much larger eddies and is less coherent (the snapshots are shown for Case $C_0^{19} n^2 k_c^{4/7}$). It is to be noted that for brevity and easy reference, we refer to the power scaling in Figure 3.7b at the top of the contour as the "$\boldsymbol{A}$" scaling, while that in the bottom of the contour as the "$\boldsymbol{B}$" scaling. It must be appreciated that a part of the region of 2D spectra between the "$\boldsymbol{A}$" & "$\boldsymbol{B}$" power law scaling behaviour, corresponding to the *attached inactive motions*, when integrated over the λ_z wavelength, would supposedly generate the classic k_x^{-1} scaling law. More specifically, we would like to mention, that the community in favour of the k_x^{-1} scaling [74, 79, 103, 104, 108], actually found evidence of this inverse law in the regime of integration, just discussed. Additionally, even though the focus of our computational study involves rough walls, previous literature [108, 111, 112] has consistently shown that smooth wall scaling laws of attached eddies also hold for rough walls and particularly if the roughness length is less than 2.5% of the boundary layer thickness ($z_0/H = 10^{-4}$ in the current simulations) as also predicted by Refs. 113,114.

1D Spectra

The comparison of the spectra for the LES models in our study (see Table 3.1) will be based on the robust theoretical scaling laws of the active and inactive motions as discussed above, since these eddies comprize of the most important dynamics of the wall

bounded flow. It must be noted that the length scale $\lambda_x \sim 10z$ is the *barrier* between the active and inactive motions. The discussion in this section would not only lead us to the most consistent model corresponding to the correct spectral behavior, but also point to the implications of the incorrect scaling laws produced by the other models in terms of numerically *inconsistent physics of the active and inactive eddies*. In the subsequent analysis, the energy spectra, cospectra are calculated as $E_{uu} = \langle \hat{u}\hat{u}^* \rangle$, $\phi_{uw} = \langle \hat{u}\hat{w}^* \rangle$, where $\hat{}$ denotes Fourier transform, $*$ denotes the conjugate transpose, and $\langle\rangle$ denotes the temporal averaging.

In Figure 3.11, we plot the mean (temporally, horizontally averaged) streamwise

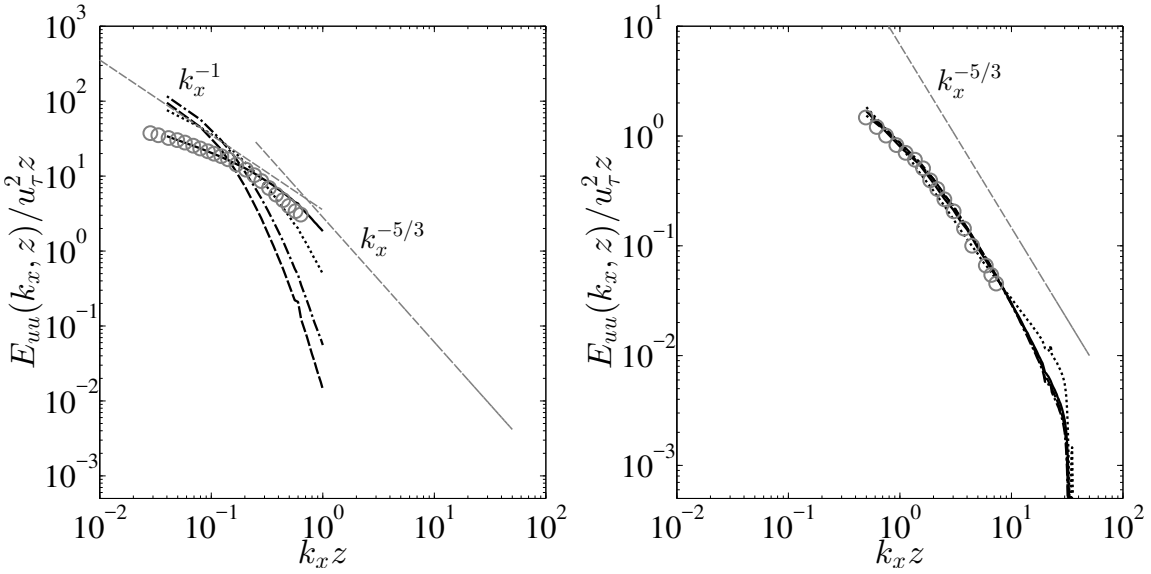

Figure 3.11: Normalized streamwise energy spectra $E_{uu}(k_x, z)/u_\tau^2 z$ vs $k_x z$ at different normalized heights (a) $\xi = z/H = 0.028$, (b) $\xi = z/H = 0.519$ compared against previous literature [44]. Case $C_0^{16} n^2 k_c^{4/7}$ (Dashed), $C_0^{17} n^1 k_c^{4/7}$ (Chain-dotted), $C_0^{09} n^2 k_c^{4/7}$ (Dotted), $C_0^{19} n^{05} k_c^{4/7}$ (Solid), Scale dependant Dynamic model [44] (Gray circle)

energy spectra for different parameters of the Smagorinsky SGS model compared against the scale-dependant dynamic model [44]. An excellent agreement in streamswise spectra for our best-performing model ($C_0^{19} n^{05} k_c^{4/7}$) at different length scales

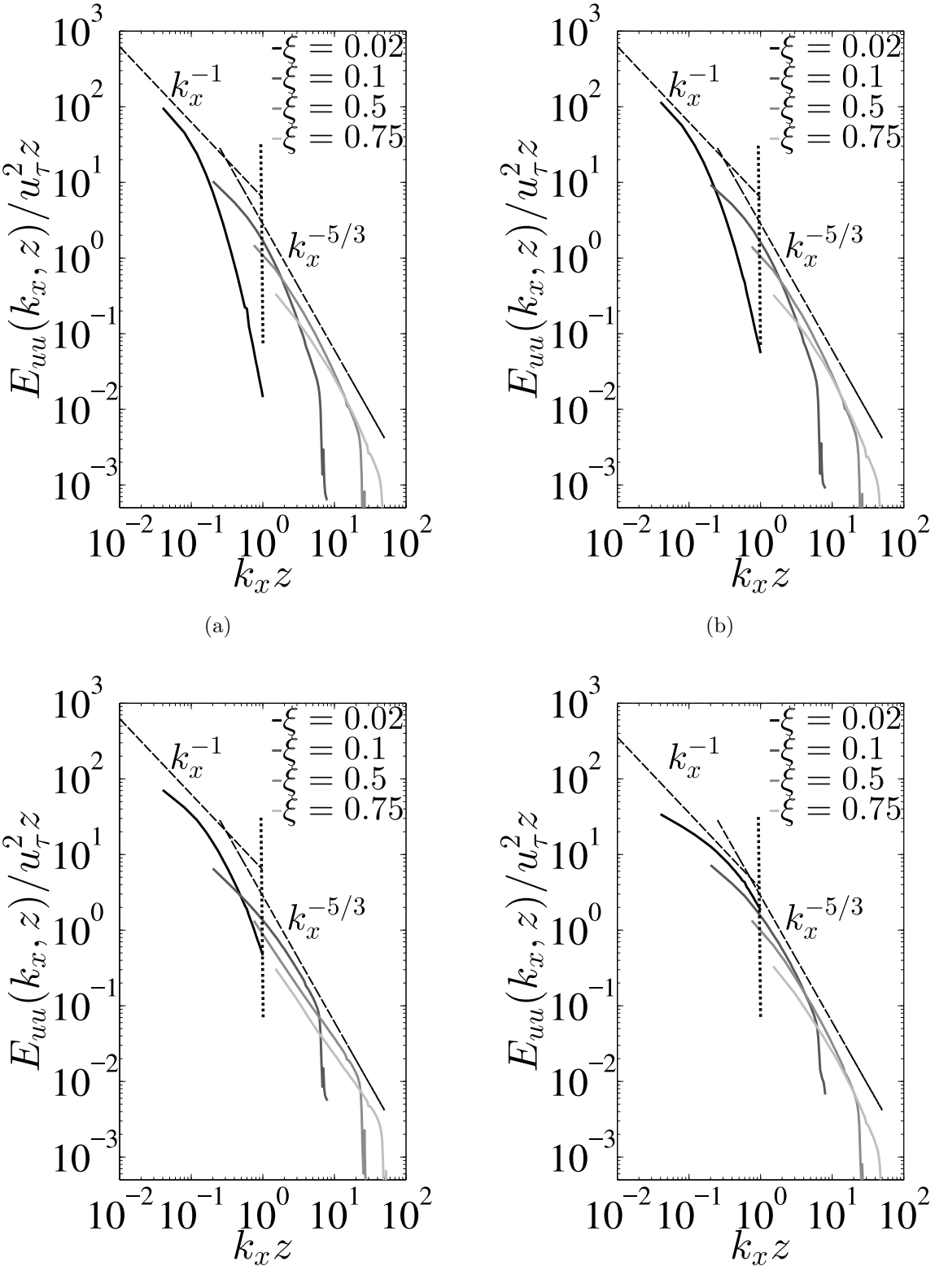

Figure 3.12: Normalized streamwise energy spectra $E_{uu}(k_x, z)/u_\tau^2 z$ vs $k_x z$ at different normalized heights $\xi = z/H = 0.02, 0.1, 0.5, 0.75$. (a) Case $C_0^{16} n^2 k_c^{4/7}$ (b) Case $C_0^{17} n^1 k_c^{4/7}$ (c) Case $C_0^{09} n^2 k_c^{4/7}$ (d) Case $C_0^{19} n^{05} k_c^{4/7}$. Vertical dotted – $k_x z = 10^0$

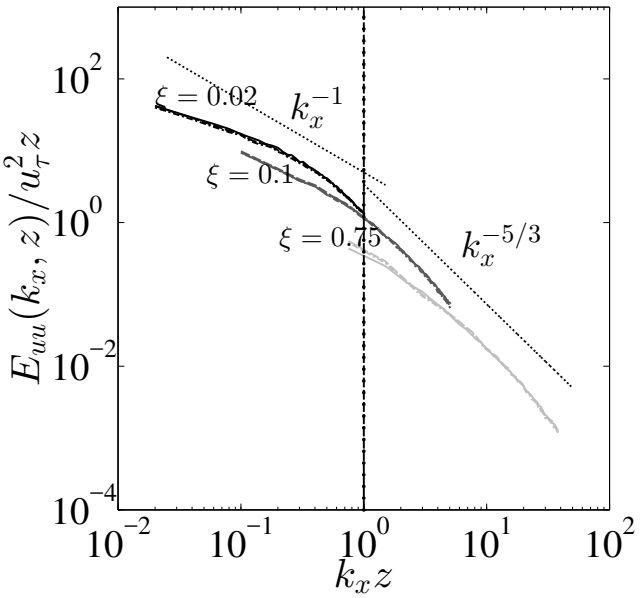

Figure 3.13: Normalized streamwise energy spectra $E_{uu}(k_x, z)/u_\tau^2 z$ vs $k_x z$ at different heights $\xi = z/H = 0.02, 0.1, 0.5$ for different values $k_c/N = 2/7$ (Solid), $4/7$ (Dashed), $6/7$ (chain Dotted) in explicit filtering of the NWM for models $\{C_0 = 0.19,\ n = 0.5\}$. Dashed circle – $k_x z = 10^0$

with the state-of-the-art LES model [44] for the neutral atmospheric boundary layer is notable. For the more detailed spectral analysis of the models, the variation of streamwise energy spectra at four different heights is shown in Figure 3.12. It was observed, that the effect of filtering in near wall models was not conspicuous in the spectra, except for, perhaps, a very slight effect at the largest scales of motions. A reference plot in Figure 3.13 for SGS model $C_0 = 0.19, n = 0.5$, with different k_c is provided to support the claim above. From hereafter, we would tailor our discussions mostly to the effect of SGS closures, since they have more significant impact on the spectral results. Furthermore, it is worth mentioning that the spectral plots in the current and subsequent sections are corroborated by a *grid sensitivity* analysis (see appendix C for details) which illustrates the fact that the scaling laws and the shape of the spectra have a more dominant effect from the wall model LES than the grid itself.

While Case $C_0^{19}n^{05}k_c^{4/7}$ predics the correct -1 and $-5/3$ scaling law along with the regime of change of the scaling at $k_x z \sim O(10^0)$, the situation is quite different for "overdissipative" (Cases $C_0^{16}n^2k_c^{4/7}, C_0^{17}n^1k_c^{4/7}$) as well as "under-dissipative" ($C_0^{09}n^2k_c^{4/7}$) models. For Smagorinsky based over-dissipative models, the $k_x^{-5/3}$ law near the wall, $z/H \ll 0.1$, is absent and the location of k_x^{-1} regime is shifted to larger length scales with a much shorter extent, indicating that the change of scaling laws occurs at $k_x z \sim O(10^{-1})$. The $-5/3$ law cascade, however is recovered in the outer layer, $z/H > 0.1$. What is surprizing, is that with "underdissipative effects" as in Case $C_0^{09}n^2k_c^{4/7}$, the improvement in the spectral scaling near the wall is not noticable. While the dissipation in the finer scales is indeed smaller, it still cannot recover the $-5/3$ law and neither does it reflect the correct location of the k_x^{-1} law. The under-dissipative effects are further pronounced at the outer layer, with the scaling law of the power scales clearly deviating from the $-5/3$ law, manifesting an inefficient cascade. A point of further concern, is the region of $k_x^{-1/2}$ scaling which was also observed from the data of the previous literature [44, 108], that is conspicuously absent in all the models, except for case $C_0^{19}n^2k_c^{4/7}$.

The fact, that the extent and location of length scales of the k_x^{-1} scaling are not captured in some of our LES simulations, e.g., Cases $C_0^{16}n^2k_c^{4/7}, C_0^{09}n^2k_c^{4/7}, C_0^{17}n^1k_c^{4/7}$, can be attributed to the effects of "incorrect SGS dissipation" at different distances from the wall, as manifested by the 1D premultiplied streamwise energy spectra contours $k_x E_{uu}(k_x, z)/u_\tau^2$ in Figure 3.14. Figures 3.14a– 3.14c, clearly indicate that only Case $C_0^{19}n^{05}k_c^{4/7}$ shows the linear growth of length scales λ_x with distance z from the wall, for a band of energy contours, corresponding to the *logarithmic layer* [74, 85]. While Case $C_0^{16}n^2k_c^{4/7}$, retains some of the linear scaling close to $z/H \sim 0.1$, a significant deviation from the linear trend occurs for scales $\lambda_x < H$. Case $C_0^{09}n^2k_c^{4/7}$ displays, perhaps the worst behaviour, with non-linear scaling of λ_x vs z even for the

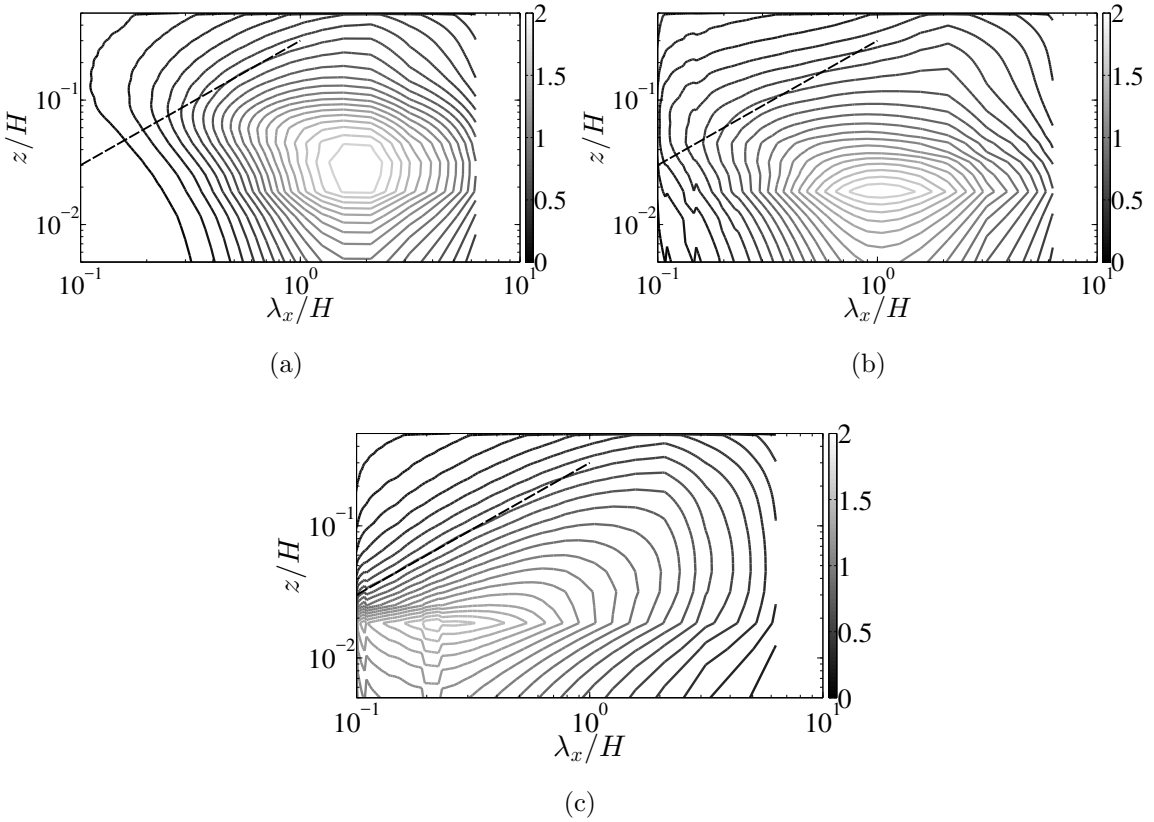

Figure 3.14: Premultiplied normalized 1D spectra contour-map $k_x E_{uu}(k_x, z)/u_\tau^2$ for different LES models in streamwise wavenumber - wall normal distance plane. Streamwise wave number λ_x and wall distance z are both normalized by ABL thickness H. (a) Case $C_0^{16} n^2 k_c^{4/7}$ (b) Case $C_0^{09} n^2 k_c^{4/7}$ (c) Case $C_0^{19} n^{05} k_c^{4/7}$. Dashed line : $\lambda_x/H \sim z/H$.

larger scales of motion, $\lambda_x \geq H$.

The discussion above suggests that a proper LES model should provide an optimum amount of dissipation in each region, and simply lowering C_0, while decreasing the near-wall filter scales and improving the near-wall behaviour of the spectra, results in *underdissipation* and incorrect scaling law predictions in the outer layer. Control of the SGS dissipation through the change of the shape function in Eqs. (2.14), (2.15) via the two parameters, C_0 and n, that permits a slower growth rate of C_s in the inner layer (Case $C_0^{19} n^{05} k_c^{4/7}$), provides an appropriate amount of dissipation for both the inner and the outer layers in the current SEM method.

We plot the shear stress spectra for the parametric variation of wall-damped SGS models at a fixed $k_c/N = 4/7$ (Cases $C_0^{16}n^2k_c^{4/7}, C_0^{09}n^2k_c^{4/7}, C_0^{17}n^1k_c^{4/7}, C_0^{19}n^{05}k_c^{4/7}$) in Figure 3.15. Similar to the streamwise spectra (Figure 3.12), distinct scaling laws also exist in the shear stress spectra. Corresponding to the two overlap regions in the E_{uu} spectra [79], i.e., k_x^{-1} and $k_x^{-5/3}$ laws, one will also have k_x^0 and $k_x^{-5/3}$ regions in the E_{ww} spectra [76, 79, 114]. For the near-wall organized motions carrying significant amount of Reynolds stresses, the large and intermediate-scale organized motions near the wall should be well correlated in terms of u, w motions, i.e., $\phi_{uw}(k_x, z) \approx E_{uu}(k_x, z)^{1/2}E_{ww}(k_x, z)^{1/2}$, where ϕ_{uw} is the spectra of the kinematic shear stress $-\overline{u'w'}$ [76]. Correspondingly, the scaling laws of the two overlap regions of the cospectra, $\phi_{uw}(k_x, z)$, would be $k_x^{-1/2}$ and $k_x^{-5/3}$ laws, respectively, with smaller scales in the far-outer region depicting the classical $k_x^{-7/3}$ law [114–116].

We observe, that only for the Case $C_0^{19}n^{05}k_c^{4/7}$ we can capture the theoretical scaling laws of the shear stress spectra in the inner and outer wall regions. Case $C_0^{09}n^2k_c^{4/7}$, even though retains the $k_x^{-1/2}$ and $k_x^{-5/3}$ laws in the near wall region, depicts strong deviation from the $k_x^{-5/3}$, $k_x^{-7/3}$ scaling laws in the outer layer. However, the overdissipative models, Cases $C_0^{16}n^2k_c^{4/7}$ and $C_0^{17}n^1k_c^{4/7}$, cannot even predict the first overlap region, illustrating an incorrect slope of what seems to be closer to $k_x^{-3/4}$ rather than the expected $k_x^{-1/2}$, even though the intermediate /small scale laws, $k_x^{-5/3}$, $k_x^{-7/3}$ are captured quite well. This incorrect $k_x^{-3/4}$ scaling will be elaborated upon further in the next section. Additionally, in all models except for the Case $C_0^{19}n^{05}k_c^{4/7}$, the normalized streamwise energy spectra and cospectra at different heights do not collapse well in the overlap regions specifying that they do not scale well with $u_\tau^2 z$ specifically in the near-wall region.

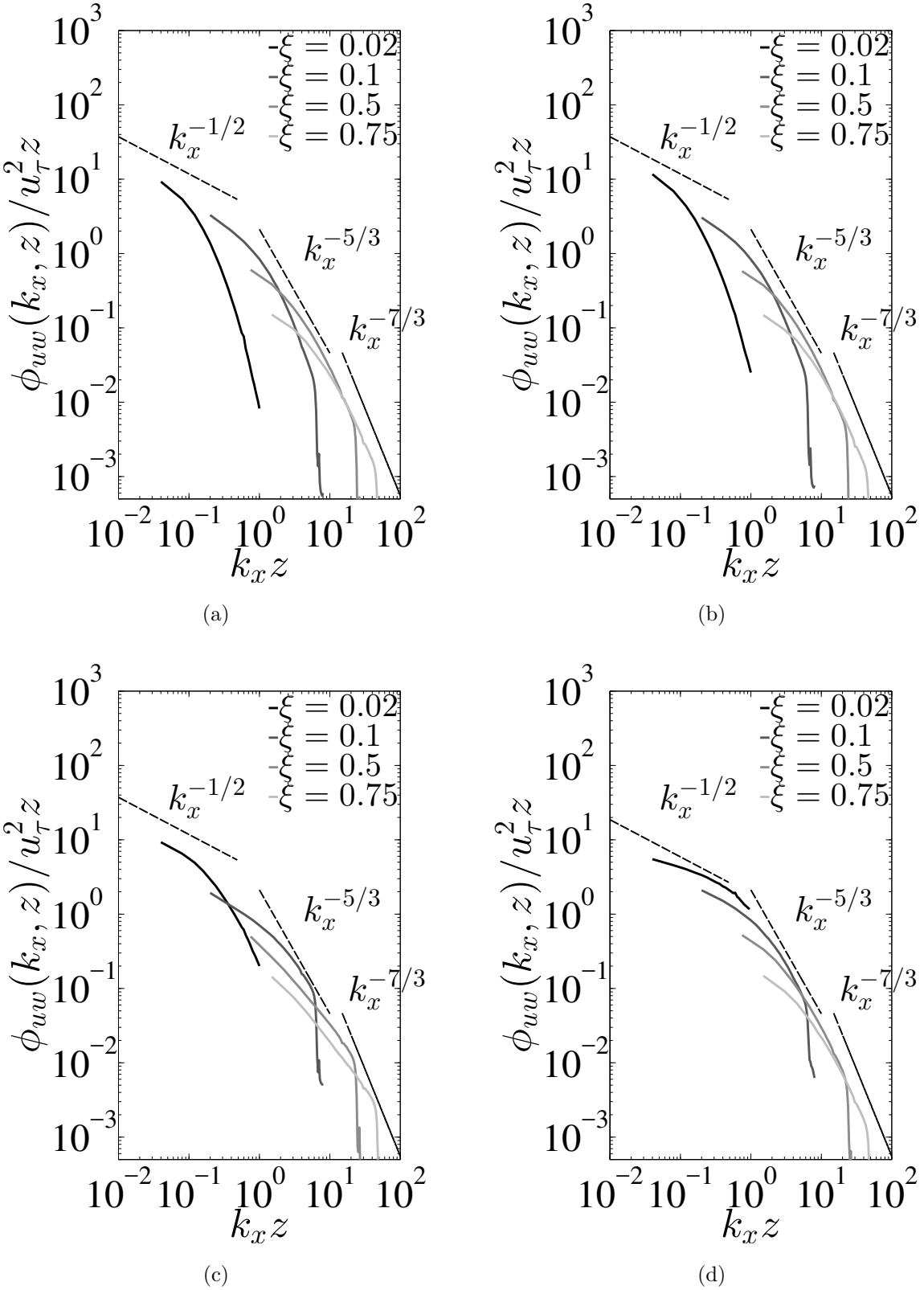

Figure 3.15: Normalized shear stress spectra $\phi_{uw}(k_x, z)/u_\tau^2 z$ vs $k_x z$ at different normalized heights $\xi = z/H = 0.02, 0.1, 0.5, 0.75$. (a) Case $C_0^{16} n^2 k_c^{4/7}$ (b) Case $C_0^{17} n^1 k_c^{4/7}$ (c) Case $C_0^{09} n^2 k_c^{4/7}$ (d) Case $C_0^{19} n^{05} k_c^{4/7}$.

Near Wall Correlations

To understand the counter-intuitive behavior of the dissipative Smagorinsky models in affecting the larger length scales of the Reynolds stresses (manifested by the fact that models $C_0^{16}n^2k_c^{4/7}, C_0^{17}n^2k_c^{4/7}$ predict a $k_x^{-3/4}$ scaling law instead of a $k_x^{-1/2}$ law of the shear stress spectra as seen in Figure 3.15a, 3.15c), we try to investigate how the u, w wall correlations of the near-wall organized structures are affected by the parametric variation of SGS models. The plots of $E_{uu}, E_{ww}, \phi_{uw}$ at two different normalized heights $\xi = 0.02, 0.025$ for the Cases $C_0^{16}n^2k_c^{4/7}, C_0^{09}n^2k_c^{4/7}, N_\sigma k_c^{4/7}, C_0^{19}n^{05}k_c^{4/7}$ are shown in Figure 3.16. It was observed that well *correlated* scaling laws in the near wall corresponding to $\phi_{uw} \approx E_{uu}^{1/2}E_{ww}^{1/2}$ exist only for the models $C_0^{16}n^2k_c^{4/7}, C_0^{17}n^1k_c^{4/7}, C_0^{19}n^{05}k_c^{4/7}$. For the correlated regions in the overlap, if $E_{uu} \sim A_1u_\tau^2k_x^{-l}$, $E_{ww} \sim A_3u_\tau^2k_x^{-m}$, and $\phi_{uw} \sim A_{13}u_\tau^2k_x^{-n}$, one would require $n = (l+m)/2$ [79].

We list the observed scaling laws for E_{uu}, E_{ww}, ϕ_{uw} for the first overlap region

Case	E_{uu} scaling	E_{ww} scaling	ϕ_{uw} scaling	Observed k_xz range	$\rho_{uw} = A_{13}/\sqrt{A_1}\sqrt{A_3}$
$C_0^{16}n^2k_c^{4/7}$	k_x^{-1}	$k_x^{-1/2}$	$k_x^{-3/4}$	$k_xz < 10^{-1}$	0.8243
$C_0^{17}n^1k_c^{4/7}$	k_x^{-1}	$k_x^{-1/2}$	$k_x^{-3/4}$	$k_xz < 10^{-1}$	0.825
$C_0^{09}n^2k_c^{4/7}$	k_x^{-1}	$k_x^{-1/4}$	$k_x^{-1/2}$	$k_xz < 10^{-1}$	–
$C_0^{19}n^{05}k_c^{4/7}$	k_x^{-1}	k_x^0	$k_x^{-1/2}$	$10^{-1} < k_xz < 10^0$	0.8333

Table 3.3: Near wall u, w scaling laws, their correlation coefficient in the first overlap region (k_x^{-1} region of E_{uu} spectra) and wavenumber range for four different parametric variations of the wall-damped SGS model $C_0^{16}n^2k_c^{4/7}$, $C_0^{17}n^1k_c^{4/7}$, $C_0^{09}n^2k_c^{4/7}$, $C_0^{19}n^{05}k_c^{4/7}$.

Case	E_{uu} scaling	E_{ww} scaling	ϕ_{uw} scaling	Observed k_xz range	$\rho_{uw} = A_{13}/\sqrt{A_1}\sqrt{A_3}$
$C_0^{19}n^{05}k_c^{4/7}$	$k_x^{-1/2}$	k_x^0	$k_x^{-1/4}$	$k_xz < 10^{-1}$	0.8365

Table 3.4: Near wall u, w scaling laws, their correlation coefficient for the large-scale motions ($k_x^{-1/2}$ region of E_{uu} spectra) and wavenumber range for the Case $C_0^{19}n^{05}k_c^{4/7}$.

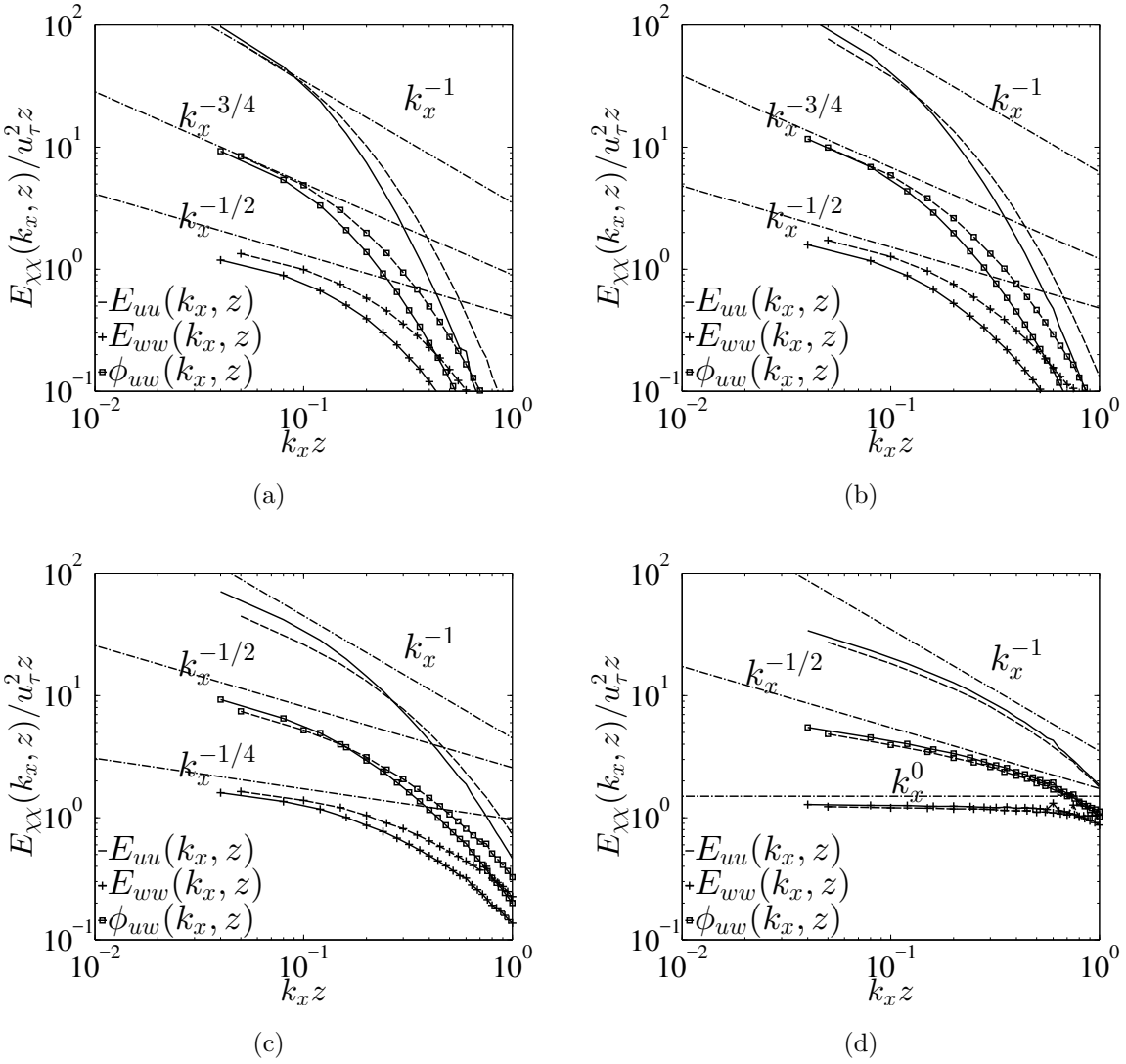

Figure 3.16: Near wall u, w spectral correlation scale comparing $E_{\chi\chi}(k_x, z) = E_{uu}(k_x, z), E_{ww}(k_x, z), \phi_{uw}(k_x, z)$ all normalized with $u_\tau^2 z$ at normalized wall distance $\xi = 0.02, 0.025$. (a) Case $C_0^{16} n^2 k_c^{4/7}$ (b) Case $C_0^{17} n_\sigma^1 k_c^{4/7}$ (c) Case $C_0^{09} n^2 k_c^{4/7}$ (d) Case $C_0^{19} n^{05} k_c^{4/7}$. Solid – $z/H = 0.02$, Dashed – $z/H = 0.025$

(corresponding to a k_x^{-1} region of the streamwise spectra) for the models $C_0^{16}n^2k_c^{4/7}$, $C_0^{09}n^2k_c^{4/7}$, $C_0^{17}n^1k_c^{4/7}$, $N_\sigma k_c^{4/7}$, $C_0^{19}n^{05}k_c^{4/7}$, together with the correlation coefficient $\rho_{uw} = A_{13}/(\sqrt{A_1}\sqrt{A_3})$, in Table 3.3. The correlation coefficient is expected to be high for well correlated models. The Table 3.3 confirms that the models $C_0^{16}n^2k_c^{4/7}$, $C_0^{17}n^1k_c^{4/7}$, $C_0^{19}n^{05}k_c^{4/7}$ depict the presence of the near-wall correlation, with the value of the correlation coefficient roughly at $\sim$ 83%. Although the models $C_0^{16}n^2k_c^{4/7}$, $C_0^{17}n^1k_c^{4/7}$ do reveal the wall correlation, the scaling laws for the co-spectra are incorrect, which, as can be seen from Figures 3.16a and Table 3.3, comes from the incorrect E_{ww} spectra. It is the model $C_0^{19}n^{05}k_c^{4/7}$ that not only produces the near-wall correlations, but also gives the correct scaling laws for the correlations. Interestingly, for model $C_0^{09}n^2k_c^{4/7}$, although it produces the correct scaling for the co-spectra, the near-wall correlation does not exist due to, again, a wrong scaling of the w component [14].

Table 3.3 also lists the range of k_xz values where the scalings characteristic to the region were observed. Note that it is $k_xz < 10^{-1}$ for the three models $C_0^{16}n^2k_c^{4/7}, C_0^{17}n^1k_c^{4/7}, C_0^{19}n^{05}k_c^{4/7}$, and $10^{-1} < k_xz < 10^0$ for the model $C_0^{19}n^{05}k_c^{4/7}$. The correlations that we see in the near-wall spectra are associated with the attached inactive motions as discussed in the previous section. The Case $C_0^{19}n^{05}k_c^{4/7}$ predicts the correct upperbound of the *active wall normal motions*, $k_xz \sim 10^0$ corresponding to $\lambda_x/z \sim O(10^1)$, while the other three Cases $C_0^{16}n^2k_c^{4/7}, C_0^{09}n^2k_c^{4/7}, C_0^{17}n^1k_c^{4/7}$, overpredict the size of these active motions by a decade, $k_xz \sim 10^{-1}$, or $\lambda_x/z \sim O(10^2)$, in addition to producing an incorrect scaling in Cases $C_0^{16}n^2k_c^{4/7}, C_0^{17}n^1k_c^{4/7}$, and uncorrelated u, w motions in the Case $C_0^{09}n^2k_c^{4/7}$. We must mention that the Case $C_0^{19}n^{05}k_c^{4/7}$ predicts the $E_{uu} \sim k_x^{-1/2}$ scaling for such large-scale eddies, $k_xz \sim 10^{-1}$, $\lambda_x/z \sim O(10^2)$, see Table 3.4, consistent with the previous observations at high Reynolds numbers [44, 108], which are also well correlated, with the same correlation

coefficient of $\sim 83\%$ as the k_x^{-1} law. As discussed in Section 3.2.3, we surmise that the $-1/2$ scaling law might possibly be a modification to the k_x^{-1} scaling with certain correction factors as predicted in [76], but also caution the readers that careful analysis needs to be performed at larger computational domains before we can conjecture on the possible implication of $-1/2$ region [77].

3.2.4 2D spectra

While the analysis of 1D spectra depicts the inner and outer layer streamwise length scales of the eddies affected by SGS dissipation, they cannot predict the structure of the eddies being influenced by the LES dissipation. The potential of 2D spectra in identifying eddy structures have been long realized since the last two decade in simulations [76–78, 117] and experiments [74, 75, 103, 118]. In the above works, 2D spectra has been utilized to estimate the streamwise and spanwise length scales of the near wall eddies consistent with the Townsend's attached eddy hypothesis [60] in wall bounded turbulence.

Figure 3.17 shows the 2D premultiplied streamwise energy spectra, $k_x k_y E_{uu}(k_x, k_y, z)$, in the plane of streamwise-spanwise wavelengths for different SGS models as in Cases $C_0^{16} n^2 k_c^{4/7}, C_0^{09} n^2 k_c^{4/7}, C_0^{19} n^{05} k_c^{4/7}$. Similar to the 1D spectra, the effect of explicit filtering has been found to be inconsequential to the analysis of active and inactive length scales and their scaling laws and has been omitted from discussion from here onwards. We compare the spectral results with $k_c = 4/7$, since this value of cut-off together with our model Case $C_0^{19} n^{05} k_c^{4/7}$, gives the best results for the log-law of the wall.

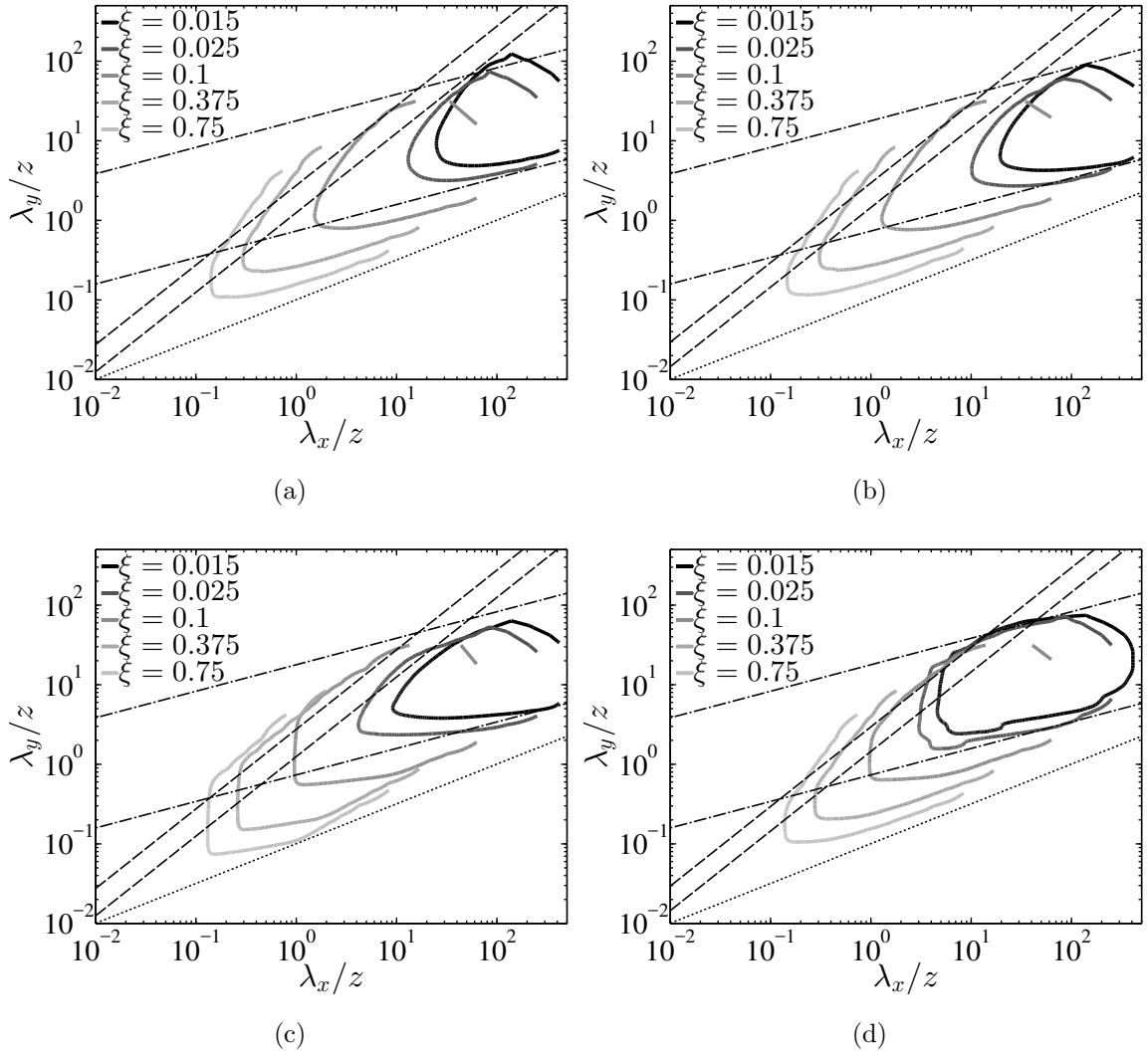

Figure 3.17: Premultiplied 2D streamwise energy spectra $k_x k_y E_{uu}(k_x, k_y)$ in streamwise-spanwise wave number plane, λ_x/z and λ_y/z, normalized with inertial length scale z, $\lambda_{x,y} = 2\pi/(k_{x,y})$. (a) Case $C_0^{16} n^2 k_c^{4/7}$ (b) Case $C_0^{17} n_\sigma^1 k_c^{4/7}$ (c) Case $C_0^{09} n^2 k_c^{4/7}$ (d) Case $C_0^{19} n^{05} k_c^{4/7}$. All plots are at 5 different heights $\xi = z/H = 0.015, 0.025, 0.1, 0.375, 0.5$, with lighter line color shades with increasing ξ. All contours are at 0.125 times of maximum. Dashed black – $\lambda_y/z \sim \lambda_x/z$; Dotted black – $\lambda_y/z \sim (\lambda_x/z)^{1/2}$; Chain dotted black – $\lambda_y/z \sim (\lambda_x/z)^{1/3}$.

Inner Layer

The theoretical scaling laws of λ_x, λ_y in the inner layer ($\xi < 0.1$) can only be observed in Case $C_0^{19}n^{05}k_c^{4/7}$ with the *active motions* corresponding to $\lambda_y \sim \lambda_x$ extending from the minimum resolved length scale to $\lambda_x \sim 10z$ at the spectral ridge, beyond which the *attached inactive motions* initiate with the power law scaling (see the schematic in Figure 3.7b in Section 3.2.3 for details), as can be judged from Figure 3.17d.

For overdissipative cases like $C_0^{16}n^2k_c^{4/7}$, Figure 3.17a, 3.17c, or underdissipative cases like $C_0^{09}n^2k_c^{4/7}$, Figure 3.17b, the near-wall dynamics are heavily influenced. For case $C_0^{16}n^2k_c^{4/7}$, the linear scaling $\lambda_y \sim \lambda_x$ of the active motions persists for scales $\lambda_x \sim 100z$, and the power law "$\boldsymbol{A}$" scaling corresponding to $p = 3$ (attached inactive motions) is completely absent. However, traces of 1/3 law "$\boldsymbol{B}$" scaling can still be found for cases $C_0^{16}n^2k_c^{4/7}, C_0^{17}n^1k_c^{4/7}$. It is suspected, that the absence of a conspicuous inactive eddy region is responsible for the smaller regime of k_x^{-1} in the 1D u spectra (see Figure 3.12a) that also occurs at larger length scales than anticipated. For Case $C_0^{09}n^2k_c^{4/7}$, however, even though the scaling corresponding to the *active motions* are present at $\lambda_x < 10z$, none of the power-law "$\boldsymbol{A}$", "$\boldsymbol{B}$" ($p = 3$) scalings corresponding to the *inactive motions* can be conspicuously identified in the near wall region.

Outer Layer

However, at the outer-layer, ($\xi > 0.1$), the models $C_0^{16}n^2k_c^{4/7}, C_0^{19}n^{05}k_c^{4/7}$ predict the square-root scaling, $\lambda_y/z \sim (\lambda_x/z)^{1/2}$ corresponding to the longer-narrower structures ($\lambda_x > \lambda_y$). The square-root scaling analysis in the outer layer would be similar to that of the inner layer, mainly due to similar dynamics of long term dispersion of background turbulence (see [76, 77] for details). This is, however, not the case for the model $C_0^{09}n^2k_c^{4/7}$, where no such square root scaling is distinctly identified, as we

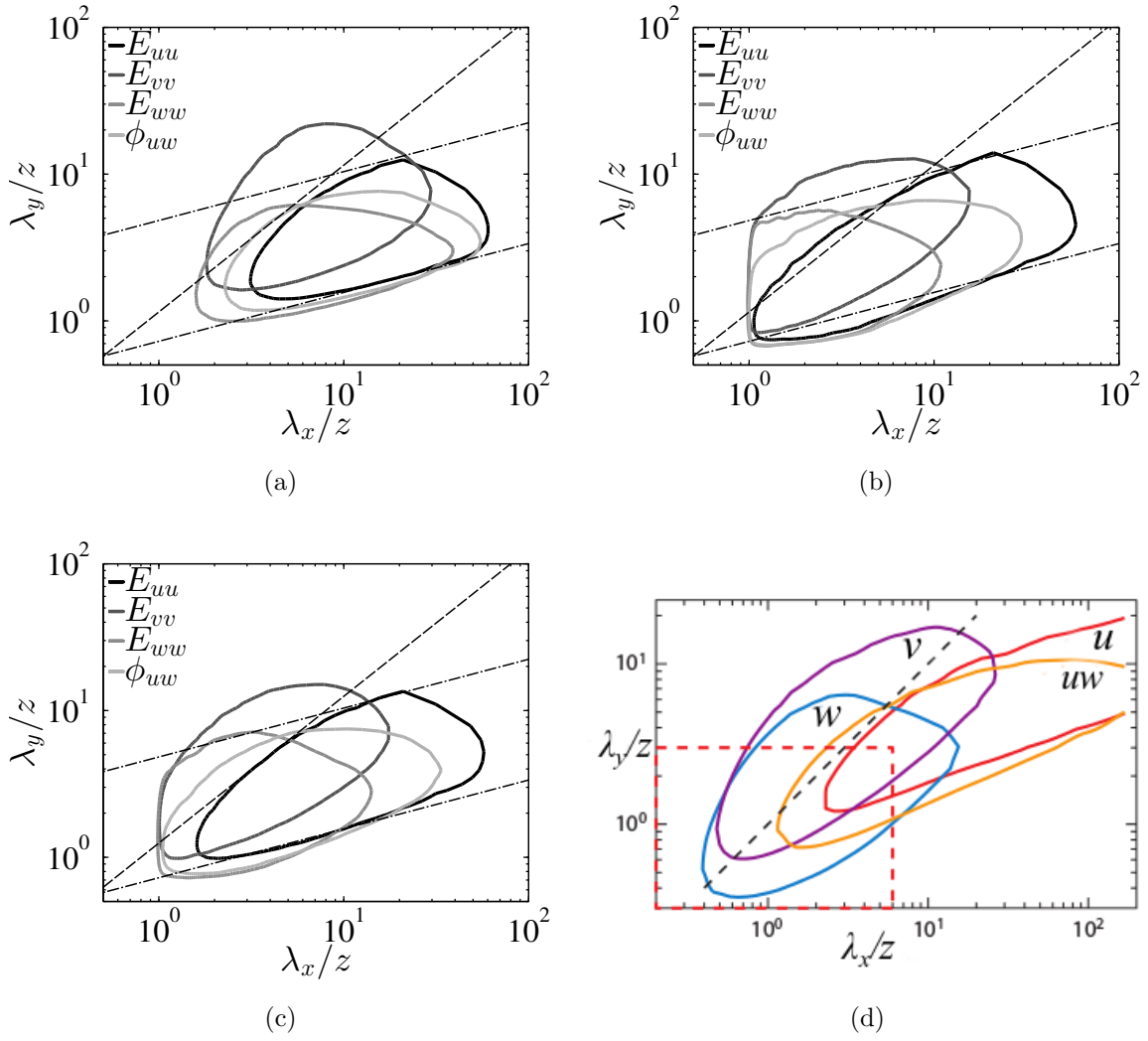

Figure 3.18: (a)–(d) Premultiplied 2D streamwise energy spectra $k_x k_y E_{\xi\xi}(k_x, k_y, z)$ ($\xi = u, v, w$) and cospectra $k_x k_y \phi_{uw}(k_x, k_y)$ in streamwise-spanwise wave number plane at $z/H = 0.15$. (a) Case $C_0^{16} n^2 k_c^{4/7}$ (b) Case $C_0^{09} n^2 k_c^{4/7}$ (c) Case $C_0^{19} n^{05} k_c^{4/7}$. Premultiplied spectra of E_{uu}, E_{vv}, E_{ww}, ϕ_{uw} are plotted in progressively lighter shades of gray. The contours in (a)–(d) are at 0.4 times of their maximum. Dashed black – $\lambda_y/z \sim \lambda_x/z$; Chain dotted black – $\lambda_y/z\,(\lambda_x/z)^{1/3}$ (e) Premultiplied 2D energy spectra and cospectra of channel flow taken from Jiménez [85] reproduced with the permission of Annual Review of Fluid Mechanics, Volume 44, 27-45 (2012) by Annual Reviews, `http://www.annualreviews.org`.

move into the far-outer layer. It is perhaps not hard to associate this absence of the square root scaling in the outer-layer, with the absence of a proper $-5/3$ law cascade of the 1D spectra, all indicating towards the underdissipative effects.

In order to understand the implications of the presence or absence of the scaling laws as described above, we also plot all the u, v, w energy and $\overline{u'w'}$ shear-stress spectra at $z/H = 0.15$ in Figures 3.18a – 3.18c, obtaining qualitatively similar structures as in Ref. 85 (reproduced here in Figure 3.18d). While Case $C_0^{19}n^{05}k_c^{4/7}$ displays a qualitatively similar picture with the DNS of the channel flow simulations in Ref. 85, with some minor discrepancies arising due to a difference in the domain size, the situation is quite different for Cases $C_0^{16}n^2k_c^{4/7}, C_0^{09}n^2k_c^{4/7}$. Due to the overdissipative effects of cases $C_0^{16}n^2k_c^{4/7}$, for scales $\lambda_x > 10z$, the linear scaling persists for the u spectra, and also w spectra erroneously extends to these large scales, implying that the 3D active turbulent motions become artificially large for case $C_0^{16}n^2k_c^{4/7}$, extending to scales where the two dimensional inactive motions should have been present. For the underdissipative case of $C_0^{09}n^2k_c^{4/7}$, the scale $\lambda_x \sim 10z$ corresponds to the long-wavelength cutoff for the w spectra, which is physically consistent from the perspective of the size of the active motions. The $1/3$ scaling law, however is absent.

The above observations are the indication of a requirement of an *optimal* SGS dissipation in our spectral-element LES models, which can be further illustrated if we look into the 2D premultiplied enstrophy spectra ($k_xk_yE_{\omega\omega} = k_xk_y\langle\hat{\omega}\hat{\omega}^*\rangle$, $\hat{\omega}$ is the Fourier transform of vorticity) in Figures 3.19a, 3.19b. Enstrophy is often considered as a surrogate for the turbulent dissipation [117, 119, 120], and in our case it is a good representative of the total (i.e., Kolmogorov + SGS) dissipation in the LES models. For Cases $C_0^{09}n^2k_c^{4/7}, C_0^{19}n^{05}k_c^{4/7}$, the smallest scales of motion in the near-wall dissipation ($\xi = z/H = 0.025$) are $\lambda_x < 10z$. In Case $C_0^{16}n^2k_c^{4/7}$, a severe near-wall dissipation hinders the growth of small scale dissipative eddies, and

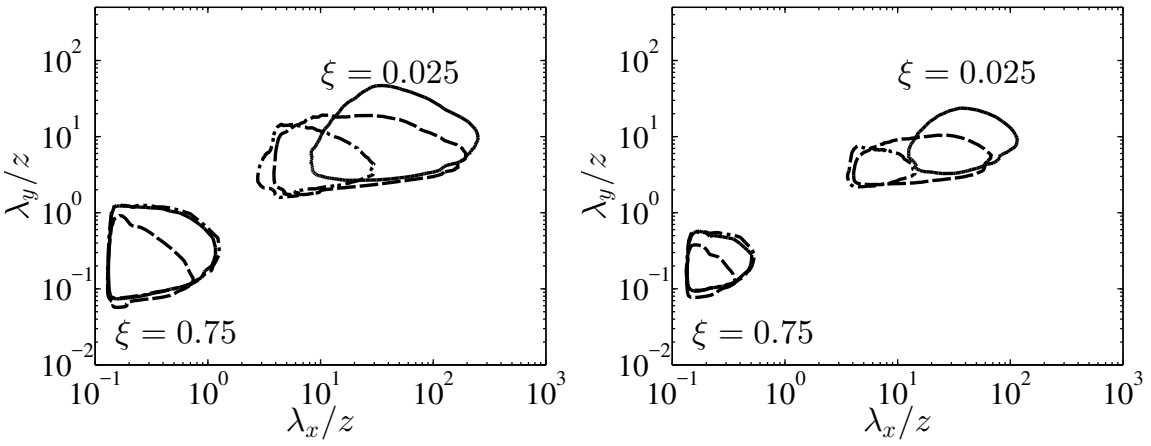

Figure 3.19: Premultiplied enstrophy spectra $k_x k_y E_{\omega\omega}(k_x, k_y, z)$ in the streamwise-spanwise wavenumber plane for different cases $C_0^{16} n^2 k_c^{4/7}, C_0^{09} n^2 k_c^{4/7}, C_0^{19} n^{05} k_c^{4/7}$. (a) contour level of 25% of the maximum. (b) contour level of 50% of the maximum. $\xi = z/H$, is the normalized distance from the wall. Solid line – Case $C_0^{16} n^2 k_c^{4/7}$, Dashed line – Case $C_0^{09} n^2 k_c^{4/7}$, Chain dotted line – Case $C_0^{19} n^{05} k_c^{4/7}$.

the smallest resolved scales are $\lambda_x \gtrsim 10z$ that correspond to the range of attached inactive motions. In the outer layer ($\xi = z/H = 0.75$), the dissipation characteristics for Cases $C_0^{16} n^2 k_c^{4/7}, C_0^{19} n^{05} k_c^{4/7}$ collapse, confirming the correct $-5/3$ cascade seen in Figures 3.12a, 3.12c, 3.12d, while for the Case $C_0^{09} n^2 k_c^{4/7}$ (Figure 3.12b), the largest scales involved in the outer-layer dissipation are much smaller than in the Cases $C_0^{16} n^2 k_c^{4/7}, C_0^{19} n^{05} k_c^{4/7}$, revealing an inefficient cascade.

In general, before we conclude, a brief Summary of the behaviour of the wall-damped Smagorinsky based SGS models with different parameters is presented in this paragraph. Figure 3.20 is a qualitative sketch (picture not to scale) of the attached eddies (hairpin vortices attached to the "wall" at an acute angle $\sim 10^\circ$) obtained from the spectral information as discussed above. The representative hairpin-like eddy I is of length scale $\lambda_x \gg 10z$, and hence at the height of z, it would essentially represent a horizontal two component u, v flow [79] corresponding to attached *inactive motions*. Eddies of scale $\lambda_x \sim O(z)$ (representative eddies II, III) are responsible

for the 3D *active motions*. For an overdissipative model, the eddy viscosity results in the mixing of the eddies near the wall and attenuation of the small scale phenomenon. This inflicts an artificial abundance of the *active* eddies of the $O(z)$ scale, and hence the 3D motions (averaged over all eddies) extend to longer scales as seen in Figure 3.18a, which is schematically illustrated in Figure 3.20a. This also weakens the vertical near-wall motions (w) manifested by the attenuation of $\widetilde{\overline{w'^2}}$ in Figure 3.6. An underdissipative case (Figure 3.20b) actually allows for much smaller eddies near the wall to be sustained, but an inefficient forward energy cascade in the outer layer (see Figure 3.12c) results in a pileup of energy at smaller length scales. For the optimally dissipative case (Figure 3.20c), the size of the near wall eddies represents the correct distribution of the length scales of the near-wall eddies [79] that eliminates the presence of "artificial viscous sublayer", in concordance with the Townsend's attached eddy hypothesis [60]. The Table 3.5 further summarizes the scaling laws and the observed correct or incorrect physics of the inner and outer layer eddies with the different parameters of the Smagorinsky-based SGS models.

LES Models	LLM	TS Trends	$E_{uu} \sim k_x^{-1/2}$	$E_{ww} \sim k_x^{0}$	$\lambda_y \sim \lambda_x^{1/2}$	$-5/3$ scaling	SR Location
$C_0^{16} n^2 k_c^{4/7}$	Yes	Incorrect	No	No	Yes	Yes	Incorrect
$C_0^{17} n^1 k_c^{4/7}$	Yes	Incorrect	No	No	Yes	Yes	Incorrect
$C_0^{09} n^2 k_c^{4/7}$	Yes	Incorrect	No	No	No	No	Incorrect
$C_0^{19} n^{05} k_c^{4/7}$	No	Correct	Yes	Yes	Yes	Yes	Correct

Table 3.5: A summary of the behaviour of different SGS models $C_0^{16} n^2 k_c^{4/7}$, $C_0^{17} n^1 k_c^{4/7}$, $C_0^{09} n^2 k_c^{4/7}$, $C_0^{19} n^{05} k_c^{4/7}$ compared against 9 important trends in physical and spectral domain that represent inner and outer layer physics. (i) LLM – Log Layer Mismatch, (ii) TS trends – scaling trends in the vertical variation of turbulent stresses near the wall at $z/H < 0.1$, (iii) $k_x^{-1/2}$ scaling of the streamwise spectra near wall. (iv) k_x^0 scaling of the wall-normal spectra near the wall, (v) $\lambda_y \sim \lambda_x^{1/2}$ scaling of premultiplied 2D streamwise spectra at the outer layer, $(viii)$ $k_x^{-5/3}$ scaling of the velocity spectra and cospectra at the outer layer, (ix) SR location – location of the spectral ridge where linear to power law scaling transition occurs for premultiplied 2D streamwise spectra, serving as a barrier between active and inactive motions.

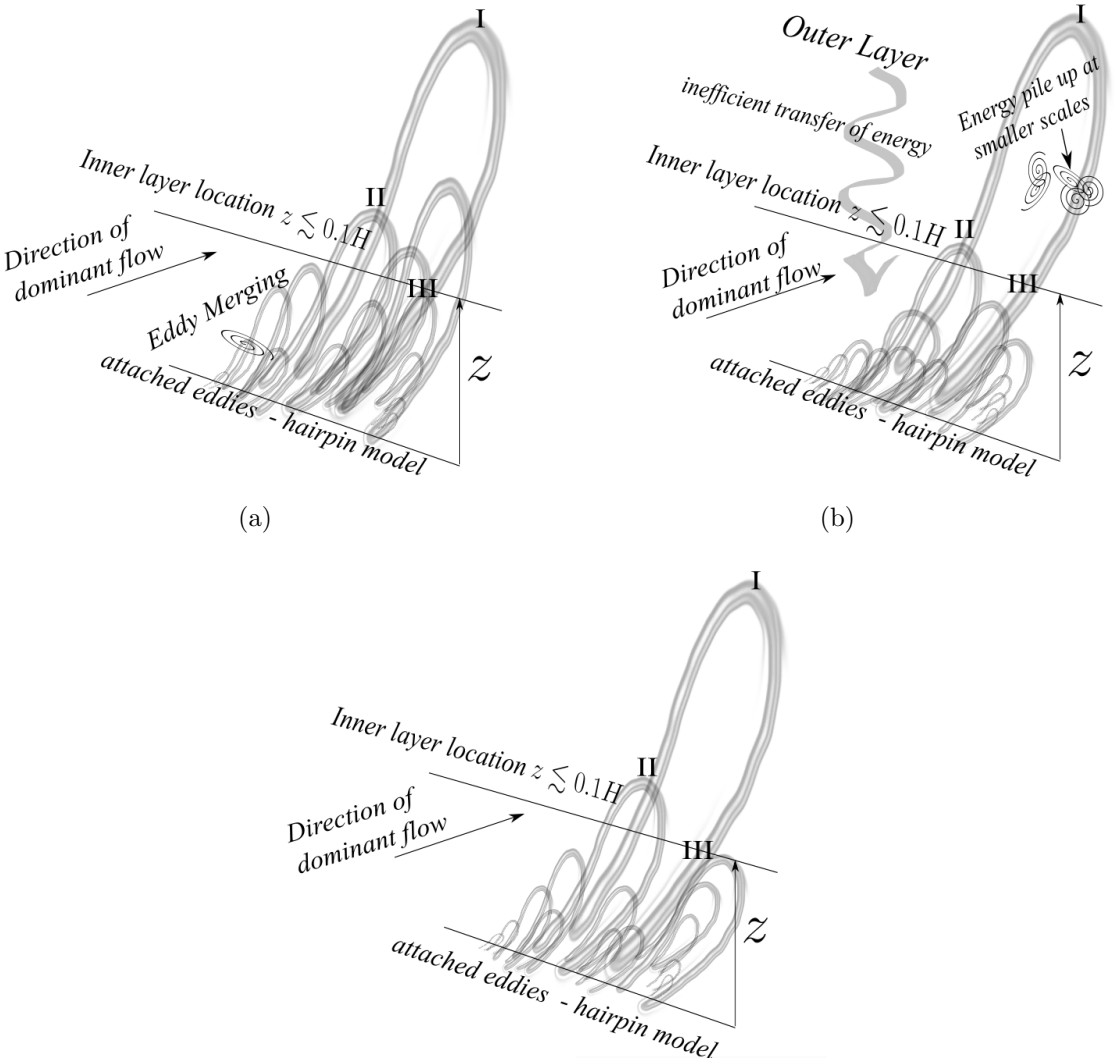

Figure 3.20: Sketch (not to scale) of the near wall dynamics for (a) overdissipative ($C_0 = 0.16, n = 2$), (b) underdissipative ($C_0 = 0.09, n = 2$) and (c) optimally dissipative ($C_0 = 0.19, n = 0.5$) wall-damped Smagorinsky SGS models. Attached eddies are illustrated using *hairpin vortices*. I, II, III are the representative eddies at different wall locations.

3.3 Conclusion

The current studies involving the different LES models not only provide the design procedure for the reliable yet inexpensive SGS models in spectral element framework, but also focus on another important aspect – the behaviour of the eddies in wall-turbulence, under the influence of artificial length scales introduced by Smagorinsky based subgrid-scale eddy viscosity closures.

We found that the LES results are extremely sensitive to the parameters of the subgrid-scale closure model, and the Smagorinsky based SGS models need to be "optimally tuned" to retrieve the correct flow physics. Our results have been further strengthened by grid sensitivity analysis (Appendix C) which also manifests the robustness of the proposed LES models designed in spectral element framework. It has been observed that the elimination of the effect of artificial SGS filtering length scales in our LES model is possible by reducing the growth rate of the filter scale l_f near the wall by reducing n while simultaneously increasing C_0 slightly, to a threshold, beyond which the physical length scales become dominant, which helps produce the correct turbulent statistics and spectra. The results, on the other hand, are not significantly affected by the explicit filtering in the near-wall modelling, except, perhaps, the amount of Log Layer Mismatch and the spectra in the largest scales of motions near the wall. The exact reason is still not entirely understood and requires further investigation, but it can be attributed to the amount of removal of the near-wall dissipative scales through filtering. Based on our computations, the model $C_0^{19} n^{05} k_c^{4/7}$ is advocated to be the best model used for LES in a spectral element framework.

Investigating the physics of the "artificial length scales" of the different LES models helps build the fundamental understanding of the *inner* and *outer* layer eddies as well as the effect of the SGS closure on the formation of "eddy viscosity" sub-layer.

The principal findings in the current work are summarized below, by the following points:

(i) Apart from influencing the fine-scale dissipative eddies and the energy cascade ($-5/3$ law) near wall, the Smagorinsky based SGS models are also found to affect the larger scales as well, e.g., the active and inactive motions.

(ii) Overdissipation of the Smagorinsky SGS models affects the lengthscales of the *3D active motions* in the inner layer, making them as large as the *2D inactive* ones possibly due to "mixing of eddies". The absence of conspicuous regions of inactive motions can be correlated with smaller, erroneous, regime of the k_x^{-1} law.

(iii) Underdissipation of SGS models results in the larger scales of motion at the outer layer not loosing enough energy, through the transfer mechanism (SGS dissipation). This is supposedly reflected in the incorrect scaling and hence dynamics of the *attached inactive motions* near the wall, supporting the fact that the outer-layer motions also influence the near-wall structures.

(iv) Both the effects of over and under-dissipation in Smagorinsky based models detrimentally influence the near-wall organization, more severely through the vertical energy, or w spectra, resulting in incorrect u, w correlations near the wall. For over-dissipation, the effect of incorrect w spectra is also seen in extending the length scales of $3D$ active motions.

(v) In the outer layer, the correct prediction of $-5/3$ scaling law as seen in the u spectra is inherently related to capturing the square-root scaling of 2D u spectra corresponding to dispersion of eddies in background turbulence.

These outcomes indicate that "optimum LES dissipation", both in the inner and the outer layer, is required for correctly resolving the large-scale flow physics in neutral ABL flows. Consequently, it is reasonable to conclude that the log-law of the wall, the location of k_x^{-1} law, and the scaling of the active and inactive motions near the wall, are closely associated with the proper SGS dissipation in every region of the flow. From a practical viewpoint, our study shows that the "optimal dissipation" can still be obtained from a fine-tuned standard wall-damped Smagorinsky model, without having to use more expensive dynamic models.

Chapter 4

MODULATION OF LARGE SCALE COHERENCE IN PERIODIC WIND FARMS

4.1 Introduction

Large organized arrays of wind turbines stretching over a span of tens of kilometers in the horizontal direction, commonly known as *wind farms* [6,7,121], are conventionally used to extract wind energy from the atmospheric boundary layer (ABL) since the last two decades. Efficient design and operation of large wind farms not only requires the presence of high mean wind speed $\bar{U}$ (annual mean) at hub-height location, but also benefits from specific considerations regarding wind turbine position, e.g., the inter-turbine streamwise and spanwise distance, staggered vs. aligned arrangements, etc [122–126]. The dynamics of the power extraction by the wind turbines in a farm are very different and far more complicated than those of a stand-alone turbine [5, 16, 20]. As an example, our recent study [127] has revealed that large scale structures with length-scales of the order of ten turbine rotor diameters (D) made significant contribution to the power generated by the wind turbines in a farm, which have not been observed so far in lone-standing turbines. While the presence of length scales $\sim D$ contributing to the turbine power in wind farms is intuitive and was reported recently [19, 20], the current literature lacks an organized study on the contributions of still larger scales of motion ($\gg D$) in the wind farms. Large scale structures near the wall are known to carry significant amount of turbulent kinetic energy and Reynolds stresses in wall bounded turbulence and were the subject of many recent studies in canonical and boundary layer flows [94–96, 107, 108, 128, 129], but not so much is known about the behaviour of such structures in the region of

wind turbine wakes. Understanding the physics of large scale structures and their organization (coherence) influencing the wind turbines is important for characterization of wind turbine wake dynamics and power generation. These structures can also potentially serve as an important metric apart from the hub-height mean wind speed in selecting land locations of wind farms.

Large wind farms are usually studied as *infinite wind farms* in the asymptotic limit [5,23,24], invoking streamwise-spanwise homogeneity through periodic boundary conditions. In this framework, the flow is "fully developed" and the wind turbine array imposes an additional *geometric roughness* $z_{0,hi}$, and friction velocity $u_{*,hi}$ (scales with streamwise–pressure gradient as $u_{*,hi}^2/H = -\frac{1}{\rho}\partial p/\partial x$ [5]) which are higher than the bottom wall aerodynamic roughness $z_{0,lo}$ and wall friction velocity $u_{*,lo} = \sqrt{\tau_w/\rho}$ (τ_w is the wall-shear stress) imposed by the topography of the land [44, 45, 54, 130]. The wind turbine array roughness $z_{0,hi} \sim z_h/s_x s_y$ is influenced both by the turbine hub-height z_h, as well as non-dimensional streamwise, spanwise turbine spacing parameters $s_x,\ s_y$ ($s_x D, s_y D$ are the physical turbine spacings in multiples of the rotor diameter D). Analogous to the rough wall boundary layer flows, the concept of infinite wind farms provides a consistent way to study the influence of vertical physics in ABL turbulence due to the presence of wind turbines [5, 127, 131, 132]. Previous literature have also illustrated the dominance of the vertical physics compared to the homogeneous horizontal counterpart in very large wind farms and have established that the vertical entrainment of mean kinetic energy (MKE) through turbulent shear stress flux, is responsible for the power generated by the turbines [5, 23, 24, 132, 133]. To the authors knowledge, there was only one recent study on large wind farms that commented on the presence of large scale energetic counter-rotating roller modes in kinetic energy entrainment deduced by Proper Orthogonal Decomposition (POD) [134], despite the fact that large scale organizations in MKE transport play a significant role

in the power generated in large farms. In this work, we aim to analyse the physics of the large-scale structures in wind farms and investigate how they are influenced by the important farm design parameters, like wind turbine hub-height z_h, and the non-dimensional streamwise, spanwise inter-turbine distances (s_x, s_y). It must be appreciated that the present work focuses on the global transport of the MKE flux in the computational domain, from the top wake region, $z_h + D/2$, to the bottom wake region, $z_h - D/2$, or vice-versa, and does not attempt to comment on how they correlate to the localized energy transfers in the wind turbine rotor region. This study is expected to improve the understanding of the MKE transport responsible for wind turbine power and the length scales involved, and also elucidate towards an efficient wind farm design that could position the wind turbines to systematically utilize the large scale structures near and around them. The numerical studies in this work involving wind farms in ABL at $Re \sim O(10^{10})$ are performed in a framework of Large Eddy Simulations with near wall modelling. The wind turbine forces are modelled using the state-of-the-art actuator line model [12], without resolving the turbine blades. Additionally, the use of periodic boundary conditions in our computations allows us to use Fourier transform in the horizontal directions and define the length scales (wavelengths) as the inverses of wavenumbers k_x, k_y.

4.2 Computational Setup

The computational domain utilized in this work to approximate the infinite wind farm setting is of rectangular geometry with dimensions $2\pi H \times \pi H \times H$ or $20\pi D \times 10\pi D \times 10D$ (H, D are the ABL thickness and the rotor diameter respectively), as in [5] (see a schematic in Figure 5.1 for details).

Wind turbines of fixed rotor diameter $D = 0.1H$ are placed in the computational

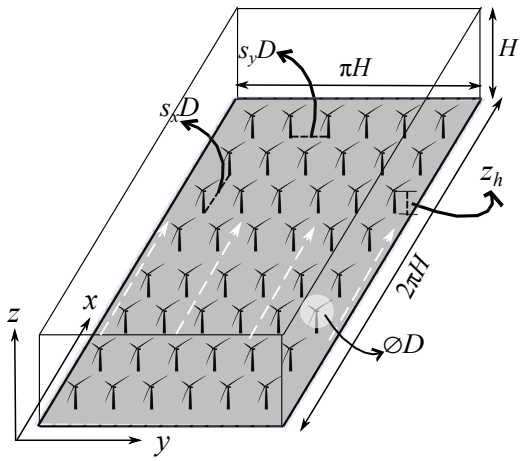

Figure 4.1: Computational domain showing the 8×6 periodic arrangement of wind turbines for the baseline case I. Hub height z_h, and rotor diameter D set to $0.1H$. The dashed white arrows indicate the direction of mean wind flow.

domain as organized arrays. Table C.1 documents the geometrical and computational parameters of the layout for the four cases simulated. The Reynolds number $Re = U_\infty H/\nu \sim 10^{10}$ has been set for all the cases, where U_∞ is the mean streamwise velocity at the top-edge of the boundary layer, which can be thought of as a representative of the geostrophic velocity in atmospheric flow driven by the pressure gradient and Coriolis forces [24,25]. Normalization with U_∞ was found to provide a meaningful comparison of variables between the different cases in the periodic wind farm setting. Case I is considered as a baseline case with $s_x = 7.85, s_y = 5.23$, and a hub height $z_h = D = 0.1H$ located in the inner layer. Case I has been chosen as a standard test case considered in several other studies [5,126,134] and is consistent with the parameters of realistic wind farms in United States and Europe. Cases IIa and IIb, (see Table C.1), will provide a way to study the influence of the streamwise and spanwise turbine distances on the large scale structures in the MKE transport, while Case III will contribute to our understanding of the MKE transport with a higher hub-height reaching into the outer layer ($z_h = 0.33H$), where the influence of the wall is diminished as compared to $z_h = 0.1H$. The bottom wall roughness $z_{0,lo} = z_0 = 10^{-4}H$

induced by topography is constant through all our simulation cases I,IIa,IIb and III. While the *geometric roughness* $z_{0,hi}$ as a function of (z_h, s_x, s_y) can be calculated from the LES simulation data, the geometric roughness by the wind turbines can also be apriori estimated from the roughness measure by Lettau [135], $z_{0,Lett} = z_h\pi/8s_xs_y$. A comparison of Lettau roughness normalized by the aerodynamic wall roughness, $z_{0,Lett}/z_0$ in Table C.1 clearly indicates that the geometric roughness is an order of magnitude higher than its aerodynamic counterpart and is sensitive to the hub-height and turbine arrangements. The LES framework for the simulations performed has been setup using a wall-damped standard Smagorinsky based closure and shear stress boundary condition at the bottom wall [42, 136], the details of which can be found in Chapter 2 of the thesis. Here we document the variation of the Smagorinsky coefficient C_s for the wind farm domain along with the neutral ABL setup in order to illustrate the differences in the subgrid dissipation among the models. Figure 4.2, shows that the filter coefficient values remain very similar throughout the vertical variation, except in regions of finer grid around the turbine rotors, where expectedly the C_s values increase while preserving the shape into account for the decreasing grid scale Δ corresponding to the filter scale associated with the subgrid mixing l_f.

Cartesian spectral element collocated grid has been used in the simulations, with the number of elements and the total grid count for each simulated case listed in Table C.1. All simulations were performed with 7th polynomial order of approximation, which required 8 GLL collocation points per element per direction. The grids were constructed to satisfy some specific resolution requirements: *a*) for the actuator line model, one requires on the order of 4 spectral elements along the actuator line in the yz rotor plane with the current GLL resolution; *b*) one needs at least one spectral element to cover the distance of one rotor diameter downstream of each turbine in the x direction. These refinements are necessary in order to capture the helical vortices

and the wakes shed by the rotating turbines downstream, and hence the number of turbines (see Table C.1) expectedly determines the grid requirements in the domain. Appendix D.1 provides a more detailed documentation of the grid structure and grid resolution of the simulated cases.

The LES simulations as in Table C.1 are computationally expensive requiring $\sim O(10^7)$ grid points and have been started with statistically stationary neutral ABL initial condition obtained from a separate precursor simulation. The wind turbine (WT) simulations have been run for long enough to allow the WT domain achieve temporal invariance in the statistical sense. After that, spatio-temporal snapshot data of velocities are collected for a span of $\sim 50T_e$ time ($T_e = 2\pi H/U_\infty$ is a flow-through time), which were used for spectral analysis involving Fourier transform.

Case	N_{turb}	s_x	s_y	$s_x \times s_y$	s_x/s_y	$z_{0,Lett}/z_0$	z_h	$N_x^e \times N_y^e \times N_z^e$	N_{xyz}
I	8×6	7.85	5.23	41.05	1.5	9.54	$0.1H$	$54 \times 56 \times 24$	2.52×10^7
IIa	4×6	15.7	5.23	82.11	3.0	4.77	$0.1H$	$45 \times 56 \times 24$	2.09×10^7
IIb	8×3	7.85	10.47	82.11	0.75	4.77	$0.1H$	$54 \times 44 \times 24$	1.98×10^7
III	8×6	7.85	5.23	41.05	1.5	31.5	$0.33H$	$54 \times 56 \times 24$	2.52×10^7
Neutral ABL	–	–	–	–	–	–	–	$30 \times 20 \times 24$	5.02×10^6

Table 4.1: LES cases for the wind farm simulations. Domain size is $2\pi H \times \pi H \times H$, and $D = 0.1H$, fixed for all cases. N_{turb} is the number of turbines in streamwise-spanwise arrangement, N_i^e is the number of spectral element in the i^{th} direction. N_{xyz} is the total number of grid points used in the computational domain. Grid of a neutral ABL simulation [136] is provided for comparison.

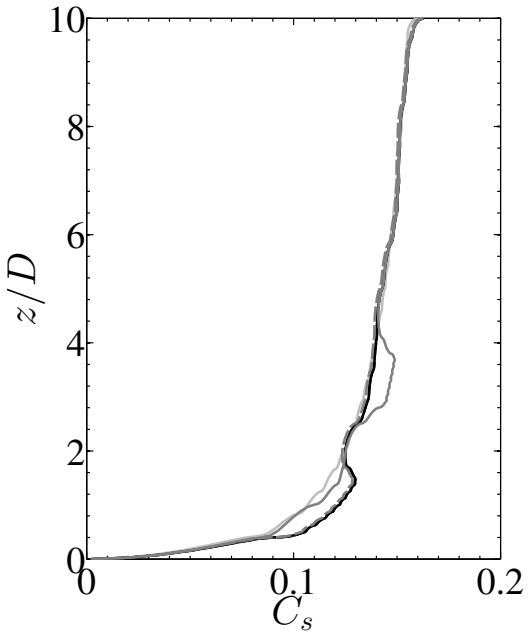

Figure 4.2: Variation of filter length coefficient C_s vs z/D (a) for different parameters of Smagorinsky model on neutral ABL grid. $\{C_0 = 0.19, n = 0.5\}$ – +, $\{C_0 = 0.17, n = 1\}$ – solid black line, $\{C_0 = 0.16, n = 2\}$ – $\triangleleft$, $\{C_0 = 0.09, n = 2\}$ – $\circ$. (b) for different flow configuration cases; neutral ABL (solid light gray), I (solid black), IIa (dashed black), IIb (dashed gray), III (solid gray).

4.3 Results and Discussion

4.3.1 Statistics of Infinite Wind Farms

The vertical variation of streamwise mean velocity profile for cases I–III is shown in Figure 4.3a. The baseline case I is validated against the actuator-disc LES simulations of Calaf et al. [5] illustrating the double log-layers as shown below

$$\langle \overline{u}(z) \rangle = u_{*,lo}/\kappa \log(z/z_{0,lo}),\ z < z_h - D/2, \tag{4.1}$$

$$\langle \overline{u}(z) \rangle = u_{*,hi}/\kappa \log(z/z_{0,hi}),\ z > z_h + D/2. \tag{4.2}$$

Here, $u_{*,lo} = \sqrt{\tau_w/\rho}$ comes from the wall shear stress, while $u_{*,hi} = \sqrt{-\frac{H}{\rho}\partial p/\partial x}$ comes from the pressure gradient force. However the friction scale velocities can also be approximated as $u_{*,lo} \approx \sqrt{-(\langle \overline{u'w'} \rangle + \langle \bar{u}''\bar{w}'' \rangle)|_{z_h - D/2}}$ and $u_{*,hi} \approx \sqrt{-(\langle \overline{u'w'} \rangle + \langle \bar{u}''\bar{w}'' \rangle)|_{z_h + D/2}}$. While the Reynolds stresses $\langle -\overline{u'w'} \rangle$ defined in the conventional way arise due to

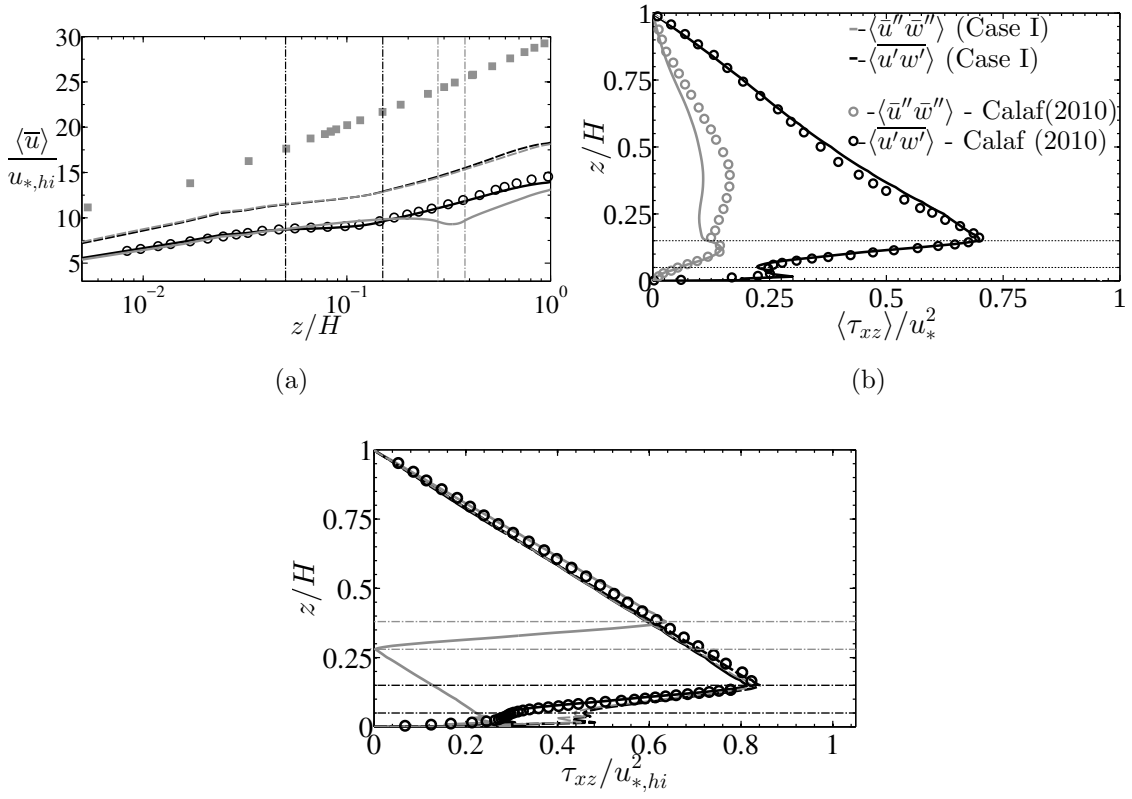

Figure 4.3: (a) Mean streamwise velocity $\langle\overline{u}\rangle$ normalized by $u_{*,hi}$ vs z/H. (b) Comparison of the Reynolds and Dispersive stresses of Case I with Calaf et al. [5] (c) Total (Reynolds + Dispersive) stresses τ_{xz} normalized by $u_{*,hi}$ vs z/H. Solid black – Case I, Dashed black – Case IIa, Dashed gray – Case IIb, Solid gray – Case III. Solid gray □ in (a) – neutral ABL; open ∘ in (a), (b) – Calaf et al.(2010) [5] (same wind farm setup parameters as in Case I). Black, gray dashed dotted vertical (a) and horizontal (b) lines: rotor swept area of Cases I–III.

the correlation between u, w velocities, the dispersive stresses, $-\langle\bar{u}''\bar{w}''\rangle$, are a manifestation of the spatial heterogeneity of the u, w velocities, with $\langle\bar{u}''\rangle = \bar{u} - \langle\bar{u}\rangle$, $\langle\bar{w}''\rangle = \bar{w} - \langle\bar{w}\rangle$ ($^-$, temporal averaging and $\langle\rangle$, xy averaging). However, the dispersive stresses are usually much smaller than the Reynolds stresses in infinite wind farms. A comparison of the total stresses τ_{xz} (Reynolds + Dispersive) for the different cases I-III (case I is also validated with [5]) is shown in Figure 4.3c. The comparison indicates that the differences in stresses in various wind turbine layouts for Cases I-III

are more illustratively seen in the bottom wake region of the rotor manifesting the vertical energy entrainment. Since all the results involve the LES filtered variables, the tilde is dropped for brevity here and in subsequent plots and analysis.

In infinite wind farms, the difference in turbulent shear stress (Reynolds + Dispersive) flux component of the Mean Kinetic Energy (MKE flux) at the top and bottom region of the rotor is responsible for the mean power per unit area generated by the wind turbines in the farm [5, 24, 124]. The MKE flux,

$$\Phi_p(z) = -(\langle\overline{u'w'}\rangle + \langle\bar{u}''\bar{w}''\rangle)\langle\overline{u}\rangle, \tag{4.3}$$

is plotted in Figure 4.4a for all the cases I-III. The MKE flux difference,

$$\Delta\Phi_p = \Phi_p(z_h + D/2) - \Phi_p(z_h - D/2), \tag{4.4}$$

was shown previously to correlate with the mean power density $\rho_{mean} \sim \Delta\Phi_p$ [5]. The mean power density, $\rho_{mean} = 1/(N_t s_x s_y D^2) \sum_{i=1}^{N_t} \bar{P}_i$, can be calculated by averaging the temporal mean power $\sum \bar{P}_i$ over all N_t turbines in the farm, and diving by the area $s_x D \times s_y D$. Figure 4.4b manifests a strong correlation between $\Delta\Phi_p$ (MKE flux difference) and ρ_{mean} in the present data, confirming the findings in [5]. The present data also indicates that the mean power density roughly scales with the geometric turbine roughness in the regime of investigated s_x, s_y. It is understood however that such relationship is not supposed to hold once separation distances fall below a certain limit. As a reference, the temporal variation of the array-averaged power $P(t) = \frac{1}{N_t} \sum_{i=1}^{N_t} \bar{P}_i$ for different cases is plotted in Figure 4.5.

4.4 Definition of Correlations and Spectra in WTABL Framework

Two point correlations

In this section we introduce the definitions of two point correlations and energy spectra

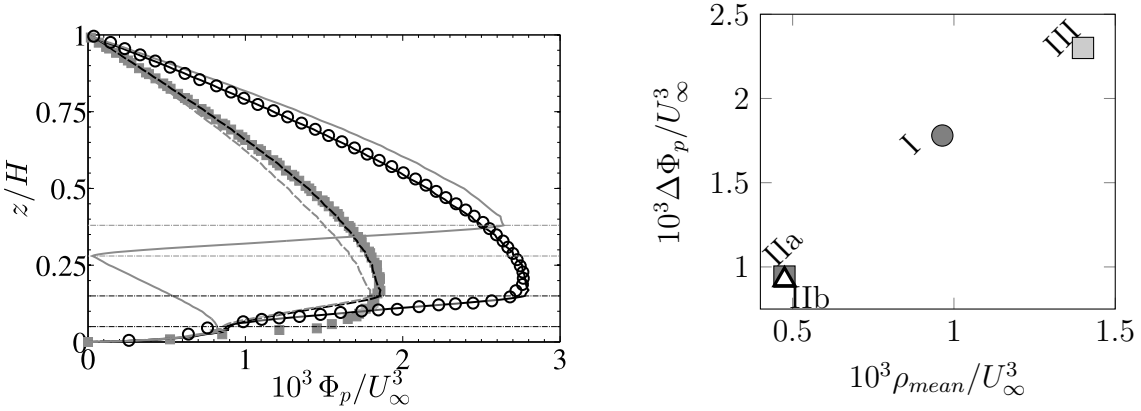

(a) (b)

Figure 4.4: (a) Vertical variation of the MKE flux for different cases. Solid black – Case I, Dashed black – Case IIa, Dashed gray – Case IIb, Solid gray – Case III. Gray square – neutral ABL. Open ∘ – Calaf et al.(2010) [5] (same wind farm setup parameters as in Case I). Dashed dotted lines: rotor swept area of Cases I–III. (b) Correlation between the difference in MKE flux $\Delta\Phi_p$ and mean power density ρ_{mean} for different cases.

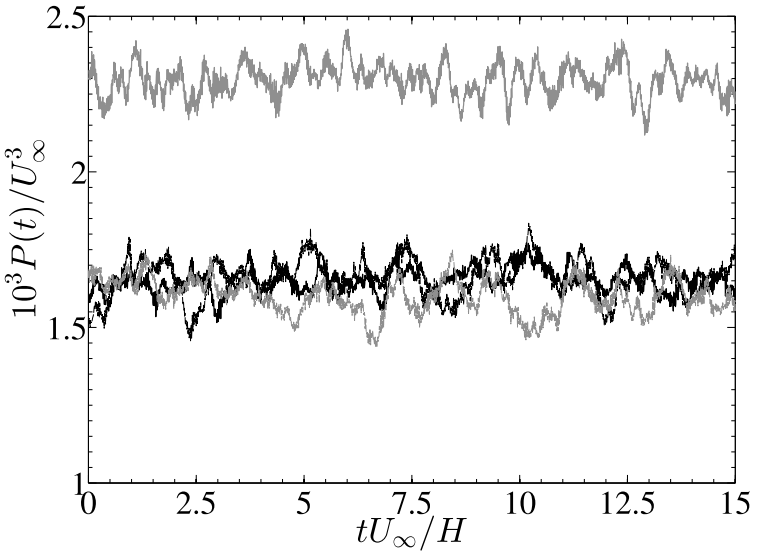

Figure 4.5: Temporal variation of the array-averaged power $P(t) = \frac{1}{N_t}\sum_{i=1}^{N_t}\bar{P}_i$ of the turbines in different layouts. Solid black – Case I, Dashed black – Case IIa, Dashed gray – Case IIb and Solid gray – Case III. Time scale is normalized with H/U_∞. Mean power gain: IIa/I – 5%, IIb/I – 2%, III/I – 40%.

in WTABL framework that will serve as a building block for all subsequent analysis in the chapter. Note that turbulence in wind turbine array boundary layers is ver-

tically and horizontally inhomogeneous. For a given height z, we define a two point correlation between the points $\boldsymbol{x}_r = (x,\ y)$, $\boldsymbol{x}_r + \boldsymbol{r} = (x + \Delta_x, y + \Delta_y)$ through an averaging in a horizontal plane

$$\mathfrak{R}_{u_i' u_j'}(\boldsymbol{r}, t; z) = \frac{1}{L_x L_y} \iint_A \langle u_i'(\boldsymbol{x}_r, t; z) u_j'(\boldsymbol{x}_r + \boldsymbol{r}, t; z) \rangle \mathrm{d}^2 \boldsymbol{x}_r. \tag{4.5}$$

Here u_i' refers to the turbulent velocity fluctuations in the i^{th} direction, $A \in [-L_x/2, L_x/2] \times [-L_y/2, L_y/2]$ is the rectangular patch corresponding to the xy plane at each z location, $\langle\rangle$ denotes the ensemble average. Due to invoking of the horizontal average, the correlation $\mathfrak{R}_{u_i' u_j'}(\boldsymbol{r}, t; z)$ is only a function of the point separation $\boldsymbol{r}$, and not the points themselves, $\boldsymbol{x_r}, \boldsymbol{x}_r + \boldsymbol{r}$.

For homogeneous turbulence, we can impose an equivalence between the spatial average and the ensemble average, thus recovering the classical definition of two point correlation, $\mathfrak{R}_{u_i' u_j'}(\boldsymbol{r}, t; z) = \langle u_i'(\boldsymbol{x}, t; z) u_j'(\boldsymbol{x} + \boldsymbol{r}, t; z) \rangle$ [1]. In inhomogeneous turbulence, we need to perform a spatial averaging explicitly to recover that. Furthermore, for statistically stationary flows, the ensemble average $\langle\rangle$ can be replaced with the temporal average $\overline{\ \ }$ (due to ergodicity), as is done in the subsequent sections owing to a statistical stationarity of both ABL and WTABL flows with the temporally-invariant mean wind, as considered in the current paper. This makes the two point correlation in (4.5) time-invariant, as $\mathfrak{R}_{u_i' u_j'}(\boldsymbol{r}; z)$.

Definition of spectra

The energy spectra for the inhomogeneous WTABL arrays can be defined from the Fourier transform of the two-point correlation as follows,

$$\hat{E}_{u_i' u_j'}(\boldsymbol{k_r}) = \frac{1}{2\pi} \iint_{\boldsymbol{r} \in \mathbb{R}} \mathfrak{R}_{u_i' u_j'}(\boldsymbol{r}; z) e^{-i \boldsymbol{k_r} \cdot \boldsymbol{r}} \mathrm{d}^2 \boldsymbol{r}, \tag{4.6}$$

where $\boldsymbol{k_r}$ denotes the two dimensional wavenumber $\boldsymbol{k}_r = (k_x, k_y)$. Thus, the spectral content of $\mathfrak{R}_{u'u'}(\boldsymbol{r}; z)$, $\mathfrak{R}_{w'w'}(\boldsymbol{r}; z)$, corresponds to the streamwise and wall normal

energy spectra, while that for $\mathfrak{R}_{u'w'}(\boldsymbol{r};z)$ is representative of the spectra of the kinematic shear stress (cospetra) which is required for the calculation of the MKE flux spectra in Equation (4.8). The energy spectra as well as the kinematic shear stress cospectra are numerically evaluated as

$$\hat{E}_{u_i'u_j'}(\boldsymbol{k_r}) = \overline{\hat{u}_i(\boldsymbol{k_r},t;z)\hat{u}_j^*(\boldsymbol{k_r},t;z)}. \tag{4.7}$$

This is an outcome of the convolution theorem, illustrating that transform of the convolution of two variables in the physical space is equal to the product or their individual transforms in the spectral space [1].

4.4.1 Spectra of MKE Flux

The spectra of the MKE flux $\Phi_p(z)$ and the MKE flux difference $\Delta\Phi_p$ defined in Equations (4.3), (4.4) is of interest in this paper. The horizontal spectra of $\Phi_p(z)$ can be defined through the corresponding spectra of two-point correlations along the lines of discussion in Section 4.4, as

$$\hat{\Phi}_p(k_x,k_y,z) = |\overline{\hat{u}(k_x,k_y,z)\hat{w}^*(k_x,k_y,z)}|\langle\overline{u}(z)\rangle, \tag{4.8}$$

where k_x, k_y are streamwise and spanwise wavenumbers, $\hat{}$ is the notation for the Fourier coefficients, and * refers to the complex conjugate. The horizontal spectra of the MKE flux difference can be defined accordingly,

$$\Delta\hat{\Phi}_p(k_x,k_y) = \hat{\Phi}_p(k_x,k_y,z_h+D/2) - \hat{\Phi}_p(k_x,k_y,z_h-D/2). \tag{4.9}$$

The Fourier coefficients can also be expressed as a function of streamwise, spanwise wavelengths, λ_x,λ_y ($\lambda_{x,y} = 2\pi/k_{x,y}$) and their integral in λ_x,λ_y space contributes to the full value,

$$\Delta\Phi_p = \int_0^\infty\int_0^\infty k_xk_y\Delta\widehat{\Phi}_p(\lambda_x,\lambda_y)\mathrm{dlog}(\lambda_x)\mathrm{dlog}(\lambda_y). \tag{4.10}$$

While Equation (5.2) illustrates a cumulative effect of streamwise and spanwise length scales λ_x, λ_y on the MKE flux difference, we can still define its one-dimensional counterpart, using a 2D Fourier transform and integrating over one wavelength direction. Equation (4.11) shows the one dimensional MKE flux difference spectra, $\Delta\widehat{\Phi}_p(\lambda_\eta),\ \eta = x, y$, isolating the spectral content in the streamwise and spanwise length scales respectively,

$$\Delta\widehat{\Phi}_p(\lambda_\eta) = \int_0^{\lambda_{\zeta,max}} \Delta\widehat{\Phi}_p(\lambda_\eta, \lambda_\zeta)\mathrm{d}\lambda_\zeta, \tag{4.11}$$

where $\eta = x$, $\zeta = y$ and vice-versa. Equation (4.12) below defines the cumulative spectral content of the 1D MKE flux difference in streamwise and spanwise length scales. For example, $\gamma_x(\lambda_0)$ shows the fraction of MKE flux difference, contained at length scales $\lambda_x \geq \lambda_0$, and $\gamma_\eta(0) = 1$,

$$\gamma_\eta(\lambda_\eta) = \frac{\displaystyle\int_{\lambda_\eta}^{\infty} \Delta\widehat{\Phi}_p(\lambda'_\eta)\mathrm{d}\lambda'_\eta}{\displaystyle\int_0^{\infty} \Delta\widehat{\Phi}_p(\lambda'_\eta)\mathrm{d}\lambda'_\eta}, \qquad \forall\eta = x, y. \tag{4.12}$$

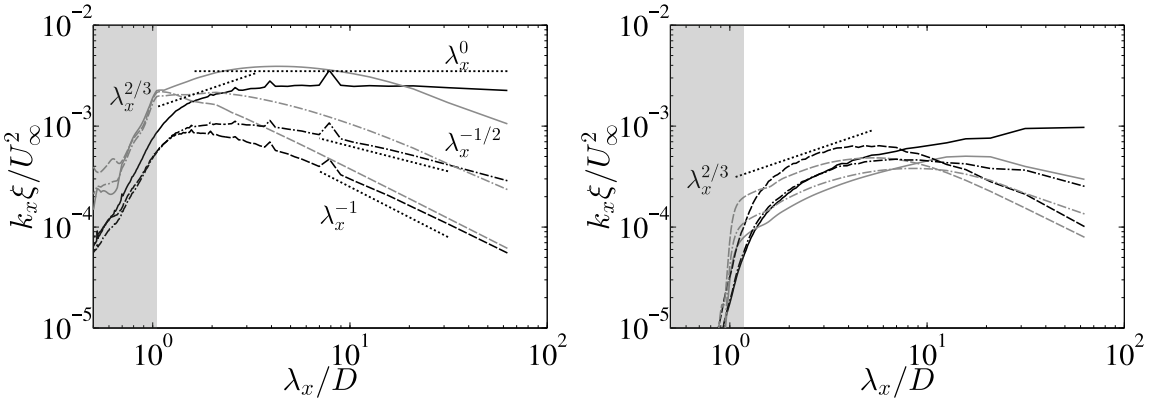

Figure 4.6: Premultiplied 1D spectra $k_x\xi$ vs normalized streamwise wavelengths λ_x/D for (a) $z = 0.25D$, (b) $z = 8.75D$. Black lines, Case I; gray lines, neutral ABL. k_xE_{uu} (–), k_xE_{ww} (––), $k_x\phi_{uw}$ (–.–). All spectra normalized by U_∞^2. Gray patch corresponds to the resolved part of the spectra directly influenced by SGS viscosity.

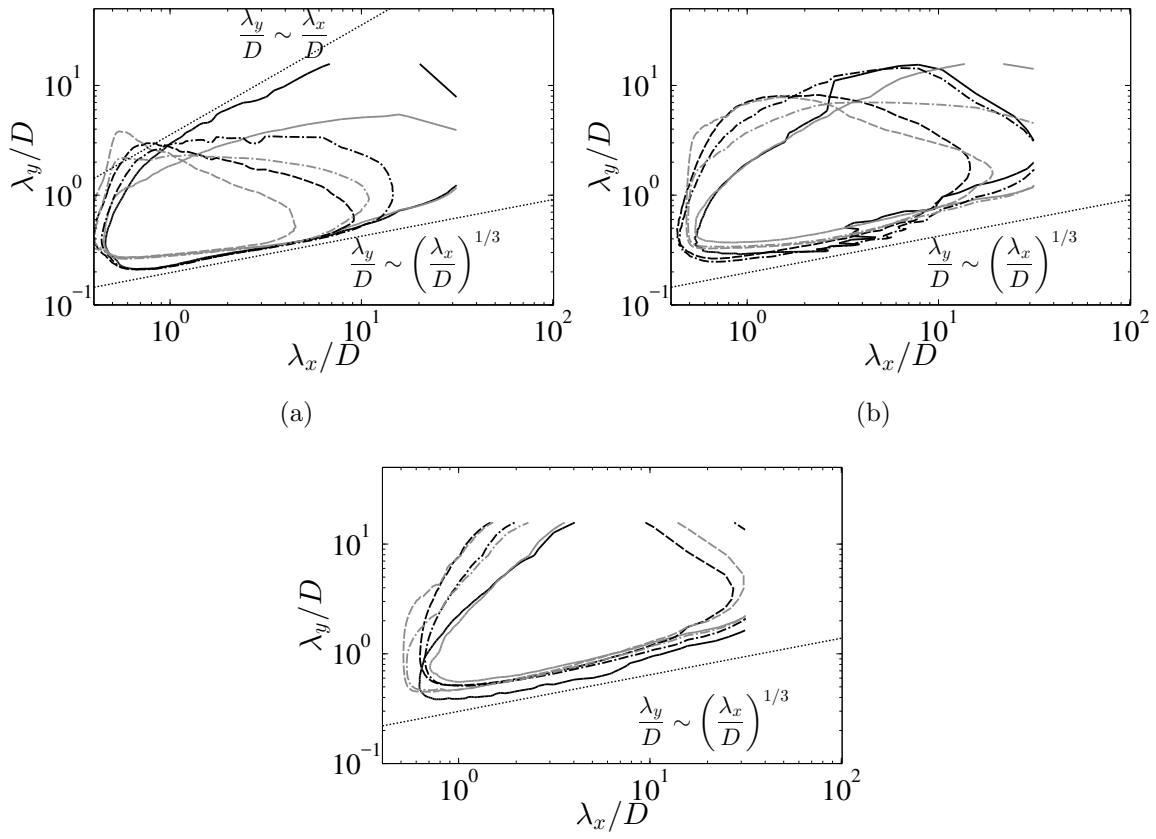

Figure 4.7: 2D premultiplied energy spectra vs normalized streamwise and spanwise wavelengths, λ_x/D, λ_y/D. Black lines, Case I; gray lines, neutral ABL. $k_x k_y E_{uu}$ (–), $k_x k_y E_{ww}$ (−−), $k_x k_y \phi_{uw}$ (−.−). (a) $z = 0.25D$ (b) $z = D$ (c) $z = 8.75D$. Contours are 0.25 of maximum at that level. All spectra normalized by U_∞^2.

In the near wall regime, robust scaling laws of the *attached eddies* [60, 79] can be observed in wind farms. For example, Case I in Figure 4.6a shows the existence of the k_x^{-1} scaling (λ_x^0 scaling in premultiplied spectra) in the u energy spectra, which are manifestations of the overlap region of the scales of attached eddies with the integral length scales [74, 103, 136]. The $k_x^{-1/2}$ scaling law ($\lambda_x^{-1/2}$ in premultiplied spectra) of ϕ_{uw} (cospectra) is an illustration of the near-wall organizations of Reynolds-stress carrying structures, as demonstrated in the correlation scaling of 1D spectra [76,136],

$$\phi_{uw} \approx E_{uu}^{1/2} E_{ww}^{1/2}, \tag{4.13}$$

with $E_{uu} \sim k_x^{-1}$ and $E_{ww} \sim k_x^0$ (see Figure 4.6a). Here $\phi_{uw} = \overline{|\hat{u}\hat{w}^*|}$, $E_{uu} = \overline{\hat{u}\hat{u}^*}$ and $E_{ww} = \overline{\hat{w}\hat{w}^*}$, where hat represents the Fourier transform and $*$ represents the conjugate transpose. These correlated scaling regions were observed throughout the inner layer $z < D$. In 1D scenario, e.g., for variation only in λ_x, integration of the spectral variables $E_{uu}, E_{ww}, \phi_{uw}$ has been performed in the λ_y direction. When compared to neutral ABL simulations (without wind turbines), we observe similar scaling laws, but for the wind turbine domain, the attached eddy scaling laws extend to larger length scales $\lambda_x > 10D$. This observation is further corroborated in the 2D premultiplied spectra shown in Figure 4.6b. The figure also illustrates that the vertical w spectra of wind farms at close to the wall locations, $z < D$, as well as u spectra and a cospectra at the same contour level, extend to much larger streamwise and spanwise length scales compared to the neutral ABL. This indicates that the 3D turbulent motions also increase in size near the wall, possibly due to the vertical entrainment of the *mean kinetic energy flux* in wind farms, which requires *downdrafts* or vertical motions from the high-speed regions above the turbine rotor towards the wall [127, 137]. Note that the higher locations in the boundary layer, e.g. at $z = D$ and $z = 8.75D$, do not show this feature, as can be seen from the corresponding premultiplied spectra plots.

In general, Figure 4.6b shows good trends of the linear dispersion, $\lambda_y \sim \lambda_x$ in the u spectra, corresponding to the *active wall-normal motions* as well as the power law scaling, $\lambda_y \sim \lambda_x^{1/3}$ in both u, w energy spectra and the $\overline{u'w'}$ cospectra corresponding to the *attached inactive motions* [77,117]. However, it must be appreciated that the 1/3 law scaling, unlike the wall-bounded turbulence [76, 136], has its contribution both from the low-speed streaks near the wall, as well as from the spanwise modulation of the velocities due to the wind turbine wakes as shown later in Equation (4.15). Similar near-wall scalings are observed in other cases (not shown here).

Figures 4.6a, 4.6b show that a considerably long region of the $-5/3$ law ($\lambda_x^{2/3}$) is present in the 1D spectra in the neutral ABL case at scales $\lambda_x > D$. These scales are adequately resolved by the grid as evident from the details of the grid resolution presented in Appendix D.1. At scales lower than D, $\lambda_x < D$, the drop in spectra is noticeable which is explained by the fact that, although the scales down to $\sim 0.6D$ are still resolved by the grid, see Appendix D.1, they are also effected by the subgrid scale viscosity, since they correspond to the highest resolved wavenumbers targeted by the subgrid scale dissipation. These scales are identified by gray patches in Figures 4.6a, 4.6b, following Ref. [14]. It can also be observed, that in neutral ABL, the decay rate of the spectrum at $\lambda_x < D$ is different in the inner and outer layer owing to decreasing eddy viscosity effects near the wall. The extent of the $-5/3$ law is smaller in wind turbine simulations that in the neutral ABL. Since these deviations are observed in the region of scales that are well resolved in both cases with and without wind turbines, this fact provides a room for hypothesis that the observed effect might be caused by the modulation of turbulence by wind turbines. Although it might be slightly obscured in the premultiplied spectra plot of the Figure 4.8, where differences in smaller length scales are artificially exaggerated by multiplying by higher values of k_x, k_y, the largest discrepancies in the spectra and hence wind turbine power amongst different Cases I-III come from the larger length scales $\lambda_x, \lambda_y > 10D$. It is clearly seen from the corresponding spectra plots that are not premultipled by wavenumbers (not included here). We do admit that larger length scales might also suffer from large uncertainties when it comes to their spectral characteristics due to their larger coherence times and a potential lack of a sufficient number of uncorrelated samples. In a separate uncertainty analysis (See Appendix D.3) of the MKE flux difference spectra at large length scales to the duration of the averaging time, it was concluded that the statistical uncertainty is less than 0.01% with the current averaging of 50 flow

through times, both for the streamwise and the spanwise spectra. Additionally, we

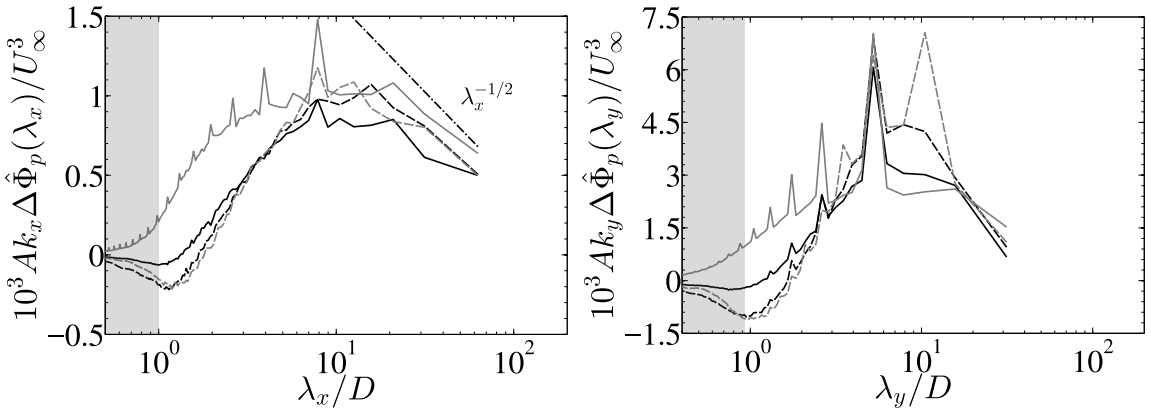

(a) (b)

Figure 4.8: One dimensional normalized premultiplied difference in the MKE flux spectra $k_\eta \Delta\hat{\Phi}_p(\lambda_\eta)$ (Equation (4.11)) between the top and bottom wake region, $z = z_h \pm D/2$. (a) versus streamwise wavelength, $\eta = x$ (b) versus spanwise wavelength, $\eta = y$. Solid black – Case I; dashed black – Case IIa, dashed gray – Case IIb; solid gray – Case III. $A = s_x s_y D^2$. Gray patch – resolved part of the spectra directly influenced by SGS viscosity.

also observe the presence of *negative contribution* of $k_x \Delta\widehat{\Phi}_p(\lambda_x)$, $k_y \Delta\widehat{\Phi}_p(\lambda_y)$ in cases I,IIa,IIb (corresponding to the lower hub-height of $z_h = 0.1H$, which is also equal to D) for streamwise and spanwise length scales in the order of turbine rotor diameter D. This negative contribution corresponds to the upward transfer of the MKE flux from the bottom to the top wake region, that does not contribute to the turbine power. It might be hypothesized that the updrafts in the small scales of motion are associated with the near-wall turbulence bursts that reach wind turbines with relatively low hub-heights of $z_h = D$. While the contribution to the flux difference at smaller length scales $\lambda_x, \lambda_y \sim O(D)$, is negative for Cases I,IIa IIb, it is observed that Case III corresponding to the higher hub-height of $z_h = 0.33H$ still contributes to 15% of $\Delta\widehat{\Phi}_p(\lambda_x)$ and 20% of $\Delta\widehat{\Phi}_p(\lambda_y)$, in those scale ranges. Since wind turbines now are three times higher ($z_h = 3D$), the near-wall energetic motions do not reach the turbine rotor region any longer. It is suspected that the contribution to the power

by the intermediate length scales $\sim D$ in Case III mainly comes from the incoherent yet energetic outer scales of motion [77]. This can also be seen in the vertical spectra at $z = z_h + D/2$ in Figure 4.9. The vertical spectra manifests the potential turbulent vertical motions ("downdrafts") due to the entrainment of mean kinetic energy, and when compared to neutral ABL data provides interesting revelations. At $z = z_h+D/2$, the differences in the neutral ABL and WT spectra (Cases I, IIa, IIb) occurs at $\lambda_x > 10D$, while for Case III, the discrepancies can be seen at scales $\lambda_x > D$ in the outer layer, all of which contribute to the turbine power.

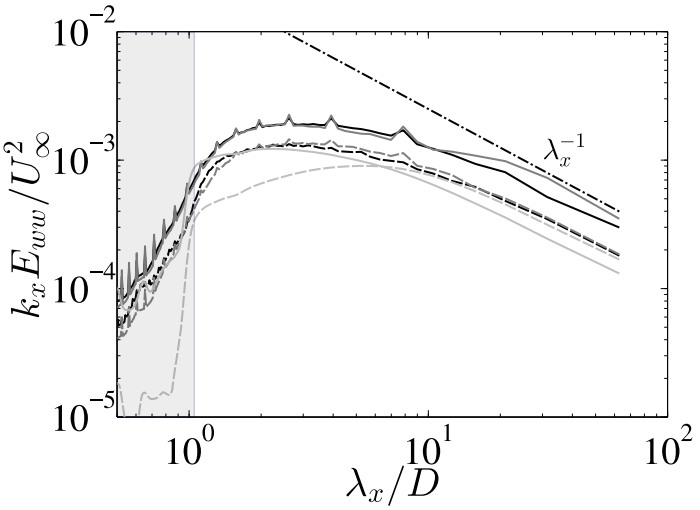

Figure 4.9: One-dimensional premultiplied vertical velocity spectra $k_x E_{ww}$ at $z = z_h+D/2$ vs normalized streamwise wavelength λ_x/D with and without wind turbines. Solid black – Case I; dashed black – Case IIa, dashed gray – Case IIb; solid gray – Case III. Solid light gray – neutral ABL, rotor region of I. Dashed light gray – neutral ABL, rotor region of III. Gray patch – resolved part of the spectra directly influenced by SGS viscosity.

Peaks in the spectral flux difference $k_\eta \Delta\widehat{\Phi}_p(\lambda_\eta),\ \eta = x, y$ (Figure 4.8), are observed, corresponding to $\lambda_x = ms_xD,\ m = 1, 2, \cdots$ in the streamwise scaling and $\lambda_y = ns_yD,\ n = 1, 2, \cdots$ in the spanwise scaling which are illustrative of the periodicity imposed by the repeated turbine arrangements in the farm. At length scales $\lambda_x \sim O(10^2 D)$, the $k_x^{-1/2}$ law of *attached eddies* ($\lambda_x^{-1/2}$ in the premultiplied spectra) can still be observed in all the cases. This is primarily because of the fact that the

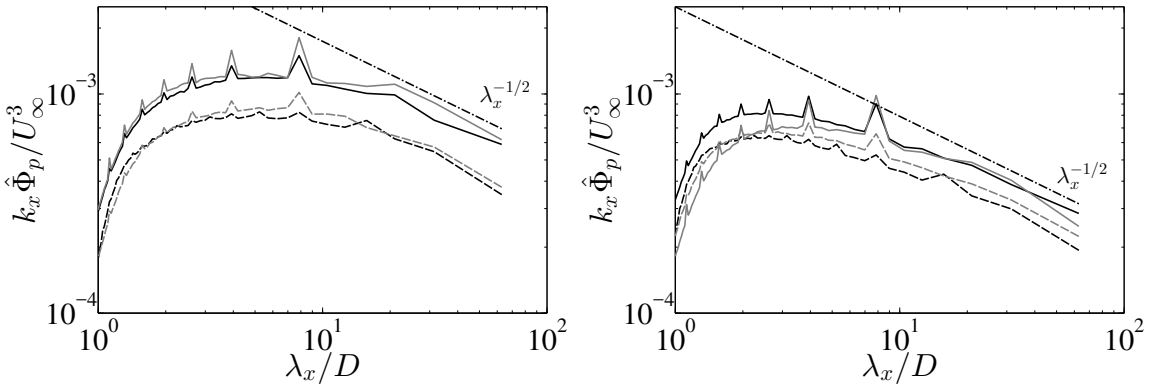

Figure 4.10: One dimensional premultiplied MKE flux spectra $k_x\hat{\Phi}_p$ versus normalized streamwise wavelength (a) at the top wake region $z = z_h + D/2$. (b) at the bottom wake region $z = z_h - D/2$. Solid black – Case I; dashed black – Case IIa, dashed gray – Case IIb; solid gray – Case III.

$-1/2$ scaling law is also observed at similar λ_x locations in both the top and bottom MKE flux, see Figure 4.10. Peaks corresponding to wind turbine placement are also observed in both the top and bottom MKE flux.

Another interesting phenomenon observed is the difference in the spectra in the cases I, IIa, IIb (different inter-turbine distances s_x, s_y), where the wind turbines have the same hub-height z_h, and hence potentially would have the access to similar large-scale structures in the logarithmic layer [94,95,98]. The array-averaged turbine power ($\rho_{mean} s_x s_y D^2$) in Cases IIa, IIb is slightly higher than in Case I (see Figure 4.5), due to a better wake recovery owing to less number of turbines per unit area [16, 124]. Cases I, IIa and IIb demonstrate a completely different dynamics at streamwise and spanwise length scales larger than D, below which the SGS dissipation is dominant. For example, at higher $s_x \times s_y$, Cases IIa, IIb compared to I manifest higher magnitudes of updrafts at scales $\sim D$ and subsequently larger magnitudes of MKE flux downdrafts at scales $> 10D$ as well, which might be related to a diminished effect of wake interference, otherwise inhibiting energetic near-wall updrafts and outer layer

downdrafts. It must be noted that, when integrated over all length scales, a relative surplus in positive and negative contributions in Cases IIa, IIb partially cancels out, subsequently providing comparable values of power in Cases I, IIa, IIb. The fact that the spectral content of the MKE flux difference (Figure 4.8) is quite different at different length scales provides a room for a hypothesis that the arrangements of wind turbines (s_x, s_y) actually modulate the large scale organizations in the log layer. From the spectra of Cases I,IIa,IIb (Figures 4.8a, 4.8b), it is thus clear that increasing s_x allows the wind farm to take advantage of much larger streamwise structures, since in Case IIa, contribution to mean power is the highest for length scales $> 10D$. Increasing s_y allows for wider structures $(\lambda_y > \lambda_x)$ to contribute to the farm power (Figure 4.8b), but streamwise horizontally anisotropic motions are more energetic than their spanwise counterparts [95], thus the spectral power contribution (MKE flux difference) in Case IIb at length scales $\lambda_x < 10D$ (Figure 4.8a) is larger than in Case IIa.

The modulation of large scale structures can be further understood from the visualization of the isosurfaces (Case I) of streamwise velocity at 65% and 95% of U_∞ in Figure 4.11, depicting the region $z < z_h + 0.75D$. The iso-surface plot shows that the presence of wind turbines generate the more energetic patches, $u = 0.95U_\infty$, propagating downstream, in between the surfaces of $u = 0.65U_\infty$, which are not prominently seen in the neutral ABL flow, without the turbines.

While the above discussion provides a qualitative visualization, a quantitative aspect of the modulation of large-scales structures can be observed from the plots of integral length scales, which demonstrate a measure of *correlated large scales* of motion. Figure 4.12a shows the variation of integral length scales $\mathfrak{L}_{uu}$ with wall-normal distance, the definition of the integral length scale used in the current study being given in Appendix D.2. Since the integral length scales are bounded by $30D$

in all cases, which is less than half of the largest resolved streamwise wavelength $L_x = 20\pi D$ imposed by the domain length, one can conclude that the computed integral length scales are not numerically influenced by the imposed periodicity of the domain. It is interesting to observe that the integral scales in Cases I, IIa, IIb, III and the neutral ABL without turbines are more or less similar in the outer layer but manifest a marked difference in the inner layer and at hub-height. This also corroborates that the modulation of the structures in wind farms are not only caused by the direct turbulence-turbine interaction at hub-heights but also due to the "downdrafts" of the MKE flux as also analyzed in Figure 4.8. The integral length scales in Figure 4.12a and the mean-squared streamwise velocity fluctuations $\overline{u'^2}/U_\infty^2$ both indicate that peaks occur at the hub-height of the turbines in the wind farm. Between Cases I, IIa and IIb, which are at the same hub-height, the integral length scales in the bulk of the boundary layer grow in magnitude as s_x/s_y is decreased. When Cases I and IIa are compared, which have the same s_y but different s_x, the Case IIa with the smaller streamwise turbine separation manifests larger length scales, since the streamwise wakes of the concurrent turbines effectively merge producing longer structures, while they have more time to recover and mix before hitting the downstream turbines in Case I. Similarly for a fixed s_x, increasing s_y from Case I to IIb allows the correlated structures in the wakes to grow more with smaller spanwise interference. Case III at a higher hub-height $z_h = 0.33H$ (outer layer) manifests a peak of a similar magnitude at hub-height as Case I with the same s_x, s_y, showing a consistent trend in the influence of the turbine separation distances on the peak integral length scales, irrespective of the hub-height. While the vertical diffusion of length scales from the hub-height location might seem smaller in Case III in Figure 4.12a, this is due to the logarithmic scaling of z axis and is, in effect, similar between all the cases. Nonetheless, the overall dependence of $\mathfrak{L}_{uu}(z)$ is markedly

different in Case III than in other cases, showing significantly smaller length scales in the inner layer, due to a reduced influence of the enhanced turbulence structures at hub-height, that are now significantly further away, on the inner layer turbulence. This can be further observed in the flow visualization of the wind farms which are documented in Figures 4.13, 4.14.

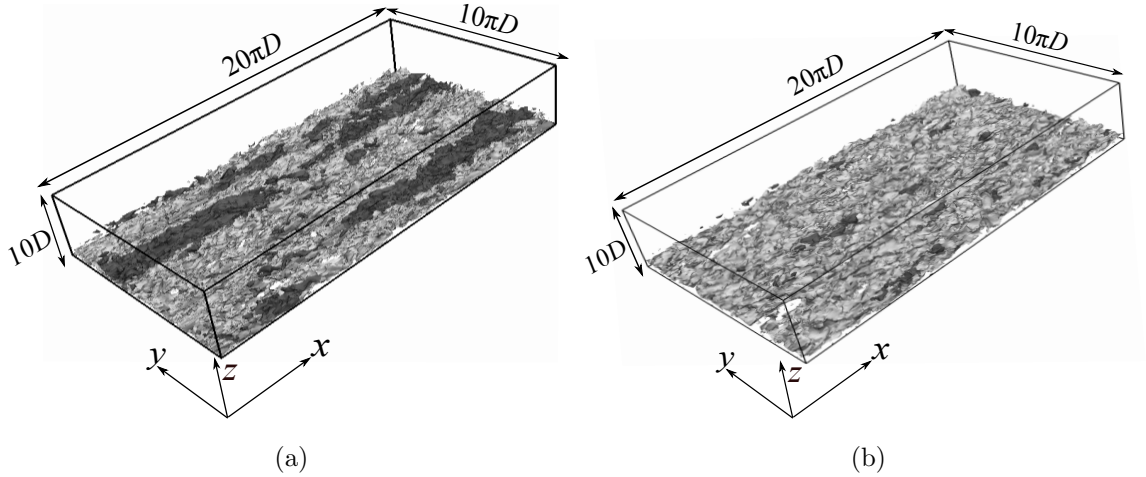

Figure 4.11: Modulation of large scale structures. Isosurface of normalized velocity magnitude $\sqrt{u^2+v^2+w^2}/U_\infty$ for $z \leq z_h + 0.75D$. (a) Wind turbine array, Case I. (b) neutral ABL, without wind turbines. Light gray patch – $0.65U_\infty$, dark gray patch – $0.95U_\infty$.

The discussions above are further corroborated by the cumulative spectral content of the MKE flux difference, γ_x, γ_y, at streamwise and spanwise length scales, for different cases (see Figure 4.15). The large scale motions with scales greater than $10D$ contain $> 80\%$, even more so for streamwise motions, of the spectral flux difference, while scales smaller than $10D$ contribute to less than 20% of the spectral flux difference among the resolved scales $0.6D < \lambda_x < 60D$, $0.5D < \lambda_y < 30D$, see Appendix D.1 for the discussion of the resolved scales. The maximum discrepancies among Cases I-III for $\gamma_x,\ \gamma_y$ occur at the large length scales $> 10D$, while they are almost identical for smaller scales $< 4D$. Further, the maximum discrepancies in the spectral content occur between Case III and the other cases both for γ_x and γ_y,

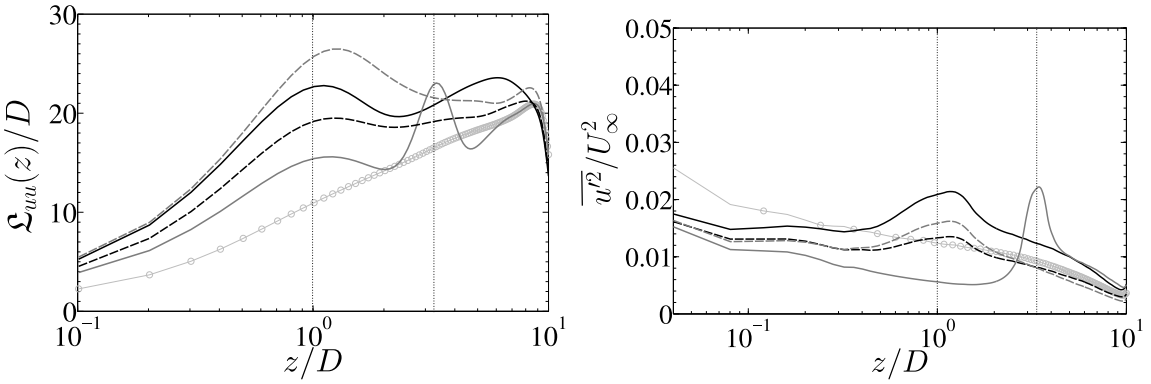

(a) (b)

Figure 4.12: Vertical variation of (a) Integral length scales $\mathfrak{L}_{uu}$ based on streamwise fluctuations, (b) normalized mean-squared streamwise fluctuations $\overline{u'^2}/U_\infty^2$ (averaged over xy planes), with and without the presence of wind turbines. Solid black – Case I; dashed black – Case IIa; dashed gray – Case IIb; solid gray – Case III; light gray ∘ – neutral ABL, without wind turbines. Dotted lines – hub heights, $z_h = 0.1H$ (Cases I, IIa, IIb), $z_h = 0.33H$ (Case III). See Appendix D.2 for the definition of $\mathfrak{L}_{uu}$ used in the current study.

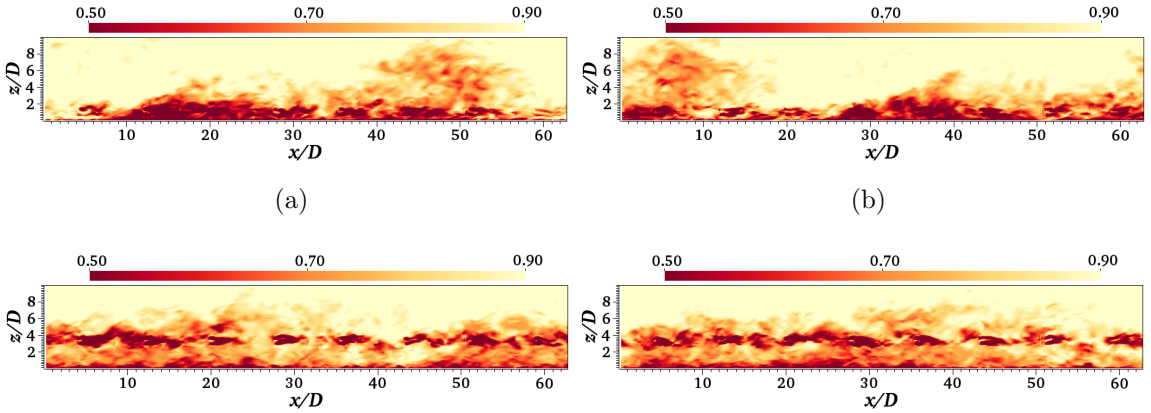

(a) (b)

(c) (d)

Figure 4.13: Temporal snapshot of velocity magnitude $\sqrt{u^2+v^2+w^2}/U_\infty$ for periodic wind farms, (a),(b) I and (c),(d) III. Snapshots are T_e times apart.

amounting to a difference of $\sim 20\%$ in γ_y. As mentioned earlier, with the statistical uncertainty in spectra of less than 0.01% over the chosen averaging time of 50 T_e, the observed discrepancies are attributed to the physical flow features and not spectral uncertainties. This indicates that the large scale structures, that are generated around the hub-height as seen earlier, in Case III have higher energy content than in Cases

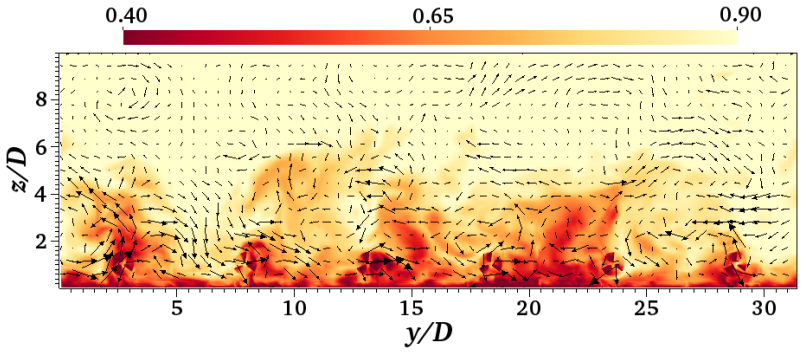

(a)

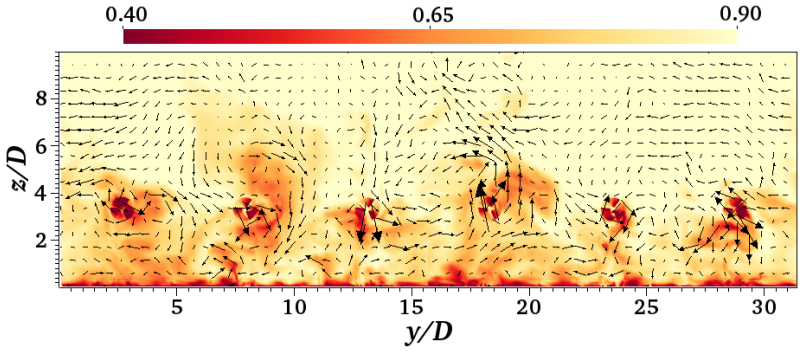

(b)

Figure 4.14: Temporal snapshot of velocity magnitude contours $\sqrt{u^2+v^2+w^2}$ and in-plane velocity vectors u, w for periodic wind farms, (a),(b) I and (c),(d) III. Snapshots are T_e times apart.

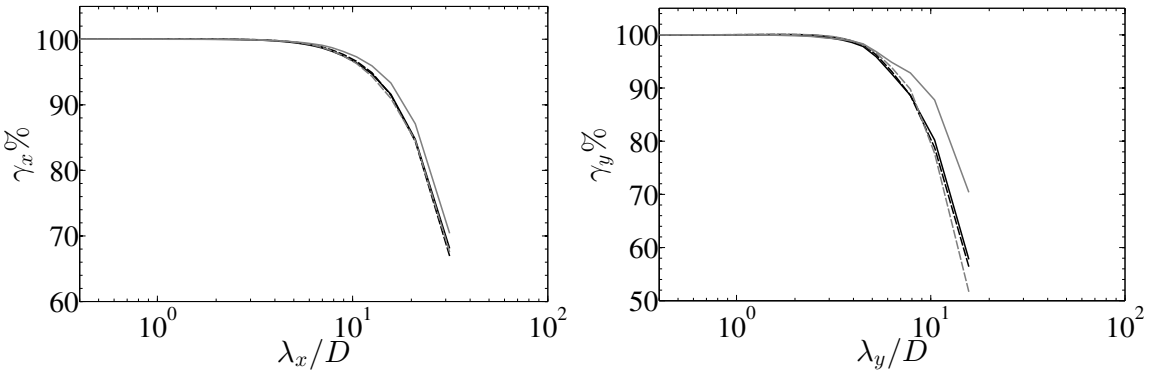

(a) (b)

Figure 4.15: Cumulative spectral content of the difference in MKE flux, $\gamma_\eta(\lambda_\eta)$ (Equation (4.12)) at different (a) streamwise wavelengths, $\eta = x$, (b) spanwise wavelengths, $\eta = y$. Solid black – Case I; dashed black – Case IIa; dashed gray – Case IIb; solid gray – Case III.

I, IIa, IIb, probably due to the fact that they reside in the outer layer where convective velocities are higher. This can also be observed in Figure 4.8, where Case III has consistently higher values of MKE flux difference at length scales $\lambda_x, \lambda_y \gtrsim 11D$. A summary of the dynamics of different length scales in our simulated wind farms is provided in Table 4.2. These results are observed to be in line with the findings of the large-scale motions [95] of wall bounded turbulence, or the large roller-mode structures in POD of infinite wind farms [134].

Length Scales ($\lambda_{x,y}$)	Dynamics
$\geq 10D$	Major contribution ($> 80\%$) to positive $P_{mean} \sim s_x s_y D^2 \Delta\Phi_p$
$\sim D$	Small positive or negative contribution to $P_{mean} \sim s_x s_y D^2 \Delta\Phi_p$, depending on hub-height z_h
$< D$	Influenced/dissipated by subgrid scale viscosity

Table 4.2: Summary of the dynamics of important length scales in wind farms resolved by LES simulations for different cases I-III.

The two dimensional premultiplied spectral difference, $k_x k_y \Delta\widehat{\Phi}_p(\lambda_x, \lambda_y)$ in Figures 4.16a– 4.16d corroborate the discussions above made with the 1D spectra, but additionally, also contain the new information about the scaling laws and anisotropy of the eddies responsible for the MKE flux. The streamwise horizontally anisotropic ($\lambda_x \gg \lambda_y$) eddies responsible for the positive contribution of the spectra show a power law scaling of the form $\lambda_y \sim \lambda_x^{1/3}$. Cases manifesting the negative contribution

of spectra (updraft), e.g., I, IIa demonstrate signatures of power law scaling $\lambda_y \sim \lambda_x^{1/3}$, and IIb shows $\lambda_y \sim \lambda_x^{1/5}$ which is quite different than the 1/3 power law dynamics. This hints towards the fact that for Case IIb, while there is an evidence of wider structures for the downdrafts, thinner intermediate scales might be responsible for the updrafts compared to cases I,IIa. Also illustrative from the figures is the fact that the eddies responsible for the negative contribution of the spectra manifest a greater degree of horizontal anisotropy ($\lambda_x > \lambda_y$) than for the eddies accountable for the positive contribution.

The 1/3 power law in the 2D spectra of the MKE flux difference (Figures 4.16a–4.16d) for different cases is expectedly also present in the spectra of the MKE flux (Figure 4.17), and also in the 2D u, w, uw spectra as shown in Figure 4.6b for the different turbine layouts in I-III. This justifies that the 1/3 power law is a manifestation of coherent interactions in the flow field, which is invariant of the turbine layout. A scaling analysis is also present below, to justify the power law.

The width of the turbine wake, δ_y, grows in the streamwise direction, in accordance with the turbulent mixing laws in the wake region, $z_h - D/2 < z < z_h + D/2$. Assuming the width and the height of the wakes are the same for circular turbine wakes, the dispersion relation of the wake width in a background turbulence is

$$\delta_y \sim (\nu_w t_e)^{1/2}, \tag{4.14}$$

where ν_w can be thought of as a wake eddy viscosity corresponding to the wake mixing [5], and t_e is the lifetime of the eddies in the wake region. The streamwise convection of wakes occurs mainly as a shear layer, with the streamwise wavelengths $\lambda_x \sim S\delta_y t_e$, where S is the velocity gradient scale in the mixing length region. As shown in Figure 4.18, the low velocity wake regions at hub-height location $z = z_h = 0.1H$ amidst the high velocity atmospheric turbulence impose a shear scale

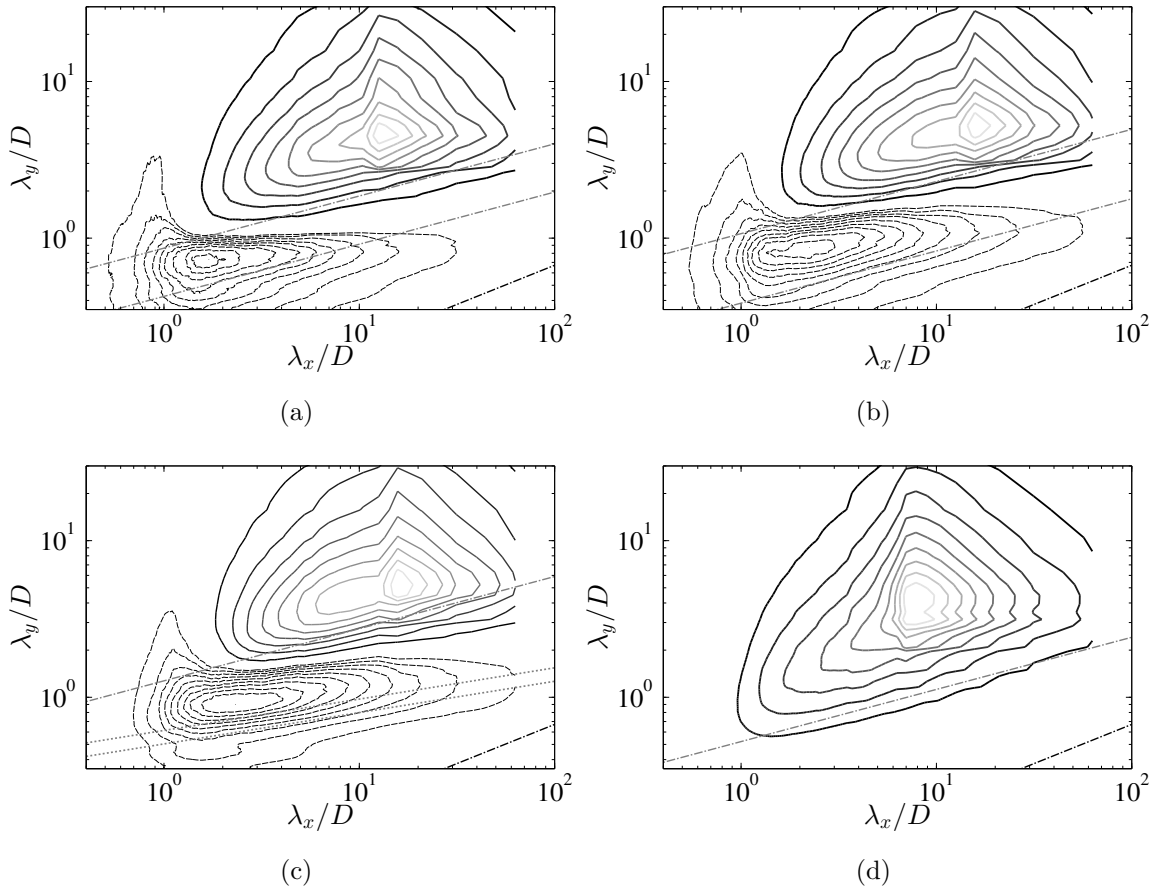

Figure 4.16: 2D premultiplied spectra of the difference in MKE flux, $k_x k_y \Delta\hat{\Phi}_p(\lambda_x, \lambda_y)/U_\infty^3$, versus normalized streamwise and spanwise wavelengths. (a) Case I (b) Case IIa (c) Case IIb (d) Case III. Solid gray – positive contours, dashed gray – negative contours. Chain dotted gray – $\lambda_y \sim \lambda_x^{1/3}$, chain dotted black – $\lambda_y \sim \lambda_x^{1/2}$. Gray dotted – $\lambda_y \sim \lambda_x^{1/5}$. Contour levels: positive – 10 levels, from 10-100% of maximum; negative – 10 levels from 10-100% of minimum.

S due to the spanwise modulation of the streamwise flow similar to the near wall streaks.

Consequently, substituting eddy lifetime $t_e \sim \lambda_x/(S\delta_y)$, in the turbulent dispersion relation $\delta_y \sim (\nu_w t_e)^{1/2}$ one can obtain an equation below in a non-dimensional form,

$$\delta_y/D = \beta(\lambda_x/D)^{1/3}, \tag{4.15}$$

with spanwise length scales $\lambda_y \sim O(\delta_y)$ giving $\lambda_y/D = \beta(\lambda_x/D)^{1/3}$. A short scaling

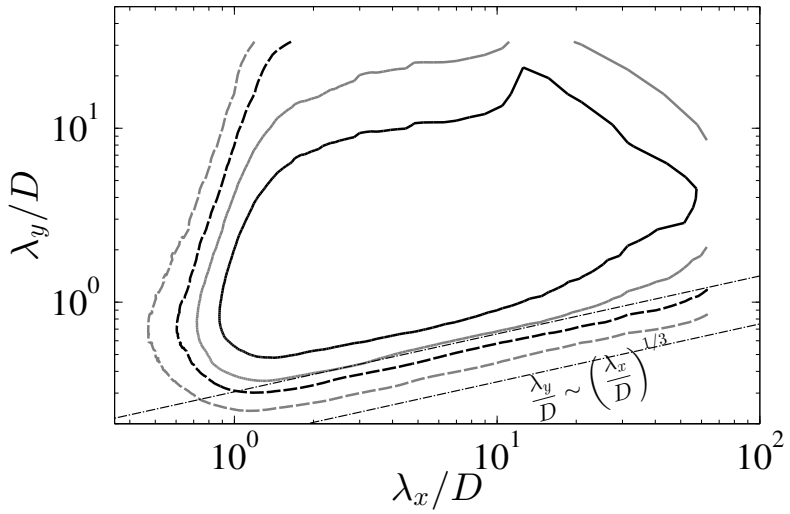

Figure 4.17: 2D premultiplied spectra of MKE flux for baseline case I at locations $z = z_h \pm D/2$. Solid – $z = z_h - D/2$, Dashed – $z = z_h + D/2$. Black – 25% of the maximum contour. Gray – 12.5% of the maximum contour. Chain dotted black line – $\lambda_y \sim \lambda_x^{1/3}$

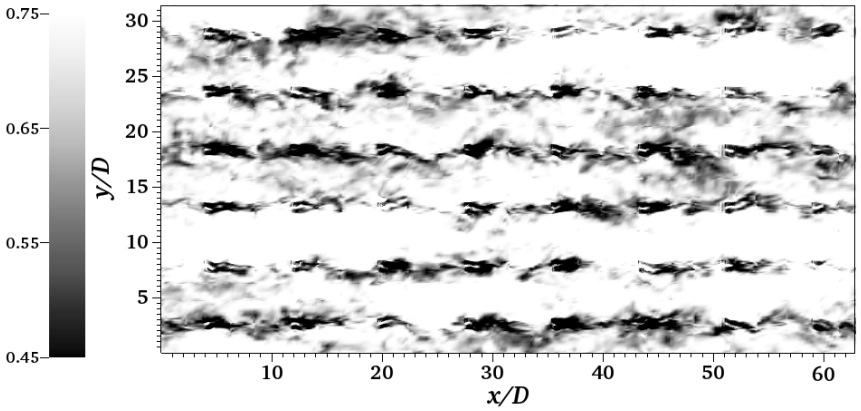

Figure 4.18: Snapshot of normalized velocity magnitude $\sqrt{u^2+v^2+w^2}/U_\infty$ contour for Case I, in xy plane at hub-height location $z = z_h$, taken at 15 flow-through times T_e after obtaining statistical stationarity.

analysis reveals that the wake eddy viscosity $\nu_w \sim U_c D$ (at high Re, the lateral and normal expansion of the wake is insignificant), with the velocity scale, $U_c \sim 1/2(\langle\overline{u}\rangle|_{z_h+D/2} + \langle\overline{u}\rangle|_{z_h-D/2})$. The shear scale $S \sim \Delta U/D$ where $\Delta U = (\langle\overline{u}\rangle|_{z_h+D/2} - \langle\overline{u}\rangle|_{z_h-D/2})$. Subsequently, this gives $\beta = (U_c/\Delta U)^{1/3}$, with $\beta \approx 10$ for cases I,IIa,IIb and $\beta \approx 80$ for case III, as computed from the mean statistics of our simulations. This illustrates that the coefficient β of the scaling law maintains the same order of

magnitude for all the cases, but is conspicuously affected by the hub-height z_h of the wind farm.

4.5 Conclusion and Future Work

In this work we study the large scale structures involved in the power generation of large wind farms with different geometric roughness $z_{0,hi}$ (different turbine layout) in the asymptotic limit using Fourier analysis. In particular, we focus on the parametric study of increasing wind farm power by increasing the geometric roughness, from the perspective of the dynamics of the length scales in the farm. By investigating the spectra of the mean kinetic energy flux difference at the top and bottom wake region over the global computational domain, we observe that large streamwise *anisotropic eddies* of length scale $> 10D$ (D is the turbine rotor diameter) that contain over 80% of the flux spectral content are responsible for the power generation in large wind farms. Rather different dynamics are observed at length scales $\sim O(D)$ for the different cases with parametric variation in s_x, s_y, z_h. For farms with lower hub-height (z_h), scales $\sim O(D)$ are also responsible for the negative contribution or the upward vertical entrainment of the MKE flux, that does not contribute to the wind turbine power.

At larger scales $\lambda_x > 30D$, the near wall $k_x^{-1/2}$ scaling corresponding to the *attached eddies* were observed in the MKE flux as well as the flux-difference spectra. We also notice a regime of robust 1/3 scaling law ($\lambda_y \sim \lambda_x^{1/3}$) in the 2D premultiplied MKE flux difference spectra, similar to the energy and co-spectra, arising due to the background turbulent dispersion of the *wake shear layer* in the wind farm. Additionally, the two dimensional spectra of the MKE flux difference also elucidate on the horizontal anisotropy of the eddies that make significant contribution to the power generation. In general, from the spectra of u, w energy, as well as the integral length

scales it is apparent that the enlargement of eddy sizes near the wall is caused by the downdraft of vertical turbulent motions due to the mechanism of MKE flux entrainment. As a final remark, we also want to highlight about the *modulation* of large scale structures in the wind farms, where eddies containing high amount of turbulent kinetic energy were observed near and around the hub-height location of wind farms (such non-uniform distribution of energy-containing eddies across the boundary layer was not seen in the case without the wind farms). These modulations of large scale structures were also quantitatively estimated by computing the vertical variation of the integral length scales showing peaks in wind farm layouts when compared to neutral ABL flows without wind turbines. These effects can be potentially explored for a possibility of efficient, *symbiotic*, design of wind farms where smaller turbines are placed in between the larger ones in a vertically staggered orientation, so that an "optimized" energy harvesting can be achieved.

Chapter 5

UTILIZATION OF MODULATED LARGE SCALES IN A VERTICALLY STAGGERED WIND FARM

5.1 Introduction

Wind farms featuring large arrays of horizontal axis wind turbines (HAWT) have become popular since the last two decades as a viable method of extracting wind energy from the atmospheric boundary layer (ABL) [5, 20, 23, 124, 126, 132, 134, 138], and converting it into electric power [139–142]. The atmospheric turbulent flow intercepted by the turbines, produces a low-velocity region downstream of the turbines known as *wakes*. In large wind farms comprising of many arrays of wind turbines, the wakes from the previous rows of wind turbines impinge on the turbines at subsequent rows, reducing the power and increasing structural loads of those turbines. Horizontal staggering of wind turbines is a popular way of optimizing the layout of wind farms [21, 23, 126, 134] to reduce wake impingements, where the wind turbine positions in two consecutive rows are offset from each other. Compared to horizontal staggering, vertical staggering of wind farms, i.e. offsetting the wind turbine hub-heights, is relatively less explored. A few experimental studies were concerned with the situation where, in a model wind farm, every second row of turbines was replaced with the turbines of smaller hub-heights, while leaving the rotor diameters intact, or lowering it slightly in proportion with the hub-height. Chamorro et al. [125] studied an experimental model wind farm where horizontal axis wind turbines (HAWTs) of two different rotor sizes and hub-heights were alternated, and demonstrated that distinctive flow features not present in a single-size (homogeneous) wind farm were

observed that led to reduced level of turbulence around the wind turbine rotors and more homogeneous flow through the wake mixing. Although potential benefits of reduced turbulence levels on turbine loading were implied, the effects on power were not directly measured. Vested et al. [143] documented experiments with a model of a vertically staggered wind farm featuring HAWTs of two different hub-heights but identical rotor sizes, and reported 25% increase in the power of shorter wind turbines operating behind the taller ones, as compared to the base configuration with short wind turbines only. In these studies, the differences between the turbine sizes (hub-heights and rotor diameters), and consequently, their power capacities, have not exceeded 30-40%, which makes wind turbines operate essentially on the same scale in terms of power production. Several recent studies [144–146] have explored the effect of hub-height optimization in vertically staggered wind farms utilizing a semi-analytical wake model called PARK model [147]. Vasel-Be-Hagh and Archer [148] used a similar optimization framework and validated their optimized layout with Large Eddy Simulations. These works have shown the potential power benefits of vertically-staggered configurations with the maximum benefit obtainable at offshore locations with tight spacing between the turbines. The aforementioned studies have focused on a hub-height being a primary optimization variable while the rotor diameters were kept fixed for all the turbines. In this paper, we aim to further explore the idea of vertical staggering of the turbines, and introduce the concept of a multiscale wind farm, where, in addition to wind turbines operating at a larger scale of power production, the turbines with significantly smaller sizes (in terms of both rotor sizes and hub-heights) and thus power capacities are added to an existing large-scale wind farm configuration. The concept is slightly different from the same-scale variable-height wind farms, in a sense that, a nearly-optimum layout for the wind turbines operated at large scales (that by itself can have variable hub-heights for best performance) is

enriched by adding more small turbines (rather than replacing the existing large turbines), and an effective increase of the wind farm capacity beyond the baseline level is expected. The turbines in such multiscale designs have a potential to influence each other both through a direct interference via wake mixing, and also through a global modulation of the turbulent boundary layer and the energetics of large-scale coherent structures. From a perspective of efficiency, for a practical multiscale wind farm design, one would expect that these interactions are at least not destructive, that is, the performance of the turbines at each scale is not negatively influenced by the presence of the turbines at the other scale. Another added benefit of a multiscale wind farm as compared to a combination of separate single-scale homogeneous arrangements is the reduced cost of the terrain and electrical power lines, as well as the decrease of overhead in operation and maintainance costs.

Along the lines of such a vertically-staggered, multiscale, wind farm design, Xie et al. [25] in their recent study performed Large Eddy Simulations of a collocated wind farm where 20 small vertical axis wind turbines (VAWT, with 100 times lower capacity and almost 6 times lower hub-heights) were placed around each large HAWT turbine. The study [25] documented 32% increase in the overall wind farm capacity, mostly coming from high density (twenty to one) of the added VAWTs. Although the increase in power levels extracted by the large turbines (by about 10%) was demonstrated as well, due to a faster wake recovery from enhanced turbulence introduced by the small turbines, the same enhanced turbulence levels were also responsible for the increase in power fluctuations (variability) which has a negative effect on turbine fatigue loading. In the current paper, we aim to explore whether such a "multiscale wind farm" idea works for more conventional, HAWT-only, wind farm designs. Note that DuPont et al. [149] have recently performed an optimization study of a similar multiscale wind farm where both the hub heights and the rotor diameters were opti-

mized simultaneously in a wind farm layout and were allowed to vary by as much as three times. The study, again, used the PARK model, and the distinction between the HAWT and VAWT turbines could not be made, since a very simplistic algebraic power model was used.

Our idea of a multiscale wind farm stems from our previous work [127, 150] that illustrated the presence of energetic and organized eddies originating around the wind turbine wakes and spreading below the rotor region, which were not seen in atmospheric flows without the wind turbines. Since large scale organizations have significant contribution to wind turbine power [22, 134], one of the goals of the current work is to show that there is a potential of an efficient harvesting of these large-scale structures by smaller turbines which can also lead to a reduced power variability in these turbines. We also document that the choice of the hub-heights for the small turbines influences the efficiency of the multiscale wind farm design. In this paper, large eddy simulations with an actuator line model for wind turbines are employed to study these effects. We note that wind turbine towers were not modeled in the current study. Although the current computations invoke the framework of asymptotically infinite wind farms through incorporation of periodic boundary conditions, we expect that the current findings can be qualitatively generalized to the finite wind farm situations, where the savings from the land cost make multiscale configurations especially enticing.

5.2 Computational Setup

The computational domain comprises of a periodic wind turbine array, with dimensions $21D_L \times 9D_L \times 3D_L$, where D_L is the diameter of the large turbine. The rows with small turbines of diameter $D_S = 0.3\,D_L$, are placed mid-way between the rows with large turbines. In the current study, the diameter of the small turbines is

kept fixed, while we consider two separate cases with different hub-height locations of these small turbines in order to study the potential benefits of vertical staggering. In order to distinguish between the cases, we will call the small turbines placed at the smaller hub-heights as "small", small turbines placed at the higher hub-heights as "intermediate", while the turbines with large rotor sizes will be referred to as "large" (note that "small" and "intermediate" turbines have the same rotor size).

The dynamics and power of the large turbines in the vertically staggered arrangements containing large-small and large-intermediate turbines is compared against the baseline case comprising of only the large turbines in a periodic arrangement. In an analogous way, the dynamics and power of the small/intermediate wind turbines in the multiscale (vertically staggered) arrangements is compared against the arrays consisting of only small/intermediate wind turbines at corresponding hub-heights arranged in a periodic arrangement. Figure 5.1 illustrates the schematics of the computational setup for the investigated multiscale and single scale periodic arrays. Unlike in previous variable-height wind farm studies involving HAWT turbines of comparable sizes and hub-heights (within roughly 70% of each other) [125, 143], our current approach involves wind turbine dynamics at disparate length scales in such multiscale wind farm designs. The following acronyms are used for the wind turbine arrangements: for large only turbines in a single scale wind farm, L is used, while LS^M and LI^M refer to the multiscale arrangements of large-small and large-intermediate turbines, and S and I are used for small and intermediate only periodic arrangements. Additionally, to distinguish between the large turbines in the single scale and multiscale arrangements, we use the acronyms L and L^M respectively. Similar treatment is done for the the small/intermediate turbines with using the superscript M to remind the readers about the multiscale arrangements.

The details of the wind turbine array parameters for all the five simulated cases,

e.g., the hub-heights, z_h of the large turbines and z_h' of the small/intermediate turbines, the ratio of turbine diameters D/D_L, the inter-turbine streamwise and spanwise distances, $\Delta x_{turb}, \Delta y_{turb}$ are provided in Table C.1. It must be noted that, due to the difference in hub-heights of the small and intermediate turbines, in the multi-scale layout LS^M, the small turbines remain outside the wakes of the large turbines, while there is a 30% overlap in the area of the rotors of the large and intermediate turbines resulting in wake mixing in the layout LI^M. The scale of the large wind turbines with respect to the ABL thickness H is $D_L/H = 1/3$. We also define the non-dimensional inter-turbine distances, s_x, s_y, for the large wind turbines, as $s_x = \Delta x_{turb}/D_L, s_y = \Delta y_{turb}/D_L$, and s_x', s_y', for the small/intermediate wind turbines, as $s_x' = \Delta x_{turb}/D_S, s_y' = \Delta y_{turb}/D_S$, that will be useful in the discussion to follow, and summarize them in Table 5.2.

The turbine geometry for the small and intermediate wind turbines corresponds to the specifications of a 2MW 3-bladed Tjæreborg turbine [12, 151]. This choice has been made due to a close match between the specified rotor diameter $D_S = 0.1H$ of the small and intermediate turbines and the Tjæreborg rotor diameter of 61.1m, when a typical thickness of a neutral atmospheric boundary layer is assumed [152], and a public availability of the data. The chord length and the pitch angle in Tjæreborg turbine vary linearly with radius as specified in Ref. [151]. The airfoil series employed are NACA 44xx airfoils varying between the thickness of 24% at the hub and 12% at the tip. The airfoil data $\big(C_l(\alpha), C_d(\alpha)\big)$ is taken from wind tunnel measurements performed on NACA airfoils at a chord Reynolds number $Re = 6 \times 10^6$ [151]. The geometry for the large wind turbines is also based on a 3-bladed turbine and is scaled up from the baseline geometry proportionally to the rotor diameter, while the same airfoil series and airfoil data are used to maintain a scale similarity between the turbines for a consistent performance comparison [153]. All turbines (small, intermediate

and large) are set to rotate clockwise if viewed from upstream with the prescribed constant tip speed ratio $\lambda = 5.5$, such that the rotational speed of each turbine Ω_k can be calculated as $\Omega_k = 2\,\lambda\,U_{hub,k}/D_k$, where $U_{hub,k}$ is the hub-height velocity and D_k is the radius of each turbine. The choice of prescribing a constant tip speed ratio for wind turbines is in line with previous simulations and experiments [21, 125, 154, 155], and corresponds to a region on a power curve between the cut-in wind speed and the rated output speed (cubic region) [149]. The simulations were run for 30 eddy turn over times, $30 \times (H/u_*)$, where u_* is the friction velocity above the wind turbine canopy involving large turbines (case L), to ensure statistical stationarity of the results. Unless otherwise mentioned, all the statistical and spectral results involve normalization with mean free-stream velocity scale, U_∞. Power was normalized with U_∞^3.

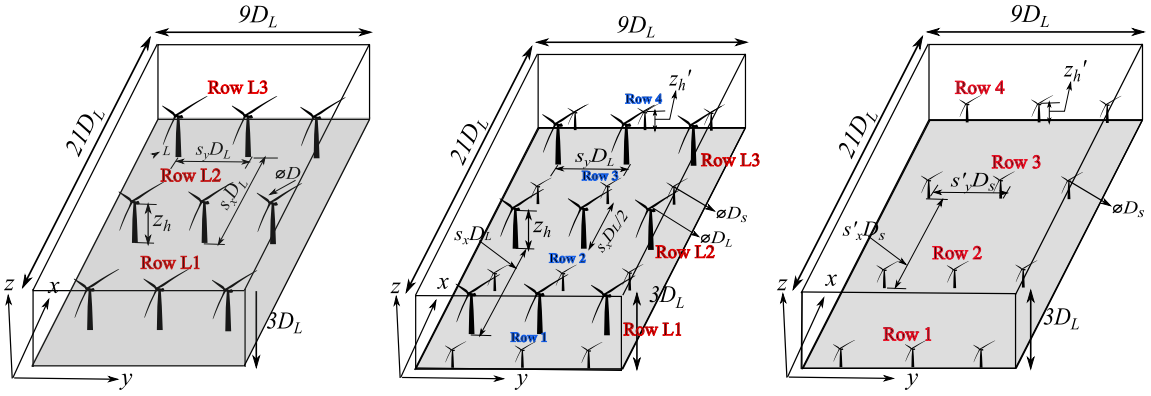

Figure 5.1: Schematic of the computational domain of (a) baseline case L, with large turbines in a periodic arrangement. (b) Vertically staggered multiscale periodic wind farm of cases $L\xi^M$ with large + small/intermediate turbines ($\xi = S,\ I$).(c) Small/intermediate turbines in periodic arrangements $S,\ I$. Inter-turbine distances, $s'_x D_S = s_x D_L$, $s'_y D_S = s_y D_L$. Rows for large turbines: $L1 - L3$. Rows for small/intermediate turbines: $1 - 4$.

Case	N_{turb}	Δx_{turb}	Δy_{turb}	z_h	z'_h	D/D_L
L	3×3(L)	$7D_L$	$3D_L$	D_L	–	$1(L)$
LS^M	3×3(L) $+ 4 \times 3$(S)	$3.5D_L$	$3D_L$	D_L	$0.3D_L$	$1(L) + 0.3(S)$
LI^M	3×3(L) $+ 4 \times 3$(I)	$3.5D_L$	$3D_L$	D_L	$0.6D_L$	$1(L) + 0.3(I)$
S	4×3(S)	$7D_L$	$3D_L$	–	$0.3D_L$	$0.3(S)$
I	4×3(I)	$7D_L$	$3D_L$	–	$0.6D_L$	$0.3(I)$

Table 5.1: Geometric parameters of large and small turbines in multiscale and homogeneous/periodic wind farm arrangements. The scale of large turbines with respect to the ABL thickness is $D_L/H = 1/3$. L, S, I in brackets refer to the large, small and intermediate turbines.

Turbines	Streamwise distance	Spanwise distance
L, L^M	$s_x = 7$	$s_y = 3$
S, I, S^M, I^M	$s'_x = 23.1$	$s'_y = 9.9$

Table 5.2: Non-dimensional inter-turbine distances normalized with D_L for large turbines, and with D_S for small/intermediate turbines.

5.3 Results: Power and Performance

In this section, the performance of the multiscale wind farm is assessed in terms of power and its variability for wind turbines operating at different scales (large and small/intermediate turbines) and compared against corresponding single-scale, homogeneous, cases in similar configurations. The total power extracted by wind turbines in a wind farm can be defined as

$$P = \sum_{k=1}^{N_t} \frac{\overline{P_k(t)}}{U_\infty^3}, \tag{5.1}$$

where N_t is the total number of the turbines in wind farm. Due to the equal turbine placement density for the large and small/intermediate turbines in the consid-

Case	$\overline{\Delta x}$	$\overline{\Delta y}$	$\overline{\Delta z}$	$N_x^e \times N_y^e \times N_z^e$	N_{xyz}
L	$0.024H$	$0.014H$	$0.0060H$	$42 \times 30 \times 24$	1.05×10^7
S	$0.028H$	$0.014H$	$0.0060H$	$36 \times 30 \times 24$	9.02×10^6
I	$0.028H$	$0.014H$	$0.0060H$	$36 \times 30 \times 24$	9.02×10^6
LS^M	$0.0206H$	$0.012H$	$0.0045H$	$48 \times 36 \times 32$	1.92×10^7
LI^M	$0.0206H$	$0.012H$	$0.0045H$	$48 \times 36 \times 32$	1.92×10^7
Calaf et al. [5]	$0.049H$	$0.017H$	$0.016H$	–	2.097×10^6

Table 5.3: The average grid sizes in the x, y and z direction for the five simulated cases, L, S, I and LS^M and LI^M as compared to the simulations of Calaf et al. [5]. $N^e_{x,y,z}$ – number of spectral elements in the x, y, and z direction, N_{xyz} is the total number of gridpoints. Calaf et al. [5] uses a uniform grid, with domain $2\pi H \times \pi H \times H$, and a rotor diameter $D = 0.1H$.

ered cases, we take $N_t = 9$ in all single-scale arrangements containing large and small/intermediate turbines, and $N_t = 18$ for the multiscale wind farms. Although technically 12 small/intermediate turbines are simulated in homogeneous as well as multiscale layouts, the turbines in the last row are essentially the same turbines as in the first tow, due to periodicity, and are not considered. In Equation 5.2, the power $P_k(t)$ is the power of the k^{th} turbine in the computational domain calculated from Equation 2.23 and, as discussed earlier, further normalized with U_∞^3 for a consistent comparison between the cases. $\overline{P_k(t)}$ refers to a temporally averaged value of $P_k(t)$. It is also useful to define the mean power density, which can be calculated by dividing the total power in wind farm by the wind farm area $A_{farm} = N_t^\xi s_x\, s_y\, D_L^2$ as $\rho_m = P/A_{farm}$, where P is the total power extracted by the wind farm defined by Equation 5.1.

To compare the turbines operating at each particular scale, it is also useful to define the mean power and variability of turbines at each scale. Mean turbine power

at each scale of operation can be defined as

$$P_{m,\,\xi} = \frac{1}{N_t^{\xi}} \sum_{k \in \xi : k=1}^{N_t^{\xi}} \frac{\overline{P_k(t)}}{U_\infty^3}, \tag{5.2}$$

where ξ is the set of the turbines of the same scale, and N_t^{ξ} is the number of the turbines of the same scale ($\xi = L, I, S$) in single-scale or multiscale arrangements. Note that at some instances in the manuscript will be referring to a time-dependent turbine-averaged mean power for each turbine scale defined as

$$P_{m,\,\xi}(t) = \frac{1}{N_t^{\xi}} \sum_{k \in \xi : k=1}^{N_t^{\xi}} \frac{P_k(t)}{U_\infty^3}, \tag{5.3}$$

where instantaneous, and not a temporally-averaged power, is further averaged among all the turbines of the same scale in a wind farm.

The power variability due to turbulence for wind turbines operated at the same scale can be further measured using the definition of coefficient of variation (standard deviation normalized by mean) and averaged over the turbines as in Equation 5.4,

$$V_{m,\xi} = \frac{1}{N_t^{\xi}} \sum_{k \in \xi : k=1}^{N_t^{\xi}} \frac{\sqrt{\left(\overline{P_k(t)^2} - \overline{P_k(t)}^2\right)}}{\overline{P_k(t)}}. \tag{5.4}$$

In the comparison of power and variability in the tables below, a case format X/Y has been used, which manifests the fact, that the percentage gain/loss in case X has been compared against case Y, as $(X-Y)/Y \times 100\%$. For brevity and easy reference, throughout the subsequent sections, cases LS^M, LI^M are also denoted as "vertically staggered" or "multiscale", and cases L, S, I as "homogeneous" arrangements.

5.3.1 Overall Wind Farm Performance

We first calculate the mean turbine power density ρ_m for all 5 considered cases and compare it to the mean kinetic energy (MKE) flux difference $\Delta\Phi_p$ in Table 5.4

Case	ρ_m	$\Delta\Phi_p$	%Deviation
L	2.61×10^{-3}	2.65×10^{-3}	1.5%
S	5.43×10^{-4}	5.70×10^{-4}	5.0%
I	6.81×10^{-4}	6.97×10^{-4}	2.3%
LS^M	3.14×10^{-3}	2.93×10^{-3}	6.7%
LI^M	3.22×10^{-3}	2.95×10^{-3}	8.3%

Table 5.4: Comparison of MKE flux difference $\Delta\Phi_p$ and mean power density ρ_m for all the single scale and multiscale wind farm cases. Both $\Delta\Phi_p$ and ρ_m are normalized with U_∞^3.

(both normalized with U_∞^3). The equivalence of the two terms (ρ_m and $\Delta\Phi_p$) was first demonstrated for a single scale wind farm by vertical integration of the temporally and horizontally averaged kinetic energy equation between the turbine rotor bottom and top tip location [5]. However, it can be extended quite straightforwardly to multiscale wind farm cases by changing the bottom and top limits of integration to $z_h' - D_S/2$, $z_h + D_L/2$, respectively, where z_h', z_h are the hub-heights of the small/intermediate and large turbines. As can be seen from Table 5.4, a deviation of less than 8% is observed for all the cases, consistent with the findings of Calaf et al. [5].

We now document the overall power gain in multiscale wind farms (cases LS^M, LI^M) compared to a baseline large-scale wind farm configuration (case L) in Table 5.5a. As expected, a significant power gain of around 20% is achieved in both cases, due to the fact that additional power capacity in the form of the small/intermediate turbines was added. To asses the individual performance and efficiency of the turbines at each scale, it is instructional to compare the power change in a multiscale wind farm against the direct sum of the powers in corresponding isolated homogeneous wind farms featuring large- and small/intermediate-scale turbines only, which is shown in

Table 5.5b. Overall, one can distinguish between an *inefficient* design, where the total power in the multiscale wind farm is less than the direct sum of the individual powers in corresponding single-scale arrangements, $P_{L\xi^M} < P_L + P_\xi$, and an *efficient* design, where the reduction in power is not observed, $P_{L\xi^M} \sim P_L + P_\xi$, for $\xi = I$ or S. As Table 5.5b indicates, the multiscale wind farm with small turbines at smaller hub-heights (Case LS^M) can be considered efficient, while the one with small turbines at larger hub-heights (Case LI^M) is less efficient. In the following analysis, we look at the performance of large and small wind turbines separately in a multiscale wind farm, in order to elucidate the effects of interaction between the turbines of different scales, and how these interactions influence the turbine operation compared to homogeneous environments.

Case	$\Delta P_{X/Y}$
LS^M/L	20.45%
LI^M/L	23.25%

(a)

Case	$\Delta P_{X/Y}$
$LS^M/(L+S)$	−0.28%
$LI^M/(L+I)$	−2.45%

(b)

Table 5.5: Change in total power in multiscale wind farms (a) with addition of small/intermediate turbines and (b) as compared to the direct sum in isolated homogeneous wind farms.

5.3.2 Large Turbines

To further assess the turbine performance, it is useful to look at the mean power of wind turbines at each scale. Temporal variation in the mean power generated by the large and small/intermediate turbines in vertically staggered and homogeneous layouts containing large turbines is shown in Figure 5.2. It can be seen that the mean

power P_m of the large turbines in multiscale layouts (LS^M, LI^M) does not change significantly ($\sim$ 1%) compared to the baseline case L (See Table 5.6a). However, while the change of power variability in large turbines in case LS^M against case L is not noticeable, variability of power in large turbines in case LI^M shows approximately 10% increase compared to baseline case L possibly due to its interaction with the intermediate turbines. These findings are inline with $\sim$ 5% power variability increment in large wind turbines in a vertically staggered farm (containing HAWTs and VAWTs) compared to HAWT-only farm of Xie et al. [25].

Case	$\Delta P_{m,X/Y}$	$\Delta V_{m,X/Y}$
L^M $(LS^M)/L$	-0.99%	-1.78%
$L^M(LI^M)/L$	-0.54%	10.7%

(a)

Case	$\Delta P_{m,X/Y}$	$\Delta V_{m,X/Y}$
S^M/S	3.87%	-24.6%
I^M/I	-8.8%	50.98%

(b)

Table 5.6: Change in mean power and variability in large and small/intermediate turbines in multiscale wind farms compared to their homogeneous counterparts of equivalent hub-heights. (a) large turbines (b) small/intermediate turbines.

5.3.3 Small/Intermediate Turbines

Figure 5.3 and Table 5.6b document the comparison of power in the small and intermediate turbines in a vertically staggered layout against the homogeneous arrangements with the same hub-heights. It is interesting to note that small turbines in a vertically staggered configuration (LS^M) are *power efficient* and manifest a gain of $\sim$ 4% in mean power compared to a homogeneous arrangement (S), with a substantial decrease in variability by more than 20%. For intermediate turbines in vertically staggered farms (LI^M), the power comparison results show a completely opposite

behaviour, i.e., they are *inefficient* manifesting a significant 8% drop in power and an increase in variability by $\sim 50\%$ against homogeneous wind farms with the same hub-heights (I). This is further corroborated in Table 5.7, where we observe that the mean power growth is significantly suppressed when the hub-heights of the small wind turbines are doubled in the vertically staggered arrangement.

From the above discussion, it is apparent, that while the addition of the small turbines does not illustrate a prominent negative influence on the performance of the large turbines, the presence of the large turbines significantly affects the performance of the small/intermediate ones. It is evident that for the case LS^M, the small turbines (that lie completely outside the wakes of the large turbines) are able to harvest more energy per turbine than they would do otherwise in isolated homogeneous wind farms with the same small-turbine layout (S), perhaps by efficient utilization of the organized, coherent structures generated by large turbines, which also amounts to reduced variability. A further evidence that the organized structures might be responsible for the power increase was also observed in the energy spectra plots discussed in Section 5.3. For intermediate turbines at hub-heights of $0.6D_L$ (that are partially in the wakes of the large turbines), on the other hand, the interference is destructive compared to the intermediate-turbine only arrangements I, with less power and higher variability in the intermediate turbines in vertically staggered wind farms, possibly coming from stronger direct interactions between the large and intermediate turbines due to their relative proximity, wake impingements and a modulation of coherent structures.

5.3.4 Power Spectra

The mean power spectra of the large and small wind turbines in the vertically staggered configuration (cases LS^M, LI^M) are shown in Figure 5.4a, 5.4b. The fact

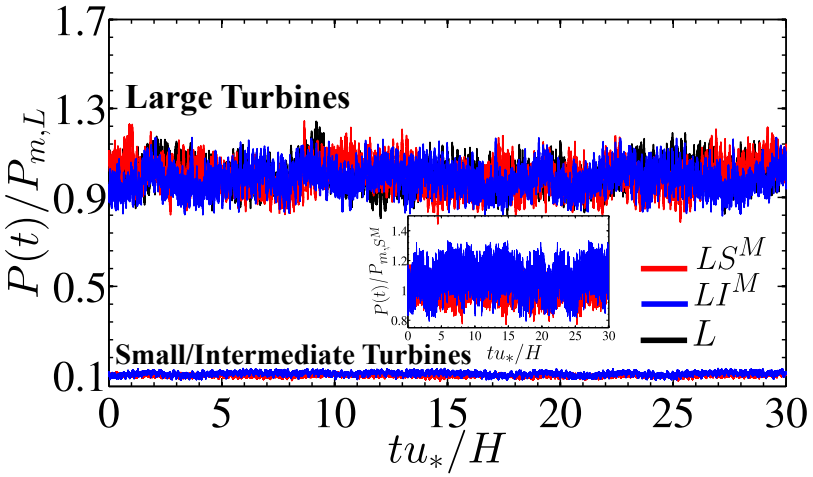

Figure 5.2: Temporal variation of the mean power (See Equation 5.3) in cases containing large turbines: Power of large turbines in cases L, LS^M, LI^M, as well as small/intermediate turbines in cases LS^M, LI^M, normalized with the mean power $P_{m,L}$ of baseline case L. Inset: Power of the small/intermediate turbines in cases LS^M, LI^M normalized with the mean power of the small turbines P_{m,S^M} in case LS^M.

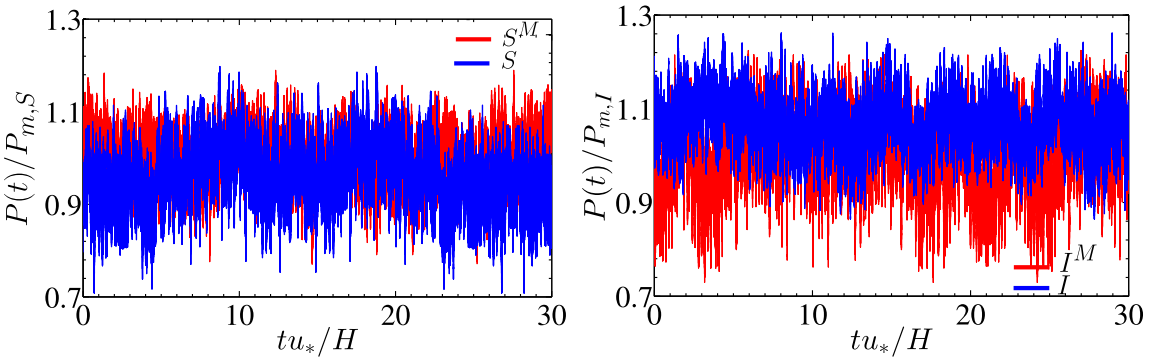

Figure 5.3: A comparison of the temporal variation of the mean power (See Equation 5.3) of small/intermediate wind turbines in a vertically staggered (LS^M, LI^M) and homogeneous arrangements (S, I). (a) Small turbines S, S^M with hub-height $z_h' = 0.3D_L$. (b) Intermediate turbines I, I^M with hub-height $z_h' = 0.6D_L$. $P_{m,\xi}$ ($\xi = S,\ I$) denote the mean power of small/intermediate turbines in a homogeneous, single scale orientation.

Case	Mean Power gain
Homogeneous (I/S)	25.15%
Vertically staggered (I^M/S^M)	10.29%

Table 5.7: Relative change in mean power from small to intermediate turbines when hub-height increased from $0.3D_L$ to $0.6D_L$, and rotor radius fixed at $D_S = 0.3D_L$.

that the large scale structures contribute to the turbine power is apparent in the plots, where the variation in the layout of the turbines are seen in the change of the spectra at frequencies $f < 10^{-2}u_*/H$ (corresponding to large temporal scales). The series of peaks observed in the spectra correspond to the frequency of the interception of the eddies with the turbine blade rotation, .i.e., $f = f_t, 2f_t, 3f_t \cdots$. Here $f_t = B\Omega/2\pi$, where Ω is the rotation speed of the turbines in radians per sec, and $B = 3$ corresponding to the number of blades. It is worth noting that the difference in the magnitude in f_t (Figures 5.4a, 5.4b) in the large ($f_tH/u_* \sim 1.67 \times 10^1$) and small ($f_tH/u_* \sim 4.64 - 4.96 \times 10^1$) turbines is due to the higher Ω in the small turbines imposed by the constraint of the fixed tip-speed ratio in the large and small turbines at different hub-height velocities.

To estimate the power spectra (power spectra density or PSD), a periodogram estimate of the discrete Fourier transform of power output time series have been performed along the lines of [156]. The power spectra plot corresponds to the square-root of the periodogram spectra. The power spectra in both the large and the small turbines (Figures 5.4a, 5.4b) manifest the f^{-1} law, at $f \sim u_*/H$, and the Kolomogorov $f^{-5/3}$ law at higher frequency scales $f \sim 10^2u_*/H$. Since the power mainly comes from the lift forces generated by the atmospheric flow, the $-5/3$ law is a testimony of the fact, that the power at higher frequency scales has significant contribution from

the turbulent kinetic energy [1].

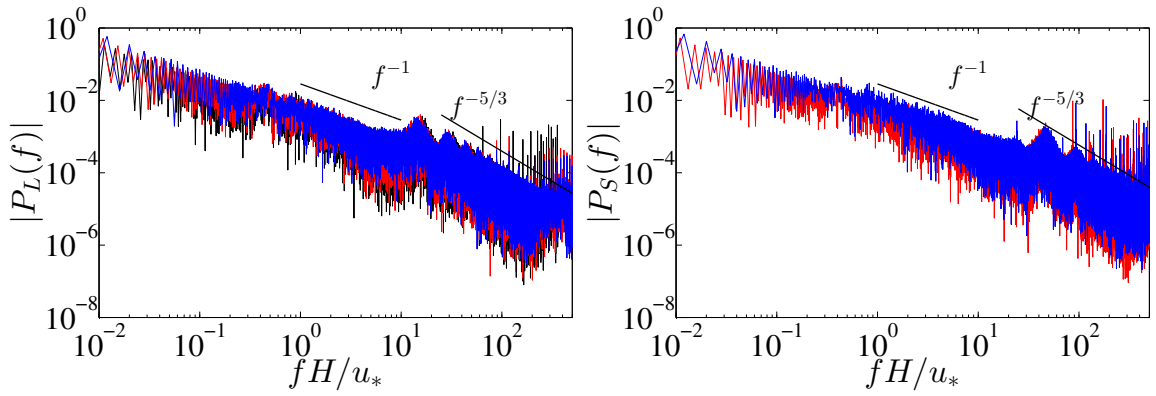

Figure 5.4: Frequency content of the wind turbine power. (a) Large turbines with cases L, LS^M and LI^M (b) Small/Intermediate turbines with cases LS^M, LI^M. The time and frequency scale are normalized with eddy turn over time scale H/u_*, $H = 3D_L$ based on the large turbines in L. Case L – black, case LS^M – red, case LI^M – blue.

5.3.5 Joint Probability Density Function

The analysis can be further extended by the joint probability density function (jpdf) of the power of the large and small/intermediate turbines in the multiscale layouts. For two random variables X and Y, a joint probability density function jpdf is related to a joint cumulative distribution function jcdf (a probability that X is no greater than $\tilde{x}$ and Y is no greater than $\tilde{y}$) as $\text{jcdf}(\tilde{x}, \tilde{y}) = \int_{-\infty}^{\tilde{x}} \int_{-\infty}^{\tilde{y}} \text{jpdf}(x, y)\mathrm{d}x\mathrm{d}y$. In a discrete computation, jpdf can be extracted from the envelope of a 3D histogram plot that computes the relative frequency of occurrence of the events within the specified bin values. If the random variables within the bin $([x_1, x_2], [y_1, y_2])$ are considered, the relative frequency of occurrence within this bin can be defined as N_{bin}/N_{tot}, where N_{bin} is the number of events falling within the bin, and N_{tot} is the total number of the events. The relative frequency of occurrence (probability that the variables are within the bin) is related to jpdf as $N_{bin}/N_{tot} = \text{jpdf} \times A_{bin}$, where A_{bin} is the bin

area, from where jpdf can be estimated by dividing the relative frequency by the bin area (frequency density). In order to obtain a smooth approximation from a discrete distribution data, a smoothing procedure in the form of a two dimensional kernel density estimation from MATLAB toolbox was used to calculate the joint pdf. The corresponding jpdf for the power of the large and small/intermediate turbines in the multiscale layouts LS^M, LI^M is plotted in Figure 5.5, where the normalized power $\bar{P}_{L^M}$, $\bar{P}_{I^M}$, $\bar{P}_{S^M}$ (normalized by the mean power of the large turbines in each multiscale layout) is considered as random variables in the 3D histogram plot and in jpdf. The convergence criterion $\int_{-\infty}^{\infty}\int_{-\infty}^{\infty} \text{jpdf}(\bar{P}_{L^M}, \bar{P}_{\xi^M})\text{d}\bar{P}_{L^M}\text{d}\bar{P}_{\xi^M} = 1$, $\xi = S, I$, is satisfied by the algorithm with the tolerance of 10^{-4}. Thus defined, jpdf essentially represents the rate of change of probability of a joint event with $\bar{P}_{L^M}$, $\bar{P}_{\xi^M}$, when the values of random variables change from $\bar{P}_{L^M}$ to $\bar{P}_{L^M} + \Delta\bar{P}_{L^M}$, and from $\bar{P}_{\xi^M}$ to $\bar{P}_{\xi^M} + \Delta\bar{P}_{\xi^M}$, $\xi = S, I$. The jpdf in Figure 5.5 indicates that the higher power in the large turbines is well correlated with the higher power of the small turbines in the same multiscale layout. From the high jpdf regions of the contour (a region of higher probability density, $\text{jpdf}(\bar{P}_{L^M}, \bar{P}_{\xi^M}) > 150$), it is apparent that in case LS^M, for a wide variation of power in large turbines, we have significantly less variation of power in the small turbines, a feature not seen in case LI^M. This illustration with joint pdf indicates the fact, that the power of small wind turbines at hub-height $z'_h = 0.3D_L$ comes from more well-organized structures, than that of the intermediate turbines at hub-height $z'_h = 0.6D_L$.

5.4 Results: Flow Analysis

Further insights regarding the physical mechanisms responsible for the change in power and variability in the multiscale wind farm arrangements will be discussed through the mean and the second-order turbulent statistics, as well as the energy

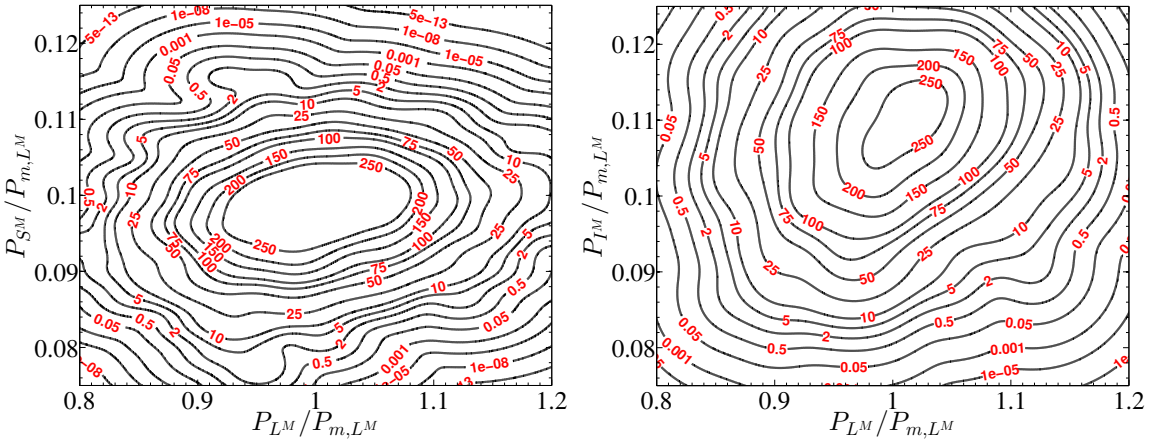

(a) (b)

Figure 5.5: Two dimensional joint probability density function jpdf($\bar{P}_{L^M}, \bar{P}_{\xi^M}$) of wind turbine power for the turbines L^M, ξ^M. $\xi = S, I$ (a) case LS^M. (b) case LI^M. All power variables are normalized with P_{m,L^M}, which is the mean power of the large turbines in LS^M and LI^M for (a) and (b) respectively. The jpdf satisfies $\int\int_{-\infty}^{\infty} \text{jpdf}(\bar{P}_{L^M}, \bar{P}_{\xi}^{M}) \text{d}\bar{P}_{L^M} \text{d}\bar{P}_{\xi^M} = 1$.

spectra, in the subsequent section.

5.4.1 Mean & Turbulent Statistics

In a conventional, homogeneous, periodic wind farm, it is known that the horizontally and temporally averaged mean streamwise velocity profile $\langle \overline{u} \rangle$ ($-$, temporal and $\langle\rangle$, xy averaging), manifests a double log layer in the vertical direction, induced by the bottom wall roughness $z_{0,lo} = z_0$ (lower log layer) as well as the wind turbine roughness $z_{0,hi} > z_{0,lo}$ (top log layer) [5]. Lettau roughness [135] is a measure of the geometric roughness $z_{0,hi}$ imposed by the organized array of wind turbines in addition to the roughness due to the topography of the land. The Lettau roughness [135] is given as $z_{0,Let} = 0.5hS/A$ where h is the effective height of the obstacle posing as a roughness, S is the silhouette area seen by the wind in the cross-wind-lateral direction (shadow area of the obstacle projected in the plane), A is the specific lot area mea-

sured in the horizontal plane or plane described by the average earth/air surface and is representative of how densely packed the roughness obstacles are. The numerical factor 0.5 corresponds to the average drag coefficient of the characteristic individual obstacle of silhouette area. For multiscale wind farms, this formula can be potentially modified as $z_{Lett} = 0.5(n_t^L z_h S_L + n_t^S z_h' S_S)/A$, where n_t^L, n_t^S is the number of large and small/intermediate wind turbines at a lot of area A, z_h and z_h' are hub-heights of the large and small/intermediate wind turbines respectively, as defined previously, and $S_L = \pi D_L^2/4$, $S_S = \pi D_S^2/4$ are the rotor areas of the large and small/intermediate turbines. In our multiscale wind farm cases, $n_t^L = n_t^S = 1$ at a lot of area $A = s_x s_y D_L^2$ (either n_t^L or n_t^S is zero in single scale wind farms), which results in Lettau roughness presented in Table 5.8 for all the cases.

Case	L	S	I	LS^M	LS^M
z_{Lett}/z_0	61.71	1.72	3.34	63.43	65.05

Table 5.8: Lettau roughness of the large and small/intermediate single scale wind farms (L, S, I), as well as the multiscale configurations LS^M, LI^M normalized by aerodynamic roughness

Table 5.8 indicates that the roughness of the small/intermediate turbines only configurations is more than an order of magnitude smaller than their large-only counterpart. Consequently, the contribution of the small turbines into the overall roughness in multiscale wind farms is less significant, and the roughness in Cases LS^M, LI^M is mostly defined by the roughness of large turbines, as seen from Table 5.8. The roughness values influence the mean streamwise velocity profile in Figure 5.6 that shows distinct double log-layer trends in Cases L, LS^M, LI^M with a significant degree of overlap (with the major discrepancies occurring in the region of mixing, $z_h - D_L/2 < z < z_h + D_L/2$), and essentially a single logarithmic trend in Cases S, I.

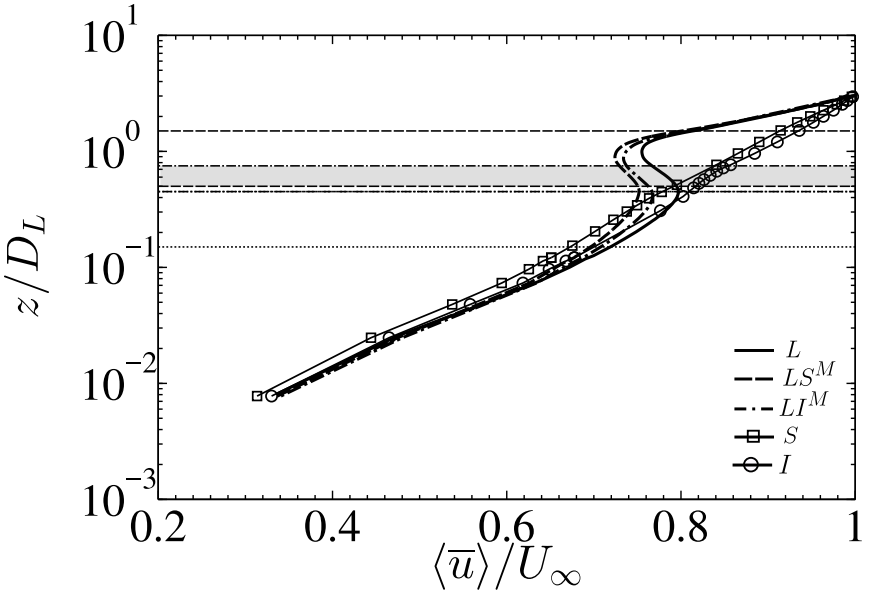

Figure 5.6: Temporally and horizontally averaged mean streamwise velocity $\langle\overline{u}\rangle/U_\infty$. Horizontal lines at the top and bottom tip of turbine rotors: Dashed – large turbines, Chain dotted – intermediate turbines, Dotted – small turbines. Gray patch – overlap area between large and intermediate turbine in LI^M.

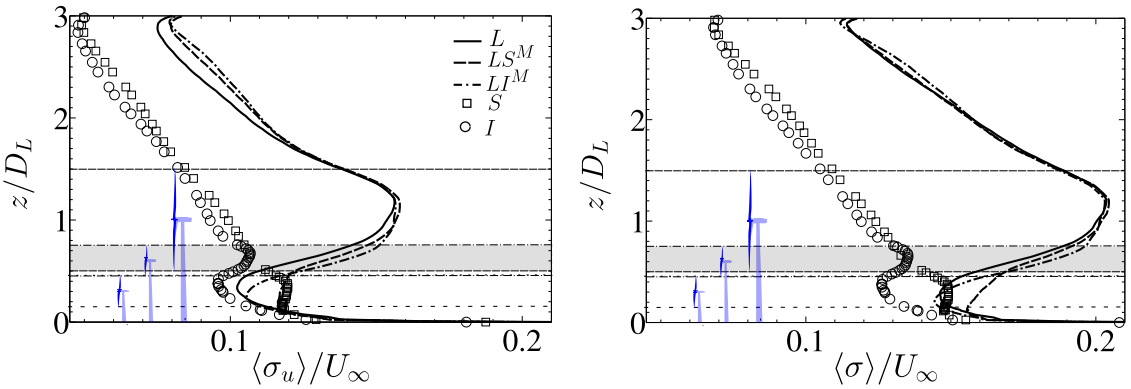

(a) (b)

Figure 5.7: Temporally and horizontally averaged (a) streamwise turbulence intensity σ_u/U_∞, where $\sigma_u = \sqrt{\overline{u'^2}}$ (b) total turbulence intensity σ/U_∞, where $\sigma = \sqrt{\overline{u'^2 + v'^2 + w'^2}}$. Normalization by mean free stream velocity scale U_∞. Rotor swept area shown as horizontal lines at the top and bottom tip of the turbine rotor with a wind turbine schematic: Dashed – large turbines, Chain dotted – intermediate turbines, Dotted – small turbines. Gray patch – overlap area between the large and intermediate turbine in LI^M.

Figure 5.7 depicts the horizontally averaged turbulence intensity for the homogeneous and multiscale wind farms. Expectedly, the homogeneous wind farms with small/intermediate turbines ($S,\ I$) show much smaller turbulence intensity throughout the domain than the homogeneous farms with large turbines (L) or the multiscale arrangements ($LS^M,\ LI^M$). In general, turbulence intensity profiles from the u' fluctuations alone and from the sum of the components ($u'^2 + v'^2 + w'^2$) are fairly similar in magnitude and shape, allowing for an argument that most of the turbulent activity around the turbine rotors comes from the streamwise fluctuations. The exception is the region near the hub-heights of the low-located small turbines ($z'_h = 0.3D_L$) in the multiscale arrangement, suggesting that, perhaps, other components play an increasingly important role in the structure of turbulence and the power production of the small turbines in this case.

5.4.2 Wake Recovery

Insights from the power generated by the wind turbines can be gained by studying the wake recovery of the mean velocity profile around the large and small turbines. From Figure 5.11a, we observe, that for the baseline homogeneous case of large only turbines L as well as the vertically staggered cases $LS^M,\ LI^M$, the wake recovery of the large turbines in the location $z_h - D_L/2 < z < z_h + D_L/2$ ($z_h = D_L$) remains similar, as is expected from the fact that the power in the large turbines was found to be similar across the cases. The recovery of the velocity deficit regions are also associated with the decay of the turbulence intensity and the kinematic shear (Figure 5.11b, 5.11c) in the turbine rotor swept region. It was observed that in general, the streamwise turbulence intensity and kinematic shear stress ($\sigma_u, -\overline{u'w'}$) are slightly increased in the cases LS^M, LI^M compared to L supposedly due to the addition of the smaller size turbines. However, for the small and intermediate turbines,

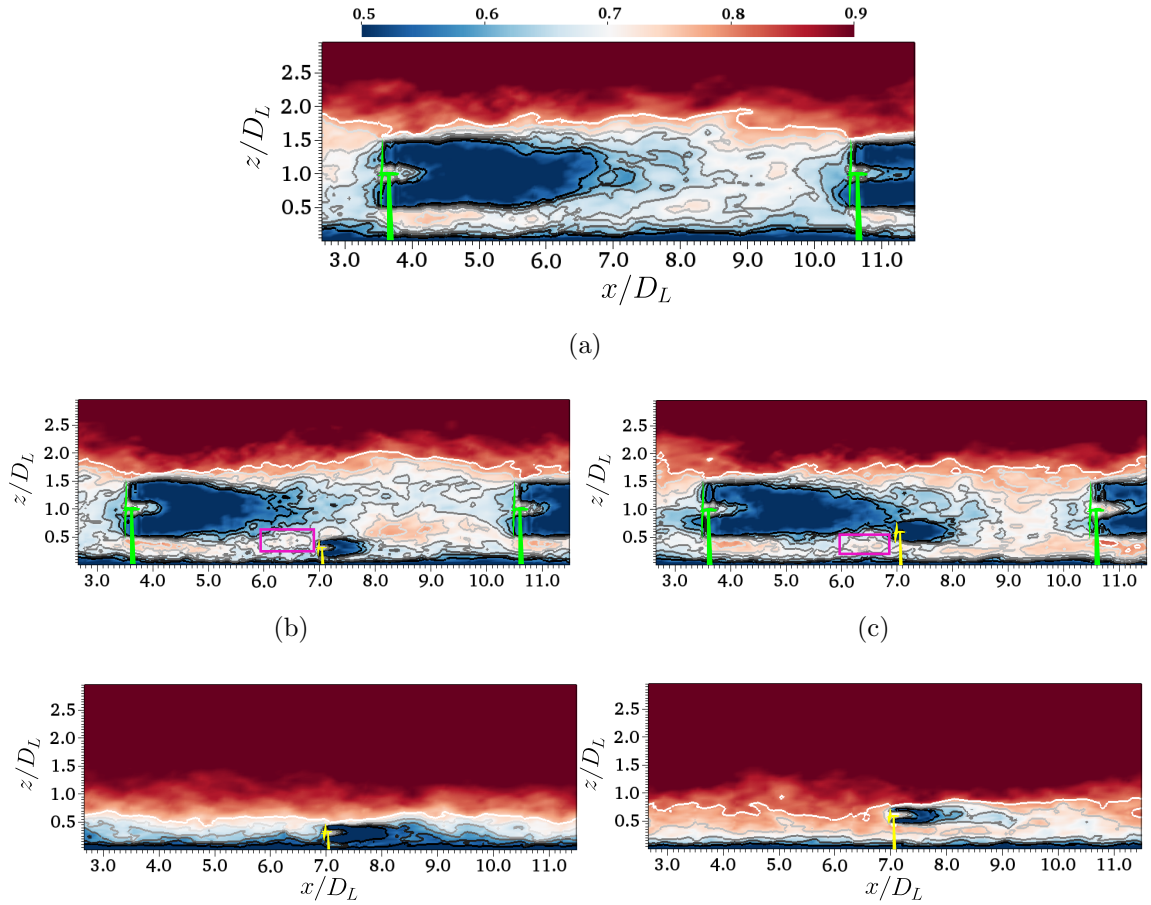

Figure 5.8: xz plane ($y = 4.5D_L$) of normalized velocity magnitude $\sqrt{u^2+v^2+w^2}/U_\infty$ in vertically staggered and homogeneous wind farms, temporally averaged for 10 eddy turn over times, based on the friction velocity of large turbines. (a) baseline case L (b) case LS^M (c) case LI^M (d) case S (e) case I. Contour lines in grayscale: 0.575 – 0.8 of U_∞. The solid magenta colored windows in cases LS^M and LI^M point to energetic structures around small and intermediate turbines (above for small turbines and below for intermediate turbines) present in multiscale arrangements that are not seen in homogeneous cases S, I. Large, intermediate and small turbines are schematically shown in color.

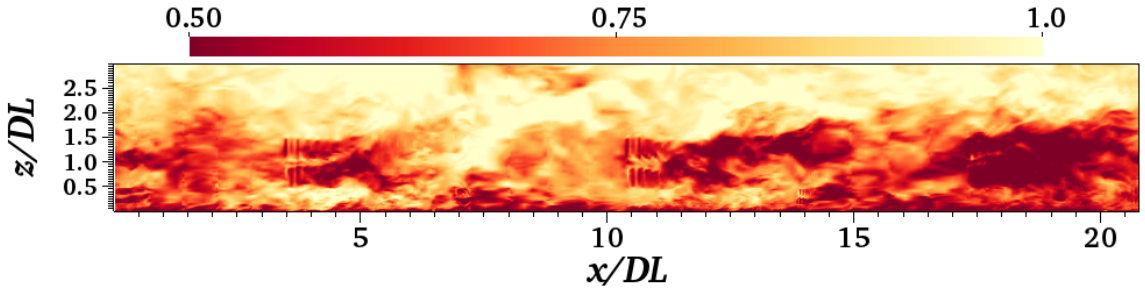

(a)

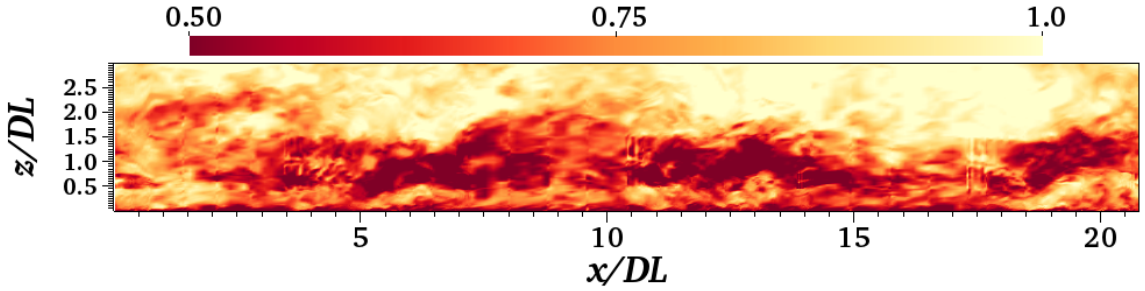

(b)

Figure 5.9: xz plane ($y = 4.5D_L$) of instantaneous velocity magnitude $\sqrt{u^2+v^2+w^2}/U_\infty$ for two different vertically staggered layouts (a) LS^M, (b) LI^M.

(Figures 5.12a–5.12d), it is apparent that the wakes ($z'_h - D_S/2 < z < z'_h + D_S/2$, $z'_h = 0.3D_L$ – small, $z'_h = 0.6D_L$ – intermediate) in vertically staggered orientation are affected by the wakes of the large turbines. Thus, while the wakes of the small/intermediate turbines recover smoothly in the homogeneous arrangement (S, I), bulges corresponding to high velocity regions of the large turbines appear at around $z \approx 0.3D_L$ for LS^M, LI^M, expediting the wake recovery for case LS^M while no such benefit occurs for case LI^M. These observations are in concordance with the power of the turbines documented in Section 5.3.3. Furthermore, near the rotor-swept regions of small turbines, cases S, I show a marked difference in the mean and turbulent statistics with the cases LS^M, LI^M since the small turbines in the latter are influenced by the dynamics of the large wind turbines. Specifically, the influence of the large turbines on the small or intermediate ones are illustrated by the

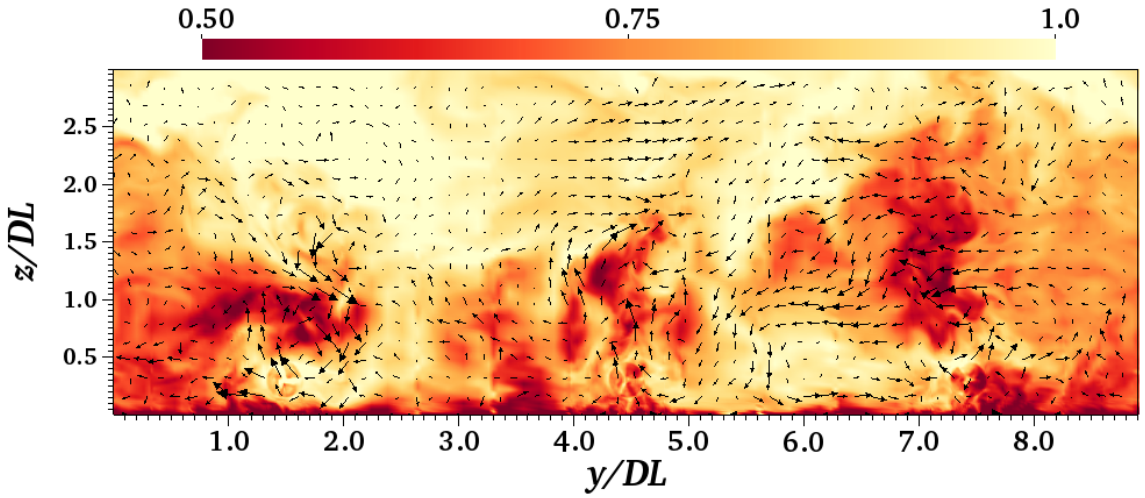

(a)

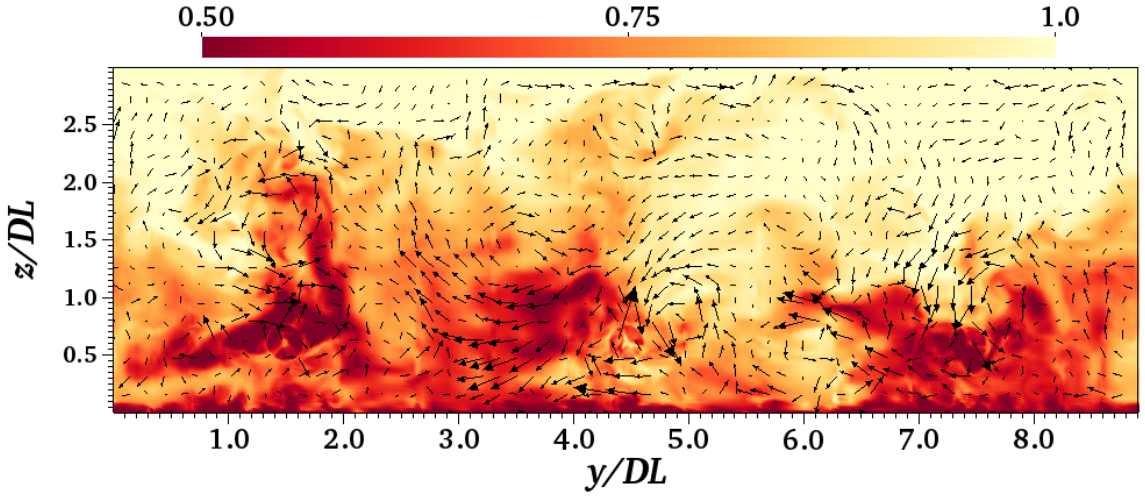

(b)

Figure 5.10: yz plane ($x = x_t + 0.5D_S$, x_t location of second row of small/intermediate turbines) of instantaneous velocity magnitude $\sqrt{u^2+v^2+w^2}/U_\infty$ contours and in-plane velocity vectors u, v for two different vertically staggered layouts (a) LS^M, (b) LI^M.

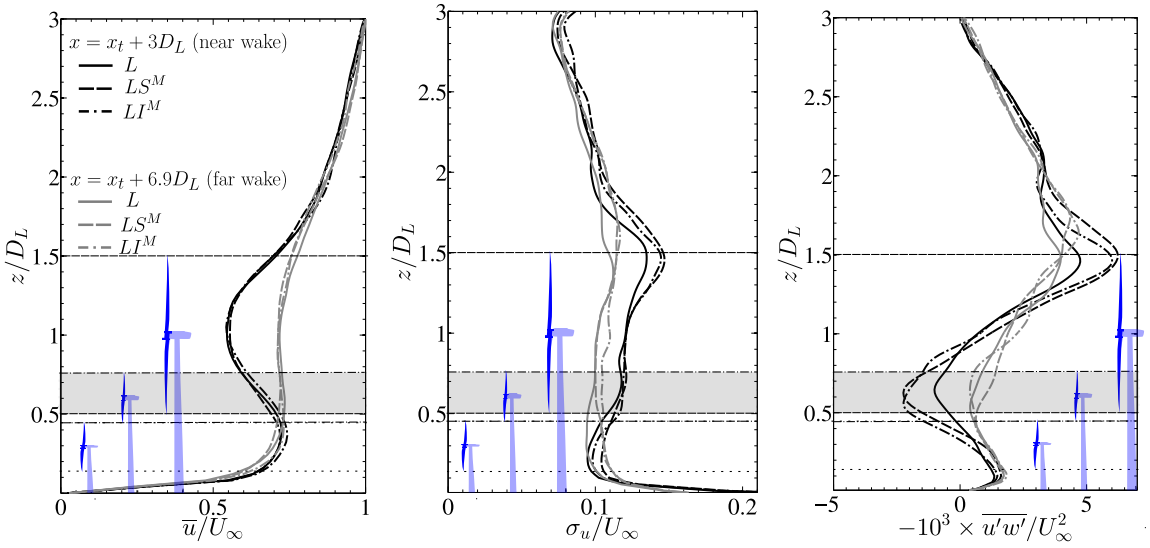

Figure 5.11: Spanwise averaged mean and turbulent statistics focused on wake recovery of the large turbines. (a) Mean streamwise velocity $\overline{u}$ (b) streamwise turbulent fluctuations $\sigma_u = \sqrt{\overline{u'^2}}$ (c) kinematic shear $-\overline{u'w'}$. Variables normalized by free stream velocity U_∞. x_t: Large turbine location in row L2 (See Figure 5.1). Rotor swept area shown as horizontal lines at the top and bottom tip of the turbine rotor with a wind turbine schematic: Dashed – large turbines, Chain dotted – intermediate turbines, Dotted – small turbines. Gray patch – overlap area between the large and intermediate turbine in LI^M.

disparate distances (scales) of the wake recovery, the decay of turbulent statistics in the rotor swept region as well as the differences in shear stress behavior. The results obtained from the above flow analysis and the turbine power data are seen to be inline with a recent study by Vasel-Be-Hagh and Archer [148] who have also found that a larger difference in hub heights is more effective than a smaller difference in vertically staggered arrangements. The authors identified two competing effects for the lower turbines: the presence of increased shear reduces power but a larger rotor area that is not exposed to the upstream wakes can increase power. It was concluded that the latter effect dominates when the spacing is tight between the turbines [148].

Figure 5.8 showing the temporally filtered velocity magnitude contours further corroborates the fact that the flow features around the large wind turbines are mainly

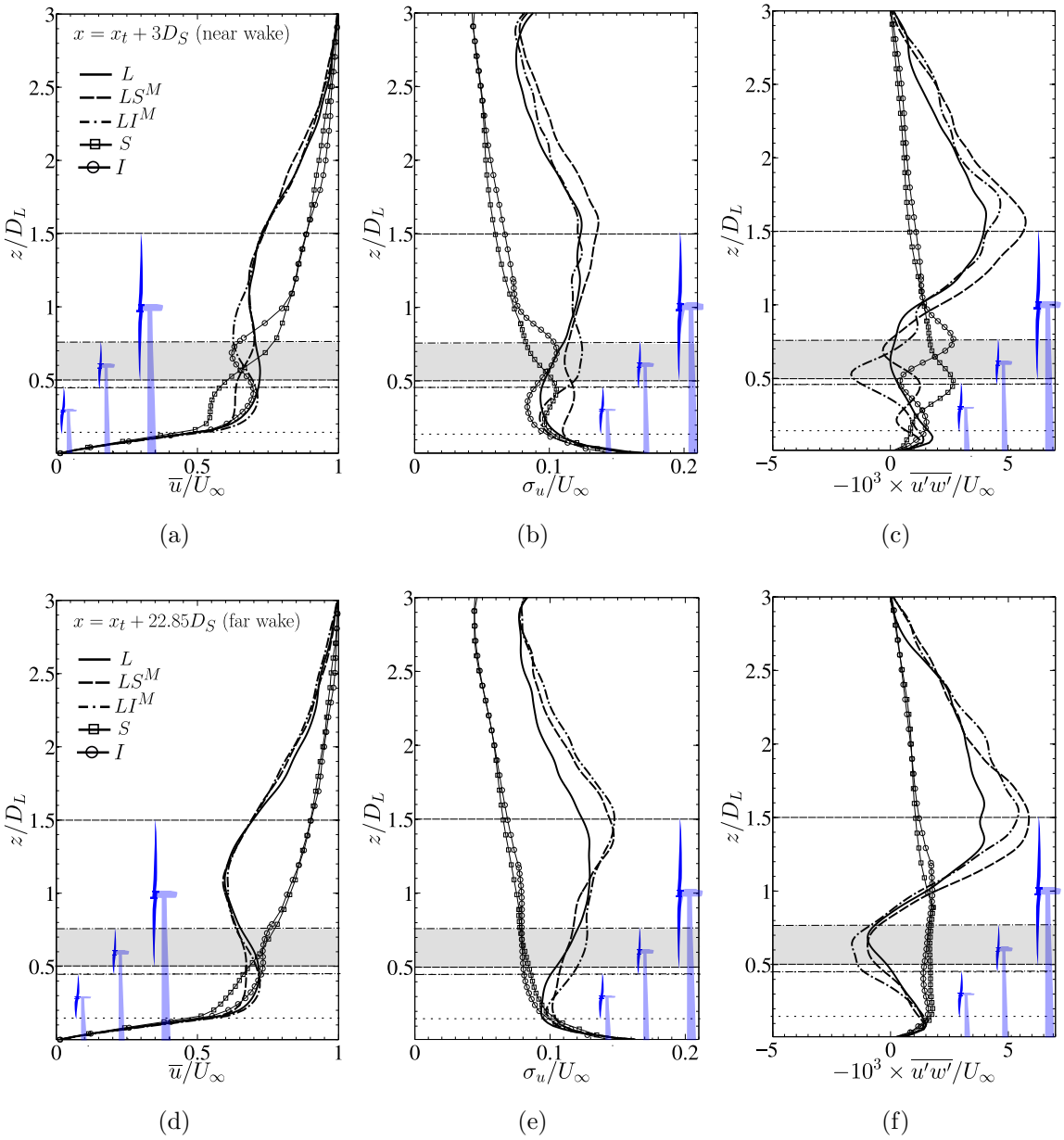

Figure 5.12: Spanwise averaged mean and turbulent statistics focused on wake recovery of the small/intermediate turbines. (a), (d) Mean streamwise velocity $\overline{u}$ (b), (e) streamwise turbulent fluctuations $\sigma_u = \sqrt{\overline{u'^2}}$ (c), (f) kinematic shear $-\overline{u'w'}$. Variables normalized by free stream velocity U_∞. x_t: Small turbine location in row 2 (See Figure 5.1).Rotor swept area shown as horizontal lines at the top and bottom tip of the turbine rotor with a wind turbine schematic: Dashed – large turbines, Chain dotted – intermediate turbines, Dotted – small turbines. Gray patch – overlap area between the large and intermediate turbine in LI^M.

unaffected in the multiscale arrangements, while features around the small wind turbines are influenced by the presence of the large ones. Further flow structures can be observed in Figures 5.9, 5.10 which illustrate the turbulent interaction between the multiscale turbines. Visual analysis of the structures shed by the large turbines corroborates the fact that they are produced in the shear layer at the bottom rotor tip and are entrained below the large turbine rotors, consistent with the previous spectral analysis [127, 150]. For the small turbines at lower hub heights (also see Figure 5.9a, 5.10a), these organized structures impinge directly on the turbine rotors and are harvested efficiently by the small turbines, increasing their power and reducing variability. For the intermediate turbines at higher hub-heights, the structures pass below the rotors (additionally, also see Figure 5.9a, 5.10a), leaving the intermediate turbines face an incoherent wake of large turbines, decreasing the power and increasing variability in intermediate turbines.

5.4.3 Premultiplied Spectra

The 1D streamwise and wall normal energy spectra of the turbulent flow field of the homogeneous wind farms is illustrated in Figure 5.13 for the cases L, LS^M, LI^M. The spanwise-averaged 1D premultiplied streamwise and wall-normal energy spectra ($k_xE_{uu},\ k_xE_{ww}$) in Figures 5.13b, 5.13c indicate that except for a slight discrepancy at length scales $\lambda_x > D_L$, the u, w energy spectra at and above the hub-height $z = D_L$ of the large turbines remain the same for the cases $L,\ LS^M,\ LI^M$. Interestingly, it is also observed that the wall-normal kinetic energy at length scales $\lambda_x \leq D_L$ is much larger than the streamwise counterpart at these locations, manifesting a potential signature for the downdrafts of energetic structures from the top of the boundary layer. This again, is in agreement with the fact that the power production in large turbines is not influenced (augmented or destructed) by the addition of the smaller-

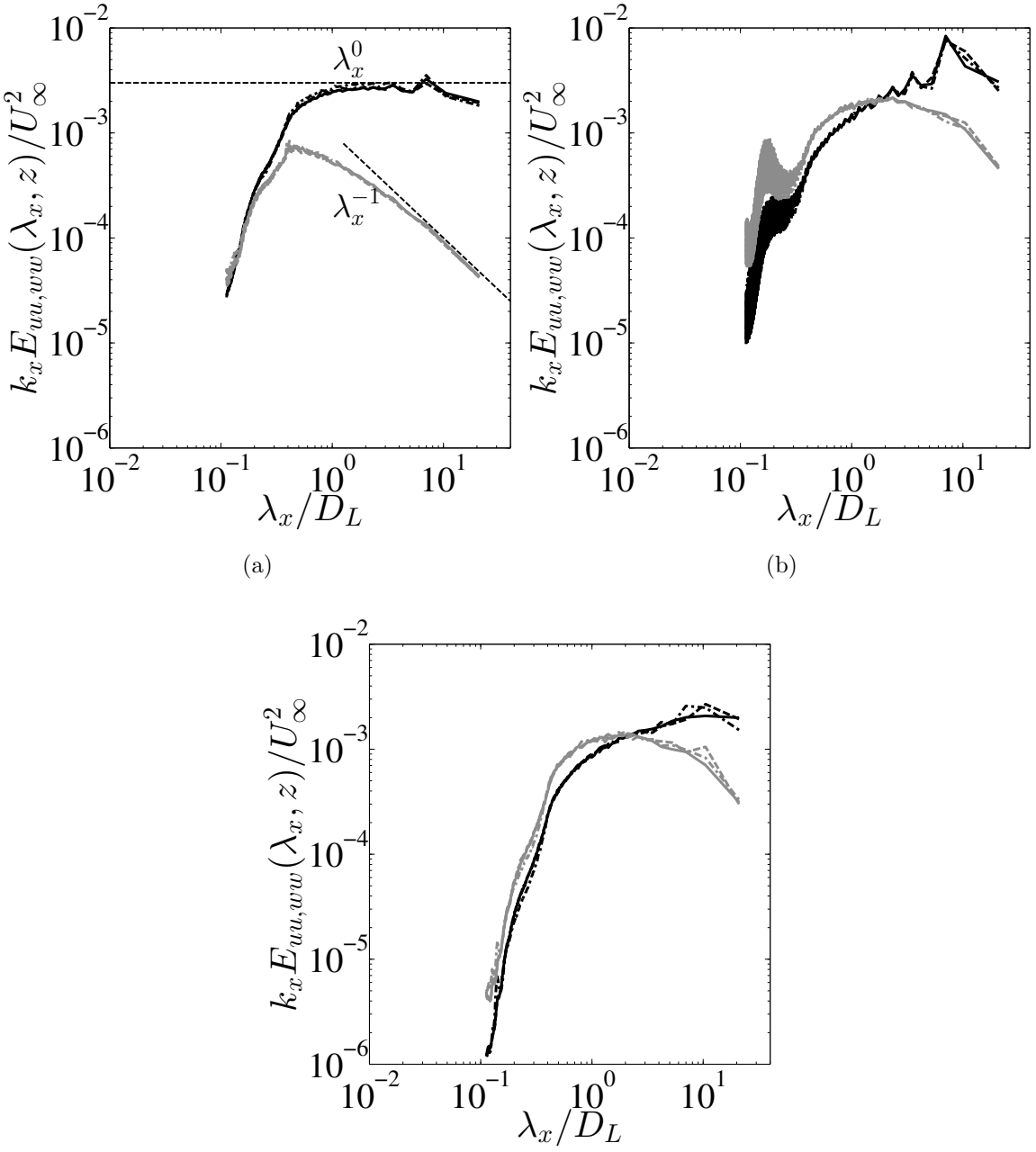

Figure 5.13: 1D premultiplied streamwise and wall normal energy spectra $k_x E_{uu}$ (black), $k_x E_{ww}$ (gray) for cases L (solid), LS^M (dashed), LI^M (chain-dotted). (a) inner layer, $z = 0.075 D_L$ (b) at hub height of large turbines $z = D_L$ (c) outer layer, $z = 2.25 D_L$. λ_x^0, λ_x^{-1} are corresponding near-wall k_x^{-1} and k_x^0 scaling of E_{uu} and E_{ww} spectra in the neutral ABL [157].

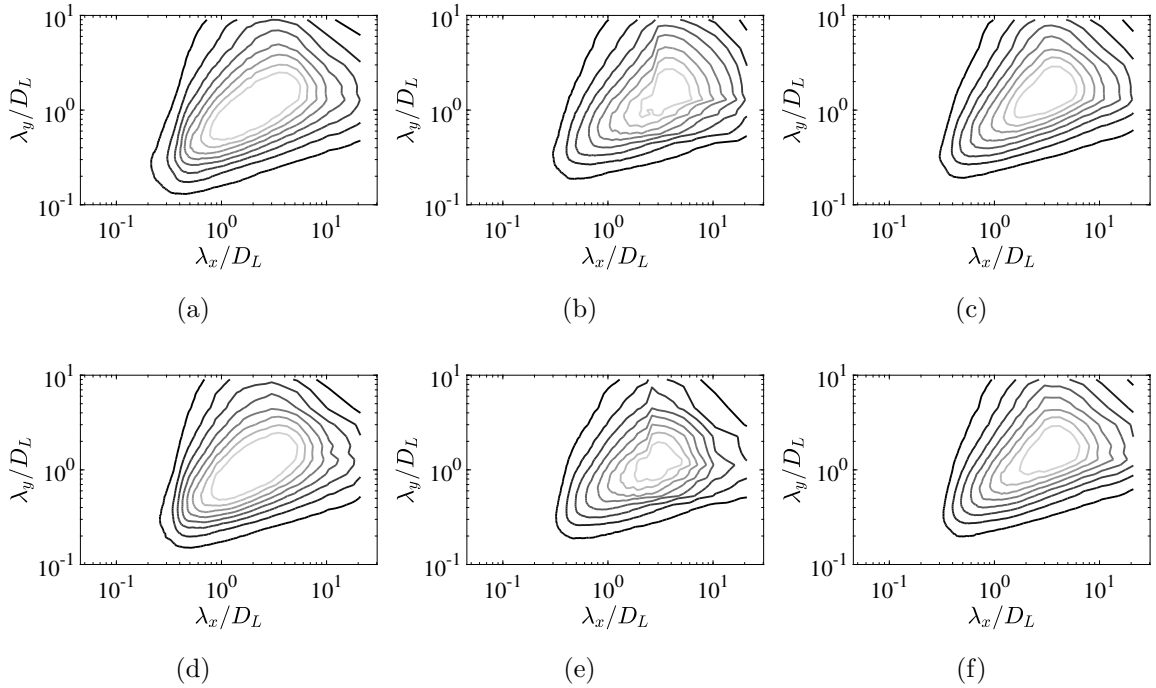

Figure 5.14: 2D premultiplied streamwise energy spectra $k_x k_y E_{uu}/U_\infty^2$ of the large turbines, top row: LS^M; bottom row: L. (a),(d) $z = z_h - D_L/2$. (b), (e) $z = z_h$. (c), (f) $z = z_h + D_L/2$. Contour levels: 10 - 80% of maximum, with the separation of 10% per each contour line, higher energy content is at lighter shades of grey.

scale turbines in the bottom layer in this multiscale HAWT wind farm. Close to the "wall" at $z = 0.075D_L$ (Figure 5.13a), we do not observe any streamwise length scales at which the wall-normal spectra dominates its streamwise counterpart. This indicates the presence of quasi-inviscid 2D "inactive" eddy structures, as observed in our previous work [157]. This phenomenon corroborates towards the evidence of vertical turbulent motions from the outer layer towards the "wall" in cases L, LS^M and LI^M. Whether these vertical motions can be utilized for power, depends on the organization of structures at the top of the rotor of the smaller turbines and discussed further in the 2D spectra.

The experimental studies by Hamilton et al. [19] and Chamorro et al. [22] as well as our recent numerical studies [127] have revealed the contribution of length scales larger than rotor diameter to the wind turbine power. With these observations in

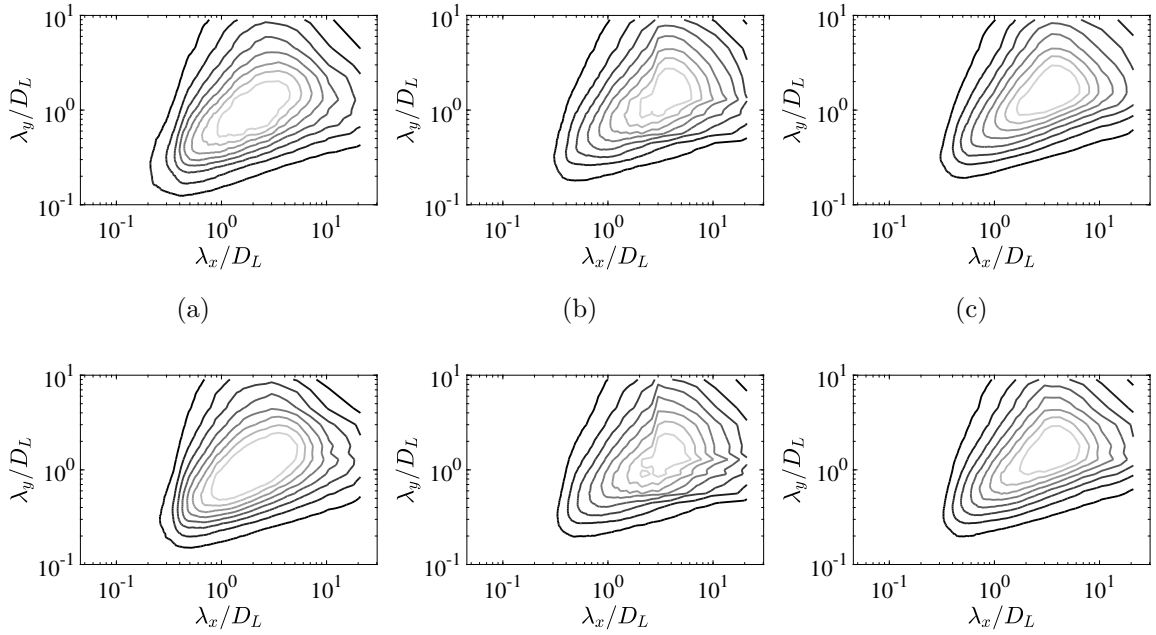

Figure 5.15: 2D premultiplied streamwise energy spectra $k_x k_y E_{uu}/U_\infty^2$ of the large turbines, top row: LI^M; bottom row: L. (a),(d) $z = z_h - D_L/2$. (b), (e) $z = z_h$. (c), (f) $z = z_h + D_L/2$. Contour levels: 10 - 80% of maximum, with the separation of 10% per each contour line, higher energy content is at lighter shades of grey.

mind, we analyze the 2D premultiplied energy spectra of the multiscale as compared to single-scale homogeneous wind farm cases with an emphasis on such energetic eddies with the scales in the range $D - 10D$ in Figures 5.14–5.17.

We first observe that the presence of the small-scale turbines does not significantly affect the spectra and energetic eddies around the large turbines (cases L, LS^M, LI^M), consistent with our previous observations. As seen from the almost identical contours of the streamwise energy spectra of cases L, LS^M, LI^M around the rotor-region of large turbines in Figures 5.14, 5.15, it appears that the presence of small turbines has almost no influence on the larger length scales of the u energy spectra.

On the contrary, the influence of the large turbines is prominently seen in the streamwise energy spectra of the flow around the rotor-swept region of the small/intermediate turbines (See Figures 5.16, 5.17). The small/intermediate turbines in LS^M, LI^M are

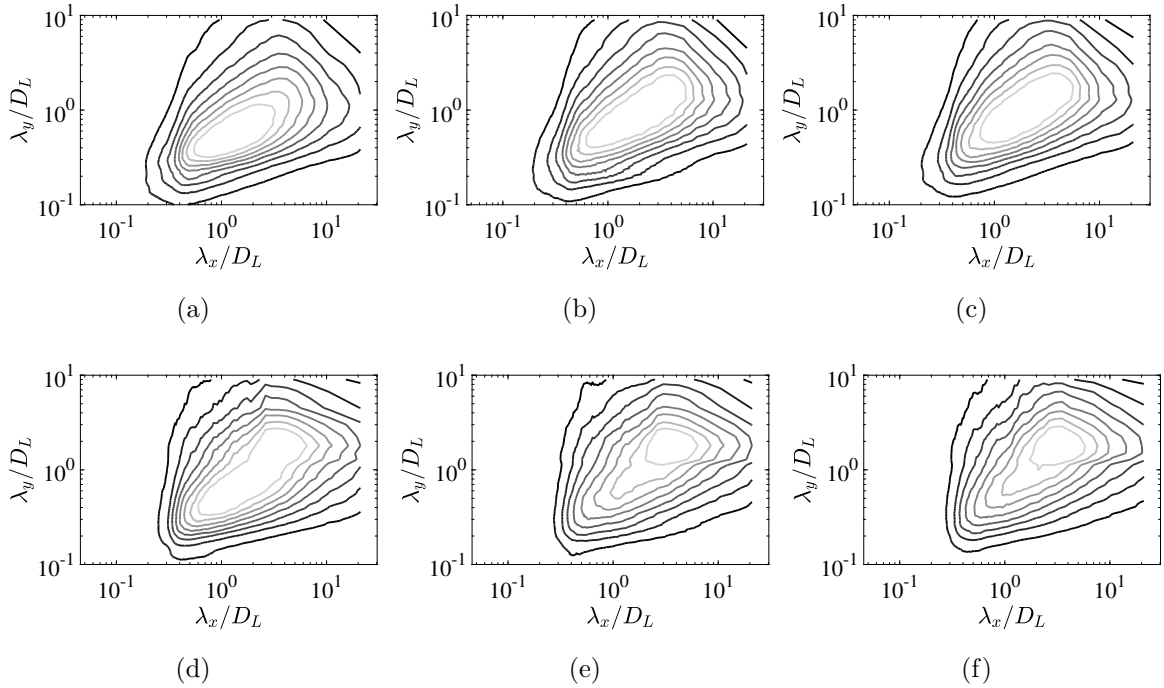

Figure 5.16: 2D premultiplied streamwise energy spectra $k_x k_y E_{uu}/U_\infty^2$ of the small turbines, top row: LS^M; bottom row: S. (a),(d) $z = z_h' - D_S/2$. (b), (e) $z = z_h'$. (c), (f) $z = z_h' + D_S/2$. Contour levels: 10 - 80% of maximum, with the separation of 10% per each contour line, higher energy content is at lighter shades of grey.

separately compared against the turbines in cases S, I respectively, to analyze the effects of their interaction with large turbines. While in the inefficient multiscale wind farm LI^M, we observe energy in the top, $z_h' + D_S/2$ and the bottom $z_h' - D_S/2$ of the rotor tip to be concentrated at larger length scales, $\lambda_x > D_L$, in the efficient wind farm LS^M, we observe a markedly different phenomenon. Even though the energy at the top rotor tip, $z_h' + D_S/2$ is concentrated at larger length scales, $\lambda_x > D_L$, the energy at the bottom rotor tip, $z_h' - D_S/2$ is shifted towards smaller scales at $\lambda_x \approx D_L$, indicating towards an efficient harvesting of large-scale structures for power production via downdraft mechanisms in these wind farms.

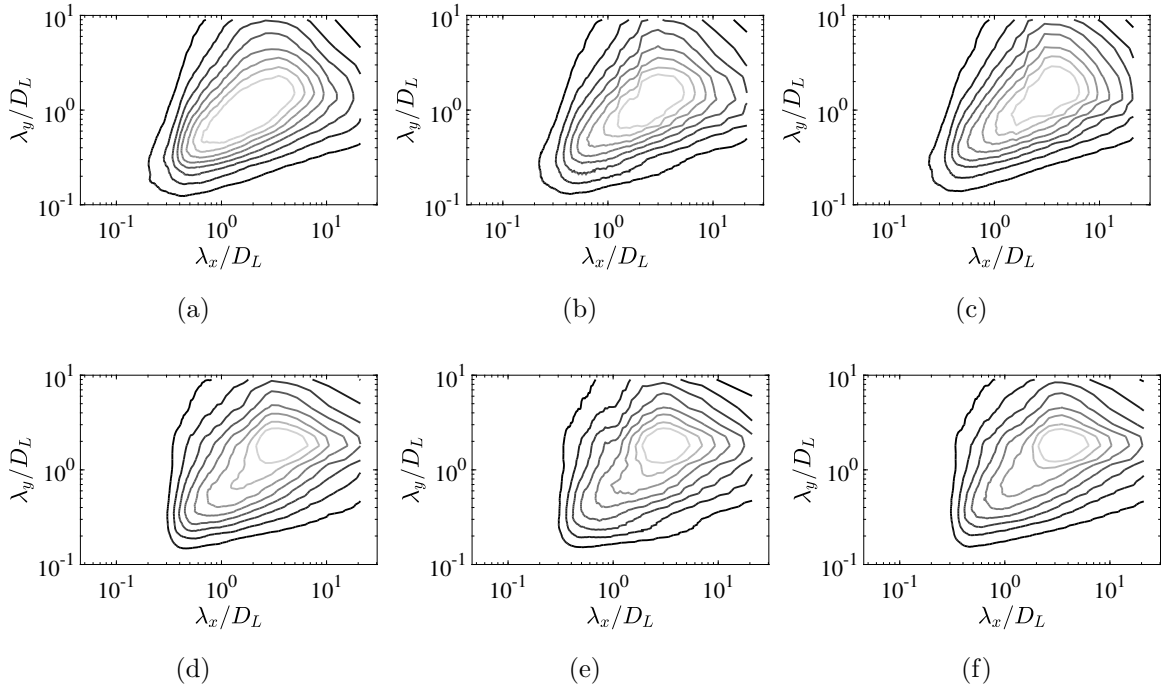

Figure 5.17: 2D premultiplied streamwise energy spectra $k_x k_y E_{uu}/U_\infty^2$ of the small turbines, top row: LI^M; bottom row: I. (a),(d) $z = z_h' - D_S/2$. (b), (e) $z = z_h'$. (c), (f) $z = z_h' + D_S/2$. Contour levels: 10 - 80% of maximum, with the separation of 10% per each contour line, higher energy content is at lighter shades of grey.

5.5 Discussion and Conclusions

In the current study, we present large eddy simulations of a "multiscale" wind farm featuring horizontal axis wind turbines with two different rotor sizes and different hub-heights in a vertically staggered arrangement. Two different multiscale arrangements were investigated: case LS^M with the smaller size turbines located at hub-heights of $0.3D_L$, and case LI^M with the smaller size turbines located at hub-heights of $0.6D_L$; large turbines were kept fixed at a hub-height of D_L in both cases. In the explored configurations, it was found that the small/intermediate turbines turbines had relatively small effect on large wind turbines mean power production. Although it was conjectured that the added smaller size turbines had little contribution to the overall roughness of the farm land, they did increase the turbulent

activity as evidenced by the increase in turbulent stresses, especially in the region corresponding to the bottom part of large turbine rotors, which resulted in a slight increase in power variability in large turbines due to an enhanced turbulence in the case LI^M. On the other hand, large turbines were found to affect the dynamics of the small/intermediate turbines significantly, both through the modulation of the inner region of the turbulent boundary layer via large-scale organized coherent motions in case LS^M, and through the direct interference and wake impingements in case LI^M. In the presented configurations, a roughly 20% of power increase in the overall wind farms has been achieved for a one-to-one ratio of large to small/intermediate wind turbines in a collocated, vertically staggered arrangement (LS^M, LI^M) compared to the baseline case L. In addition to an overall power increase, multiscale wind farms containing small wind turbines at hub-heights of $0.3D_L$ (case LS^M) exhibited an efficient operation with close to zero power losses when compared against a linear sum of their respective single-scale counterparts, resulting from a more efficient operation of small turbines in mutliscale arrays than in homogeneous arrays. The mechanisms responsible for these effects were linked to an increased downdraft of kinetic energy to small turbines by the large-scale structures generated by the presence of large turbines. The evidence of these enhanced downdraft mechanisms were found in the increased levels of wall-normal turbulence fluctuations around small turbines, as well as in the 1D and 2D spectra of the turbulent kinetic energy. To the contrary, the intermediate wind turbines at hub-heights of $0.6D_L$ were found to operate inefficiently and with increased power variability, possibly due to a direct inference of the large turbines on the small turbines through the mixing of wakes that alter the large-scale structure dynamics and suppress similar downdraft mechanisms. We note that the effects that wind turbine towers, both from large turbines and small/intermediate turbines, would have on the multiscale wind farm dynamics, were not investigated in

the current study.

The current study has two potential implications. First, it is instructive to explore whether the overall capacity of the multiscale wind farm in the current HAWT-only configuration can be further increased by increasing the density of the small turbines with respect to the large turbines. Although a total power gain of as much as 23% was already observed in the current study, a potential can be larger. In a recent study of Xie et al. [25], the overall wind farm capacity was increased by 32% in a combined HAWT-VAWT configuration with the ratio of the small VAWT turbines to the large HAWT turbines of twenty to one. Since the small turbines in the current configuration are spaced nearly 23 and 10 diameters apart in streamwise/spanwise directions (scaled with the small turbines diameter), there is potentially a room for increasing their density while still keeping an undesirable wake interference at a low level. This opens up an interesting possibility of optimizing such layouts, with respect to the density and streamwise location of small/intermediate turbines which might result in an overall gain in multiscale wind farm power against the individual linear sum of single scale large and small/intermediate only turbines. Second, the possibility of using large passive disked structures to modulate the flow around the turbines by generating bluff body wakes and organized coherent motions with a similar "shielding" effect, would be of interest.

Chapter 6

LARGE SCALE STRUCTURES IN FINITE SCALE WIND TURBINE ARRAY

6.1 Introduction

In order to optimize power generation and control in wind farms, some of the important questions that needs to be answered is directly linked to understanding the dynamics of *large scale structures* in atmospheric boundary layer, their interaction with the turbines, and how these structures contribute to the power generation in a global scale or localized area of turbines. While recent work by [23, 127, 134] incorporated the studies involving the dynamics of large scale structures in wind farms, they are mostly limited to the wind turbine array boundary layer (WTABL) [5] in the asymptotic limit. WTABL is a conceptualization for studying large wind farms in the infinite limit using periodic boundary conditions in the horizontal direction, thus allowing one to analyze the vertical physics of turbulence as in channel flow or the multiscale phenomenon of the global domain invoking *Fourier transform* [150]. However, WTABL due to its imposition of streamwise periodicity in the statistical sense neglects many important phenomenon owing to the streamwise inhomogeneity, like the "growth of the inner layer" and "wake impingement" effects in the second row of turbines and beyond [5, 134]. These phenomenon are important in the first few rows of turbines in a large wind farm, or if the size of the wind farm is short $\sim O(10D)$ in the dominant wind direction.

Fourier transform in WTABL cases depicts the global modulation of length scales due to the wind turbine in ABL without accounting for the spatial variability of the scales. *Wavelet* transform [158–160] is a methodology that invokes the concept

of length scales similar to a Fourier transform, but without losing the spatial information. Instead of using basis functions $e^{i\boldsymbol{k}\cdot\boldsymbol{x}}$ as in Fourier transform which map a variable from physical $\boldsymbol{x}$ to wavenumber $\boldsymbol{k}$ space, wavelet transform maps a variable from $\boldsymbol{x}$ space to $(\boldsymbol{x}, \boldsymbol{k})$ space with the accuracy of spatial and spectral information following Heisenberg's uncertainty principle [161, 162]. Due to this property of retaining both spatial and spectral information of a signal, wavelet transforms have been used predominantly in the previous literature for analyzing turbulent flows with spatial/temporal inhomogeneity [163, 164]. Orthonormal wavelet spectra [165] were popular in the last two decades and were being used as an alternative to Fourier spectra to understand the spatial variability of length scales, denoising the turbulent spectra and extraction of coherent vorticity of organized structures in turbulent flows [166–169]. The wavelets and their variants were also utilized for understanding the physics of turbulence at production wavenumbers and as a tool for extracting subfilter scale information in LES models [170, 171]. Studies by [172, 173] have used two dimensional wavelet transform to understand the heterogeneity of the spectral content of subgrid scale flux (energy transfer from large to small scales), e.g. the ejection and sweep mechanisms and the spatial variability of spectral budget of turbulent kinetic energy with the motivation of designing subgrid scale models in large eddy simulations. Recently a renewed interest in using wavelets in the field of turbulence has been noted, e.g. the study of large scale modulation of small scales in near wall turbulence [174], understanding the turbulence cascade mechanism [175] and using wavelet filters for understanding coherent structures in isotropic [176] and particle laden turbulence [177]. A compilation of the extensive body of numerical and experimental work involving wavelets in turbulent flows in the past two decades can be found in the review by [178].

We use a wavelet based spectral analysis in order to understand the spatial vari-

ability of length scales that are responsible for the power generated by the turbines in a heterogeneous farm. The choice of our wavelet, in particular using continuous wavelet transform method for capturing a span of continnum wavelength in turbulent flow is guided by the discussion in [178]. Despite some works in understanding the interaction of wind turbines with atmospheric turbulence [179, 180] using temporal signals, the authors are not aware of any studies using the wavelet analysis for understanding the spectral content in heterogeneous convective direction of turbulent flows past wind farms. Furthermore, while many of the previous studies in turbulence with wavelets relied on direct numerical simulation (DNS) data at low to moderate Reynolds number, working with large eddy simulation at the Reynolds number corresponding to atmospheric turbulence, is not known to the authors. In this respect, our present work is the first attempt to understand the spatial variability of the multiscale physics in wind turbine array interacting with atmospheric boundary layer using high-fidelity large eddy simulation (LES). In this chapter, we use our previous knowledge of the large-scale structures in massive wind farms [127, 150] that are well resolved by the grid upto scales smaller than rotor diameter, in order to build on a quantitative model which illustrates how these structures are modulated by a finite scale wind turbine array. Our previous work on periodic wind farms [150], using Fourier analysis, shows the presence of *mean kinetic energy flux*, which essentially acts as downdrafts from the energetic structures above the wind turbine rotor [137] contributing to wind power. These downdrafts were shown to be responsible for increased length scales of the "attached eddies" and "active 3D motions" [77] in near wall turbulence.

However, this understanding is somewhat restricted to periodic boundary conditions, where the effects of heterogeneity of the wind farms in the ABL is not properly understood. In the current study, we use a finite scale wind farm comprising of a 3×3

wind turbine array, where the first row of turbines are intercepted by the atmospheric boundary layer, and the wakes recover to atmospheric turbulence past the third row of turbines. In this respect, the wavelet spectral methods address the shortcomings of their Fourier counterparts used in the previous analysis on periodic wind farms. Using wavelets, the spatial variability of energy spectra and spectral coherence of turbulent fluctuations can be studied for and around each row of the turbines. This study serves as a stepping stone to illustrate the underlying mechanisms for the spatial variability of the organized coherent eddies, that are present around the wind turbine arrays, modulated by the turbines themselves and playing an important role in the power generation.

In the current chapter, we perform a large eddy simulation study of a finite scale wind farm at $Re \sim O(10^{10})$ with the objective to understand the behaviour and modulation of large scale structures (resolved by LES and minimally influenced by subgrid scale viscosity) that contribute to the wind power. The chapter is organized as follows. In the section 6.2 we discuss the computational setup for the large eddy simulation, which generates the high-fidelity LES data for our present analysis. Next, in section 6.3.1 we illustrate the instantaneous snapshots as well as time averaged mean and turbulent statistics of the flow past the turbine array. In section 6.3.2, we present some results of the wavelet energy spectra, validated against its Fourier counterpart, mainly to assess its usefulness in the analysis. Next, in section 6.3.3 we discuss large scale eddies and its spatial variablility through wavelet spectral coherence responsible for power generation. Finally in section 6.4 we conclude. A small appendix for mathematical tools used for the wavelet spectra has been provided in E.

6.2 Computational Setup

The computational domain comprises of a neutral ABL precursor simulation of size $2\pi H \times \pi H \times H$ (H is the ABL thickness, See [157], [150]), the midplane of which ($x = \pi H$) is being spectrally interpolated into the inflow condition [57,181,182] of the wind farm domain. For details of the spectral interpolation technique using stationary overlapping mesh methodology, the reader is referred to [183].

The domain size for the finite scale wind turbine array is $3\pi H \times \pi H \times H$, with the statistically stationary ABL simulation serving as an initial condition to the wind turbine array. Consequently, a seperate ABL simulation at that domain length has been run with a uniform discretization of $40 \times 24 \times 20$ elements to generate realistic initial conditions for turbine array simulations. The domain size rescaled in terms of turbine rotor radius (diameter) is given as $94R \times 32R \times 10R$ ($47D \times 16D \times 5D$), where $R = 0.1H$ is the radius of each turbine-rotor ($D = 2R$ is turbine-rotor diameter). The 9 turbine rotors have been arranged in a 3×3 matrix arrangement in the computational domain. The design of the computational domain and the arrangement of different turbines are done in concordance with the experimental set up as in [184].

The first row of 3 rotors are placed at $\pi H/2$ or $7.85D$ distance from the inflow boundary. The streamwise distance between the turbines is $7D$, while the spanwise distance is $3D$. The hub-height of all the rotors have been set at D. These dimensions are designed to conform the experimental set-up as in [184]. Two different stabilization of outflow boundaries have been utilized, namely the the sponge layer and the stabilized natural outflow boundary condition (See Chapter 2 Section 2.5 and Appendix B). For the sponge boundary condition, the physical streamwise extent of the domain is $38D$, after which the non-reflective sponge layer initiates with a coarse 2 element stretch to $x = 47D$ coupled with a simple outflow boundary condition (See

Equation B.5). Consequently, the wake of last row of 3 sets of rotors has a capacity to convect a physical distance of $16D$ which is more than twice the inter-rotor streamwise spacing. However, for implementing stabilized natural boundary condition [59], it was observed in the previous literature as in [34] that extended domains are still required such that the stabilized boundary conditions do not affect eddies upstream in the flow. A comparison of the two different outflow boundary conditions is documented in [181], which shows that only minor discrepancies in the mean velocity profile can be seen in the outer layer, far away from the wind turbine wakes. However, since the stabilized natural boundary conditions does not contain regions of artificial diffusion unlike the sponge layer, is expected to genarate physically consistent results and have been subseuqently used in all our simulations using inflow outflow. The turbulent inflow conditions are implemented as a stationary overlapping mesh methodology [183], where both the simulations are run simultaneously with the inflow condition from ABL simulation being generated by spectrally interpolating the mid-plane of the ABL domain (yz plane at $x = \pi H$) to the inflow boundary of the computational domain of turbine array (direct memory copies). Since, the spectral interpolation is done in parallel using Message Passing Interface (MPI) it removes the I/O overhead significantly in the computation.

The current spectral element grid with 1.28×10^7 grid points has a capability of capturing length scales $\sim 0.3D$ far away from the turbine wakes, while smallest scales close to the turbine rotors is $\lesssim 0.1D$ (See Table 6.1). The resolved length scales is defined as twice the resolved grid resolution according to the Nyquist frequency criterion. Please note, that the definition of grid resolution only takes into consideration the variability in the size of spectral elements and not the variability of the GLL node clustering within an element similar to the discussion in Appendix D. After achieving statistical stationarity, the simulation has been carried out for 600

flow through times ($T_e = 3\pi H/U_\infty$) to collect statistics (Snapshots are placed $1/4T_e$ apart) ensuring enough decorrelated snapshots for the large length scale comparable to the streamwise boundary length. All our spectral results are shown till the smallest length scale of $0.4D$, which is slightly greater than the minimum resolved scale far away from the turbines.

Case	Geometry	$N_x^e \times N_y^e \times N_z^e$	Grid points
Sponge Layer	$3\pi H \times \pi H \times H$	$42 \times 32 \times 24$	1.122×10^7
Stabilized NBC (Dong et. al)	$3\pi H \times \pi H \times H$	$48 \times 32 \times 24$	1.281×10^7

Table 6.1: Numerical setup for wind turbine array computational domain for two different outflow boundaries. 8 GLL nodes has been used per cartesian direction

Direction	$\max \Delta_\eta/p$	$\min \Delta_\eta/p$	$\overline{\Delta}_\eta/p$
x	0.1683	0.0238	0.1402
y	0.1658	0.0179	0.0701
z	0.0471	0.0179	0.0298

Table 6.2: Maximum, minimum and average grid size of 3×3 wind turbine array.

6.3 Results

6.3.1 Mean and Turbulent Statistics

In this section we discuss about the instantaneous snapshots and temporally averaged flow variables in the flow past the wind farms. The instantaneous snapshots of velocity magnitude, vertical velocity and the product of wall normal and streamwise velocity fluctuations (temporal average – kinematic shear) are documented in

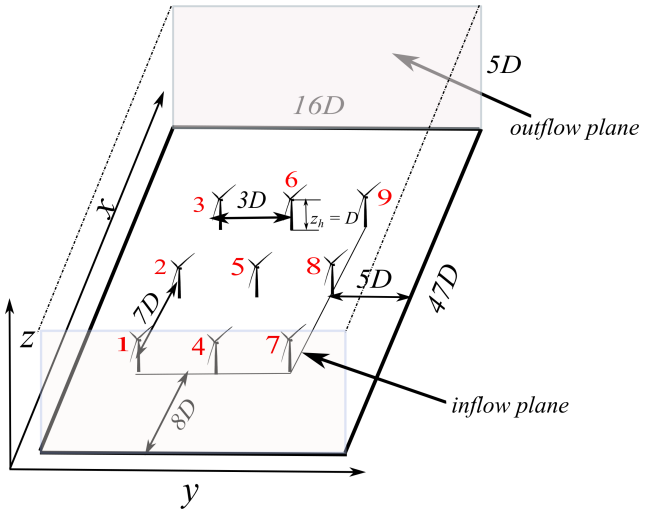

Figure 6.1: Computational domain of Wind Turbine Array simulations with inflow-outflow condition. Numbers 1–9 in red indicate the turbine number.

Figure 6.2. The velocity magnitude in Figure 6.2a illustrates the presence of wake meandering effects. Interesting to note, that the vertical velocity structures (Figure 6.2b) are finer ($\sim D$) at the hub-height compared to the total velocity magnitude dominated by the streamwise velocity structure. This phenomenon is further observed in the wavelet spectral analysis in the later sections. The instantaneous snapshot of instantaneous turbulent kinetic energy $\frac{1}{2}(u'^2 + v'^2 + w'^2)$ and product of streamwise, wall-normal velocity fluctuations $u'w'$ reveal large scale energetic bulges close to the top-tip of the rotor which were not seen in the bottom tip of the rotor. The contour plots of the mean and turbulent statistics can be found in Figures 6.3, 6.4. The mean velocity contours indicate that the wake velocity deficits increase in the subsequent rows after the first, due to the effects of wake impingement from the previous rows. This is further reflected in the second order statistics such as turbulent kinetic energy, mean kinetic energy flux, turbulence production, which manifest the growth of the inner layer and the wake-impingement effects, accounting for an increased "turbulent activity" in the second and third row of turbines. Figure 6.5 illustrates the velocity profile at different streamwise stations at three different rows of the turbines. It

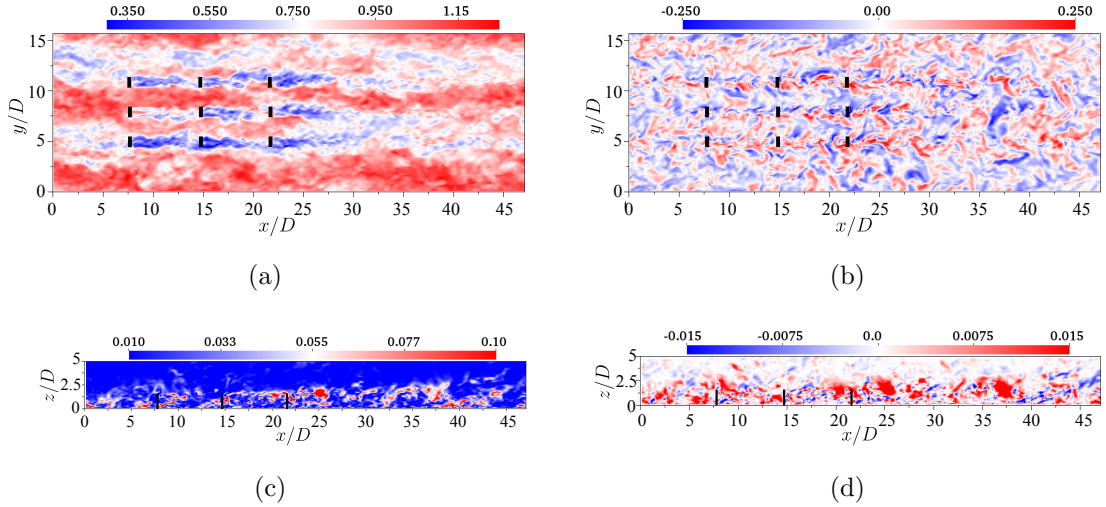

Figure 6.2: Instantaneous temporal snapshot of (a) velocity magnitude $\sqrt{u^2+v^2+w^2}$, (b) vertical velocity w in xy plane, at $z = z_h$, hub-height. (c) instantaneous turbulent kinetic energy $\frac{1}{2}(u'^2+v'^2+w'^2)$ (d) product of streamwise and wall normal velocity fluctuations, $u'w'$ in xz plane at $y = 7.85D$, middle column of turbines. Normalization velocity scale: U_∞

clearly indicates that the wake recovery in the first row is quicker and quite different than that in the subsequent rows. Further more, beyond $z = 2.5D$, no significant discrepancies in the velocity profile at different streamwise stations can be noted, indicating that the height of the wind turbine inner layer is $\sim 2.5D$.

The wake-deficit in the wind turbine arrays can be defined as $\delta U(x,y,z) = U(z) - U_w(x,y,z)$, where U is the mean streamwise velocity at the inflow, and U_w streamwise "wake" velocity downstream of the turbines. The velocity deficit is normalized by the maximum of the velocity deficit δU_{max} . The radial distance r from the centre of the turbine rotor (hub height location) has been normalized by the distance $r_{1/2}$, which can be defined as the distance at which the velocity deficit $\delta U = 1/2\delta U_{max}(x)$.

$$f(\xi) = \frac{\delta U(x,y,z)}{\delta U_{max}(x)} \tag{6.1}$$

where $f(\xi)$ is the self-similar shape function, and ξ is the similarity radial coordinate. Using a gaussian form, $f(\xi) = \exp^{-a\xi^2}$, we observe that at $\xi = 1$, $f(1) = 1/2$,

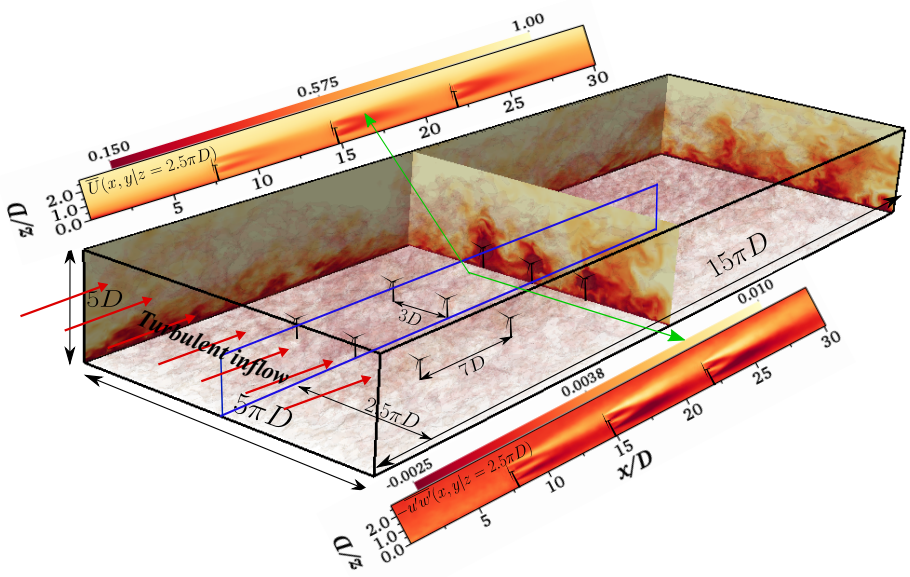

Figure 6.3: (a) Computational domain of wind turbine array showing flow structures. Velocity magnitude $\sqrt{u^2+v^2+w^2}/U_\infty$ snapshots at plane $x = 21.85D$ (third row of turbines), $x = 47.12D$ (outflow) and $y = 0$. Mean and turbulent statistics taken at a plane $y = 2.5\pi D$. Red arrows: turbulent inflow from precursor ABL.

which leads to $a = \log 2$. If the similarity scaling law holds good, with such normalizations, it is expected that the normalized velocity deficit profile would collapse into a single curve in ξ coordinate.

From Figure 6.6, it is observed that while the first row manifesting an interception with atmospheric turbulence does not collapse well with the gaussian form of $f(\xi) = \exp(-\xi^2 \log 2)$, the subsequent rows (Row 2 and 3) intercepting the wakes from the previous rows illustrate an approximate collapse with the gaussian form, and thus the scale similarity would approximately hold for the subsequent rows.

POD modes

For such inhomogeneous flows, proper orthogonal decomposition (POD) [24,137,185, 186] serves as an important tool to identify large flow structures ranked according to the turbulent kinetic energy (tke) content. Even though, POD is not the focus of the

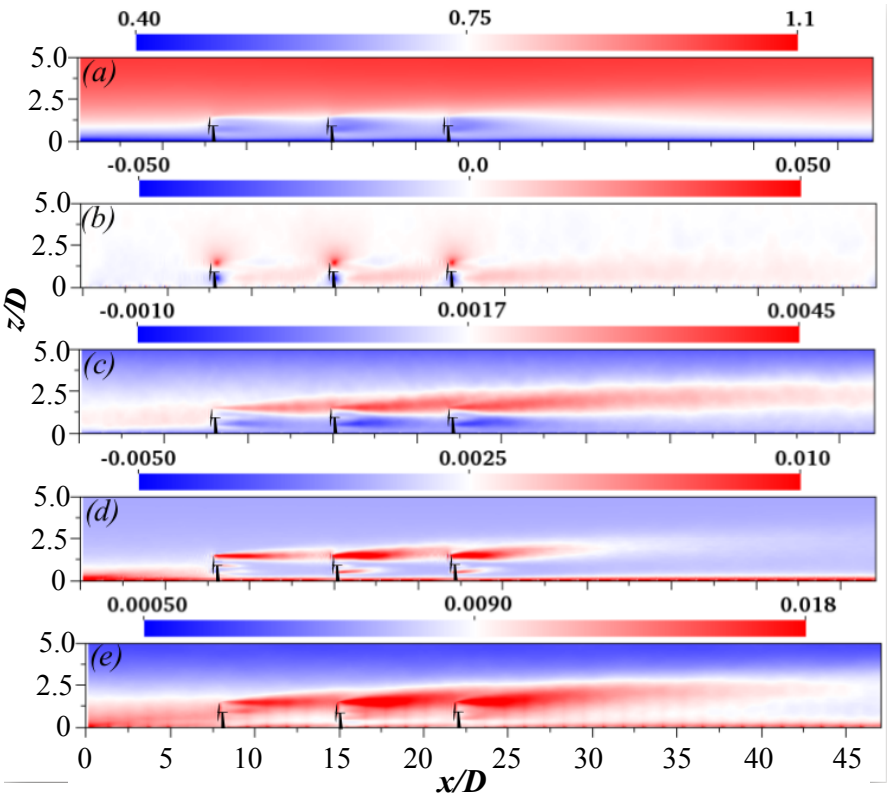

Figure 6.4: xz plane of temporally and spanwise averaged normalized mean and turbulent statistics. (a) streamwise velocity U (b) wall-normal velocity W (c) mean kinetic energy flux $-\overline{u_i' u_j'}\bar{U}_i$ (d) dominant term of turbulence production $-\overline{u'w'}\partial\bar{U}/\partial z$ (e) Turbulent kinetic energy $1/2\overline{u_i' u_i'}$. Normalization velocity U_∞ , normalization distance D.

chapter, some results from our previous work are illustrated in order to understand the large scale dynamics predominant in wind farm arrays and thus serves as a first step towards understanding their spatial variability subsequently analysed using wavelet decomposition. The POD modal picture (Figure 6.7) reveals the roller-modes type of structures with counter rotating eddies with diameters $> 10D$ as observed in [134]. The figure is adapted and replotted from our previous work in [137]. The calculation of the three dimensional POD modes is performed using a method of snapshots along the lines of Sirovich [185] and the reader is referred to Appendix F for further details. For the POD study conducted in [137], we obtained convergence for the first 5 POD modes, for roughly 2000 snapshots separated 1/4 flow through

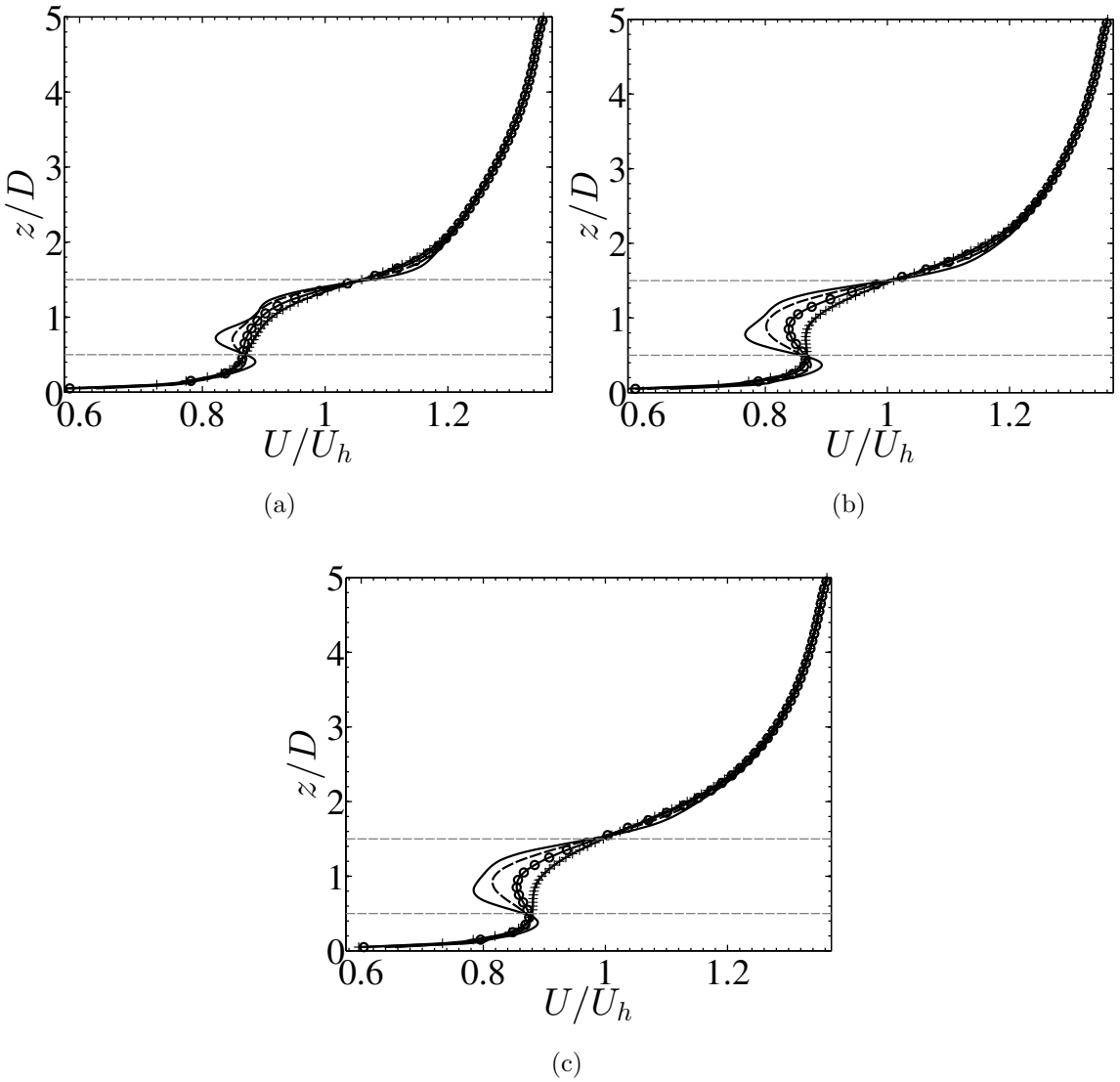

(a) (b)

(c)

Figure 6.5: Spanwise averaged mean streamwise velocity profile at different streamwise location. (a) First row, (b) Second row, (c) Third row. Solid – $x = x_t + D$, Dashed – $x = x_t + 2D$, $\circ$ – $x = x_t + 3D$, $+$ – $x = x_t + 4D$. x_t is the streamwise location of the corresponding turbine rows. Dashed line – rotor region.

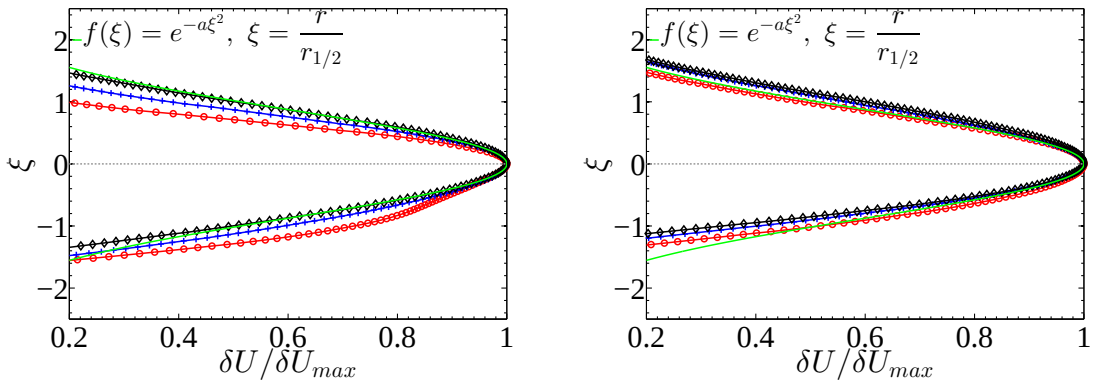

(a)

(b)

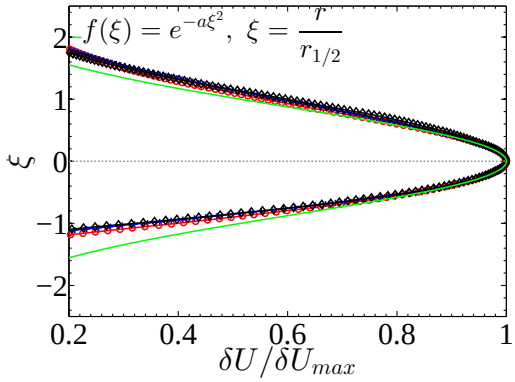

(c)

Figure 6.6: Normalized wake velocity deficits vs the normalized radial distance from the turbine rotor center. $a = \log 2$ (a) First row, (b) Second row, (c) Third row. Red $\circ$ – $x = x_t + 2D$, Blue $+$ – $x = x_t + 3D$, Black $\diamond$ – $x = x_t + 4D$. x_t is the streamwise location of the corresponding turbine rows.

times apart. The first 2 POD modes clearly reveal regions of energetic high velocity structures around the turbine rotor region, associated with downdraft or negative vertical velocity component. This indicates that even for finite scale wind farms, the "downdraft" mechanism would play an important role in the power generation of wind farms. In infinite wind farms, the flux difference of the mean kinetic energy entrainment at the top and bottom rotor tip , i.e. $-\overline{u_i' u_j'}\bar{U}_i\Big|_{z_h - D/2}^{z_h + D/2}$ is known to be a significant contributor to power. In finite scale wind farms, due to the growth of

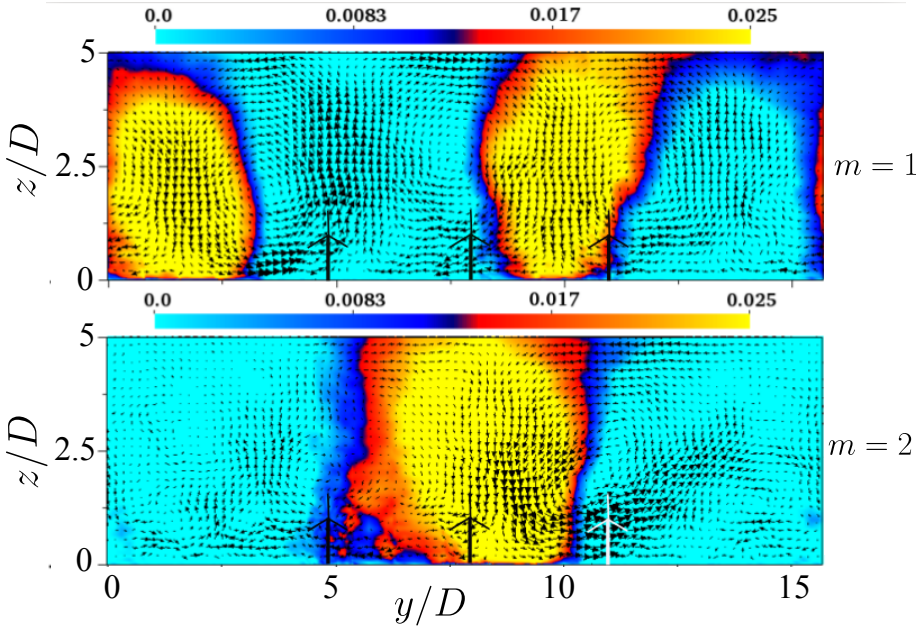

Figure 6.7: yz ($x = \pi H$, first row of turbines) plane of the streamwise u POD modes $\phi_m^1\sqrt{\Lambda_m}/U_\infty$ (contour) and spanwise, wall normal i.e., v, w POD modes $\phi_m^2\sqrt{\lambda_m}/U_\infty$, $\phi_m^3\sqrt{\Lambda_m}/U_\infty$ (in-plane vector) for 2 different modes, maximizing turbulent kinetic energy $1/2\overline{u_i'u_i'}$. Λ_m – m^{th} eigenvalue of the POD mode.

the inner layer and wake impingements, the MKE flux is not the sole contributor to the farm power, but still plays a major role. Table 6.3 shows the modal contribution of turbulent kinetic energy λ_m and the mean kinetic energy flux $-\lambda_m\phi_m^i\phi_m^j\overline{U}_i$ for a few modes, $m \leq 10$. This clearly indicates that a significant fraction of the MKE flux is captured by far less number of modes than required for a similar percentage of turbulent kinetic energy, for which the POD modes are optimized in the least squares sense along the lines of [134]. Table 6.3 further illustrates the significance of roller modes ($m = 1, 2$) in being instrumental to the MKE flux generation, the entrainment of which contributes to turbine power.

6.3.2 Wavelet Spectra – Cascades and Validation with Fourier Spectra

The wavelet coefficients (using analytical Morlet wavelet) of a spatially varying velocity across the streamwise direction at $y = 7.85D$, $z = z_h,\ z_h + D/2$ have been

POD mode	Contribution to TKE (%)	Contribution to MKE flux difference (%)
1	6.13	12.88
2	3.93	4.05
4	1.67	2.76
5	0.78	1.18
9	0.62	0.54

Table 6.3: Contribution to turbulent kinetic energy $1/2\overline{u_i' u_i'}$ and mean kinetic energy flux difference $-\overline{u_i' u_j'}\bar{U}_i\Big|_{z_h - D/2}^{z_h + D/2}$ at different POD modes.

documented here. While figure 6.8 illustrates the real part of the instantaneous u, w wavelet coefficients at $z = 7.85D$ (middle coumn of the rotor) the wavelet spectra of the turbulent kinetic energy is manifested in Figure 6.9. It is intriguing to note that Figure 6.8 displays the fork like structures reminiscent of the turbulence cascade with the large eddies breaking down to smaller ones as was observed in a similar work by Farge [178] and Bassene et al. [175] for isotropic turbulence.

An estimation of the length scales at which the wavelet coefficients at specific wavelengths are completely decorrelated illustrates the fidelity of the wavelet transform for our current wind turbine array domain. For this, an autocorrelation of the absolute value of the wavelet transform coefficients $\mathcal{W}[u](\lambda_x, x),\ \mathcal{W}[w](\lambda_x, x)$ of u and w velocities have been performed (Figure 6.10). The autocorrelations, $\rho_{uu}(\Delta_x; \lambda_x),\ \rho_{ww}(\Delta_x; \lambda_x)$ are normalized by their zero-lagged value, $\Delta_x = 0$, which are essentially the variance of the wavelet transformed cofficients $\mathcal{W}[u](\lambda_x, x)$, $\mathcal{W}[w](\lambda_x, x)$. This ensures that $\rho_{uu}(\Delta_x = 0; \lambda_x) = \rho_{ww}(\Delta_x = 0; \lambda_x) = 1$. The auto-correlation value indicates that at length scales of $5 - 10D$ considered for investigation in the current chapter, the spatial signal is decorrelated at $\sim 20D$, even though slight negative correlations might exist at larger separations. It can also be seen that the correlation

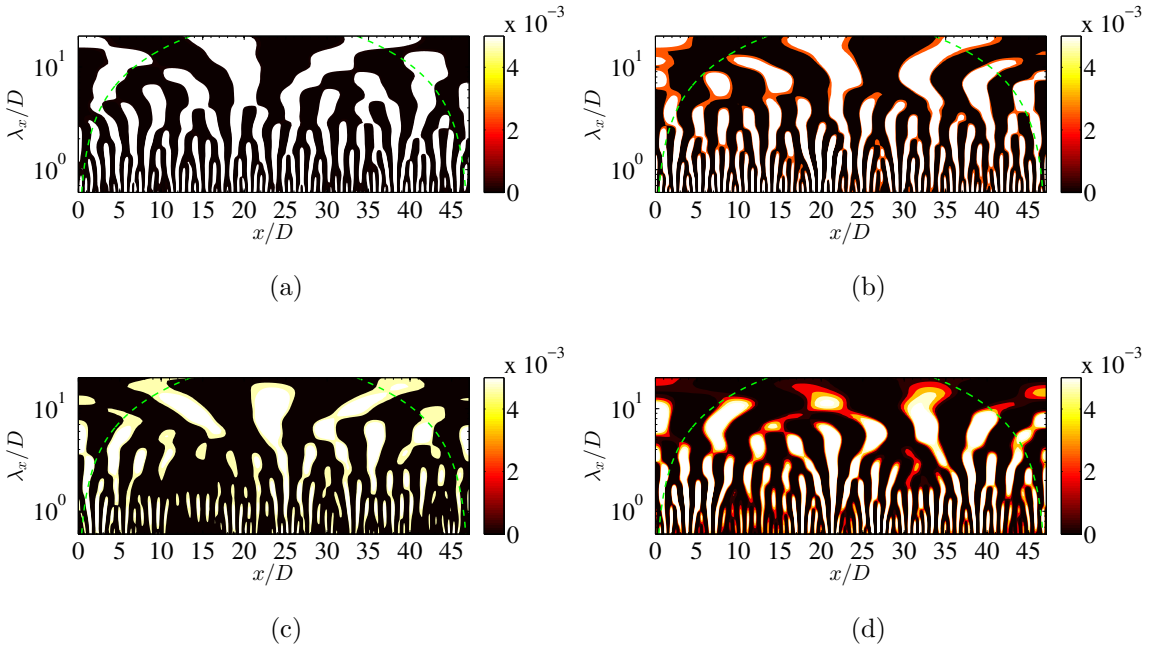

Figure 6.8: Instantaneous real part of wavelet transform of u, w velocities, (a), (c) $\mathbb{R}[\mathcal{W}[u](k_x, x)]$, & (b), (d) $\mathbb{R}[\mathcal{W}[w](k_x, x)]$ at a typical time snapshot using Morlet wavelet. First row – $z = z_h$, hub-height; Second row – $z = z_h + D/2$, top-tip of the rotor. Spanwise location, $y = 7.85D$, the second column of turbines.

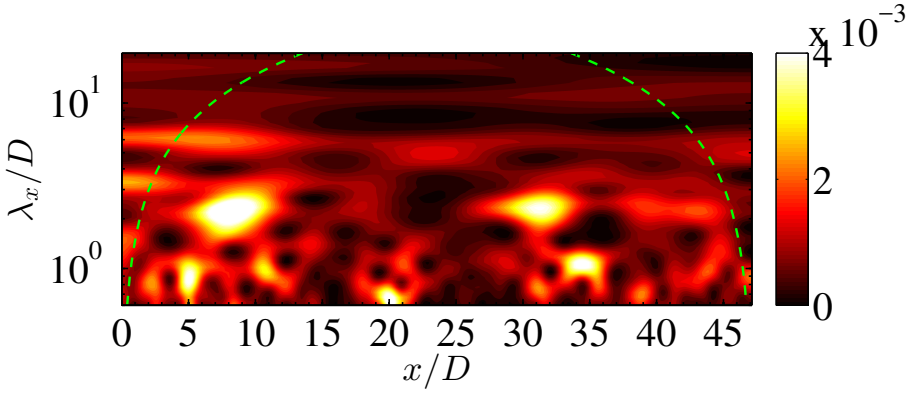

Figure 6.9: Kinetic energy in the spectral space obtained from wavelet transformed velocities $\mathcal{W}[u_i](k_x, x)$, at hub height $z = z_h$ and spanwise location $y = 7.85D$ (middle column of turbines).

function manifests multiple peaks (of much smaller magnitude) for $\lambda_x \sim 0.6D, 3D$ at $z = z_h + D/2$ indicative of spatial organization even at smaller scales at the top tip of the rotor.

Figures 6.11, 6.12 and illustrate a validation of the streamwise integrated wavelet spectra (as a function of streamwise wavelength, λ_x) which essentially acts as a band pass filtered Fourier spectra (Appendix E) over the whole range of calculated wavelengths. Note, in an analogous fashion, the wavelet energy spectra for Figure 6.13 is spanwise integrated and documented as a variation of spanwise wavelength, λ_y. Figure 6.11a– 6.11d manifest the streamwise u energy spectra vs the streamwise wavelength, λ_x for four different wall locations, near wall at $z = 0.125D$ as well as the bottom tip, hub-height and top tip in the rotor region, $z_h,\ z = z_h \pm D/2$. The bottom tip ($z = z_h - D/2$) of the rotor still lies in the inner layer of ABL containing large organized structures, while the hub-height ($z = z_h$) and the top-tip ($z = z_h + D/2$) of the rotor lies in the outer layer containing incoherent background turbulence. The comparison with Fourier spectra has been performed against the Morse, Morlet and the syncrosqueezed transform of the Morlet wavelet. In general, the Morse and Morlet wavelet compares fairly against their Fourier counterpart, except perhaps at the smallest resolved scales ($\sim 0.6D$), where the Morlet [158, 187] performs better owing to the fact that it has more higher order vanishing moments than the Morse [162,188] counterpart (See Appendix E). This observation is inline with Perrier et al. [189], who observed that to properly capture a scaling law of the energy spectra $E(k) \propto k^{-\beta}$ (k is the wavenumber), the number of vanishing moments of the wavelet (Appendix E) $n > (\beta - 1)/2$. Thus for the $-5/3$ law only two vanishing moments would be required to capture the Kolomogorov scale. Note, however that since the wavelet spectra are band-pass filtered Fourier spectra the peaks in the Fourier spectra observed close to the smallest resolved scales have been smoothed out in their Morse/Morlet wavelet

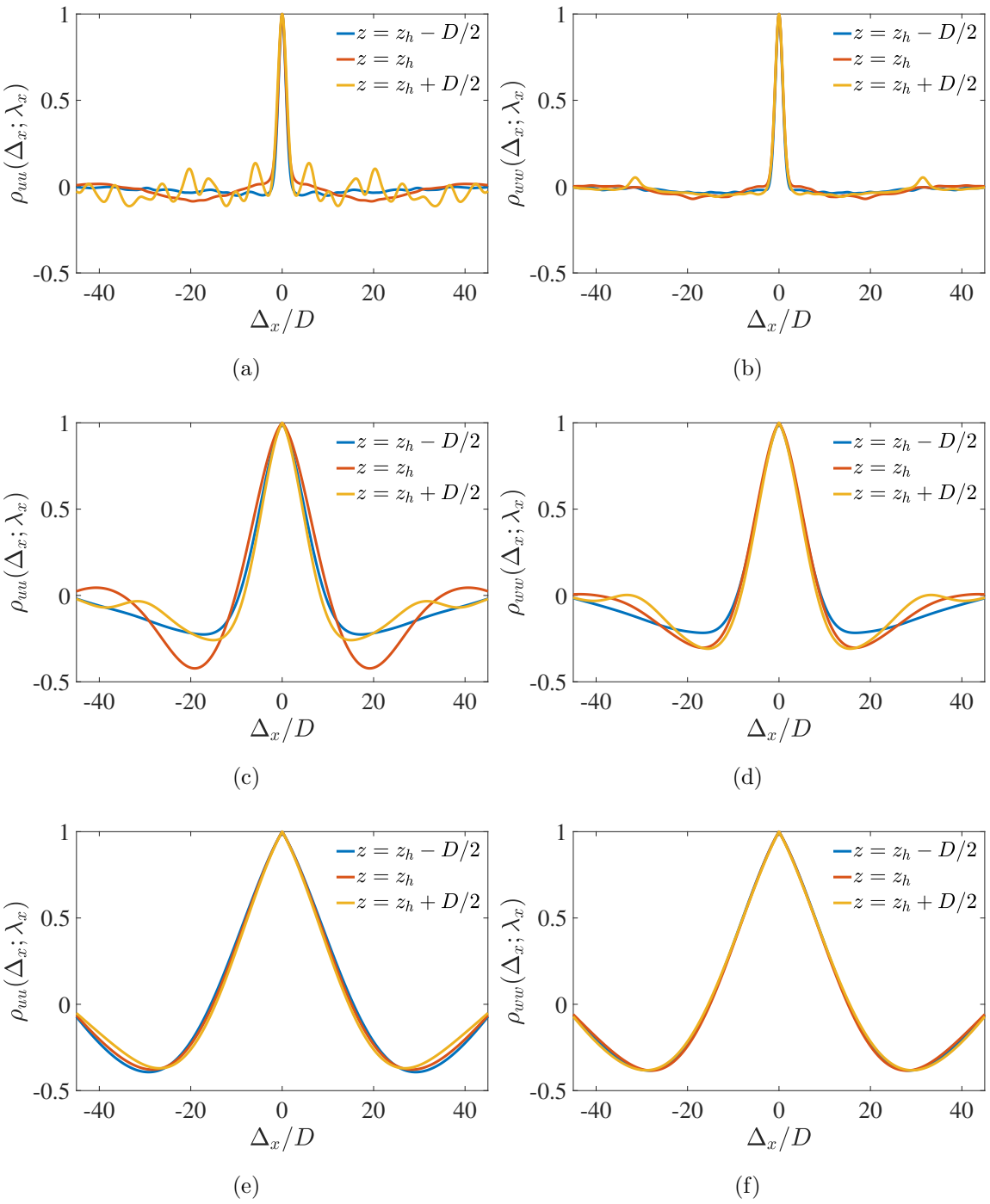

Figure 6.10: Streamwise autocorrelation $\rho_{\xi\xi}(\Delta_x;\lambda_x)$ of the wavelet transform of u (left), w (right) velocities. (a), (b) – $\lambda_x = 0.6D$, (c), (d) – $\lambda_x = 3D$, (e),(f) – $\lambda_x = 7D$.

counterpart. All the wavelet spectra and the Fourier spectra manifests prominent λ_x^0 scaling law near wall, as well as the Kolomogorov scaling law, $\lambda_x^{2/3}$ corresponding to turbulent cascade. In general figures 6.11 – 6.13, serve as a way to validate the wavelet algorithms by comparing against the scaling laws and amplitudes of the Fourier spectra. The syncrosqueezed transform of the morlet wavelet [190,191] was also performed in the current study to reduce the smearing out effects at different wavelengths by partially inverting the continuous wavelet transform of the signal over different bands of wavelengths and ignoring the other bands. Such transforms are known to identify events with very close wavelengths [192] and even singularity as such. We observe 2 unphysical peaks/singularities comparable to the domain size in the synchrosqueezed transform (both the streamwise integrated as well as the streamwise varying spectra). The reason lies in the definition of the synchrosqueezed transform as noted by [190]. The synchrosqueezed transform is better at capturing events characterized by wavelengths that are distinctly separate from one another [192]. Even though the synchrosqueezed transform does capture the peaks corresponding to the inter-turbine distances ($7D$, seen in Fourier spectra) that are smeared out in their wavelet transformed counter-part, two peaks larger that the inter-turbine distances ($14D,\ 21D$) are also observed. A similar argument can be proposed for the spanwise integrated spectra where subharmonics corresponding to twice and thrice of the length scales corresponding to interturbine distance $\lambda_y = 3D$ have been documented. This may be attributed to the "beating phenomenon" at the contiguously present larger scales which [192] noted, but further investigation is necessary to justify the hypothesis.

For completeness, Figure 6.14 shows a comparison of the wavelet energy spectra depicted in the three turbine rows obtained from the large eddy simulation of a finite size 3×3 wind turbine array (Chapter 6) using different wavelets, e.g., Morse, Morlet and its synchrosqueezed transform. The figure clearly illustrates that smaller scales

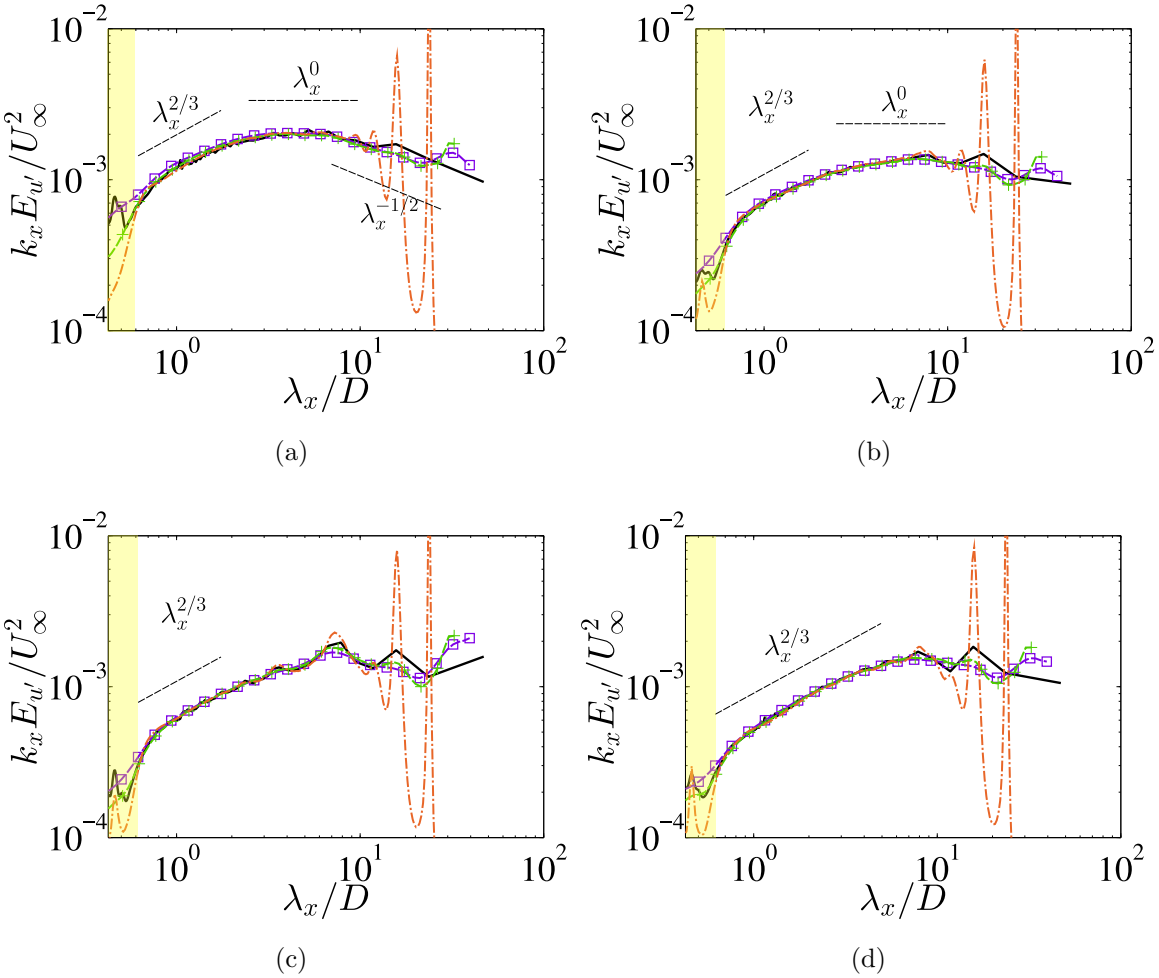

Figure 6.11: One dimensional spanwise and temporally averaged u energy spectra vs streamwise wavenumber λ_x at (a) $z = 0.125D$, inner layer; (b) $z = z_h - D/2$, bottom tip of the rotor; (c) $z = z_h$, hub-height of the rotor (d) $z = z_h + D/2$, top tip of the rotor. Solid black – premultipled Fourier spectra, $k_x E_{u'}(\lambda_x)/U_\infty^2$. Dashed violet □ – Morse wavelet spectra, Solid green + – Morlet wavelet spectra, $k_x \widetilde{E}_{u'}(\lambda_x)/U_\infty^2$. Chain dotted orange – Syncrosqueezed transform of Morlet wavelet spectra. All wavelet spectra integrated over streamwise domain.

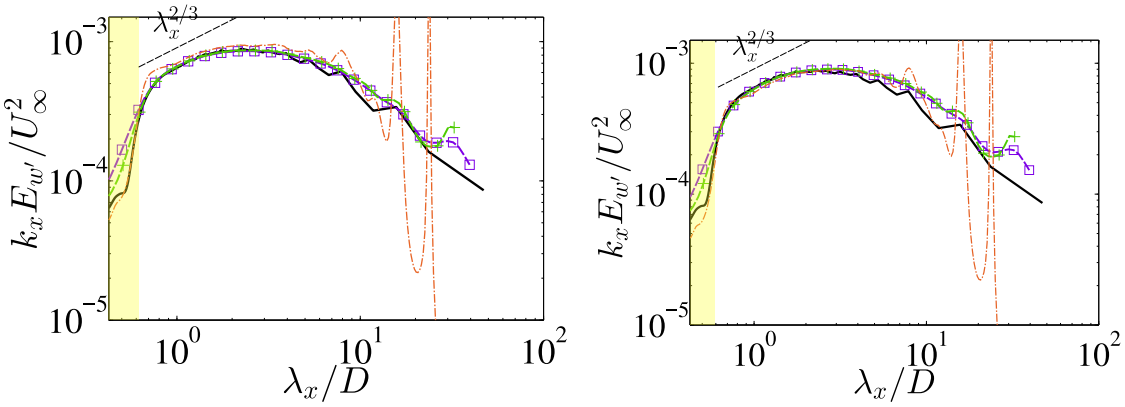

(a) (b)

Figure 6.12: One dimensional spanwise and temporally averaged w energy spectra vs streamwise wavelength λ_x Locations – (a) hub-height, $z = z_h$, (b) top tip of the rotor, $z = z_h + D/2$. Solid black – premultipled Fourier spectra, $k_x E_{w'}(\lambda_x)/U_\infty^2$. Dashed violet □ – Morse wavelet spectra, Solid green + – Morlet wavelet spectra, $k_x \widetilde{E}_{w'}(\lambda_x)/U_\infty^2$. Chain dotted orange – Syncrosqueezed transform of Morlet wavelet spectra. All wavelet spectra integrated over the streamwise domain.

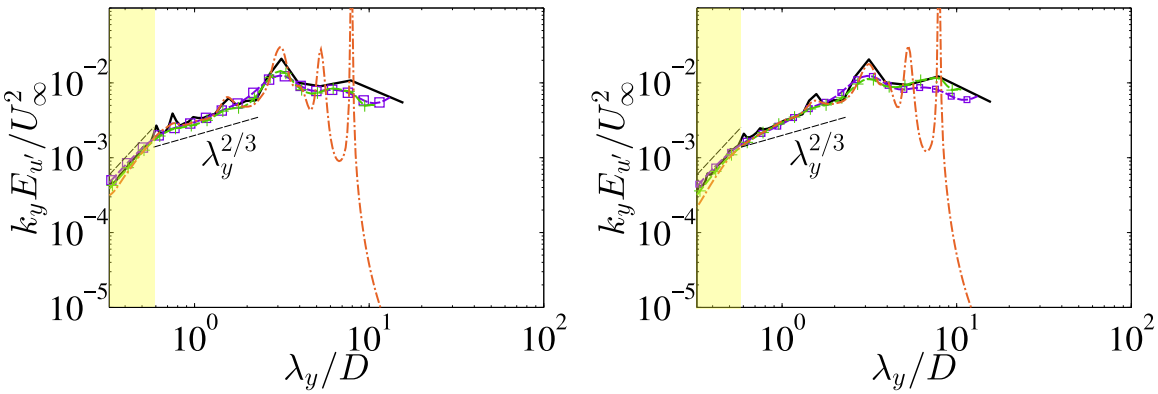

(a) (b)

Figure 6.13: One dimensional streamwise and temporally averaged u energy spectra vs spanwise wavelength λ_y. Locations – (a) hub-height, $z = z_h$, (b), (d) top tip of the rotor, $z = z_h + D/2$. Solid black – premultipled Fourier spectra, $k_y E_{u'}(\lambda_y)/U_\infty^2$.Dashed violet □ – Morse wavelet spectra, Solid green + – Morlet wavelet spectra, $k_y \widetilde{E}_{u'}(\lambda_y)/U_\infty^2$. Chain dotted orange – Syncrosqueezed transform of Morlet wavelet spectra. All wavelet spectra integrated over spanwise domain.

less than the rotor diameter manifest a dependency of the results on the wavelet kernel (the mother wavelet function, translated and dilated, that is convoluted with the variable in physical space). The discrepancy is more prominent in the comparison of Morlet wavelet and its synchrosqueezed transform, especially at length scales very close to the resolved part of the spectrum where the influence of subgrid scale closures cannot be neglected. Hence, the wavelet results in subseqent sections have been analysed at scales $\gtrsim 0.6D$, where the results involving the spectra are little influenced by the wavelet kernels.

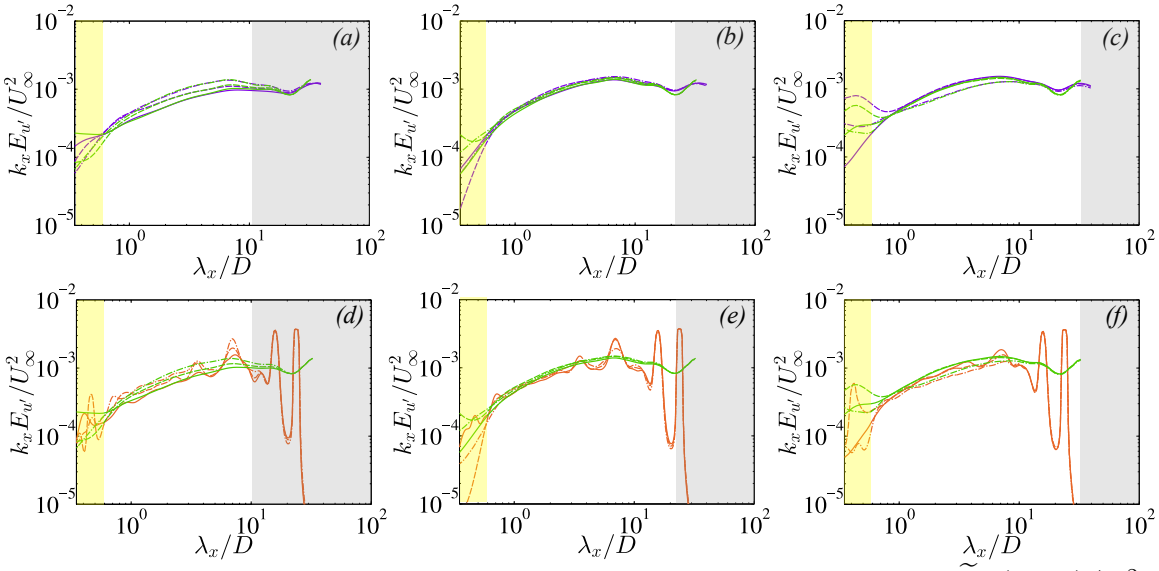

Figure 6.14: Spanwise and temporally averaged wavelet spectra $k_x\widetilde{E}_{u'}(\lambda_x, x)/U_\infty^2$, at different streamwise stations. Left: Row 1, Middle: Row 2, Right: Row 3. Violet – Morse, Green – Morlet, Orange – Syncrosqueezed Morlet. Location – $z = z_h + D/2$, top tip of the rotor. Yellow patch – region affected by SGS viscosity. Gray patch – region affected by cone of influence (COI) of the wavelet.

Figures 6.15, 6.16 illustrate the spectral variation in the streamwise row by row and spanwise column by column of wind turbines respectively. In particular, the row by row variation in Figure 6.15 reveals that the spectra $\widetilde{E}_{u'}(k_x, \widetilde{x}; z)$ at inner layer is fairly homogeneous, compared to the top tip spectra, with the local heterogeneity at large scales being close to the rotor area and more observable in the first

and third rows. While the streamwise integrated wavelet spectra $\widetilde{E}_{u'}(k_x; z)$ reveals the $\lambda_x^{2/3}$ Kolomogorov cascade, the spectra without the spatial integration close to length scales $\gtrsim D$ manifest deviations from it indicating modulations by wind turbines. Also note, that at smaller scales $\lambda_x < D$, the spatial heterogeneity is more prominent. Interestingly it can be observed that for the spanwise spectra $\widetilde{E}_{u'}(\widetilde{k}_y, \widetilde{y}; z)$ in Figure 6.16, in the absence of a dominant convection in the y direction, the heterogeneity is only localized to the smaller scales $\sim D$ and is perfectly symmetric about the middle column of turbines at $y = 7.85D$. This observation is in line with the fact that our domain is perfectly symmetric about $y = 7.85D$ with periodic (homogeneous) boundary conditions being imposed in the spanwise directions. While discussing figures 6.15, 6.16, it is essential to note the two shaded regions highlighted in the spectra. The upper bound of the yellow shaded region is approximately twice the coarsest resolved length scale of the domain (even though scales close to the wind turbines are very fine), beyond which we would heuristically expect to have minimal influence of the subgrid scale viscosity. Close to the turbines the grid scales are fine ($\sim 0.04D$ in x direction, $\sim 0.02D$ in y direction) and the streamwise spectra indicates growths/peaks in the spectra at the smallest resolved scales, which indicates that the phenomenon is definitely not a characteristic outcome of the dissipative SGS viscosity. However, it is hard to completely decouple the effect of grid and physics of such spectral peaks in LES. Thus, even though the finer resolution near the turbines does indicate, that the spectral peaks/growth are an outcome of the modulation of wind turbines due to the interception of eddies, further investigation, with perhaps even finer resolution is required in order to understand the dynamics of the phenomenon. Now, we focus on the gray shaded region of the spectra, close to the largest length scales. This is the region affected by the "cone of influence" [159,160] of the particular wavelet method affecting only the largest scales. For a mother wavelet, $\psi(x)$ with

compact support $[-B, B]$, the compact support for all translated and dilated wavelets $\psi_{\eta,\xi}(x) = 1/\sqrt{\eta}\psi(\frac{x-\xi}{\eta})$ can be calculated as $[\xi-\eta B, \xi+\eta B]$. The cone of influence can be calculated as a set of all $r \in [\xi-\eta B, \xi+\eta B]$, i.e. the set of wavelet coefficients influenced by the value of the signal at the given position. For a heterogeneous direction, the signal is padded with zeros before performing a convolution of the wavelet (See appendix E), and hence close to the largest scales, a discontinuity is generated as is evident with slight discrepancies with the Fourier spectra and streamwise integrated wavelet spectra. Note that with periodic boundary conditions, no zero padding is essential and no cone of influence is present, hence the spanwise wavelet spectra at the largest scales were observed to be closer to their Fourier counterpart compared to the streamwise spectra (See Figure 6.13).

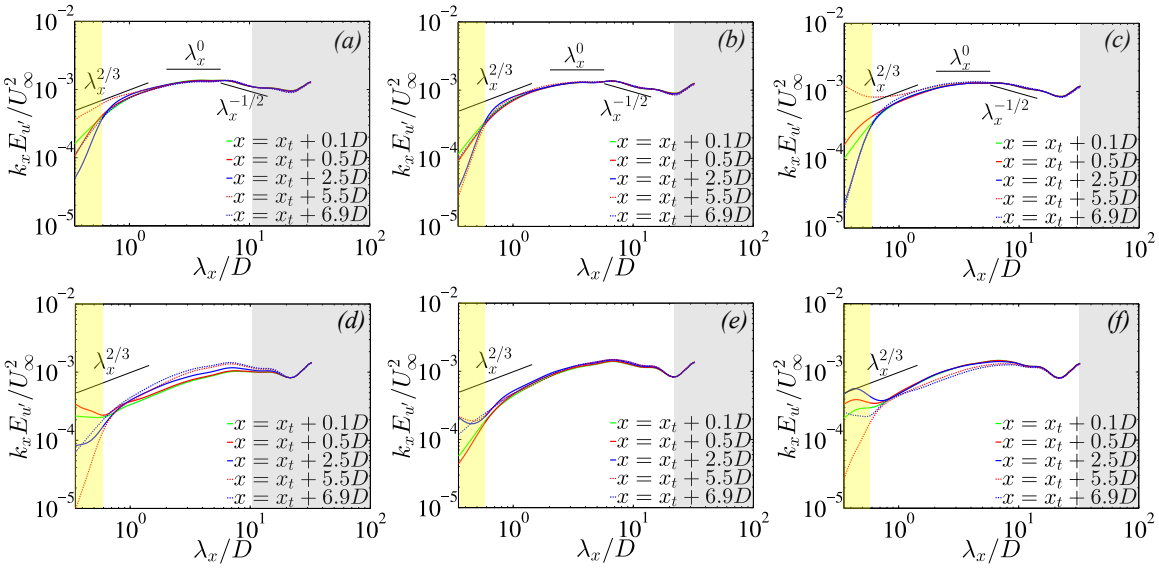

Figure 6.15: Spanwise and temporally averaged Morlet wavelet spectra $k_x\widetilde{E}_{u'}(\lambda_x, x)/U_\infty^2$ at different streamwise stations for different rows of the turbines. Left: Row 1, Middle: Row 2, Right: Row 3. (a)-(c) – $z = 0.125D$, inner layer (d)-(f) – $z = z_h + D/2$, top tip of the rotor.Yellow patch – region affected by SGS viscosity. Gray patch – region affected by cone of influence (COI) of the wavelet.

To better understand the spatial variability of the wavelet energy spectra, we document the intermittency function of u, w energy spectra in the streamwise direction

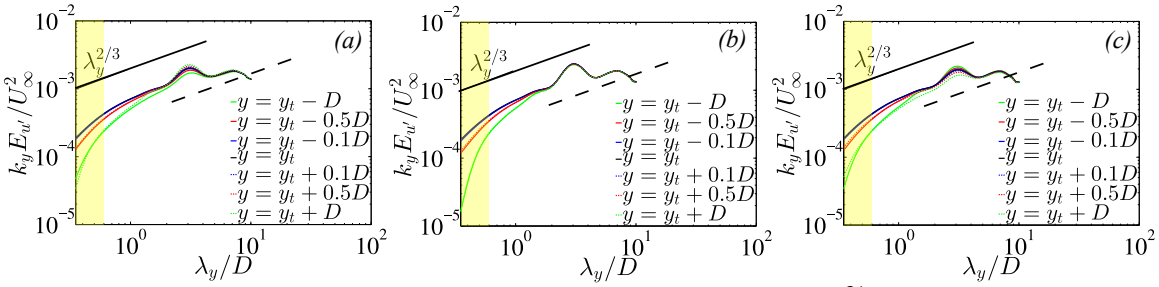

Figure 6.16: Streamwise averaged Morlet wavelet spectra $k_y\widetilde{E}_{u'}(\lambda_y, y)/U_\infty^2$ at different streamwise stations for different rows of the turbines. (a) Column 1 , (b) Column 2, (c) Column 3. Location – $z = z_h + D/2$, top tip of the rotor. Yellow patch – region affected by SGS viscosity.

(also see Appendix E),

$$I_\xi(x;\lambda_x) = \frac{\widetilde{E}_\xi(k_x, x; z)}{\widetilde{E}_\xi(k_x; z)} \tag{6.2}$$

where $\xi = u',\ w'$ are the streamwise and wall-normal turbulent velocity flucatuations. This definition is along the lines of Farge [178] and is a measure of the deviation of the energy spectra at different streamwise locations from its streamwise integrated counterpart thus reflecting on the streamwise heterogeneity. Please note, that despite its dependence on height, in the expression of I_ξ the argument of z has been dropped for brevity. Figures 6.17– 6.20 document the streamwise variability of the wavelet energy spectra at different wall normal locations, close to the log-layer as well as the region around the rotors. The gray patch in the plots corresponds to the region of "edge effects" owing to the cone of influence of the wavelet coefficients at the maximum wavlength plotted, $\lambda_x = 12D$. It is straightforward to note that wavelet coefficients corresponding to smaller wavelengths thus have smaller region of influence, which completely lie inside the cone of influence of the largest scale.

In Figure 6.17, the u and w intermittency function of the Morlet wavelet spectra and its synchrosqueezed transform reveal that the dynamics of the inner layer, $z = 0.125D$ is fairly homogeneous at the larger scales, $\lambda_x \sim O(10D)$. It is interesting to note that the smaller scale $0.6D$ (twice the coarsest resolved scale) in I_u illustrates

intermittent peaks throughout domain (outside the cone of influence). This is more prominent in the Morlet wavelet in Figure 6.17a than its synchrosqueezed transform in Figure 6.17b. Since these peaks in I_u are not limited to the region of wind turbines, it is apparent that these peaks are possibly not an outcome of the modulation by wind turbines, but rather the effect from the "wall" possibly coming from the turbulent "burst" events. However, this hypothesis needs further investigation. The variability of w spectra, or I_w however clearly manifests 3 distinct peaks in the region of wind turbine array. They can be identified as remnants of the "downdraft" mechanism intercepted by the rotating blades, that when reach the bottom wall manifest as peaks or strong deviations from the streamwise averaged wavelet spectra.

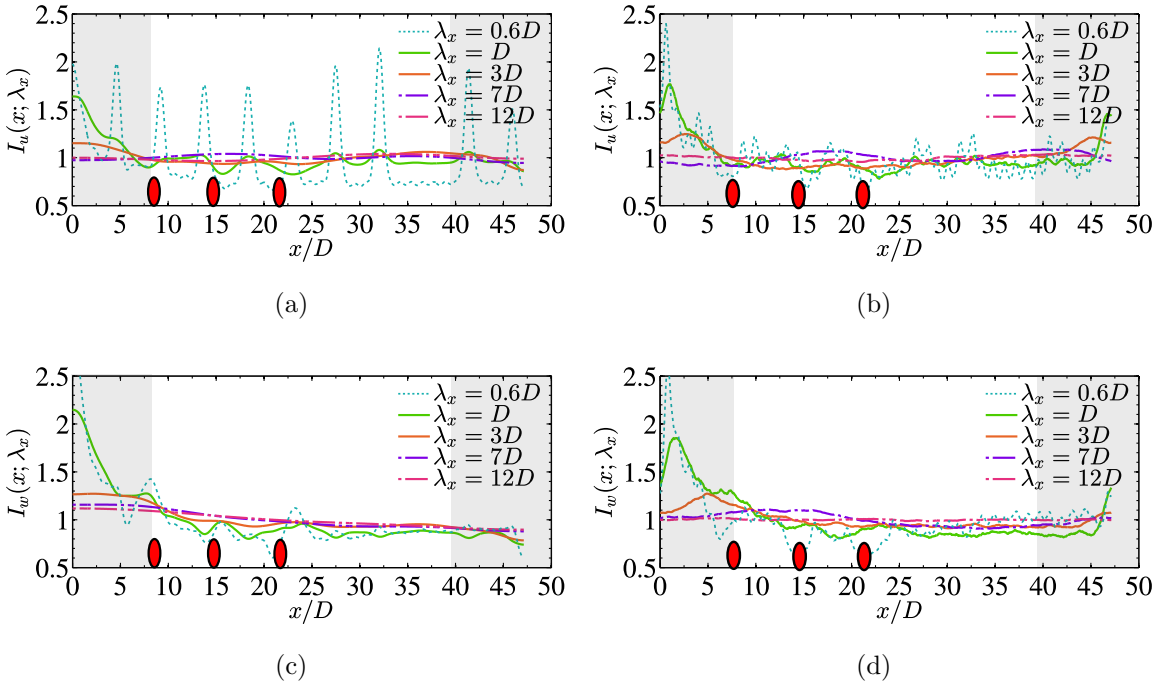

Figure 6.17: Streamwise intermittency function for (a),(b) u velocity, $I_u(x;\lambda_x)$ and (c), (d) w velocity, $I_w(x;\lambda_x)$ at $z = 0.125D$, inner layer for different length scales. Gray patch – region affected by cone of influence (COI) of the wavelet for the maximum wavelength considered, $\lambda_x = 12D$. Left: Morlet wavelet, Right: Syncrosqueezed transform of Morlet. Red ellipses – streamwise location of turbine rows.

Figures 6.18 – 6.20 illustrates the intermittency function I_u and I_w in the rotor

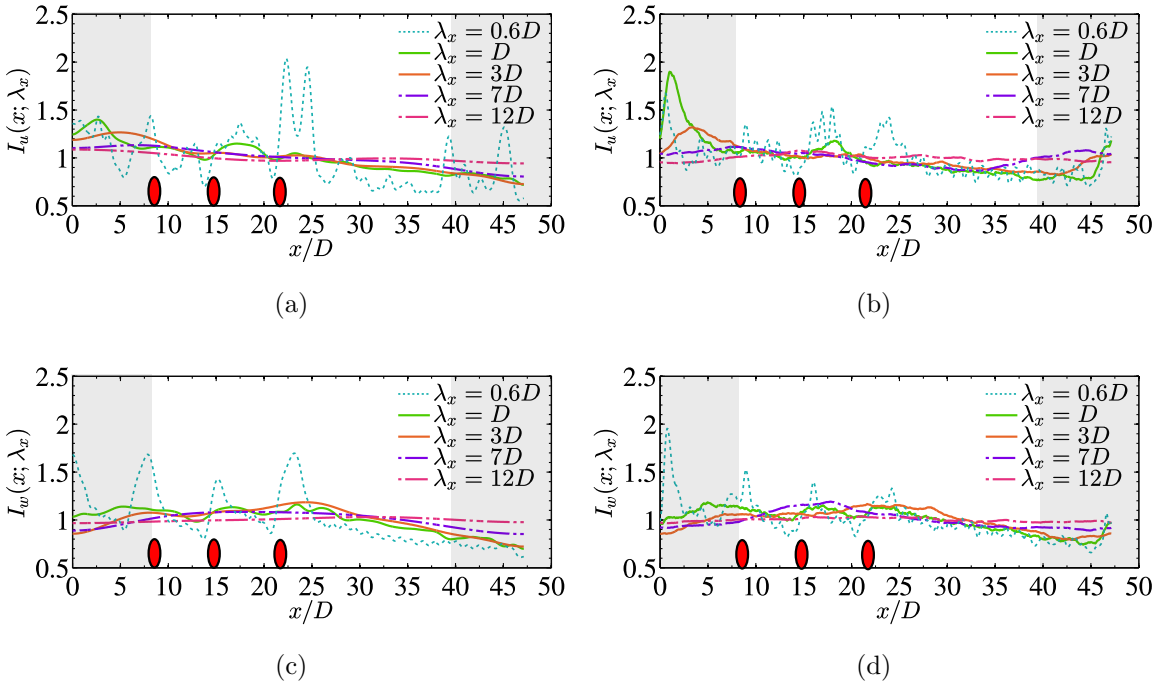

Figure 6.18: Streamwise intermittency function for (a), (b) u velocity, $I_u(x;\lambda_x)$ and (c), (d) w velocity, $I_w(x;\lambda_x)$ at $z = z_h - D/2$, bottom tip of the rotor for different length scales. Gray patch – region affected by cone of influence (COI) of the wavelet for the maximum wavelength considered, $\lambda_x = 12D$. Left: Morlet wavelet, Right: Syncrosqueezed transform of Morlet. Red ellipses – streamwise location of turbine rows.

region, $z = z_h \pm D/2$ both using the Morlet wavet and the syncrosqueezed transform of the same. Note, that the bottom tip of the rotor $z_h - D/2 = 0.5D = 0.1H$, lies in the inner log-layer, while the top tip of the rotor, $z_h + D/2 = 1.5D = 0.3H$, lies in the outer layer. Thus, streamwise homogeneity of I_u, I_w are apparent in Figure 6.18 at $z = z_h - D/2$. The syncrosqueezed transorm further corroborates this fact that the streamwise homogeneity is probably not an outcome of the smearing effect of the wavelets at larger length scales. Further, as $z = z_h - D/2$ is closer to the turbine rotor despite being in the inner layer, the three distinct peaks can be observed for both I_u and I_w using both methods of Morlet wavelet and its syncrosqueezed counterpart. As we move to the outer layer, at $z = z_h,\ z_h + D/2$, the turbulence is incoherent, and large scale spatial variability can be observed. The maximum variability manifests

itself in the length scale, of $\lambda_x = 7D$, which is the streamwise distance between the row of turbines. This is a clear indication of the fact, that the dynamics of turbulence turbine interaction is quite different than just the outer layer ABL without the rotors. It is interesting to observe, that length scales $> O(D)$ manifest such global variability in the streamwise direction at the hub-height and top tip of the rotors. Furthermore, the streamwise variability of the u spectra is much higher than that of the w spectra. Smaller scales in the w spectra contribute more to the spatial variability than its u counterpart. This result indicates the fact, that while there is a large scale modulation of the u energy due to the interception with turbines, the downdraft of energy from the top tip of the rotor occurring via vertical velocities predominantly occurs at smaller scales $\lesssim 3D$.

Spatial Variability of Wavelet Spectra – Upstream and Downstream of Turbines

Another interesting observation demonstrated in the plots involving the intermittency function is the characteristics of turbulence in the upstream and far downstream ($10-15D$ downstream of the rotors) of the turbines. Around the rotor region ($z \geq z_h$), the intermittency is most conspicuous, but the regions upstream and downstream of the turbines both show similar to a quasi-gaussian type of decay from the peaks in the turbine regions ($\lambda_x > D$) with longer tails downstream. Interesting to note, that these global modulations manifested more prominently in the u spectra, indicate that the large scale turbulence ($\sim \gtrsim 3D$) intercepted by the first row of wind turbines, results in organization of structures upstream of the turbine arrays as evident by the growing I_u function in the upstream region. The bottom tip of the rotor ($z = z_h - D/2$) still preserves some of the essence of being in the log layer, but the intermediate length scales especially $\lambda_x \leq 7D$ predict a very slow decay in the intermittency functions,

indicating that there is a drop in the energy spectra downstream of the turbines compared to its upstream spectra. This might be related to the energy capture by the turbine rows in the streamwise direction in addition to the downdraft mechanisms. However, further investigation is necessary to support this hypothesis.

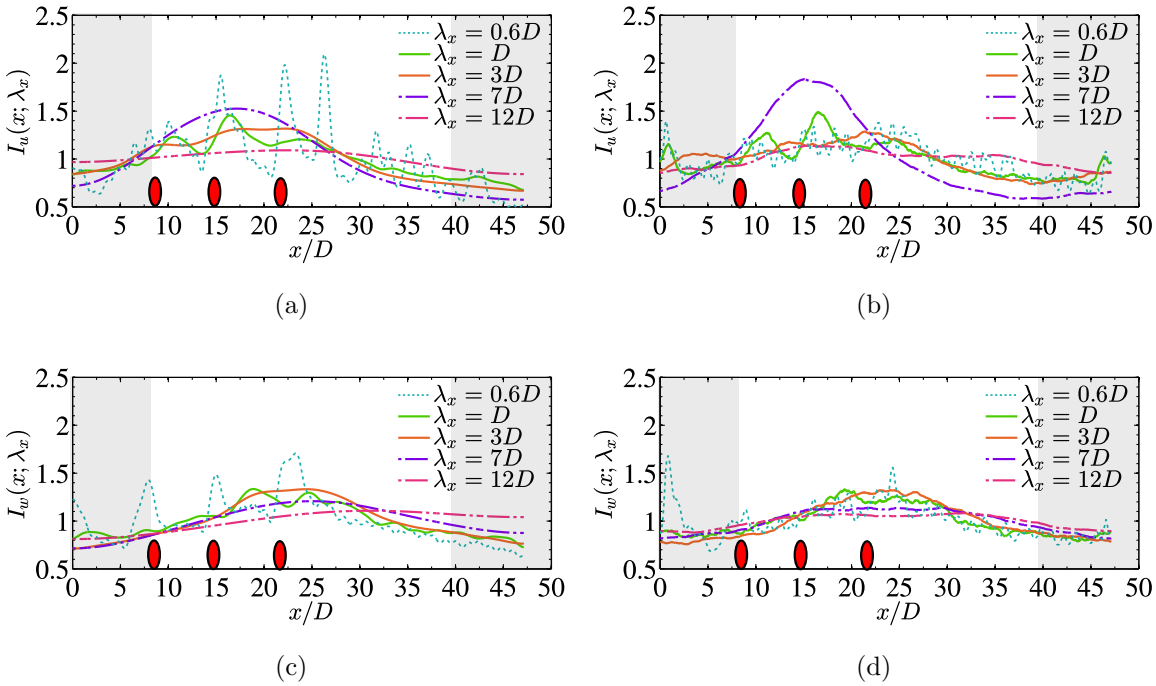

Figure 6.19: Streamwise intermittency function for (a), (b) u velocity, $I_u(x;\lambda_x)$ and (c), (d) w velocity, $I_w(x;\lambda_x)$ at $z = z_h$, hub-height of the rotor for different length scales. Gray patch – region affected by cone of influence (COI) of the wavelet for the maximum wavelength considered, $\lambda_x = 12D$. Left: Morlet wavelet, Right: Syncrosqueezed transform of Morlet. Red ellipses – streamwise location of turbine rows

6.3.3 Wavelet Coherence

The dynamics of the large scales in the WT array ($\lambda_x \sim 10D$) in this chapter are further illustrated by the temporally averaged wall-normal correlation of wavelet transform of the signals. The "coherence" [193,194] of the wavelet transformed signals (turbulent fluctuating velocity) u_i' at two distinct wall normal z, z' locations can be

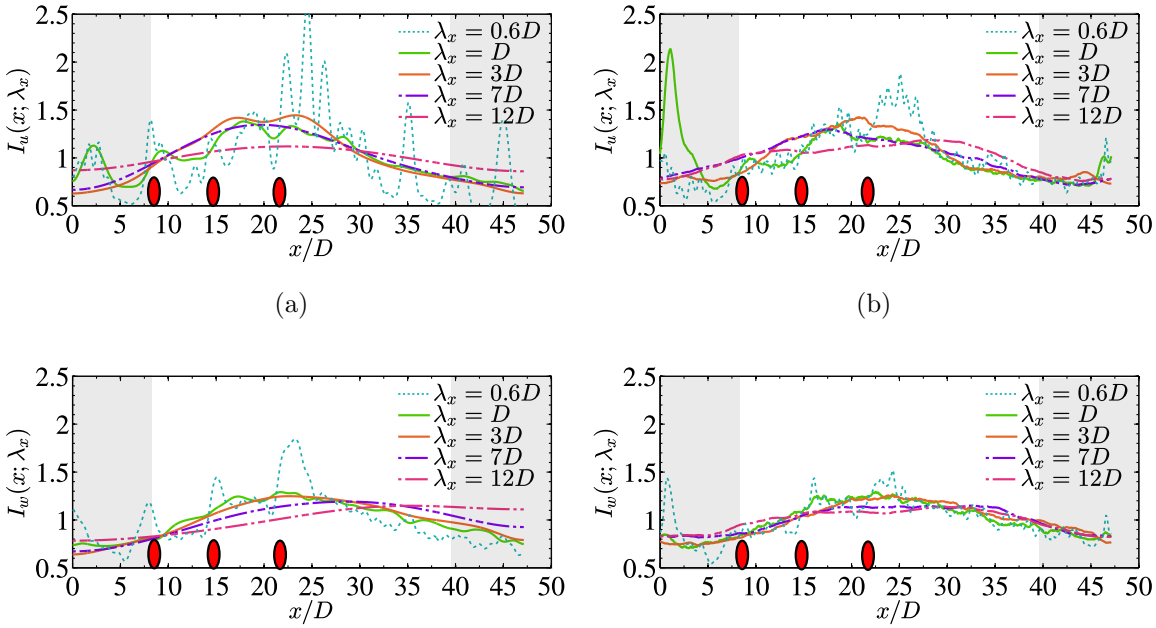

Figure 6.20: Streamwise intermittency function for (a), (b) u velocity, $I_u(x;\lambda_x)$ and (c), (d) w velocity, $I_w(x;\lambda_x)$ at $z = z_h + D/2$, top tip of the rotor for different length scales. Gray patch – region affected by cone of influence (COI) of the wavelet for the maximum wavelength considered, $\lambda_x = 12D$. Left: Morlet wavelet, Right: Syncrosqueezed transform of Morlet. Red ellipses – streamwise location of turbine rows

defined as a correlation function,

$$\rho_{\mathcal{W}_\psi[u_i',u_j']}(z,z',k_\eta,\eta,|\zeta,t) = \frac{\left|\mathcal{W}_\psi[u_i'](k_\eta,\eta)|^*_{\zeta,z,t}\mathcal{W}_\psi[u_j'](k_\eta,\eta)|_{\zeta,z',t}\right|}{\left|\mathcal{W}_\psi[u_i'](k_\eta,\eta)|_{\zeta,z,t}\right|\left|\mathcal{W}_\psi[u_j'](k_\eta,\eta)|_{\zeta,z',t}\right|} \tag{6.3}$$

In the current chapter, we use the temporally and ζ (spanwise or streamwise) averaged wavelet coherence as

$$\rho_{\mathcal{W}_\psi[u_i',u_j']}(z,z',k_\eta,\eta) = \int_{\zeta\in\mathbb{R}} \left\langle \rho_{\mathcal{W}_\psi[u_i',u_j']}(z,z',k_\eta,\eta,|\zeta,t\right\rangle_T \mathrm{d}\zeta, \quad \eta = x,y \quad \zeta = y,x$$

Figure 6.21 shows the spectral coherence of u' fluctuations in the streamwise wavenumber, streamwise location plane with correlations near the bottom tip of the rotors with the hub-height, $z' = z_h, z = z_h - \xi$ and near the top tip of the rotors with the hub-height, $z = z_h, z' = z_h + \xi$ ($\xi = D/2,\ D/4$). This clearly indicates that the eddies above the hub-height are better correlated in the wall normal direction near the

top tip region than the eddies near the bottom tip of the rotors. Similar observation is documented for the coherence of w' fluctuations in Figure 6.22. However, unlike the u' spectra which illustrates almost homogeneous character at large scales $\sim 10D$, the w' coherence displays heterogeneity even at large scales, with slightly higher correlations evident as we move towards the downstream of the turbines. This might be the manifestation of the large scale roller structures that were observed in the POD modes of wind farm [24, 137] contributing to downdrafts developing downstream of the turbines reflected by the growth of the correlation coefficient value past the first row of wind turbines.

The coherence in the spanwise direction (Figures 6.23, 6.24) also indicates that the eddies near the top tip of the rotor are better correlated than those near the bottom tip. Also note, that the spanwise direction does not have a dominant direction of convection and are modelled with periodic boundary conditions. Consequently, all scales of the coherence spectra manifest a symmetric behaviour, with the line of symmetry passing through the middle column of turbines at $y = 7.85D$. Additionally, the small scales $\lesssim D$ show a well defined repeating pattern with the coherence magnitude fluctuating from high (turbine locations) to low (inter-turbine regions).

We also show the spectral coherence of the kinematic shear stress $\overline{u'w'}$ $(z = z')$ at top and bottom tip of the rotor as well as the hub-height (Figure 6.25) which manifests a high amount of heterogneity in the streamwise direction even at large scales $\sim 10D$. However, the coherence of $u'w'$ does not manifest a distinct coherent region at the top tip of the rotor as opposed to the bottom tip region.

To better understand the wavelet coherence, one dimensional line plots versus streamwise directions are considered for different streamwise wavelengths as in Figures 6.26, 6.27. The $u',\ w'$ coherence at Figure 6.26 indicates that for the streamwise velocity coherence, the correlation magnitude drops significantly, as we go from a

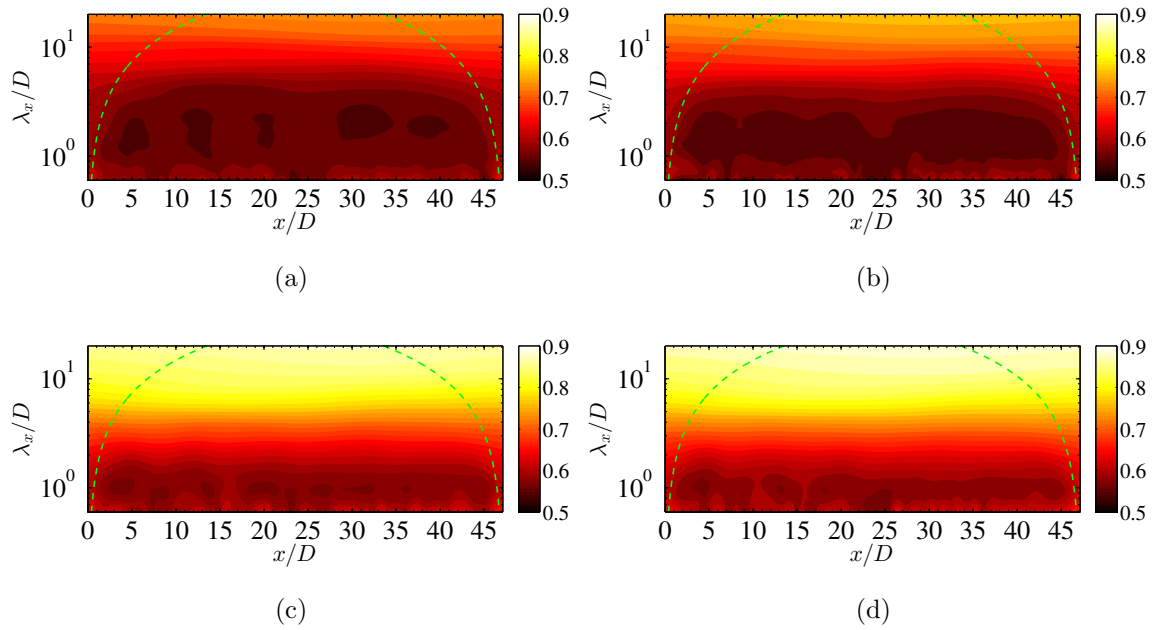

Figure 6.21: Wavelet spectral coherence of u velocity with the hub-height, $\rho_{\mathcal{W}_\psi[u',u']}(z,z',k_x,x)$ at (a), (b) bottom tip, & (c), (d) top tip of the rotor. (a) $z = z_h - D/2$ and $z' = z_h$, (b) $z = z_h - D/4$ and $z' = z_h$, (c) $z = z_h$ and $z' = z_h + D/2$. (b) $z = z_h$ and $z' = z_h + D/4$. Green dashed linw –boundary of the Cone of Influence (COI)

length scale $12D$ to $3D$, while not so much is observed for the vertical velocity coherence. At relatively smaller scales, $\lambda_x \sim 0.6D$, the coherence is highly correlated at the top and bottom tip of the spectra for w coherence. This indicates that even at the smaller scales a similar dynamics is playing a role at the top and bottom tip of the turbines, which can only be conceived through the theory of "downdraft" mechanisms. Another interesting observation lies in Figure 6.27, which clearly indicates that the spectral coherence of the kinematic shear at all length scales have larger correlations at the bottom tip compared to the top-tip of the rotor. This clearly indicates that while more wider and thicker structures are responsible for the downdraft mechanisms from the top tip of the rotor than are present at the bottom tip, the kinematic shear stress is more organized at the bottom tip (inner layer) possibly owing to the interaction of the wall bursts and the downdraft mechanisms, which are

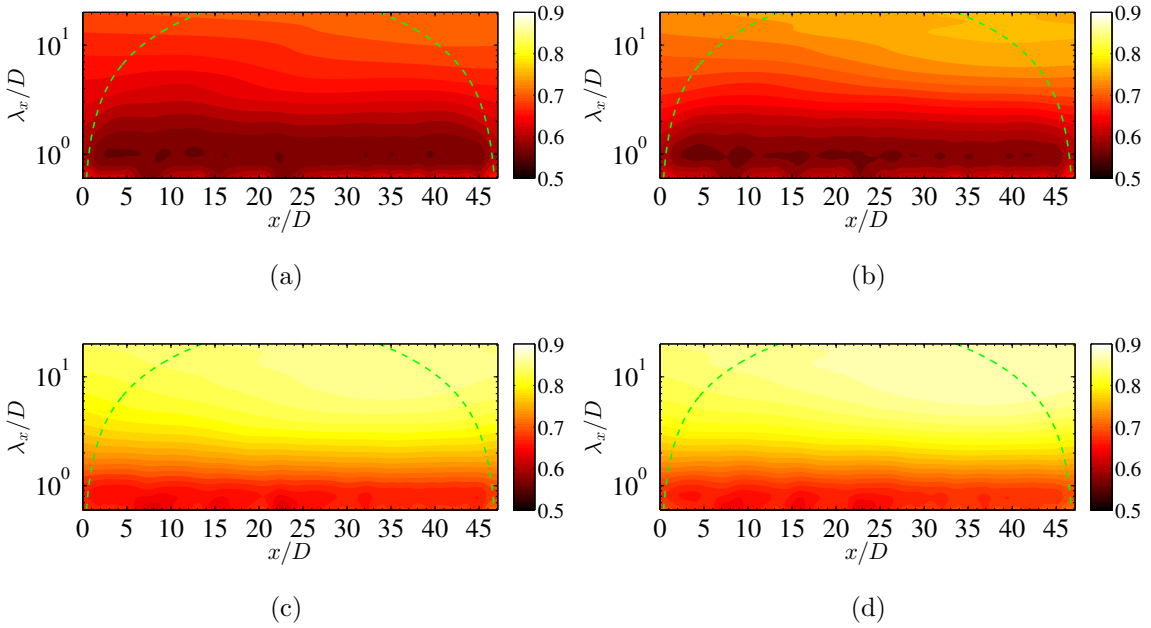

Figure 6.22: Wavelet spectral coherence of w velocity with the hub height, $\rho_{\mathcal{W}_\psi[w',w']}(z, z', k_x, x)$ at (a), (b) bottom tip, & (c), (d) top tip of the rotor. (a) $z = z_h - D/2$ and $z' = z_h$, (b) $z = z_h - D/4$ and $z' = z_h$, (c) $z = z_h$ and $z' = z_h + D/2$. (b) $z = z_h$ and $z' = z_h + D/4$. Green dashed line –boundary of the Cone of Influence (COI)

absent in the top tip region and dominated by relatively incoherent turbulence.

Near Wall Dynamics

Figure 6.28 illustrates the wavelet spectral coherence of velocity u', w' and pressure p' fluctuations near wall, where dynamics of log-layer are dominant. Despite the heterogeneity in the outer layer, the inner layer correlations manifest strong homogeneity at scales $> D$. While there is drop in correlation in the u' coherence $(z - z' = 0.0625D, 0.1D)$ as we move to smaller scales, the w' and $u'w'$ correlations are pretty close at length scales $3D, 12D$. The pressure fluctuations are highly correlated at scales $> D$ and also display homogeneous behaviour. At smaller scales $\lambda_x \sim 0.6D$, the one-dimensional coherence signals, even though display oscillations in the streamwise directions are highly correlated for different $z - z'$.

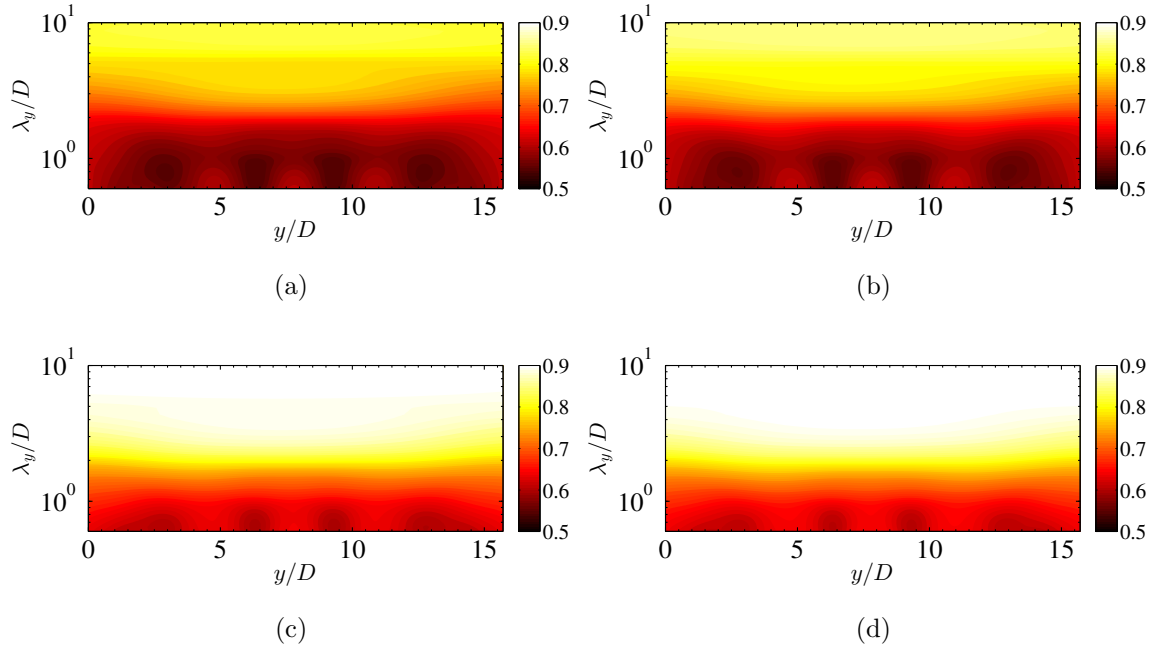

Figure 6.23: Wavelet spectral coherence of u velocity with the hub-height, $\rho_{\mathcal{W}_\psi[u',u']}(z, z', k_y, y)$ at (a), (b) bottom tip, & (c), (d) top tip of the rotor. (a) $z = z_h - D/2$ and $z' = z_h$, (b) $z = z_h - D/4$ and $z' = z_h$, (c) $z = z_h$ and $z' = z_h + D/2$. (b) $z = z_h$ and $z' = z_h + D/4$.

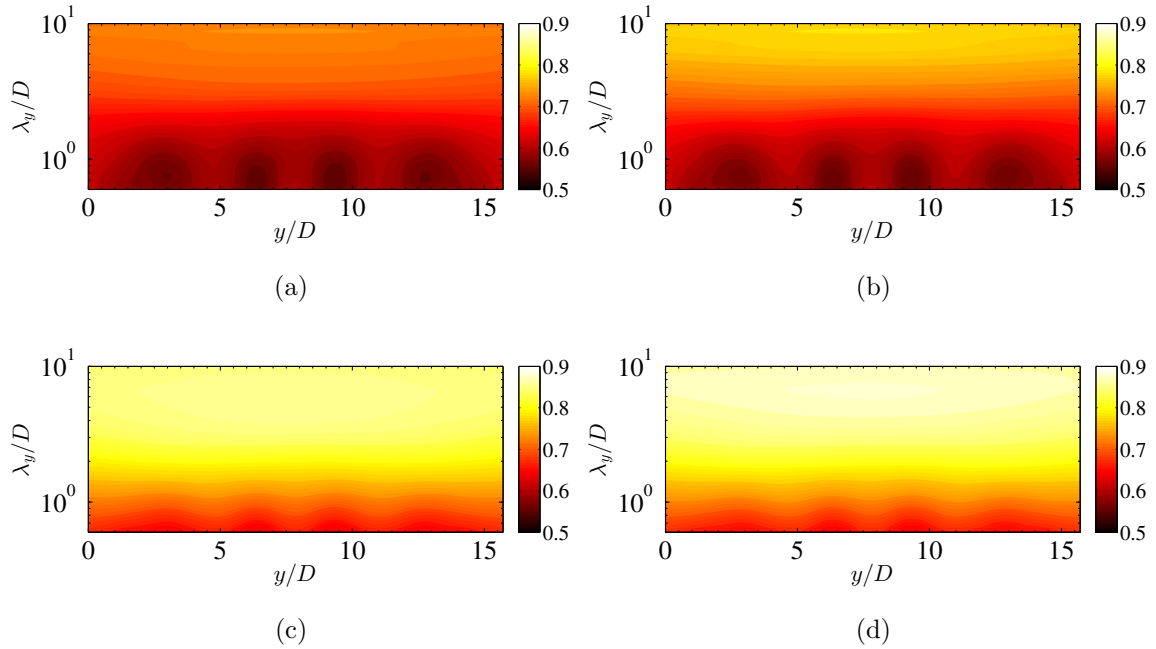

Figure 6.24: Wavelet spectral coherence of w velocity, $\rho_{\mathcal{W}_\psi[w',w']}(z, z', k_y, y)$ at (a), (b) bottom tip, & (c), (d) top tip of the rotor. (a) $z = z_h - D/2$ and $z' = z_h$, (b) $z = z_h - D/4$ and $z' = z_h$, (c) $z = z_h$ and $z' = z_h + D/2$. (b) $z = z_h$ and $z' = z_h + D/4$.

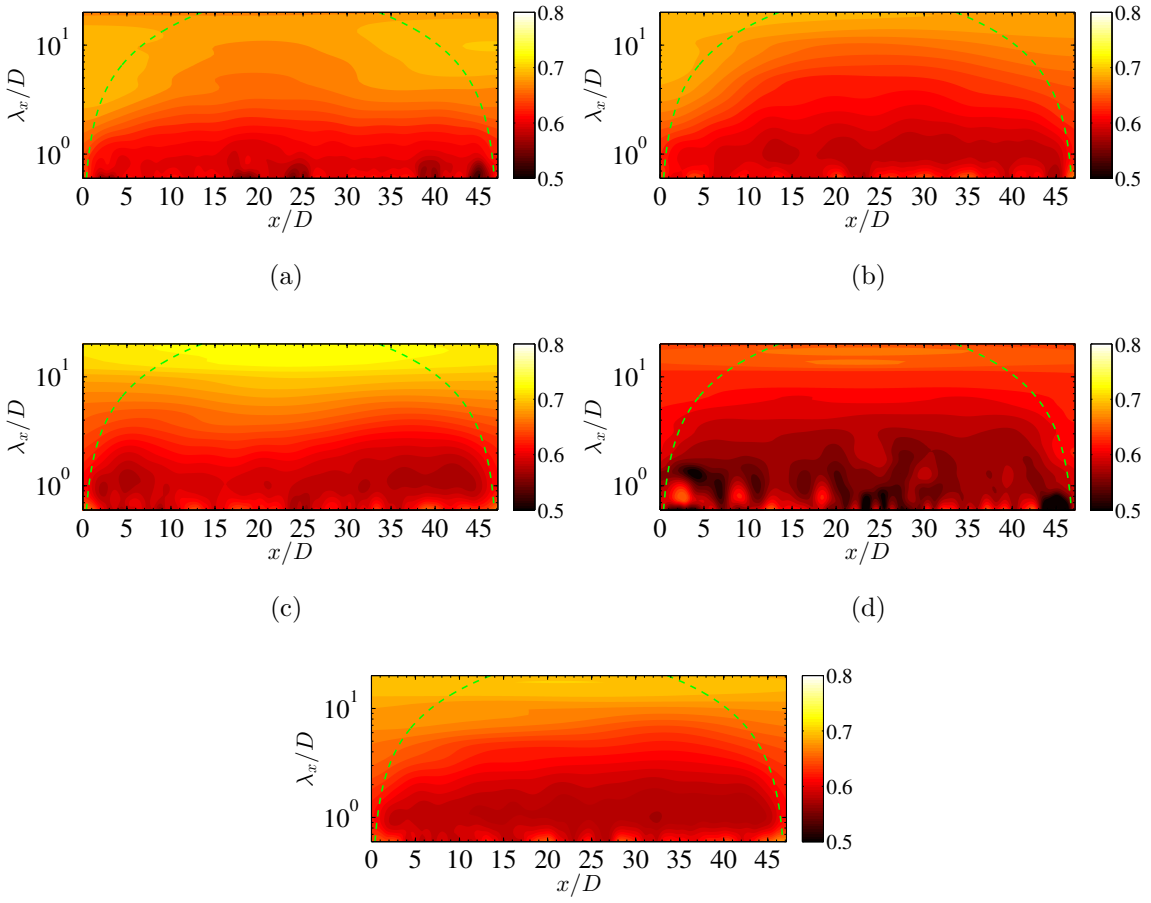

Figure 6.25: Wavelet spectral coherence of $\overline{u'w'}$, $\rho_{\mathcal{W}_\psi[u',w']}(z, z', k_x, x)$ in the rotor region. $z = z'$ (a) $z = z_h - D/2$ (b) $z = z_h - D/4$, (c) $z = z_h + D/4$ and (d) $z = z_h + D/2$ (e) $z = z_h$. Green dashed line –boundary of the Cone of Influence (COI)

In Figure 6.29, we plot the two dimensional Fourier spectra of the coherence of turbulent velocity and pressure fluctuations, u' and p'. The definition of Fourier coherence remains analogous to Equation 6.3, but the 1D wavelet transform is replaced by the 2D Fourier transform. The figures do indicate the presence of highly correlated anisotropic eddies (observed in [136, 150]) in the near wall region. The plots further indicate that the near wall attached anisotropic ($\lambda_x \gg \lambda_y$) inactive motions [77] are highly correlated in velocity, pressure in the near wall logarithmic region. The smaller

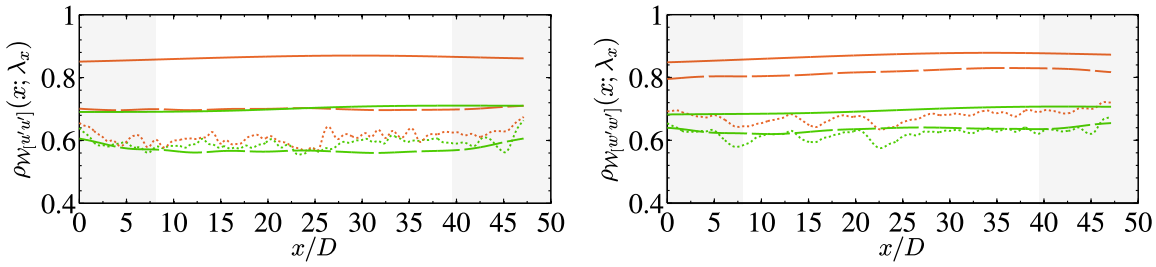

(a) (b)

Figure 6.26: Streamwise variation of wavelet coherence function at four different streamwise wavelengths λ_x. (a) $\rho_{\mathcal{W}_\psi[u',u']}(z,z',k_x,x)$ (b) $\rho_{\mathcal{W}_\psi[w',w']}(z,z',k_x,x)$. Green – $z' = z_h - D/2$, $z = z_h$. Orange – $z = z_h$, $z' = z_h + D/2$. Solid – $\lambda_x = 12D$, dashed – $\lambda_x = 3D$ and dotted – $\lambda_x = 0.6D$.

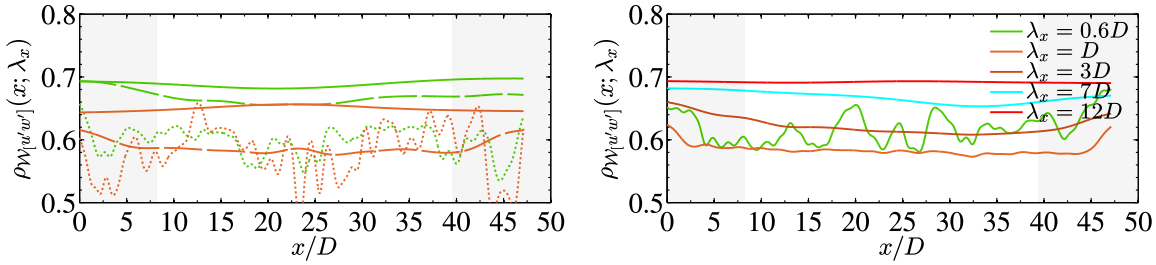

(a) (b)

Figure 6.27: Streamwise variation of $u'w'$ wavelet coherence function at four different streamwise wavelengths λ_x. $\rho_{\mathcal{W}_\psi[u',w']}(z,z',k_x,x)$ (a) . Green – $z' = z_h - D/2$, $z = z_h$. Orange – $z = z_h$, $z' = z_h + D/2$. Solid – $\lambda_x = 12D$, dashed – $\lambda_x = 3D$ and dotted – $\lambda_x = 0.6D$. (b) Different wavelenths at same location, $z = z_h$.

scales as seen in the coherence of wavelet spectra manifests some oscillations but the mean stays constant without a growth or decay. Hence, even in the presence of a wind turbine array, homogeneity of the near-wall length scales (dominated by wall dynamics) far away from the turbine rotors at around $z \sim 0.0625D$ are preserved.

6.4 Concluding Remarks

In this chapter we aim to understand how large scale eddies above the wind turbine array, are modulated by ABL structures due to the turbines themselves, their spatial variability in the dominant convection direction, and how they are responsible

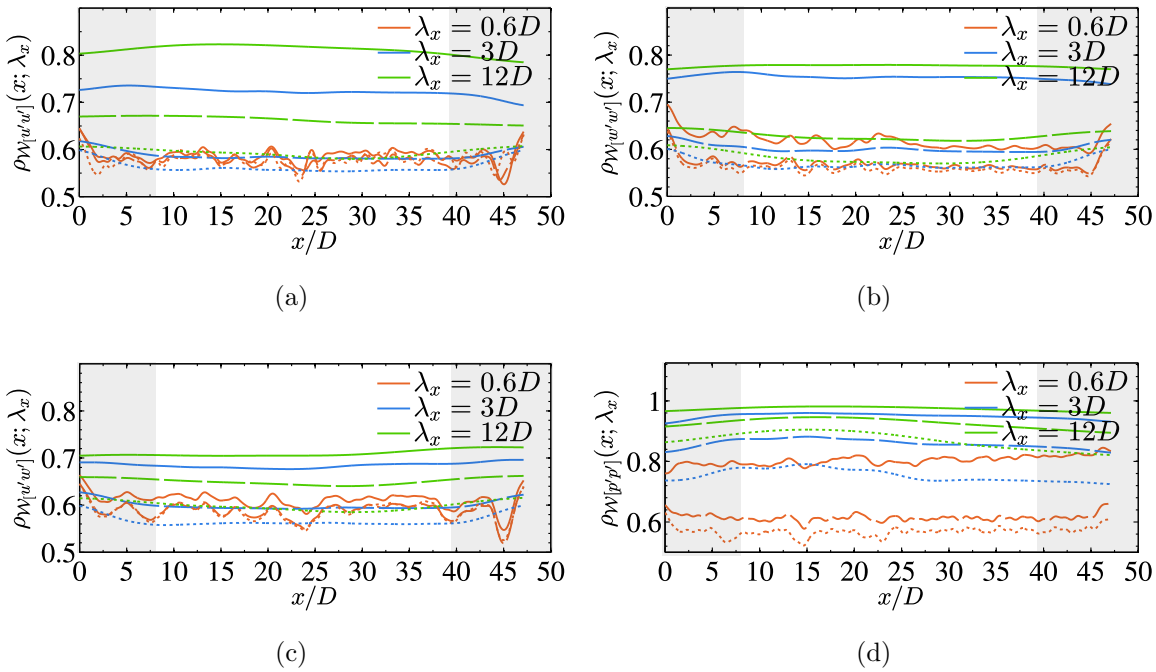

Figure 6.28: Streamwise variation of wavelet coherence function of turbulent fluctuations at four different streamwise wavelengths λ_x. $\rho_{\mathcal{W}_\psi[\xi',\eta']}(z,z',k_x,x)$ (a) $\xi' = \eta' = u'$ (b) $\xi' = \eta' = w'$ (c) $\xi' = u'$, $\eta' = w'$ (d) $\xi' = \eta' = p'$. Solid – $z = 0.0625D$, $z' = 0.0875D$, Dashed – $z = 0.0625D, z' = 0.1625D$, Dotted – $z = 0.0625D, z' = 0.2625D$.

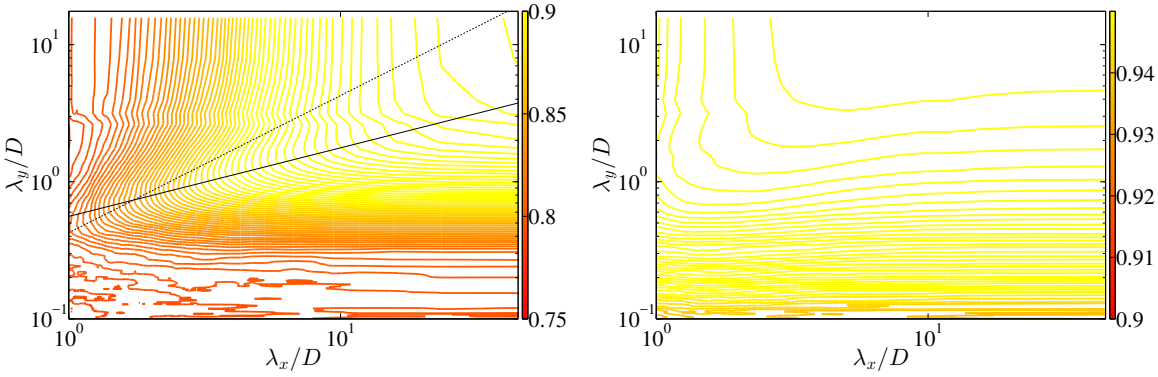

Figure 6.29: Streamwise spanwise variation of Fourier transormed coherence function of turbulent fluctuations at different wavelengths λ_x, λ_y. $\rho_{[\xi',\eta']}(z,z',k_x,k_y)$ (a) $\xi' = \eta' = u'$ (b) $\xi' = \eta' = p'$. $z = 0.0625D$, $z' = 0.0875D$. Solid line – $\lambda_y \sim \lambda_x^{1/2}$, Dashed – $\lambda_y \sim \lambda_x^{1/3}$.

for the power generated by the turbine array. Since, the wind turbine array considered is a finite scale type, the concept of wind turbine array boundary layer cannot be considered, and the power is generated both by the energetic structures carried by the streamwise convection as well as the downdrafts from the top of the turbine rotor. The wind turbine array spans a length of $14D$ in the streamwise direction and $6D$ in the spanwise direction. Thus the upstream and downstream regions of the turbine array serves as a platform to study how the ABL turbulence is affected by the wake effects of wind turbines. Specifically, we have used a wavelet spectral method which takes into consideration the spatial/local variability of the length scales of eddies, unlike its Fourier counterpart, where spatial information is completely lost in the spectral space. Wavelet spectra illustrates the presence of significant local spatial variability of spectral energy content at length scales of the order of turbine rotors, $\lesssim D$ in the inner layer, but are fairly homogeneous due to the presence of large scale anisotropic attached eddies. The dynamics at the inner layer are dominated by the wall effects and "turbulent bursts" rather than the interaction of wind turbine with the atmospheric turbulence. The results further indicate, that highly correlated long and wide structures of length scales $\sim O(10D)$ which also exhibit strong coherence in the vertical direction are present above the wind turbines, which are responsible for downdraft of energetic eddies contributing to turbine power. These structures display fairly homogeneous character in terms of the variability of their correlation coefficient, but manifest high spatial variability in their energy content. The downdraft mechanism involves vertical velocity structures which are predominant at relatively smaller scales. It was also noted that the correlation of the u', w' velocities, or the kinematic shear is more well-organized at the bottom tip of the rotor which lies in the inner layer, rather than at the top tip, where the turbulence is contributed from a relatively incoherent dynamics. Furthermore our study indicates that there is a high spatial

variability of the energy spectra even at scales $> D$ near the hub-height and top tip region of the rotors. Unlike the variability at small scales $\sim D$, which are intermittent and are manifested as 3 peaks, the large scale variability, as seen in the intermittency functions manifests itself as a quasi-gaussian behaviour with long tails downstream of the turbines. This global peak indicates that wind farm ABL interaction results in a significant modulation of atmospheric turbulence in the rotor region at or above the hub-height. Additionally, these global modulations manifested more prominently in the u spectra, indicate that the large scale turbulence ($\sim \gtrsim 3D$) intercepted by the first row of wind turbines, results in an organization of eddies upstream of the turbine arrays. Surprizingly, despite some differences, the bottom tip of the rotor, which still lies in the inner layer is seen to illustrate the "near wall dynamics" at the log layer.

At present, our grid resolution allows capturing of length scales $\sim 0.3D$ far away from the turbines and $0.1D$ close to the rotors, which is roughly two orders of magnitude smaller than the larger scales, the focus of this chapter. To have a complete understanding of wind turbine-ABL interaction, we also aim to understand the dynamics at length scales $\sim 0.1D$, which are linked with the high frequency power fluctuations. Wavelet spectral analysis would be a perfect candidate for this study. We envision to carry out this computational study by conducting LES simulations at a finer grid as a part of our future investigation.

Chapter 7

LARGE EDDY SIMULATION WITH REALISTIC GEOPHYSICAL INFLOW: A COMPARISON WITH LIDAR BASED FIELD EXPERIMENTS

7.1 Introduction

The wake interactions in the downstream turbines and the power generated by the wind turbines in wind farms depend significantly on the turbulent inflow wind conditions from atmospheric boundary layer (ABL) [18, 195, 196]. Many computational and laboratory studies involving flow past the wind farms assume constant mean wind speed and wind direction neglecting large scale geophysical effects [16, 138, 197]. These effects are important for wind farm performance and hence studies in the past have attemped to bridge the gap by performing the wind farm simulations driven by realistic winds from Weather Research and Forecast (WRF) model (mesoscale) to finer turbulence (microscale). WRF models utilized are usually driven by data assimilation methodologies [198, 199]. In several of these studies field experimental results from remote sensing LIDAR scans have been used for comparison. For example, [200] performed Reynolds-Averaged Navier Stokes (RANS) simulation on a complex terrain driven by mesoscale WRF. Further, [201] have investigated the wake evolution of turbines under different atmospheric stability conditions in a nested large eddy simulation (LES) of finer grids around the wind turbine model, inside a coarser LES mesh driving precursor ABL coupled with weather forecast model. The results have been compared against the vertical profiling of LIDAR data involving dual LIDAR scans. However, the computational expense for LES models nested inside the coarser grid based precursor domain (interpolation from the coarse mesh to the finer mesh

for all the interior domain boundaries) is extremely high if large wind farm domain with varying mean wind directions are used. [201] attempts to ameliorate this computational bottleneck, by performing nested simulations for a single wind turbine. A more recent study [202] attempts to evaluate RANS and Detatched-Eddy Simulation (DES) in complex terrain with LIDAR measurements. The computational results have indicated some prediction of the trends of velocity and turbulent stresses with a reasonable amount of scatter.

In this context, our previous study [57] as a computationally inexpensive alternative has incorporated geophysical effects of varying mean wind flux and mean direction from cup and vane anemometer data into an LES framework. The study has revealed that these large scale geophysical effects (in particular, temporally varying mean wind flux and direction) can have significant impact on the power generated by the wind farms (See Figure 7.1).

Although presenting a methodology for incorporating large scale geophysical effects into the LES simulations, our previous work [57] did not provide a comparison of the wind turbine wakes with the field data. In the current chapter, our focus is on comparison of wind turbine wakes obtained with a similar mean wind based data-driven methodology, with the velocity measurements downstream of wind turbines. The single LIDAR measurements are taken at the off-shore wind farm called Alpha Ventus located in the North Sea by the Environmental Remote Sensing group at Arizona State University. The LES results are compared against these LIDAR scans. The objective of the current work lies in understanding the capability of the present LES methodology fed by the mean wind information in capturing the realistic large scale structures observed in field experiments.

In the current chapter, comparison of the temporally filtered LES velocity fields as well as the time variation of the spatially filtered fields in the location between two

turbines with that of the LIDAR experimental scan have been carried out. We build on the methodology already developed and discussed in Chapter 6, but now extended with the capability of incorporating temporally varying mean wind magnitude and direction. The physical consistency of simulation results for the current domain have been tested with the spatial energy spectra and temporal turbine power spectra which indicate the presence of the $-5/3$ law in accordance with the Kolmogorov turbulence cascade.

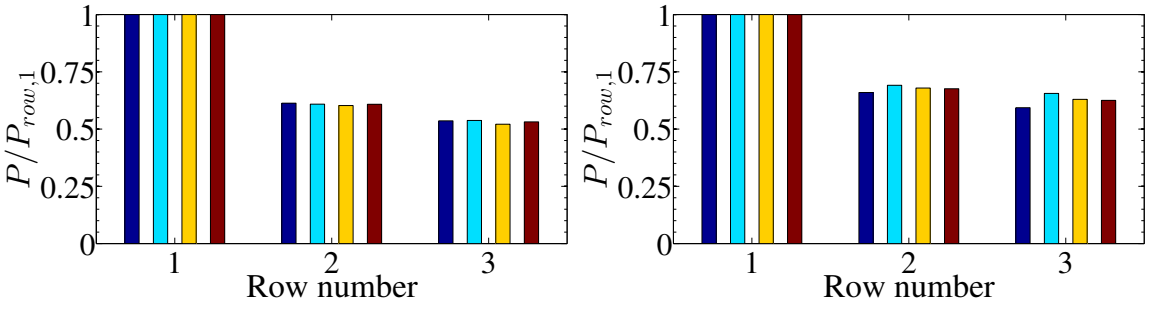

Figure 7.1: Power normalized by the first row of a 3×3 typical wind turbine array (a) without and (b) with temporally varying mean wind flux and direction. Blue – Left Column, Cyan –Middle column, Yellow – Right column, Red – averaged accross all three columns. Figure adapted from our previous work [57].

7.2 Computational Setup

Wind Turbine	N_t	z_h	D	Ω	rated power	rated wind speed
Adwen AD 5-116	3×2	90 m	116 m	$5.9 - 14$ rpm	5 MW	12.5 m/s
Senvion 5M	3×2	92 m	126 m	$6.9 - 13.1$ rpm	5 MW	13.0 m/s

Table 7.1: Turbines in Alpha Ventus wind farm. N_t – the number of turbines, D – turbine rotor diameter, z_h– wind turbine hub-height. Ω – speed of the rotation of the turbine rotor. Turbines T3,T7,T11,T4,T8,T12 – Senvion 5M turbines, T1,T5,T9,T2,T6,T10 – Adwen AD 5-116 turbines.

The computational domain comprises of the wind turbine array containing 12

Case	Geometry	$N_x^e \times N_y^e \times N_z^e$	Grid points
precursor ABL	$54D \times 27D \times 8.6D$ (6.2 km $\times$ 3.1 km $\times$ 1 km)	$30 \times 20 \times 24$	5.03×10^6
WT array	$54D \times 21D \times 8.6D$ (6.2 km $\times$ 2.4 km $\times$ 1 km)	$46 \times 40 \times 24$	1.53×10^7

Table 7.2: Computational domain size (normalized with turbine rotor diameter and also in kilometres) and grid-requirements for ABL & wind turbine array computational domain. 7^{th} order Legendre polynomial has been used per cartesian direction to expand variables in each spectral element. Domain normalized with D, the diameter of Adwen AD 5-116 turbines.

turbines (arranged as in Alpha Ventus wind farm) and is set up with inflow-outflow boundary conditions in the streamwise direction along similar lines as in Chapter 6 but now with a capability of variable mean wind speed and wind direction as discussed later in Section 7.2.1.

For the LES with near wall modeling framework, a computationally inexpensive wall-damped standard Smagorinsky model using Mason and Thompson wall damping [42] (with the accuracy comparable to the state-of-the art dynamic models) has been used for the subgrid scale closure [136]. Shear-stresses emulating the log-law of the inner layer [44, 136] has been used at the bottom "wall" for near-wall modeling [136]. The rotating turbine blades have been modeled with experimental lift and drag coefficients of different NACA40xx series airfoils using "actuator lines". Constant tip speed ratio, $\lambda = 4.6$ has been used for the Adwen turbines, while $\lambda = 5.0$ has been used for the Senvion ones, corresponding to their rated wind speed and rotational speed of the rotor. The tip-speed ratios are defined as $\lambda = \Omega D_{turb}/(2U_{hub})$, where D_{turb} is the diameter of the turbines and U_{hub} is taken as a temporal mean velocity of the precursor ABL at hub-height. For precursor simulation, periodic boundary conditions have been used in the streamwise and spanwise directions, while shear stress and stress free boundaries have been used in bottom and top boundary planes respectively. The boundary conditions for the wind farm domain remain the same as the precursor

ABL, except in the streamwise direction where inflow-outflow methodology has been used [57, 181]. The inflow is driven by a precursor neutrally-stratified ABL [136] with the temporal variation of mean wind flux and wind direction obtained from the data of cup and vane anemometer (CVA) located at the FINO platform (See Figure 7.3b). While the incorporation of mean wind flux variation has been performed by adjusting the Stokes equation and hence the divergence free velocity field at each timestep (See [57] for details), the change in wind direction has been incorporated by rotating the domain of precursor simulation. The details of the turbine configurations, e.g., the rotor size, hub-height and rated speed for the Alpha Ventus wind farm can be found in Table 7.1.

7.2.1 Incorporating Mean Wind Flux and Direction in LES

Incorporating the geophysical effect of the varying mean wind speed is implemented by changing the pressure gradient forcing through the Stokes solver in the preprocessor step. Note, this splitting scheme is applied only for the doubly periodic precursor simulation, where a forcing function is necessary to drive the flow. The precursor simulation is solved concurrently along with the wind turbine domain, which drives the flow past the array of turbines as inflow to the domain via spectral interpolation [57, 181, 182].

The Navier-Stokes (NS) equation in the operator form can be given as

$$\mathfrak{L}_1(\mathbf{u}) + \mathfrak{L}_2(p) = \mathfrak{NL}(\mathbf{u}, \nabla\mathbf{u}) + \mathbf{f} + B.C. \tag{7.1}$$

where the linear operators, $\mathfrak{L}_1 = \partial/\partial t - (\nu + \nu_t)\nabla^2$, $\mathfrak{L}_2 = 1/\rho\nabla$, and the non-linear operator $\mathfrak{NL}(\mathbf{u}, \nabla\mathbf{u})$ has been used as compact notations for the corresponding NS operators. In this analysis, the NS equations involved are in the LES framework, and

hence the variables represent the filtered quantities. ν is the kinematic viscosity of the fluid, while ν_t is the LES filtering eddy viscosity based on Smagorinsky type of closure. The splitting scheme for the NS equation (Equation 7.1) can be given as follows.

$$\mathfrak{L}_1(\mathbf{u}^{'}) + \mathfrak{L}_2(p^{'}) = \mathfrak{NL}(\mathbf{u}^{'}, \nabla\mathbf{u}^{'}) + B.C. \tag{7.2}$$

$$\mathfrak{L}_1(\mathbf{u}_0) + \mathfrak{L}_2(p_0) = \mathbf{f}_0 + B.C.(0) \tag{7.3}$$

The forcing function $\mathbf{f}_0$ represents the time-invariant unit pressure gradient forcing corresponding to the homogeneous linear NS equation. BC in Equation 7.2 is the boundary condition for the 3D inhomogeneous problem, corresponding to the shear stresses at the bottom "wall". The homogeneous boundary condition $BC(0)$ for the linearized split NS equation (Equation 7.3), comprises of periodic boundary conditions in the streamwise and spanwise directions, while homogeneous Neumann type stress-free boundary conditions are implemented in the wall-normal direction.

The reconstruction of the total NS velocity, forcing and pressure variable from the splitting terms can be obtained as

$$[\mathbf{u}\ p\ \mathbf{f}] = [\mathbf{u}^{'}\ p'\ 0] + \alpha[\mathbf{u}_0\ p_0\ \mathbf{f}_0] \tag{7.4}$$

α being a free parameter, which can be calculated at each time step from the specified flow rate constraint at that particular time. With flow-rate at time t, being $c(t)$, and A and V being the cross-sectional area of the flow and computational volume of the domain respectively, the flow rate can be written as

$$c(t) = \frac{A}{V}\int_\Omega \mathbf{u}\mathrm{d}\Omega = \frac{A}{V}\int_\Omega (\mathbf{u}^{'} + \alpha\mathbf{u}_0)\mathrm{d}\Omega \tag{7.5}$$

Consequently,

$$\alpha(t) = \frac{(c(t) - \frac{A}{V}\int_\Omega \mathbf{u}^{'}\mathrm{d}\Omega)}{\frac{A}{V}\int_\Omega \mathbf{u}_0\mathrm{d}\Omega} \tag{7.6}$$

The algorithm thus proceeds as follows. Equation 7.3 is solved once at the preprocessor step and its solution is stored in memory. At each subsequent time steps, Equation 7.2 is solved for $\mathbf{u}^{'}, \mathbf{p}^{'}$. The resulting solution corresponding to a specified flow rate $c(t)$ calculated from the cup and vane anemometer data (proportionately scaled from the bottom tip to the bulk mean assuming a a logarithmic profile for the mean velocity) as described below is then obtained from Equations 7.6 and 7.4 at each time t without any iterations.

The variation in the wind direction (wind veering – geophysical effect) has been incorporated by rotating the precursor inflow along the lines of Munters et al. [18] but without using domain-mapping methodology since the wind turbine domain inflow regime is completely overlapped by the precursor domain. Equation 7.7 shows the horizontal inlet velocities u_{inlet}, v_{inlet} obtained from horizontal velocities u, v of precursor ABL in the midplane, $x = \pi H$, with the mean wind direction $\theta_{mean}(t)$. At each timestep, the inflow domain is rotated by $\theta_m(t)$ about the point $[x_c, y_c]^T = [0, L_y/2]^T$ which serves as the center of rotation ($[-L_x/2 \; L_x/2] \times [0 \; L_y]$ is the extent of the precursor domain). The rotation matrix $\boldsymbol{R}(\theta(t))$ applied to the precursor domain coordinates and the horizontal velocities u, v can be given as

$$\boldsymbol{R}(\theta(t)) = \begin{bmatrix} \cos(\theta_m(t)) & -\sin(\theta_m(t)) \\ \sin(\theta_m(t)) & \cos(\theta_m(t)) \end{bmatrix}, \text{with} \begin{bmatrix} u_{inlet} \\ v_{inlet} \end{bmatrix} = \boldsymbol{R} \begin{bmatrix} u \\ v \end{bmatrix} \tag{7.7}$$

Here $\theta_m(t)$ in Equation 7.7 is obtained from the mean wind direction data (Figure 7.4b). Due to the rotation of the precursor simulation, the data to the inflow plane in the wind turbine array domain is being spectrally interpolated at each timestep from the precursor domain. Along the lines of Munter et al. [18], we can define a z dependant ratio $\varphi(z) = \frac{\Omega L_h}{U_h(z)}$, where $\Omega = d\theta_m/dt$ is the rate of change of wind direction, $L_h = \sqrt{(L_{m,x}^2 + L_{m,y}^2)}$ is the horizontal diagonal of the main domain ($L_{m,x}$ and $L_{m,y}$ are the streamwise and spanwise extent of the main domain respectively) and $U_h(z)$

is the temporally and horizontally averaged mean velocity of the precursor domain. A conservative upper-bound for the ratio φ is $\approx 2/3$, which ensures that the artificial elongation and compression of structures can be neglected. In this methodology, the timescale in the change of wind direction is significantly lower than the timescale imposed by the microscale turbulence, which is justified by the fact that our $\varphi \approx O(10^{-2})$ even in the inner layer, where the flow is dominated by the low mean velocities ($\sim 2-3$ m/s).

7.2.2 A Note on the Spanwise Periodicity in the Wind Turbine Domain

In our computation, the inflow plane is spectrally interpolated from the midway streamwise location of the precursor ABL domain (See Figure 7.2), while the spanwise boundary conditions are assumed periodic. The design of the domain overlapping is done in such a manner that the precursor box rotates by approximately $\approx \pm 40^{\circ}$ without leaving any inflow plane out of bounds with respect to the precursor domain. This approach in our two-domain LES simulations is offered as an attempt to a computationally cheaper alternative to full-nested simulations [201] requiring a wider precursor domain or precusor rotation with domain mapping [18].

However, the periodicity in the spanwise extent of $\sim 21D$, may create locked-in large scale structures (coupled with the effect of precursor ABL with locked-in structures of its own) [203], which gets convected in the direction of mean-wind. Furthermore it can be imagined that the spanwise periodicity ensures that the wind turbines are periodically extended in the spanwise direction and hence our simulations take a first step to emulate and fundamentally understand the streamwise evolution of ABL turbulence driven by realistic varying mean wind flux and wind direction. In addition, our spectral analysis (Figure 7.24, 7.23) reveals that this methodology successfully

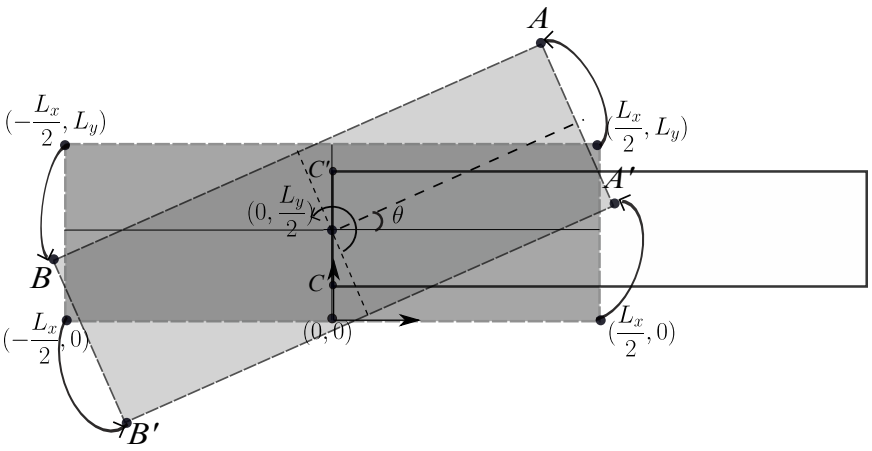

Figure 7.2: Instantaneous schematic snapshot of rotating the inflow domain (solid gray rectangle) by θ in the counter-clockwise direction. Outflow domain – white rectangle with black borders. The axis of rotation is z passing through the point $[0, L_y/2]^T$

captures the turbulence in the streamwise and spanwise scales $\lesssim 5D$ as is evident in the Kolomogorov -5/3 cascade ($\lambda_{x,y}^{2/3}$ in premultiplied spectrum vs wavelengths).

Note that only one LIDAR (located in the FINO platform, See Figure 7.3b) has been used for low-elevation PPI scan. A lidar scan essentially is completed in 45 secs, but since multiple snaphots of raw LIDAR scans have been used in the 2D VAR optimization algorithm, the two retrived snapshots are usually 1-2 minutes apart. In the retrieval methodology, only inplane velocities (i.e. in the plane scanned by the line of sight of LIDAR) have been considered. The mean wind speed and direction obtained from the LIDAR retrieval have been validated against the CVA data within 5% accuracy. Refer to [204] for more details regarding the 2D VAR algorithm and LIDAR data retrieval.

It is also to be noted that the resolution of LES simulations of WT array is $\sim 0.25D$ or 30 metres in the coarser regions of the mesh, while near the wind turbine array it is around $0.04D$ or 5 metres. The LIDAR retrievals (available for a planar data in PPI scan) manifest a coarser mesh of $\sim 0.25D$ or 30 metres throughout the domain

which is comparable to the coarser region of the LES mesh. However, a disparity in the temporal resolution between the LES and LIDAR resolutions are evident in the fact that the resolution of LES simulations is 0.06 secs, while that of the LIDAR retrieved scans $\sim 1 - 4$ minutes.

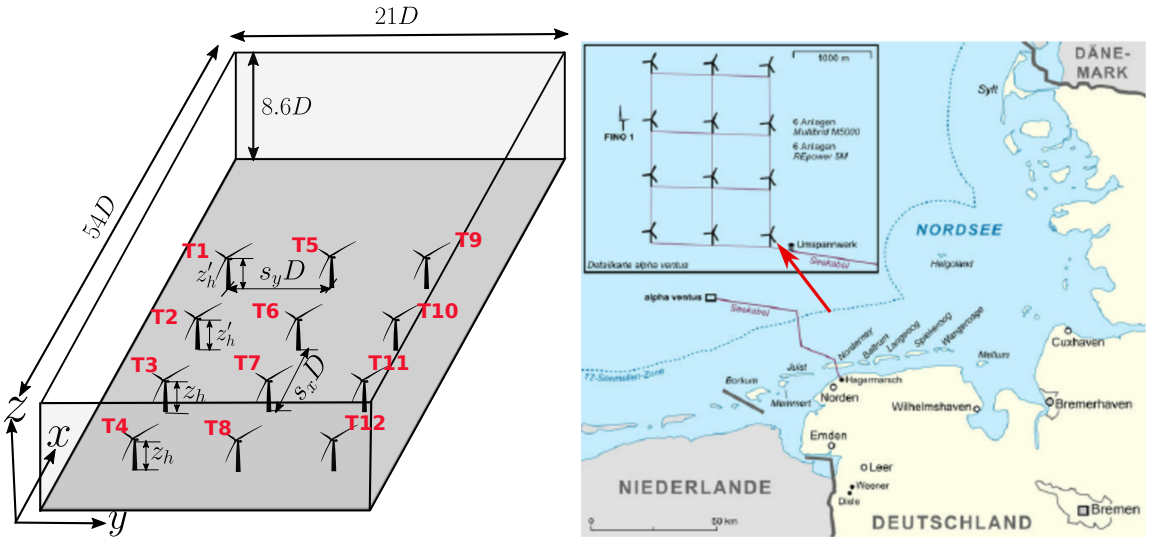

(a) (b)

Figure 7.3: (a) Computational domain to simulate realistic flow past the 12 turbines in Alpha Ventus farm. (b) Location of the wind farm at North Sea.

7.3 Results

In this section we present a comparison of the temporally filtered LES and LIDAR scan data in an effort to see if the variation in mean wind flux and direction coupled with LES has the capability of representating the velocity structures that were observed in LIDAR scans.

We begin by showing several visualizations of neutrally stratified turbulent flows past the wind farm from field experiments as well as from the current LES simulations. Figure 7.5 illustrates the snapshots (horizontal velocity magnitude) obtained by 2D-VAR retrieval algorithm around the bottom tip of the rotor from raw LIDAR data manifesting large scale structures at three different time-stamps, 6:13 am, 6:30 am and

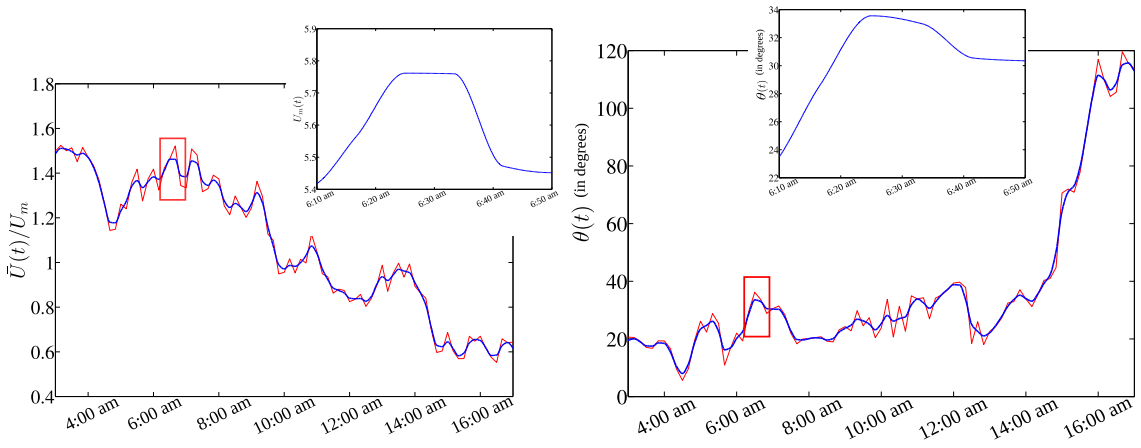

(a) (b)

Figure 7.4: Variation of (a) Mean wind velocity (b) Mean wind direction with local time on 31st August 2016 collected by the cup and vane anemometer from the meterological mast around the bottom tip of the turbine at FINO platform. Red thin – mean from 10 minute averaged wind data interpolated using piecewise cubic hermite polynomials corresponding to temporal LES resolution ($\Delta t \approx 0.06$ secs.). Blue thick – Gaussian smoothing performed on the 10 minute averaged wind using non-overlapping windowing involving 5 points. The red boxes indicate the extent of the data used to feed our LES simulations and the inset shows the zoomed-in fed mean wind velocity and wind direction data to simulations.

6:44 am. The snapshots show some high velocity large scale energetic structures near y $\sim$ 400 metres and 1200 metres. Some of those structures have completely dominant x directional flow, despite a prescribed mean wind direction. These might be attributed to the large scale geophysical/convectively unstable flow effects that are not captured by the simulation. It could also be present partly due to the inaccuracy of the LIDAR retrieval schemes close to the azimuthal sweeping range of the scans. Hence, when subsequent comparison with the LES simulations have been performed later, we have extracted data in the inter-turbine region in the spanwise direction (i.e. locations away from the boundaries), with some discrepancies observed due to those high-velocity turbulent structures not captured by the LES simulations. Similar temporally filtered snapshots (filtered for 0.5 minutes and 2 minutes) from LES simulations (timestamps of 6 : 13 am, 6 : 44 am) are also documented in Figure 7.6, 7.7 at hub-height, bottom

tip and top-tip location of the wind turbines. Please note, that the vertical location of the snapshots documented at the hub-height z_h and bottom/top tip locations $z_h + D/2$ corresponds to the Adwen AD 5-116 turbines in the farm. For streamwise, spanwise velocities u, v (obtained from LES simulations), the temporal filtering is defined as $\{\widehat{u}_{\langle T \rangle}, \widehat{v}_{\langle T \rangle}\} = \frac{1}{T}\int_0^T \{u, v\} \mathrm{d}t$, where t is the instantaneous time variable and T is the time-span for which filtering is performed. For a temporal filtering of 0.5 minutes, 5000 snapshot realizations from LES (generated at each timestep of the LES solver) have been used. In contrast, the LIDAR retrieved data has significantly less number of samples (2-3) to generate even a 2 minute temporally filtered data. For brevity in subsequent plots, symbols u, v have been used even for temporally filtered variables $\widehat{u}_{\langle T \rangle}, \widehat{v}_{\langle T \rangle}$. The temporal filtering is performed to remove noise from the instantenous velocity snapshots facilitating the attempt to compare with the field experimental results.

To complement the above plots, Figure 7.8, manifests the snapshots of instantaneous horizontal velocity magnitude, (timestamps of 6 : 13 am, 6 : 44 am) at the bottom tip and hub-height location of the wind turbines. It is clear that due to the noise present in the instantaneous snapshots capturing turbulence, the wakes are not as prominently visible as they are in the temporally filtered snapshots (both 0.5 and 2 minutes filtered LES data in Figures 7.6, 7.7)

Additionally, in Figure 7.9 we document the instantaneous vertical velocity structures captured by the LES simulations. In particular, Figures 7.9c, 7.9d illustrate the z variation of vertical velocity just behind the second row of turbines, while Figures 7.9a, 7.9b show the vertical velocity at the bottom tip of the rotors at two different timestamps, 6:13 am and 6:44 am. Note that 2D-VAR retrieval scheme retrieves only in-plane horizontal velocities from the low elevation angle PPI scan ($\approx 0.5^\circ$), thus neglecting the vertical velocity effects. This is a reasonable approximation, since even

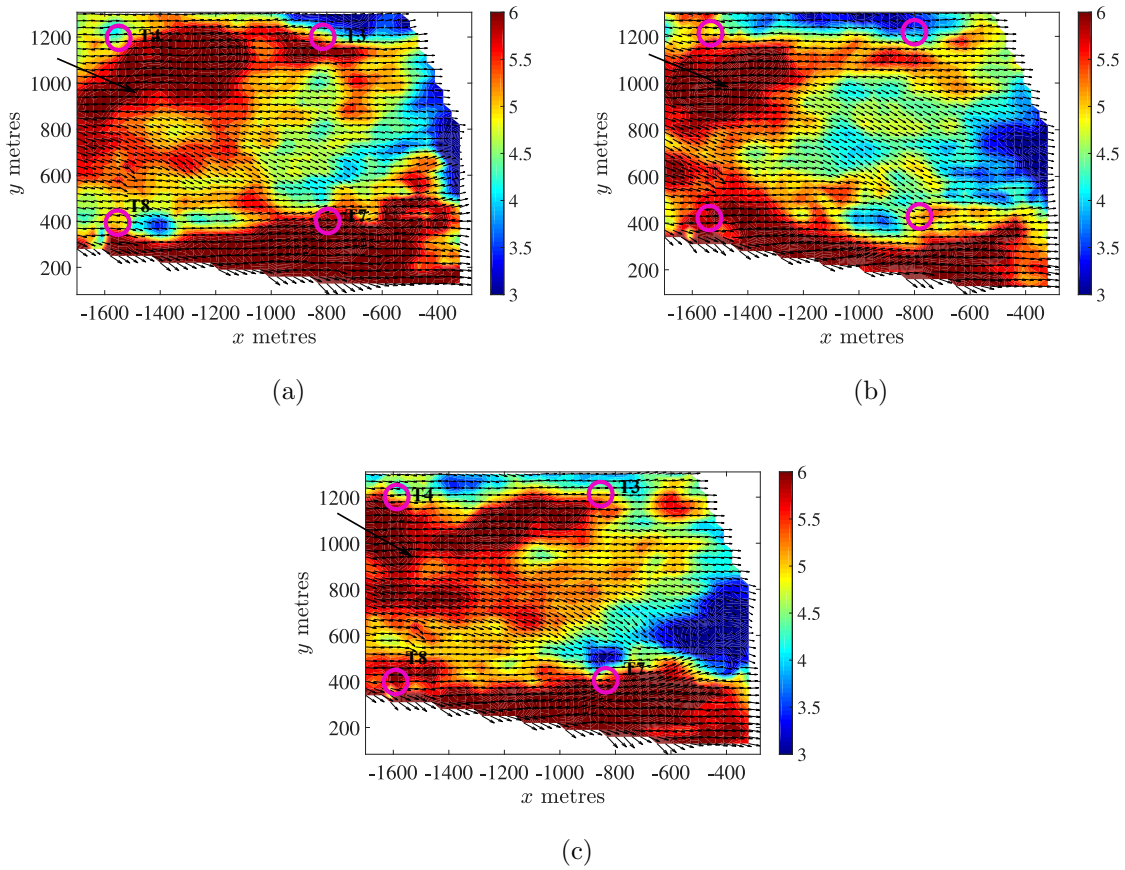

(a) (b)

(c)

Figure 7.5: Snapshot of horizontal velocity magnitude $\sqrt{u^2 + v^2}$ m/s for flow past the wind farm obtained from the retrieval of LIDAR scan data using 2D VAR algorithm. z location at the bottom tip of the rotor. Data at local time (a) 6:13 am (b) 6:30 am (c) 6:44 am. LIDAR data collected at 31st August 2016. Arrow – direction of mean wind at corresponding local times; Magenta circles: Location of turbines

though the vertical velocity at the outer layer contains large structures ($w \sim$ 15-20% of horiziontal velocity magnitude) depicted by LES simulations, near the bottom tip of the rotor ($\sim$ 30 - 40 metres from the bottom "wall") such energetic vertical velocity events are rare with vertical velocity structures of around $\sim$ 2% of the horizontal velocity magnitude (See Figure 7.9a, 7.9b).

Before moving on to the comparison of LES and LIDAR scan results, we present the simulation results of neutral ABL precursor simulation. The instantaneous velocity structures in the z location corresponding to the bottom tip and hub-height of

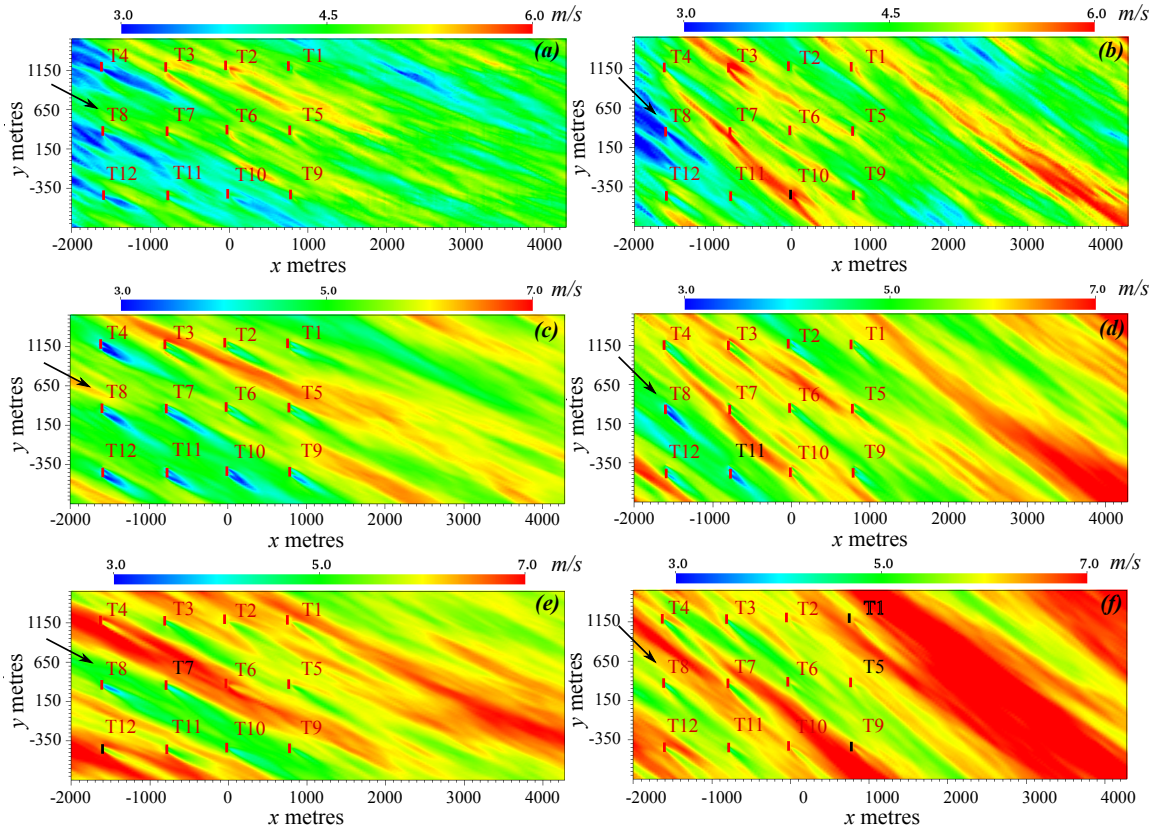

Figure 7.6: Horizontal velocity magnitude $\sqrt{u^2+v^2}$ in m/s in the xy plane temporally filtered for 0.5 minutes. Timestamp location: Left – 6:13 am, Right – 6:44 am. z location: First row – $z_h - D/2$ (bottom tip), Second row – z_h (hub height), Third row – $z_h + D/2$ (top tip). z_h, D corresponds to Adwen AD 5-116 turbines in the farm. Arrows - Mean wind direction at corresponding local times.

wind turbine array (Figures 7.10a, 7.10b) indicate that the inflow condition due to precursor properly reflects the turbulence generated in the flow upstream of the wind turbine array. The 10 minute temporally filtered ABL data (Figure 7.10c) illustrates the locked-in large scale structures (banded velocity structures in the spanwise direction), due to the limited streamwise extent of the precursor domain. These locked-in structures propagated to the wind turbine domain through the inflow conditions, and along with similar locked-in effects due to the spanwise periodicity of the wind turbine domain, may be responsible for some of the large-scale structures seen in the wind turbine array simulations as depicted in Figures 7.6, 7.7.

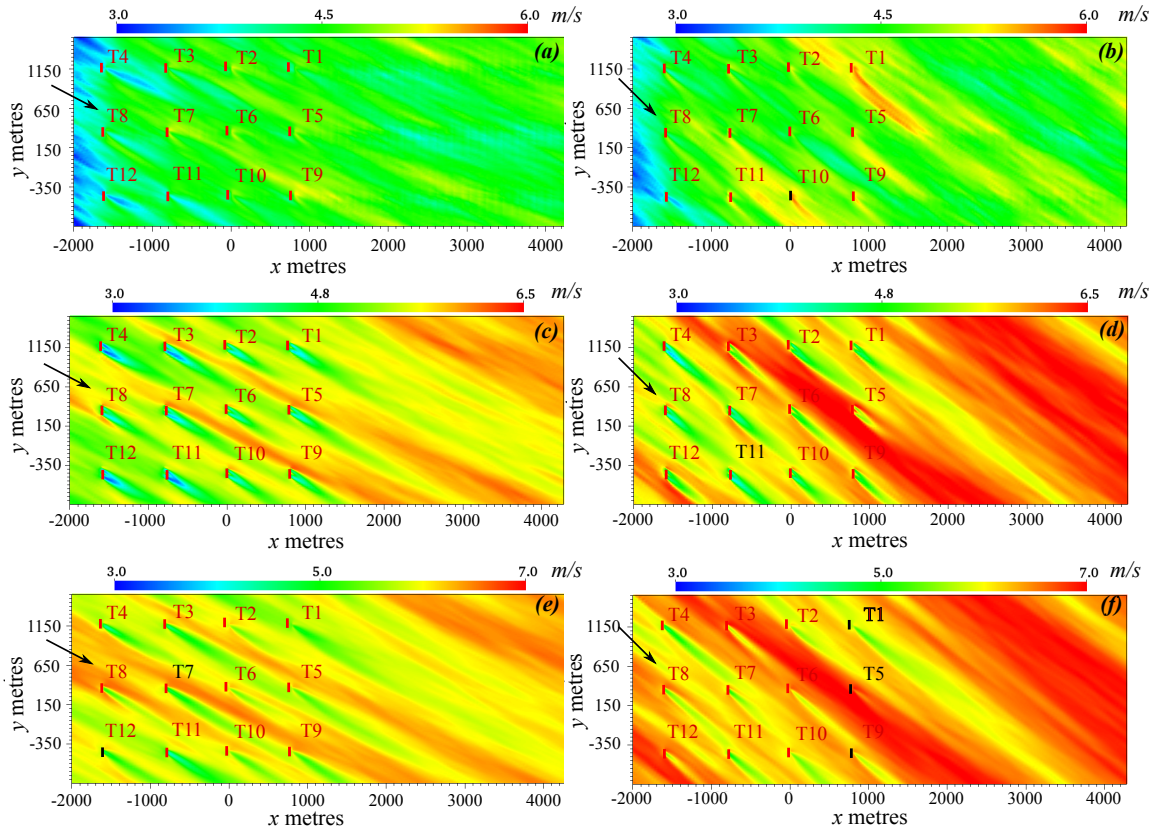

Figure 7.7: Horizontal velocity magnitude $\sqrt{u^2+v^2}$ in m/s in the xy plane temporally filtered for 2 minutes. Timestamp location: Left – 6:13 am, Right – 6:44 am. z location: First row – $z_h - D/2$ (bottom tip), Second row – z_h (hub height), Third row – $z_h + D/2$ (top tip). z_h, D corresponds to Adwen AD 5-116 turbines in the farm. Arrows - Mean wind direction at corresponding local times.

The spanwise periodic boundary condition gives rise to the locked-in large scale structures which are generally unavoidable and no effective solution has been found to deal with them, except perhaps with shifted periodic boundary conditions as noted by Munters et al. [18] which were found to influence the spectral scaling of the turbulence at smaller scales, where Kolmogorov cascade is dominant. Studies involving data assimilation, where the spatio-temporal velocity data from the field experiments is coupled with the simulations, would still have these locked in features and hence need careful analysis. Furthermore, it must be noted that since locked-in structures are typically a large scale phenomenon, with length scales involving 5-10 times the

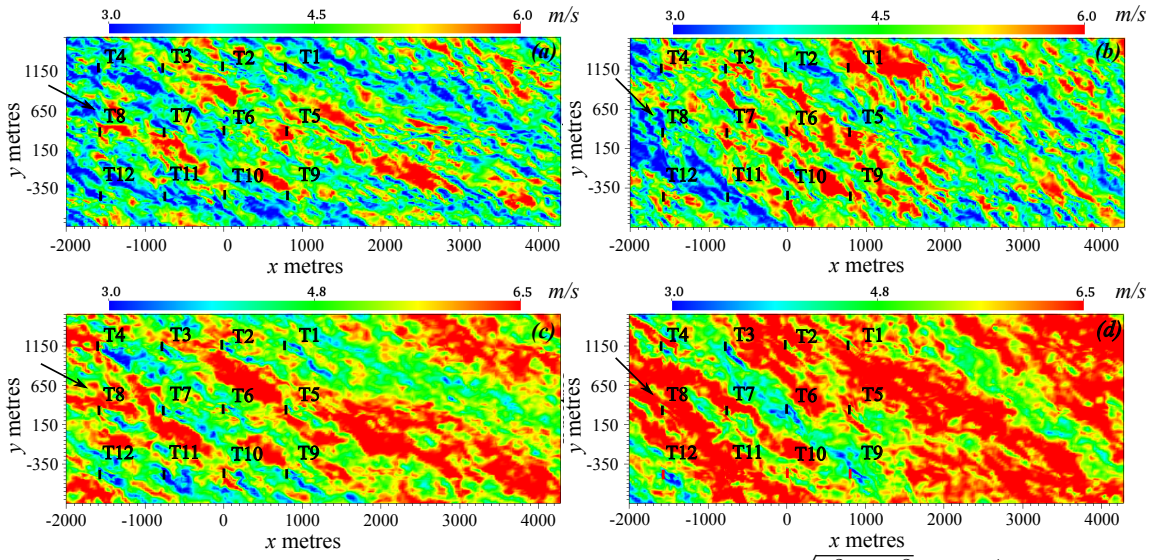

Figure 7.8: Instantaneous horizontal velocity magnitude $\sqrt{u^2+v^2}$ in m/s in the xy plane. Timestamp location: Left – 6:13 am, Right – 6:44 am. z location: First row – $z_h - D/2$ (bottom tip), Second row – z_h (hub height). z_h, D corresponds to Adwen AD 5-116 turbines in the farm. Arrows - Mean wind direction at corresponding local times.

domain size, significant increment of the domain size is required, which would create extremely high computational overhead on the LES simulations. Despite being a large scale event, the locked in structures are local and are not known to influence the spatially averaged results or the two dimensional energy spectra. Furthermore, despite the use of periodic boundary condition, realistic turbulence in the spanwise direction (evidenced in the cascades of spanwise spectra, Figure 7.24) could be observed, which indicates that the small scale turbulence are not influenced by the short spanwise extent of boundary conditions. Overall, the current LES simulation would serve as a first important step towards a fundamental understanding of flow and their streamwise-temporal evolution past the wind farms driven by the realistic variation in mean wind speed and wind direction.

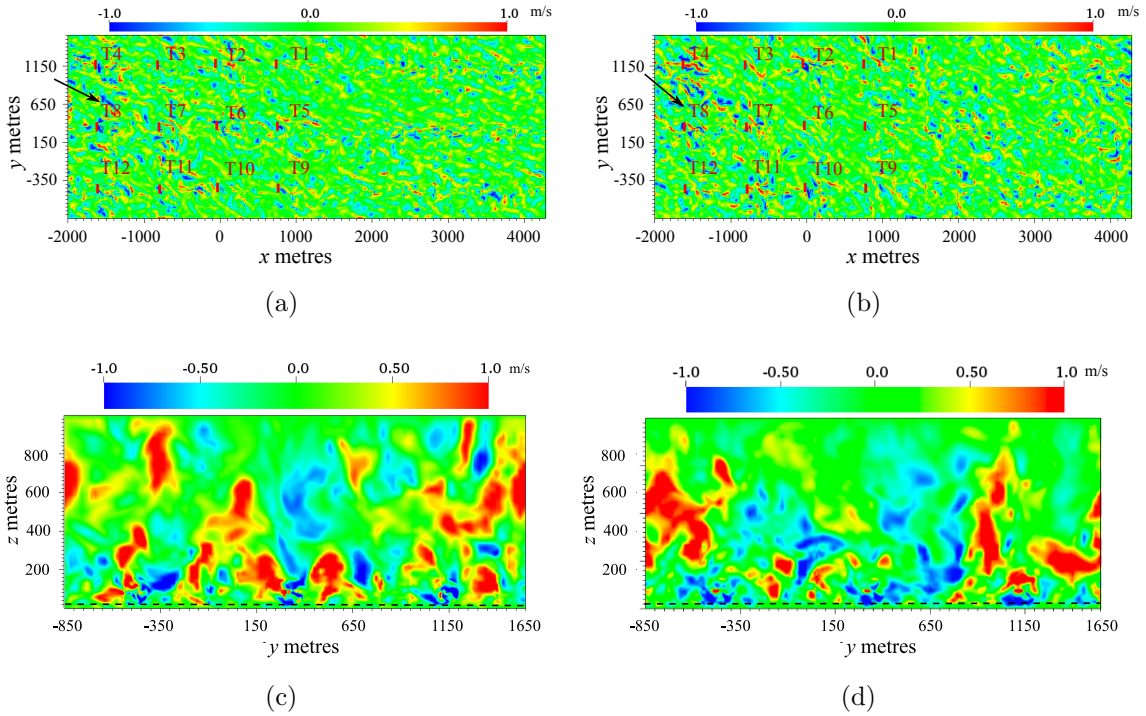

Figure 7.9: Instantaneous vertical velocity w in m/s in the xy plane at $z = z_h - D/2$ (bottom tip). Timestamp location: (a) 6:13 am, (b) 6:44 am. Vertical velocity in yz plane at $x = x_t + 0.5D$, at timestap location 6:. x_t location of second row of turbines. Timestamp location: (c) 6:13 am, (d) 6:44 am. Black dashed line – $z = z_h - D/2$. z_h, D corresponds to Adwen AD 5-116 turbines in the farm. Arrows - Mean wind direction at corresponding local times.

7.4 Influence of Coriolis Forces

In this section we investigate the influence of Coriolis forces in Alpha-Ventus wind farm driven by the same mean wind (Figure 7.4a, 7.4b). The motivation of using Coriolis forces is to examine if some of the large scale features observed in LIDAR scans could be better represented by the Coriolis effects. Of course it must be noted that since Coriolis force causes turning effects, the large scale structures would develop an additional curvature that depends on the stength of the Coriolis effect, or the non-dimensional Rossby number Ro ($Ro = \frac{U}{fL}$, U is a reference velocity scale, L a reference length scale and $f = 2\Omega \sin(\phi)$ is the Coriolis frequency parameter, Ω is the rotation of the Earth and ϕ is the latitude). The Coriolis forces have been added as a horizontal

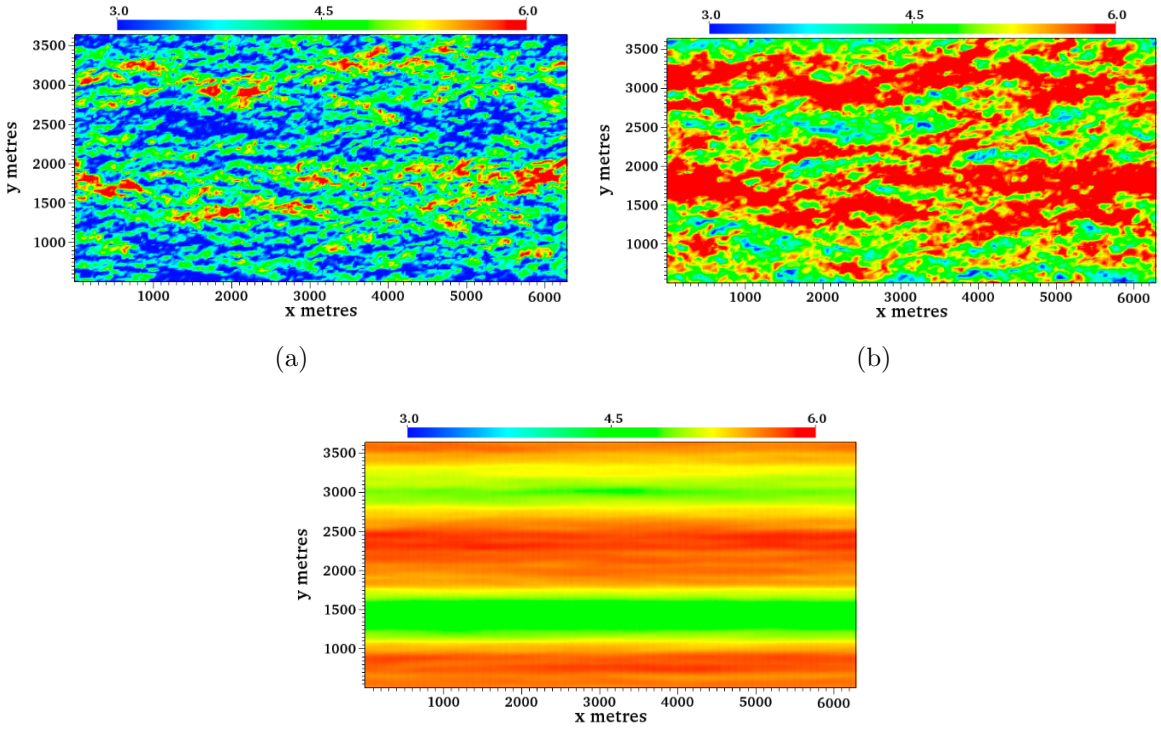

(a) (b)

(c)

Figure 7.10: Instantaneous horizontal neutral ABL velocity $\sqrt{u^2+v^2}$ in m/s in the xy plane at vertical height locations, (a) $z = z_h - D/2$ (b) z_h. (c) Time-averaged velocity at z_h depicting locked-in structures. z_h, D corresponds to Adwen AD 5-116 turbines in the farm.

forcing term $(fv, -fu)$ in the Navier-Stokes equation.

The Navier-Stokes equation along with the Coriolis force components can be written as

$$\frac{\partial u}{\partial t} + u\frac{\partial u}{\partial x} + v\frac{\partial u}{\partial y} + w\frac{\partial u}{\partial z} = -\frac{1}{\rho}\frac{\partial p}{\partial x} + (\nu + \nu_t)\nabla^2 u + fv \tag{7.8}$$

$$\frac{\partial v}{\partial t} + u\frac{\partial v}{\partial x} + v\frac{\partial v}{\partial y} + w\frac{\partial v}{\partial z} = -\frac{1}{\rho}\frac{\partial p}{\partial y} + (\nu + \nu_t)\nabla^2 v - fu \tag{7.9}$$

$$\frac{\partial w}{\partial t} + u\frac{\partial w}{\partial x} + v\frac{\partial w}{\partial y} + w\frac{\partial w}{\partial z} = -\frac{1}{\rho}\frac{\partial p}{\partial z} + (\nu + \nu_t)\nabla^2 w, \tag{7.10}$$

where ν_t is the eddy viscosity supplied the subgrid scale model. The effect of Coriolis forces in neutral (and conventionally neutral) atmospheric boundary layer and wind farms in particular have been investigated in the past [205–209], with Rossby

numbers varying from $O(10^{-1}) - O(10^{3})$ based on representative length scales of interest. In particular, [205] noted that the Coriolis effects can be neglected in atmospheric boundary layer studies, if the Rossby number is $\sim O(10^{3})$. In our current study we are interested in the regime of low-moderate Rossby numbers ($Ro \sim 10^{2}$), such that the effects of Coriolis forces are not neglible, yet they are not low enough to have geophysical circulations. Note, that in our current simulations, we have used a fixed Rossby number (similar to what has been proposed in the literature) of $Ro = 300$, using the bulk mean velocity of the inflow (temporally averaged), U_m fed by the neutral ABL precursor as a representative velocity scale and the streamwise domain size, L_x as the representative length scale. Consequently, we can calculate $f = U_m/(RoL_x)$, that has used in our wind farm computations. It can be observed, that the definition of a length scale would have impact on the magnitude of the Rossby number. For completeness, it is worthwhile to note that, using a length scale corresponding to ABL thickness would generate a Rossby number ≈ 1800, or a length scale corresponding to the diameter of the wind turbine rotors (e.g., Adwen AD-5-116 turbines), would generate a Rossby number $\approx 1.55 \times 10^{4}$. The choice of the Rossby number was made in an effort to understand, as a first step, how Coriolis force would influence the flow past the wind turbine arrays driven by a realistic temporally varying mean wind.

In our simulation setup, we have incorporated Coriolis forces in the wind farm domain while the precursor ABL is driven by the pressure gradient forcing with temporally changing mean wind direction and magnitude. This setup is similar to one of the cases studies by Akbar and Porté-Agel [208] in an effort to isolate the wind veering effects due to the Coriolis forces with respect to an already existing changing mean wind direction resulting from the combination of geophysical effects and serving as a direct input to the data. Furthermore, [208] has not observed significant differences in the incoming mean wind and turbulent stresses in the first $100 - 150$ metres (around

the hub-height of wind turbines) from the wall in neutral ABL with Coriolis forces, when compared against ABL simulations driven by constant pressure gradient. This setup with the neutral ABL precursor being driven by pressure gradient forces (without Coriolis forces) is beneficial for two reasons, (a) it helps to decouple the effect of Coriolis forces in the wind farm with identical inflows and (b) it circumvents the need of an artificial yaw-angle controller in the direction of mean wind, since the wind direction with Coriolis forces incorporated would not be known apriori at hub-height due to the development of Eckman spiral [207, 209].

The wind farm spreads less than 0.01 degrees of lattitude (at $\sim 54^{\circ}$ N) in the Northern Hemisphere, and hence a constant Coriolis parameter is assumed in our simulations (i.e. neglecting the β plane approximation [210].)

Figures 7.11, 7.12 illustrate the 0.5 minute and 2 minute temporally filtered horizontal velocity field influenced by the Coriolis forces. Similar large scale structures could be identified for cases without the Coriolis effects (Figures 7.6, 7.7), but the contours with Coriolis forces illustrate some turning effects with the large scale structures comparable to the size of the domain turning towards its left. Even though for wind turbines perceived as an added roughness to the ABL, the Coriolis effects essentially turn the large scale structures towards their left in the Northern Hemisphere (owing to an increased spanwise momentum) as was seen in previous studies [208, 211], a recent RANS based study by van der Laan and Sørensen [212] has revealed that the wind turbine structures turn towards their right, owing to a complex interaction with the Coriolis forces and turbulent stresses in the lateral and wall-normal direction. Even though our simulations do indicate the importance of lateral stresses [208] via spectral analysis (shown later), our results illustrate the turning effect towards their left in accordance with what was observed prior to [212]. The instantaneous horizontal and vertical velocity profiles with Coriolis forces are depicted in Figures 7.13, 7.14. The

velocity flow field observed is qualitatively very similar to that without the Coriolis effects considered, especially for flow structures $\gg D$ (Figures 7.8, 7.9).

7.4.1 Comparison of LIDAR Retrieved Data with LES Simulations – with and without Coriolis Forces

In order to visualise the effects of Coriolis forces on the flow field, a one-to-one comparison of the flow field in the yz plane with and without Coriolis forces is presented in Figure 7.15. The 0.5 minute temporally filtered total velocity field $\sqrt{u^2 + v^2 + w^2}$ indicates, that the high velocity structures in the outer layer with Coriolis forces are shifted by less than 50 metres towards their right when compared with the velocity field without it, while no conspicuous changes are observed in the low velocity inner layer region. This is understandable, since the Coriolis forces are proportional to the horizontal velocity fields, hence the discrepancies without the Coriolis effects would be prominent in the higher velocity region. The streamwise contours with and without Coriolis effects (xz plane) in Figure 7.16 also depict that inconspicuous differences can be observed in the streamwise evolution of structures in the inner and outer layer. The vertical variation of streamwise velocity profile at 3 distinct streamwise stations close to the wind turbine with and without Coriolis forces (Figure 7.17) also indicates some differences in velocity, especially close to the turbine hub-height.

In Figure 7.18, the temporal evolution of the spatially filtered horizontal velocity magnitude (integrated in between the line-region of two turbines T3-T7) has been depicted which illustrates a comparison of the temporal variation of LIDAR retrieved data with the present LES simulations. The plots manifest various levels of temporal low-pass filtering (l0.5 minutes, 2 minutes) and expectedly, for filtering involving larger timespans, the small scale features are smoothened out, thus manifesting the large scale variations. Interestingly, the 2 minute filtered horizontal velocity mag-

nitude without the Coriolis forces show excellent trends with the mean wind of the ABL precursor at the bottom hub-height of the turbine rotor. The simulations with Coriolis forces illustrate that the 2 minute temporally filtered horizontal velocity magnitude also display a similar trend with the data without the Coriolis forces and are well correlated in time, but underpredict the mean wind by $\sim 3\%$. Since, time averaged velocity profile (Figure 7.17) has shown negligible differences in the streamwise velocity with and without Coriolis forces, the discrepency observed in the 2 minute filtered data is possibly due to the reorganization of velocities due to Coriolis effects in the horizontal and vertical directions. Further investigations are necessary to understand if such discrepancies in the velocities are owing to mixing of the turbulent flow induced by the Coriolis forces (Mixing due to Coriolis forces have been observed in flows of different length scales [213], [214]). Both the LES simulations with and without Coriolis effects have been included in the plot. The plot is further supported by the Figure 7.19, where the instantaneous as well as time-filtered velocity fields for cases without the Coriolis effects have been documented for reference. For clarity of the plots in Figure 7.19 we have only shown the data without Coriolis forces.

The spatial filtering can be defined as $\{\widehat{u}_{\langle y \rangle}, \widehat{v}_{\langle y \rangle}\} = \dfrac{1}{Y_{span}} \displaystyle\int_{y_{T_3}}^{y_{T_7}} \{u, v\} \mathrm{d}y$, where y is the spanwise coordinate and Y_{span} is the spanwise distance between the turbines T3 and T7, which is $\approx$ 800m. Analogous to temporal filtering, subsequent plots involving spatial filtering utilize symbols u, v which has been used for spatially filtered velocities.

Figures 7.20, 7.21 depict the comparison of LES simulations (with and without Coriolis forces) with LIDAR retrieval between the turbines T3 and T7 for 3 different timestamps of 6:13 am, 6:30 am and 6:44 am. Spanwise plots at 400 metres upstream location of the T3-T7 turbine row are also shown for comparison. The plots contain two different vertical locations (bottom tip and $0.15D$ below the bottom tip) for the LES simulations depicted by lines while the symbols illustrate the 2D-VAR retrieved

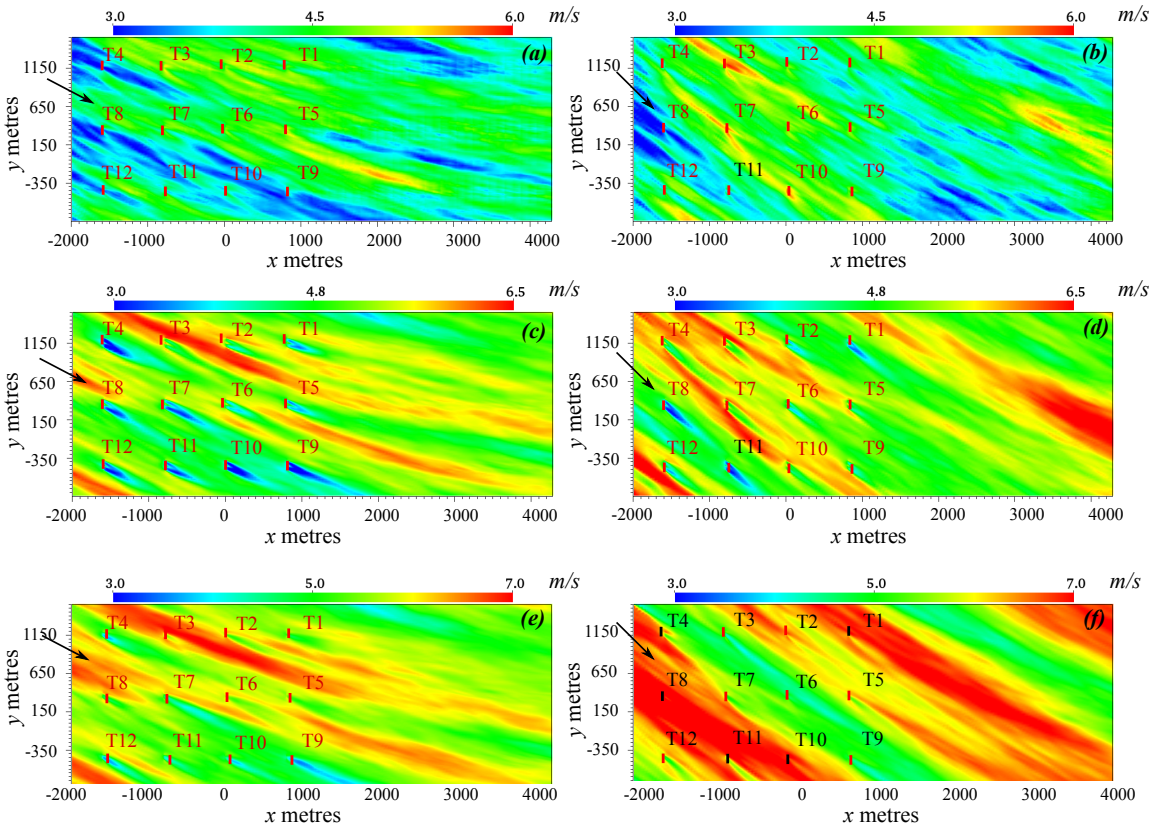

Figure 7.11: Horizontal velocity magnitude $\sqrt{u^2 + v^2}$ in m/s in the xy plane temporally filtered for 0.5 minutes. Timestamp location: Left – 6:13 am, Right – 6:44 am. z location: First row – $z_h - D/2$ (bottom tip), Second row – z_h (hub height), Third row – $z_h + D/2$ (top tip). Arrows - Mean wind direction. With Coriolis forces – $Ro \approx 300$.

LIDAR scan data collected near the bottom tip of the rotor. As can be observed, the plots depict a reasonable agreement within a band that is comparable to a potential uncertainty of a LIDAR data due to the grid size limitation in 2D-VAR retrieval algorithm. Nonetheless, some descripancies could be noted possibly due to the inability of the LES model to capture high velocity structures which might arise either from the geophysical effects not modeled by the system or from the inaccuracy of the LIDAR retrieval schemes near the maximum and minimum range of the azimuthal scans. At this point, due to a lack of enough data, the reason of those high velocity structures in LIDAR scans is not clearly understood and requires further investigation.

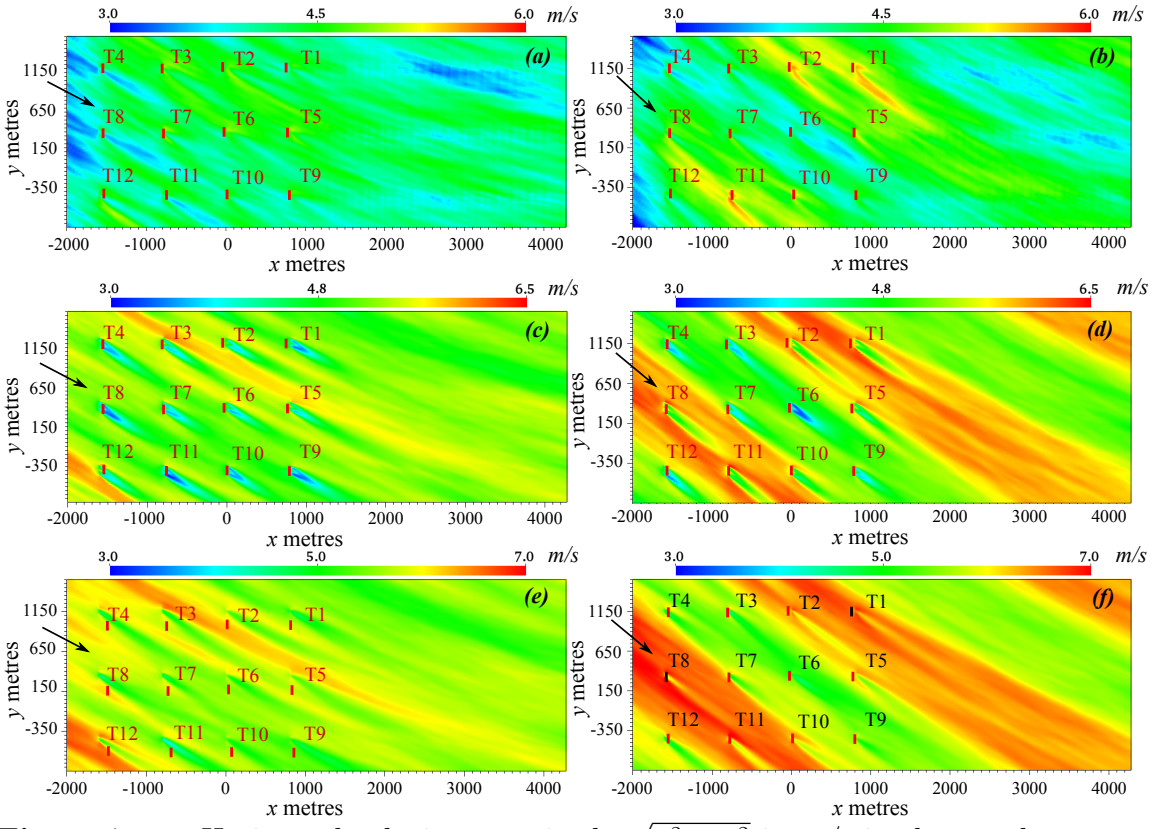

Figure 7.12: Horizontal velocity magnitude $\sqrt{u^2 + v^2}$ in m/s in the xy plane temporally filtered for 2 minutes. Timestamp location: Left – 6:13 am, Right – 6:44 am. z location: First row – $z_h - D/2$ (bottom tip), Second row – z_h (hub height), Third row – $z_h + D/2$ (top tip). Arrows - Mean wind direction. With Coriolis forces – $Ro \approx 300$.

7.4.2 Power and Energy Spectra

In this section, we begin by investigating the mean power and the frequency content of the turbine power in Alpha Ventus wind farm. The power spectral results in Figures 7.22a, 7.22b reveal that large scale temporal dynamics and hence power are affected by the "turning effects" of the Coriolis forces. This is further illustrated in the mean power of the farm, which shows the effects of Coriolis forces that are shown in the subsequent rows in the spectra. However, cross correlation spectra (Figures 7.22c, 7.22d), dos not reflect any deviations between the cases with and without Coriolis effects. The wind direction at the inflow is such that the wakes of

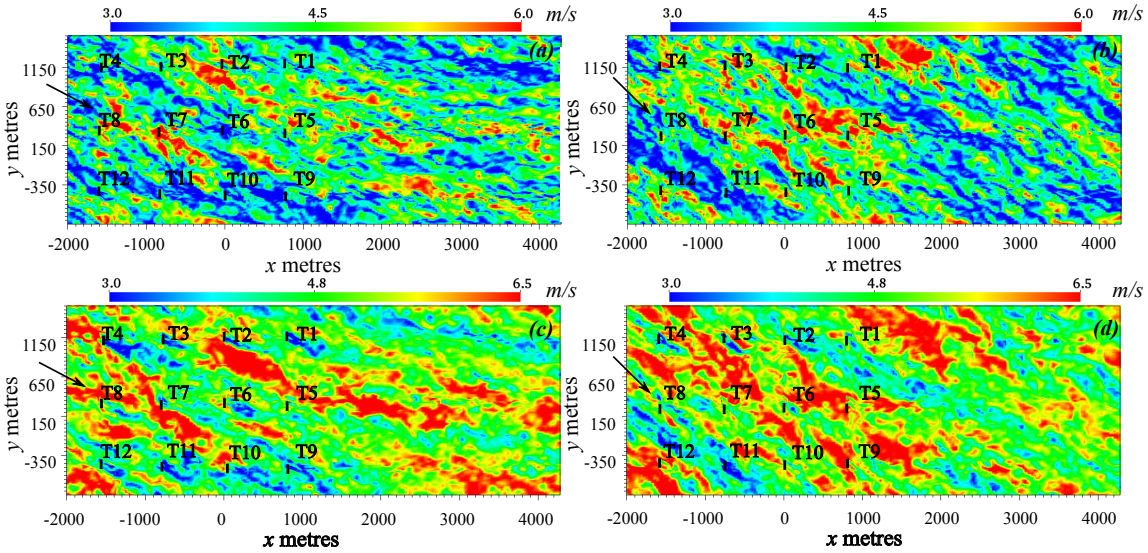

Figure 7.13: Instantaneous horizontal velocity magnitude $\sqrt{u^2+v^2}$ in m/s in the xy plane. Timestamp location: Left – 6:13 am, Right – 6:44 am. z location: First row – $z_h - D/2$ (bottom tip), Second row – z_h (hub height). Arrows - Mean wind direction. With Coriolis forces – $Ro \approx 300$.

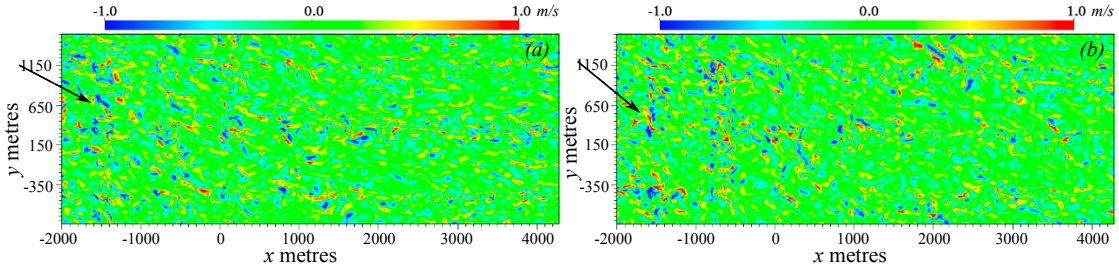

Figure 7.14: Instantaneous vertical velocity w in m/s in the xy plane at $z = z_h - D/2$ (bottom tip). Timestamp location: (a) 6:13 am, (b) 6:44 am. Arrows - Mean wind direction. With Coriolis forces – $Ro \approx 300$.

the first row affects the third row and that in the second affects the fourth. This is manifested in the row by row power variation in Figure 7.22e. Furthermore, it is observed that due to the turning effects of the large scale structures by the Coriolis forces, the row averaged power in the subsequent rows after the first drops compared to the case without Coriolis effects, due to the turning effects on the large scales, which results in those structures missing the turbines in the last two rows of the wind farm. Note, due to the lack of turbine power data from LIDAR field experiments, a power comparison is not possible and is currently planned for future studies as the

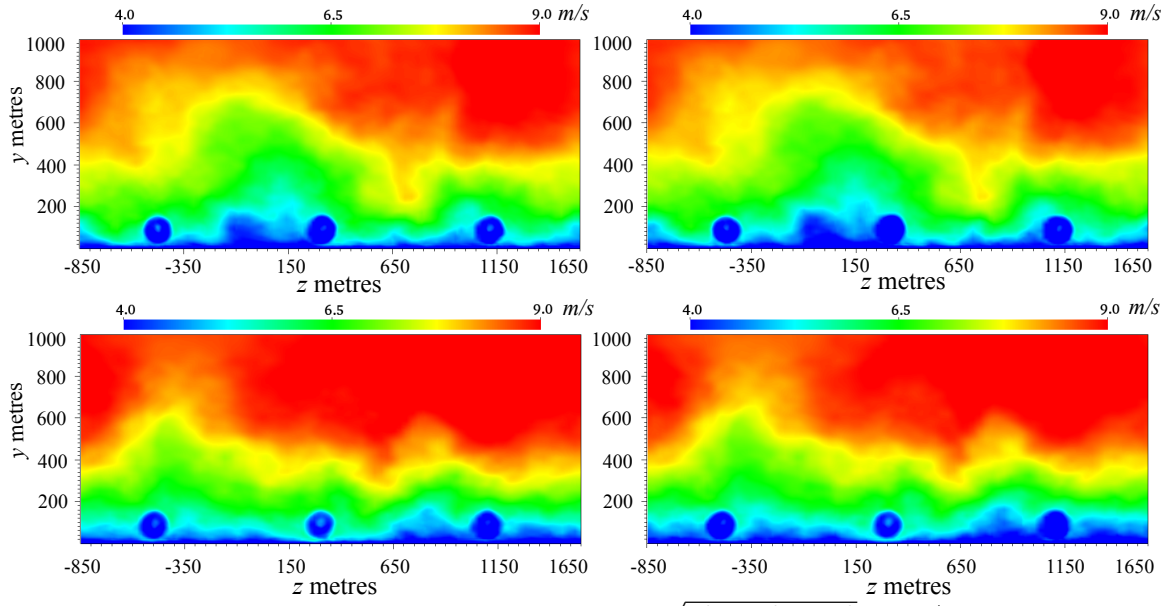

Figure 7.15: Temporally filtered total velocity $\sqrt{u^2+v^2+w^2}$ in m/s in the yz plane at $x = x_t + 0.5D$ (x_t location of second row of turbines). Timestamp location: 6:13 am (top), 6:44 am (bottom). Left – without Coriolis forces. Right – with Coriolis forces – $Ro \approx 300$.

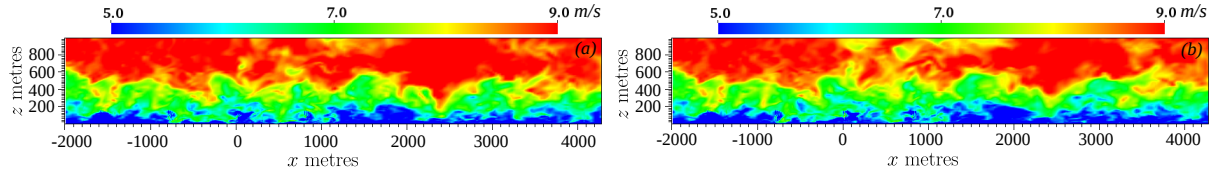

Figure 7.16: Instantaneous total velocity $\sqrt{u^2+v^2+w^2}$ in m/s in the xz plane at $y = y_t$ (y_t location of middle column of turbines). Timestamp location at 6:10 am. Left – without Coriolis forces. Right – with Coriolis forces – $Ro \approx 300$.

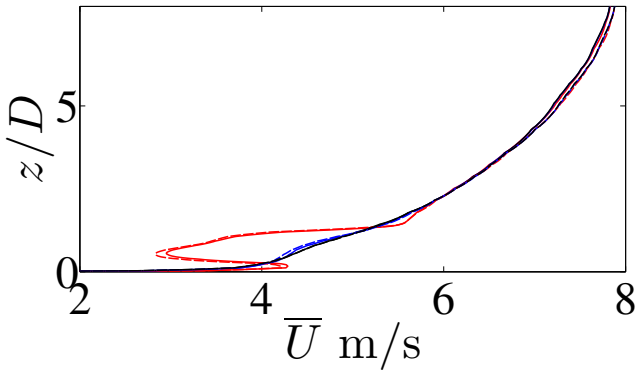

Figure 7.17: Spanwise and temporally averaged vertical profile of streamwise velocity in m/s. y location: corresponding to the middle column of the turbines. Solid – without and Dashed – with Coriolis forces, $Ro \approx 300$. Red – $x = x_t + 0.5D$, Blue – $x = x_t + D$, Black – $x = x_t + 1.5D$, where x_t is the streamwise location of second row of turbines.

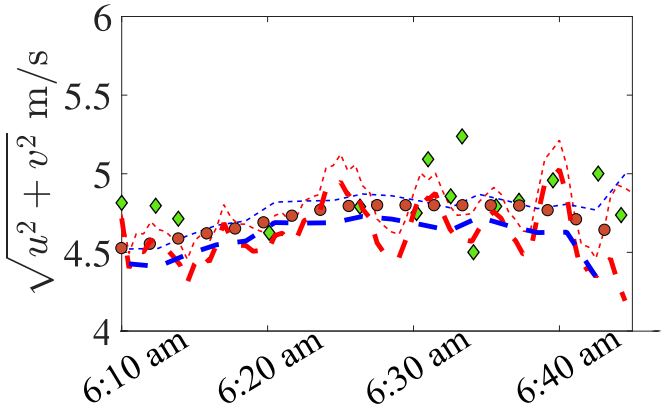

Figure 7.18: Temporal variation of 0.5 mins (dashed red) and 2 mins (dashed blue) temporally filtered horizontal velocity magnitude spatially filtered in the spanwise direction between turbine locations T3 and T7. Instantaneous data is low-pass filtered (5 point moving average filter) to illustrate the large scale trends. Thick – With Coriolis, Thin – Without Coriolis. Circles – Variation of mean wind. Diamond – data from LIDAR retrieval scan at the location of second row of turbines.

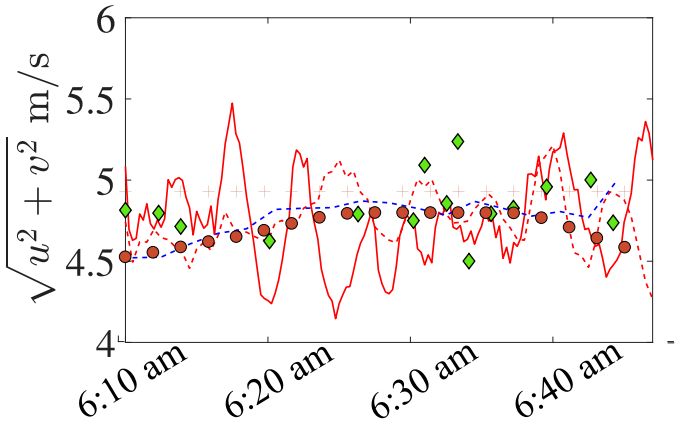

Figure 7.19: Temporal variation of instantaneous (solid red), 0.5 mins (dashed red) and 2 mins (dashed blue) temporally filtered horizontal velocity magnitude without Coriolis forces, also spatially filtered in the spanwise direction between turbine locations T3 and T7. Diamond – data from LIDAR retrieval scan at the location of second row of turbines. All data collected/calculated at $z = z_h - D/2$.

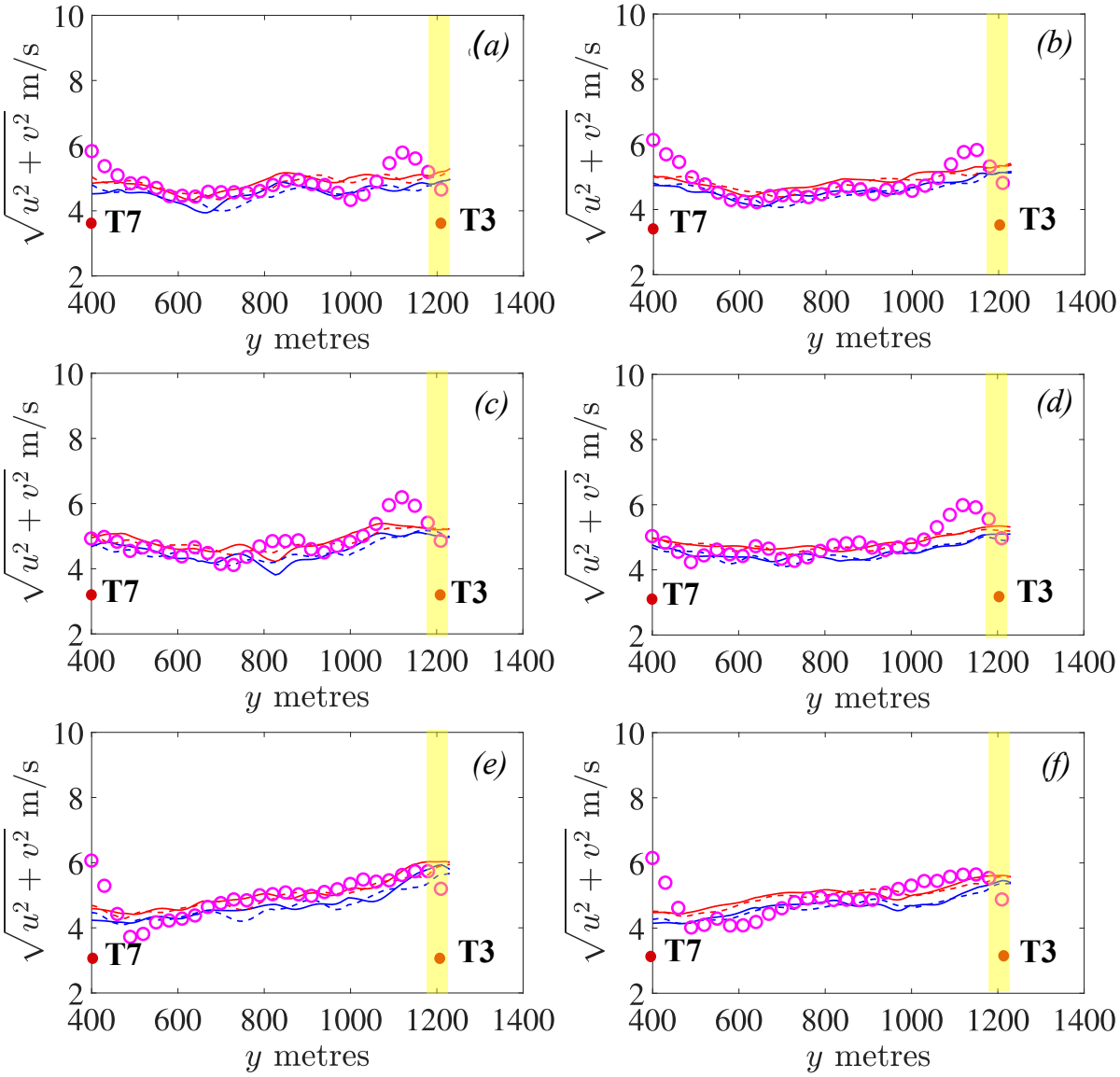

Figure 7.20: Comparison of LES and LIDAR scan experiments. Lines – LES data, Magenta symbols – LIDAR scans. Data temporally filtered for 2 mins (left), 4 mins (right). Streamwise location – turbine row T3 – T7. Solid (without Coriolis), Dashed (with Coriolis). z locations: – $z_h - D/2$ (Red); – $z_h - D/2 - 0.15D$ (Blue). Estimated location of turbines T7 (left), T3 (right) marked in red circles. LIDAR data collected at 31st August 2016, local start time – (a),(b) 6:10 am (c),(d) 6:30 am (e),(f) 6:44 am from which temporal filtering started.

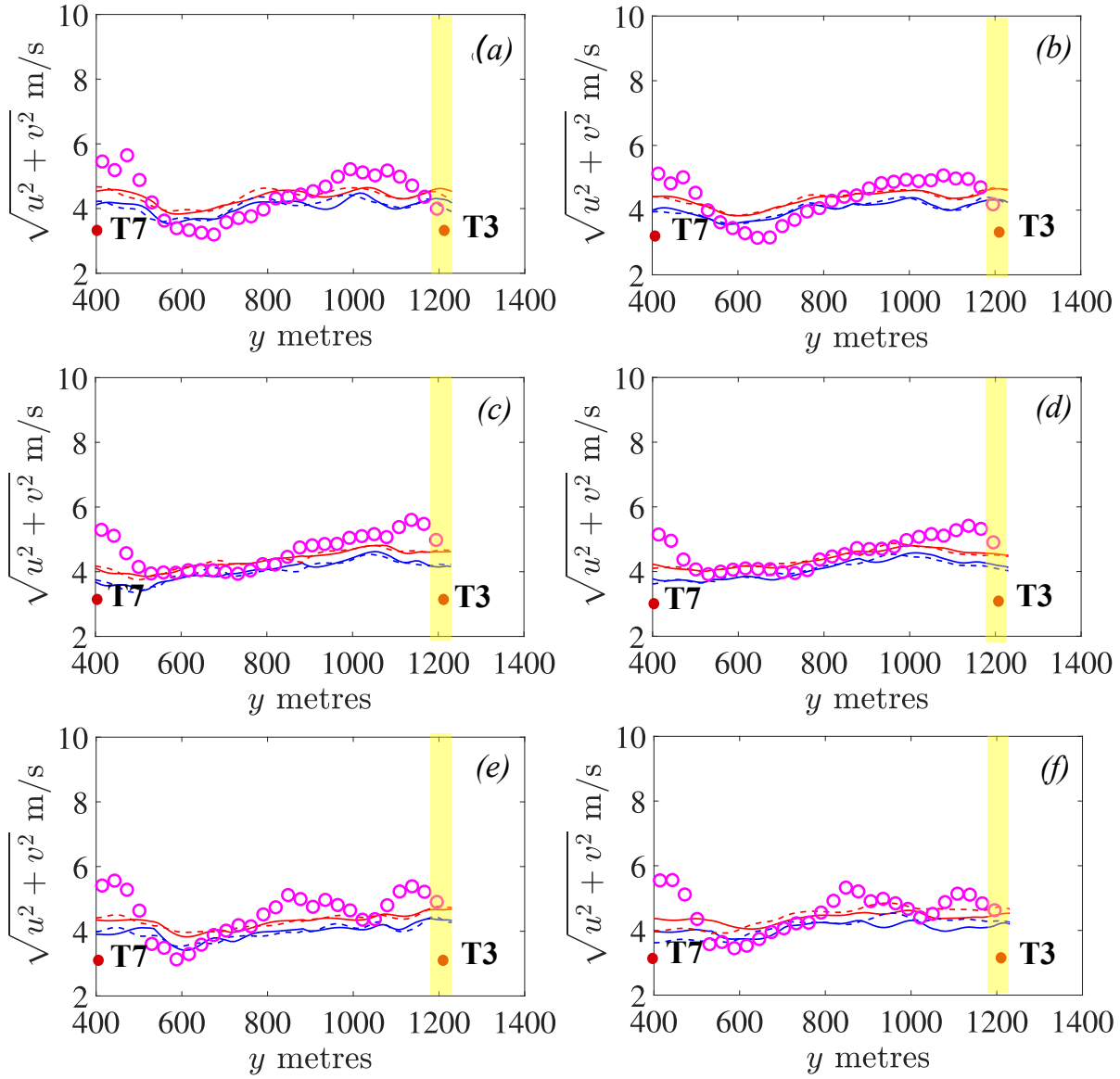

Figure 7.21: Legends same as Figure 7.20. LES and LIDAR data taken midway between two turbine rows at T3 –T7 and T4 – T8. markers – T3, T7: $\sim$ 400 metres upstream of turbines T3, T7.

experimental data becomes available.

Additionally, we further examine the energy spectra of the LES data in order to elucidate more on the flow dynamics at different length scales. Figures 7.24, 7.23 depict the spatially averaged streamwise and spanwise u, v and w energy spectra (with and without Coriolis effects) for different time-stamps, 6:13 am, 6:18 am, 6:25 am and 6:44 am. These spectral information provides credibility to the simulations in the fact that realistic turbulence in terms of Kolomogorov $-5/3$ scaling is produced at scales $\gtrapprox D$. The spectral information in Figure 7.25 (without Coriolis effects) indicate that the smaller scales $\sim O(D)$ of the spectra converge quickly towards the $-5/3$ cascade ($\lambda_{x,y}^{2/3}$ for premultiplied spectra in wavelengths) due to small eddy turn over times, but the large scales $\gtrsim O(10D)$ do not hint towards a trend due to large eddy turn over or decorrelation times. The u and v energy spectra in the current flow is much larger than their wall normal w counterpart except perhaps at scales $\lambda_{x,y} \lesssim D$. While for spanwise spectra (λ_y direction), the spectral content of u energy is always greater than the v counterpart, for streamwise spectra (λ_x direction), a threshold scale exists ($\sim 7D$), below which the v spectra is dominant. Furthermore, a comparison of the spectra with and without Coriolis forces reveal the differences between the two not conspicuously observed in the flow visualizations discussed in the above sections. For the streamwise and the spanwise energy spectra E_{uu}, E_{vv}, the influence of Coriolis forces can be observed at large scales of motion $\lambda_{x,y} \geq 10D$, where D is the rotor diamater of the Adwen AD 5-116 turbines in Alpha-Ventus wind farm. Such differences are not prominent in the wall-normal energy spectra E_{ww}.

7.5 Conclusion

In the present chapter we have proposed an LES methodogy for flow past the wind farms using atmospheric boundary layer precursor inflow driven by variable mass flux

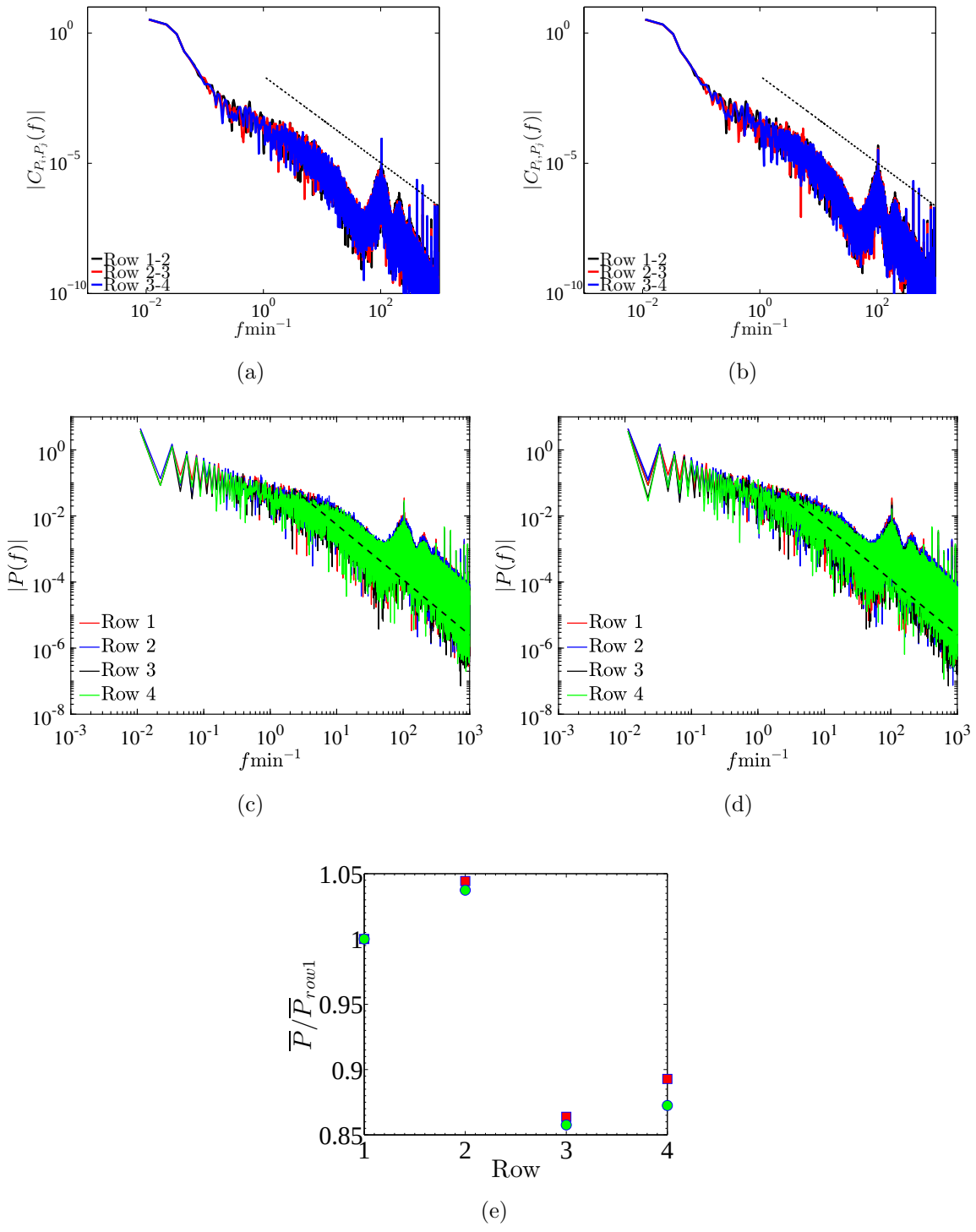

Figure 7.22: (a)-(d). Power spectral density and spectra of normalized cross correlations of power (convoluted with a Hamming window) at different rows in Alpha Ventus wind farm. (a), (c) Without Coriolis forces, (b), (d): With Coriolis forces, $Ro \approx 300$. (e) Row averaged mean power in Alpha-Ventus wind farm, Red square – without Coriolis forces, Green circle – with Coriolis forces ($Ro \approx 300$). Dashed lines in spectra – $f^{-5/3}$ scaling.

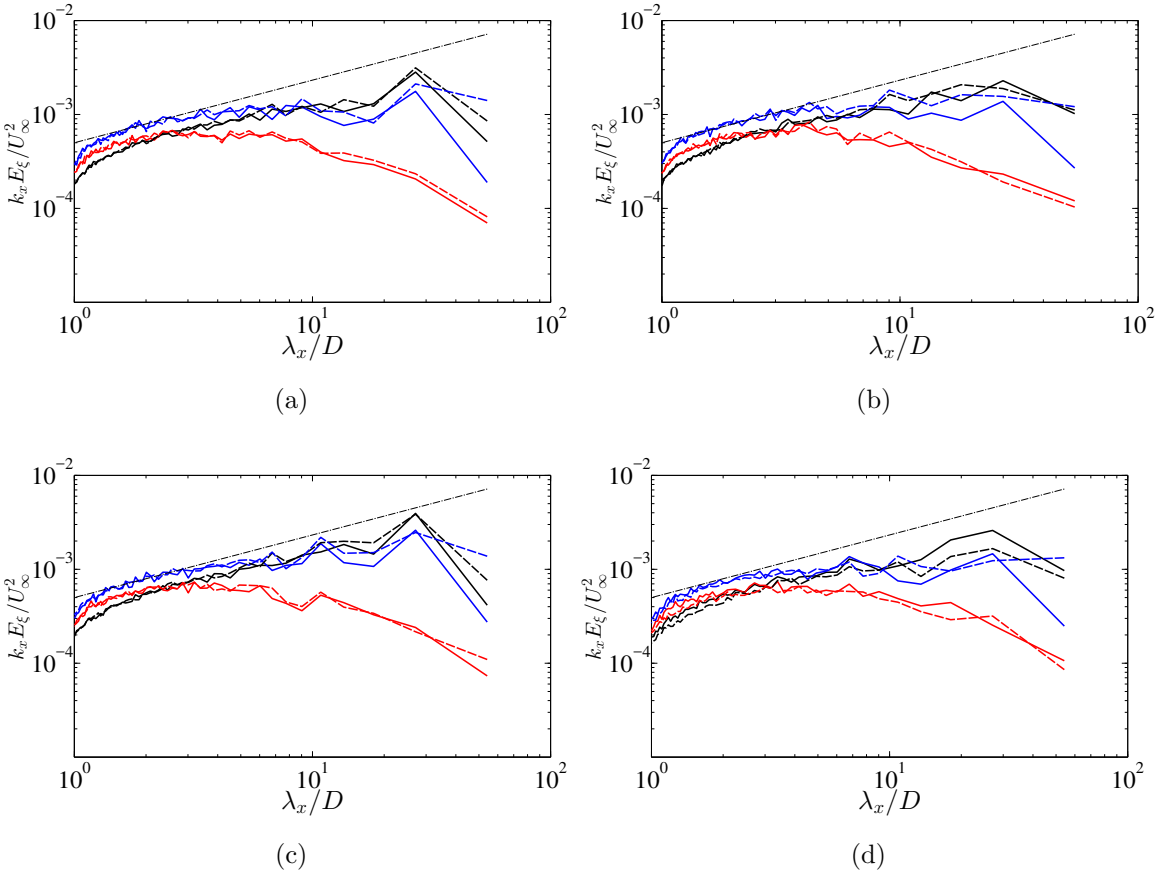

Figure 7.23: Temporal snapshots of streamwise energy spectra averaged in the spanwise-wall normal direction. Black – E_{uu}, Blue – E_{vv}, Red – E_{ww} spectra. Solid – without Coriolis forces, Dashed – with Coriolis forces, $Ro \approx 300$. Chain dotted lines in spectra – $\lambda_y^{2/3}$ (Kolomogorov - $-5/3$) scaling. Spectral data collected at $6:13$ am, $6:18$ am, $6:25$ am and $6:38$ am (local time) from LES simulations.

and wind direction obtained from a cup and vane anemometer data during a LIDAR field experimental campaign. The methodology serves as an important step towards fundamental understanding of realistic flows past large wind farms. The LES results have been compared against the LIDAR field experimental data (retrieved using a 2D VAR algorithm [204]) reconstructing the horizontal velocities (u, v) near the bottom tip of the rotor. Both the temporally filtered data at the inter-turbine spatial location as well as the temporal evolution of the spatially filtered data in LES and LIDAR scans lie wihin comparable bounds, despite some discrepancies in their trends. These

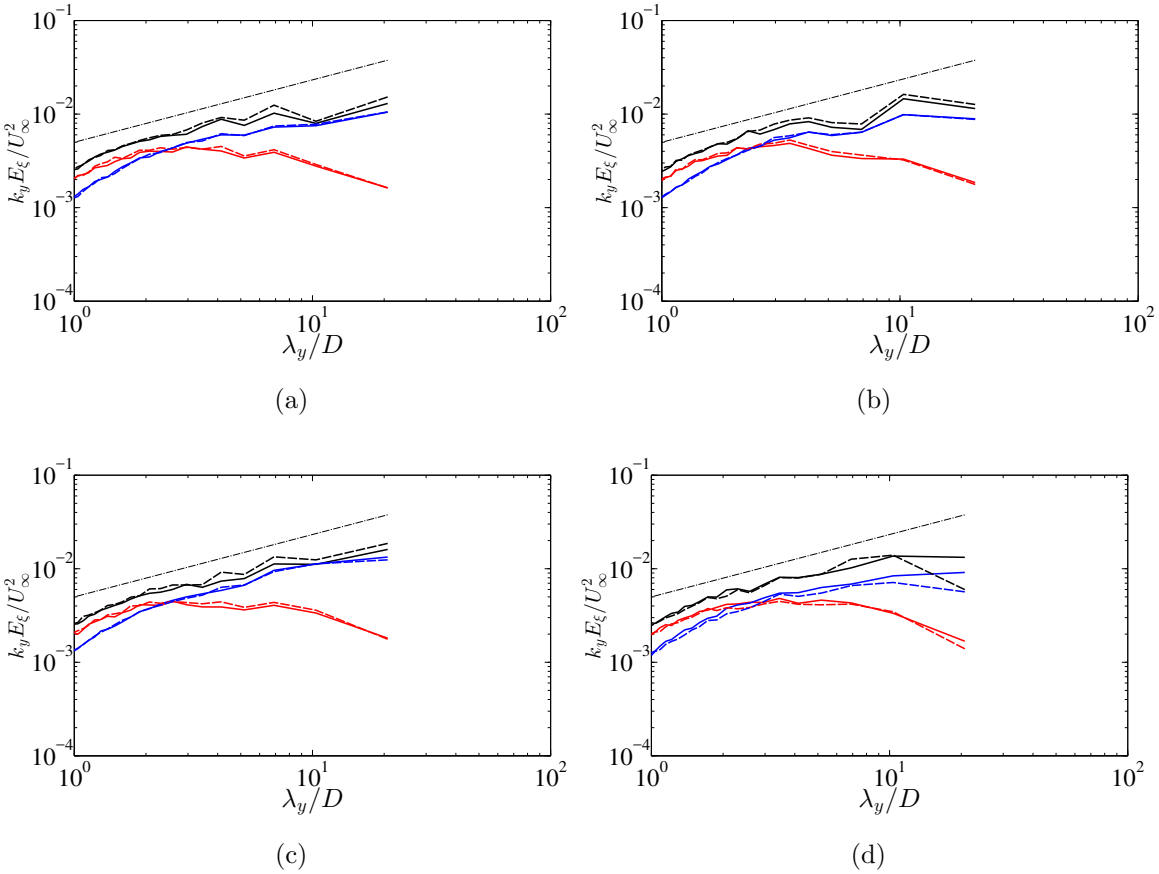

Figure 7.24: Temporal snapshots of spanwise energy spectra averaged in the streamwise-wall normal direction. Black – E_{uu}, Blue – E_{vv}, Red – E_{ww} spectra. Solid – without Coriolis forces, Dashed – with Coriolis forces, $Ro \approx 300$. Chain dotted lines in spectra – $\lambda_y^{2/3}$ (Kolomogorov – $-5/3$) scaling. Spectral data collected at $6:13$ am, $6:18$ am, $6:25$ am and $6:38$ am (local time) from LES simulations.

differences are attributed to uncertainties in measuring locations, stability of ABL and large scale variations imposed by the geophysical effects not considered in our neutral LES simulation with near-wall modelling driven by the mean wind.

Presently, the LES model is designed in a neutral framework. We would further extend its capability towards handling stably stratified and convectively unstable boundary layers to facilitate comparison at other timestamps where stratification of the boundary layers would play a conspicuous role. As a final remark, the discrepancies observed between the LIDAR retrieval results and LES simulations driven by

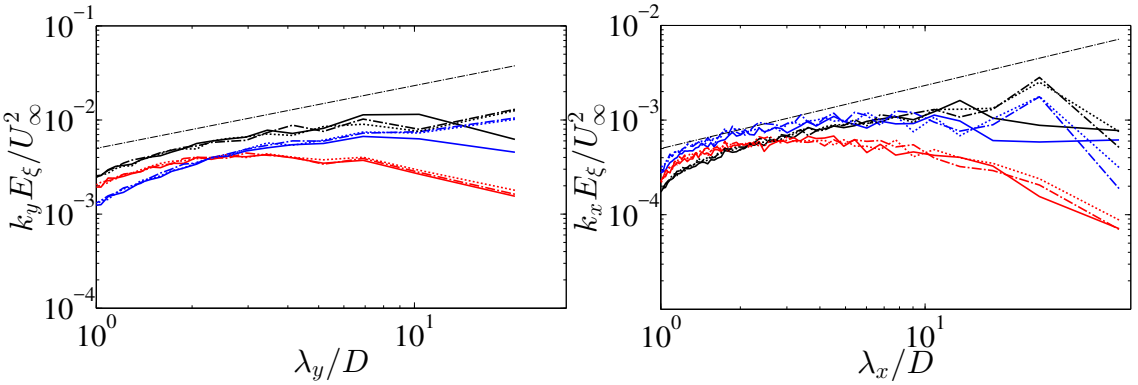

(a) (b)

Figure 7.25: Temporal snapshots of (a) spanwise and (b) streamise energy spectra of LES data averaged in the streamwise/spanwise, wall-normal direction. Black – u (streamwise), Blue – v (spanwise), Red – w (wall normal). Chain dotted, solid and dotted – spectra at a particular timestamp and $2\frac{1}{2}$ minute before and after the timestamp – 6:13 am. Dashed gray line - $\lambda_{x,y}^{2/3}$ scaling. Plots without Coriolis forces.

realistic mean wind and attributed to the inability of LES to capture some large scale structures, indicates towards a potential need of data assimilation, i.e. coupling the instantaneous LIDAR retrieval fields (as a function of space and time) to the coarse LES (or WRF) precursor simulations for capturing more realistic time-resolved flow structures past the wind farm.

Chapter 8

CONCLUSION AND FUTURE WORK

The main objective of the thesis is to understand the interaction and dynamics of wind turbines with atmospheric boundary layer at multiple scales in a framework of high-fidelity large eddy simulation. For this purspose we have developed a robust LES methodology with near wall modeling in higher order spectral elements to capture the dynamics of the neutral atmospheric boundary layer in the inner and outer layer. Using an exponentially higher order discretization in an open-source research code Nek5000, we have shown that our static wall-damped Smagorinsky based subgrid scale closure [136] is capable of reproducing the multiscale physics of neutral ABL comparable to its state-of-the art scale dependent models [44]. Understanding the dynamics of neutral ABL is essential since the wind turbines are located in the inner layer of ABL. We have used neutral ABL framework along with the state-of-the art actuator lines models [12, 127, 150, 215] (modeling turbine blades) to study massive wind farms under a useful theoretical conceptualization of wind turbine array boundary layer (WTABL), where flow develops to a state of statitical homogeneity in the horizontal directions. This concept is true for massive wind farms and if the focus of the study is in the core interior away from the boundary effects. In such a framework, vertical entrainment of mean kinetic energy plays a dominant role in the power generated by the wind turbines. Our study using massive wind farms with different layouts have illustrated the presence of large scales greater by atleast an order of magnitude than the turbine rotor diameters responsible for the power generated by the wind farms. The study further reveals that the presence of wind turbines modulate the large scales near wall due to the presence of downdraft mechanism or the vertical

entrainment of the mean kinetic energy. This information about the modulation of large scale eddies near wall has led to our study involving vertically staggered wind farms with wind turbines of different length scales (hub height and rotor diameter). The study shows that small turbines depending on the hub-height placed in between two very large turbines can utilize oraganized motions from the top tip of the rotor contributed from the downdrafts of the large ones, resulting in a power gain and decreased power variability when compared to the small turbines only wind farm.

The use of WTABL conceptualization enforce periodic boundary conditions in the horizontal directions allowing us to investigate the spectral dynamics using Fourier transform. We further extend this study to a more realistic inflow-outflow configuration where we incorporate heterogeneity in the streamwise direction by using a finite scale wind turbine array. The inflow is being fed from a separate neutral ABL precursor simulation. Wavelet transforms instead of their Fourier counterpart have been used to study the spatial (streamwise) variability of their spectral dynamics. The results have shown that apart from the spatial variability at the small/inertial scales where the Kolomogorov cascade is dominant, spatial variability of the large scales have also been observed owing to the transition of roughness due to the presence of wind turbine array. The study further illustrates on the spatial variability of the organized eddies present in the inner layer and around the turbine rotor tips that are responsible for the power generated by the wind turbines.

Finally we have extended the LES methodology with inflow and outflow driven by a neutral ABL precursor to incorporate a realistic variable mean wind magnitude and direction from a cup and vane anemometer data/LIDAR field experiments. The results compared against the 2D-VAR retrieved LIDAR experimental data, shows that the velocity fields captures some trends with a reasonable amount of scatter even though some large scale effects are not captured by the LES. These large scale

featues are probably an outcome of the geophysical effects that are not captured by the mean wind variation. The methodology proposed serves as an important step towards a fundamental understanding of realistic flows past large wind farms and also as a testimony of the fidelity of the LES framework in capturing the realistic flow past wind farms.

8.1 Future Directions

8.1.1 Fourier POD – Towards Decoupling of Length Scales

Our effort to understand the physics of wind turbine array at multiple length scales using Fourier and wavelet spectra has revealed that the dynamics are different for length scales $< D$ and $\gg D$, where D is the rotor diameter. All our analysis so far, have relied on decoupling the scales in the x, y, z direction for the highly anisotropic turbulent flow in order to provide improved understanding. For example, in periodic wind farms, we have used two dimensional spectra at different wall-normal z locations which automatically decouples the scales in the $x,\ y, z$ directions. A similar treatment was performed for the wavelet analysis. Inspired by these ideas, we have further extended our study using proper orthogonal decomposition (POD) [137]. The advantage of POD lies in the fact that unlike Fourier transform, the basis functions are emperical, constructed from the data and hence can take care of any kind of inhomogeneity imposed by the flow. However, since in general the eigenvalue problem of POD works on the three dimensional data, the large scale structures are essentially 3D features and it is impossible to decouple the effect of dominant streamwise length scales from the spanwise and the inhomogeneous wall-normal counterpart. As an example, a recent 3D POD analysis of periodic wind farms by Verhulst et al. [24] shows the presence of $m^{-0.9}$ scaling law of the POD eigenvalues (turbulent kinetic energy) for higher modes, $(m > 16)$, but the coupled information of the directional length scales

fails to identify the exact physics which causes such scaling, barring some speculation related to the resemblace with inverse k_x^{-1} scaling law of wall-bounded turbulence [79, 136, 216]. It is at this point of failure to understand the flow physics correctly, that the decoupling of length scales in the x, y, z direction deemed necessary gave rise to the concept of Fourier-POD modes for wind turbine array. The Fourier-POD array essentially performs a proper orthogonal decomposition of a complex variable obtained by Fourier transform of the velocity variable in the periodic (spanwise/homogeneous) direction. The mathematical details can be found in Appendix F.

The Fourier-POD methodology was developed to circumvent some of the caveats of three dimensional proper orthogonal decomposition. For 3D POD, convergence of higher order modes is problematic as increasingly more number of snapshots are required for convergence. For example, even for the snapshots more than one flow through times apart (Figure 8.1), the higher modes depict a $m^{-0.5}$ scaling as opposed to the $m^{-0.9}$ scaling predicted by Verhulst [24] which would require snapshots more than 3 flow through times apart (to ensure that the temporal scales are decorrelated) and significantly more number of snapshots. We observe that for snapshots seperated for 1.25 flow through times, the egivenvalues converge for the first 5-6 modes.

However, using Fourier-POD methodology, we can perform the POD at different spanwise length scales and thus decoupling the interaction between the spanwise and streamwise scales. Figure 8.2 shows the converged wavelength dependent eigenvalues for different modes in the FPOD analysis. It is observed that for large spanwise length scales comparable to the size of the doman, the $m^{-0.9}$ scaling can be retrieved, while the modes at smaller spanwise scales (Figure 8.2b) still show the $m^{-0.5}$ scaling as we observed in the three dimensional POD. Such scaling was also observed when snapshots were 1/2 flow through times apart. This result has two implications, (a) less number of snapshots and lower snapshot collection frequency is sufficient to capture

the modal scaling law atleast for very large spanwise scales, for which the three dimensional POD method remains unsuccessful so far and (b) The FPOD as opposed to POD, by decoupling the scales indicates that the $m^{-0.5}$ scaling observed in the three dimensional method mainly comes from the thinner ($\lambda_y \lesssim D$) anisotropic scales in the domain. Thus essentially, $m^{-0.5}$ scaling is an outcome of a phenomenon similar to "aliasing" observed in Fourier transform, where the smaller scales not "well resolved" pile up their energy to the larger scales thus generating an unphysical spectrum.

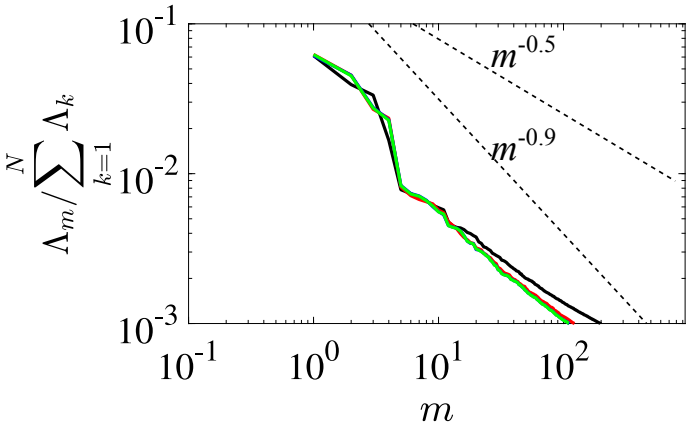

Figure 8.1: Eigenvalues Λ_m of three dimensional POD of wind turbine array for different modes. Different colours represent various snapshot collection frequency. Black – snapshots, 0.25 flow through times apart. Red – snapshots, 0.5 flow through times apart, Green – snapshots, 1.25 flowthrough time apart.

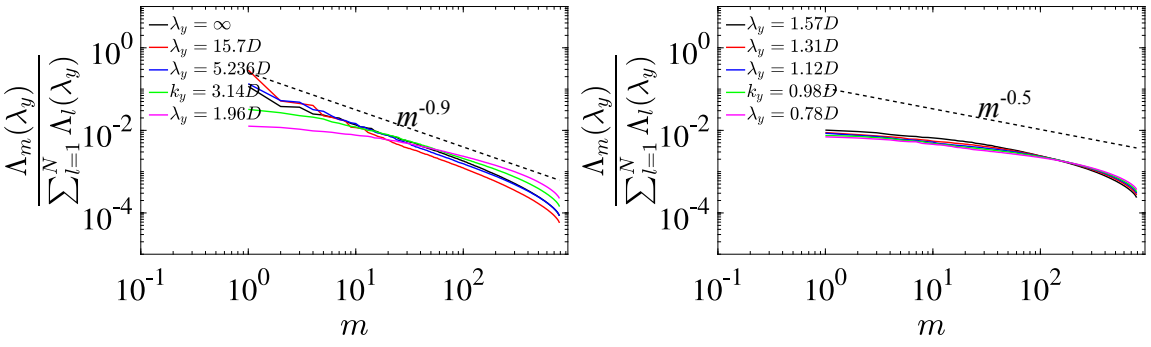

(a) (b)

Figure 8.2: Spanwise wavelength dependent eigenvalues $\Lambda(\lambda_y)$ of Fourier-POD of wind turbine array for different modes. (a) at large length scales, $> D$ (b) at smaller length scales, $\leq D$.Snapshots 1.25 flow through time apart.

Figure 8.3 shows some of the Fourier POD modes (for which $m^{-0.9}$ scaling was observed) for reference. While the lowest order modes, shows feature reminiscent of the roller-mode structures observed in [24,137], higher order modes (at larger spanwise length scales) shows wall modulation of eddies and inclined wall structures similar to what was reported by [77, 85] as attached eddies or collection of hairpins [94].

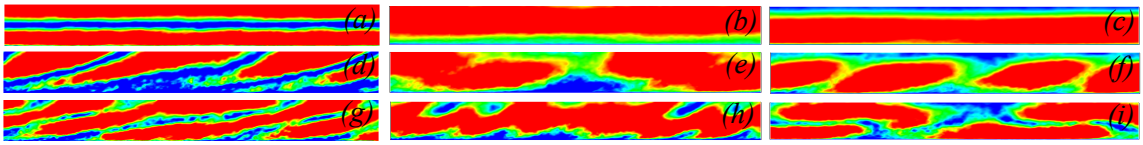

Figure 8.3: Magnitude of two dimensional complex Fourier-POD modes $\widetilde{\boldsymbol{\varphi}}(x, z; \lambda_y)$ normalized by $\Lambda^{1/2}$ (Λ is the eigenvalue) for different wavelengths λ_y. Left: $\lambda_y \to \infty$ (spanwise averaged mode). Middle: $\lambda_y \approx 15.7D$, Right: $\lambda_y \approx 7.85D$. (a) –(c): mode 1; (d) –(f): mode 2, (g) – (i): mode 5. Snapshots shown as xz plane. Colours – Blue (low), Red (high)

Our preliminary investigations using Fourier-POD methodology shows a lot of promise in terms of extracting information of the flow dynamics of wind farms and turbulent flow with one homogeneous boundary condition in general. Our future investigations would envisage this scale decoupling technique to further illustrate on the large scale eddies modulated by the wind farms and responsible for turbine power generation.

8.1.2 Coupling of Field Data to LES – Towards Data Assimilation

Another future direction towards extending our work in flow past the wind farms driven by realistic mean wind stems from the limitations observed in the methodology. It was noted that even though the inflow is driven by realistic mean wind flux and direction, it fails to capture some of the large scale features observed from field data. This indicates towards the possibility of coupling a spatial and temporally evolving field data into the large eddy simulation framework using data assimilation techniques. Some of the popular numerical techniques of data assimilation developed since the

1970s include the optimal interpolation technique, extended Ensemble Kalman Filtering [217],or the more complicated variational data assimilation techniques like the 2D-VAR or 4D-VAR [218] methods or even the more recent Newtonian Relaxation type nudging method (Back and Forth Nudging, see [219, 220]), which despite its simplistic behaviour has the capability to compete with the more accurate Variational methods (2D-Var and 4D-VAR). In our current platform of LES framework in higher order spectral elements, preliminary investigations on nudging techniques, which essentially acts as forcing functions in the Navier-Stokes equation have shown a lot of promise and thus has a potential of being used in this framework. As a future investigation, the current realistic inflow methodogy in LES framework, could be extended to incorporate back and fourth nudging forcing functions to nudge the temporally evolving microscale turbulence guided by LES closures to realistic wind flow dominated by geophysical effects resulting in better prediction of turbine power.

REFERENCES

[1] S. B. Pope, *Turbulent Flows*. Cambridge Press, 2000.

[2] D. Chapman, "Computational aerodynamics, development and outlook," *AIAA J.*, vol. 17, pp. 1293–313, 1979.

[3] W. C. Reynolds, "The potential and limitations of direct and large eddy simulations," in *Lecture Notes in Physics*. J. L. Lumlery, Ed., Springer-Verlag, Berlin, 1990, vol. 357, pp. 313–343.

[4] S. S. A. Ivanell, "Numerical computations of wind turbine wakes," Ph.D. dissertation, Dept. of Mechanics, Gotland Univ., Stockholm, Sweden, 2010.

[5] M. Calaf, C. Meneveau, and J. Meyers, "Large eddy simulation study of fully developed wind-turbine array boundary layers," *Phys. Fluids*, vol. 22, p. 015110, 2010.

[6] F. Porté-Agel, Y.-T. Wu, and R. J. Conzemius, "Large-Eddy Simulation of Atmospheric Boundary Layer Flow Through Wind Turbines and Wind Farms," *J. of Wind Eng. and Ind. Aerodynamics*, vol. 99, pp. 154–168, 2011.

[7] M. J. Churchfield, S. Lee, P. J. Moriarty, L. A. Martinez, S. Leonardi, G. Vijayakumar, and J. G. Brasseur, "A large-eddy simulation of wind-plant aerodynamics," AIAA Paper 2012-0537, 2012.

[8] M. J. Churchfield, J. Michalakes, and P. J. Moriarty, "A numerical study of the effects of atmospheric and wake turbulence on wind turbine dynamics," *J. Turbul.*, vol. 13, no. 14, pp. 1–32, 2012.

[9] W. J. M. Rankine, "On the mechanical principles of the action of propellers." *Trans. Inst. Naval Architects*, vol. 6, 1865.

[10] H. Glauert, "Airplane propellers," in *Aerodynamic Theory*, ser. ed. W. F. Durand. New York 4, Div. L, 1963, pp. 128–143.

[11] R. Mikkelsen, "Actuator disc methods applied to wind turbines," Ph.D. dissertation, Technical University of Denmark, 2003.

[12] N. Troldborg, "Actuator line modeling of wind turbine wakes," Ph.D. dissertation, Technical University of Denmark, 2008.

[13] Y. Peet, P. Fischer, G. Conzelmann, and V. Kotamarthi, "Actuator line aerodynamics model with spectral elements," AIAA Paper 2013–1210, 2013, 51st Aerospace Sciences Meeting, Grapevine, TX.

[14] R. Stevens, M. Wilczek, and C. Meneveau, "Large-eddy simulation study of the logarithmic law for second and higher-order moments in turbulent wall-bounded flow," *J. Fluid Mech.*, vol. 747, pp. 888–907, 2014.

[15] R. J. Stevens, "Dependence of optimal wind turbine spacing on wind farm length," *Wind Energy*, vol. 19, pp. 651–663, 2016.

[16] Y.-T. Wu and F. Porté-Agel, "Large-eddy simulation of wind-turbine wakes: Evaluation of turbine parametrisations," *Boundary Layer Metereol*, vol. 138, pp. 345–366, 2011.

[17] Y.-T. Wu and F. Porté-Agel, "Atmospheric turbulence effects on wind-turbine wakes: An les study," *Energies*, vol. 5, pp. 5340–5362, 2012.

[18] W. Munters, C. Meneveau, and J. Meyers, "Turbulent inflow precursor method with time varying direction for large eddy simulations and applications to wind farms," *Boundary Layer Metereol.*, vol. 159, pp. 305–328, 2015.

[19] N. Hamilton, H. S. Kang, C. Meneveau, and R. B. Cal, "Statistical analysis of kinetic energy entrainment in a model wind turbine array boundary layer," *J. Renewable Sustainable Energy*, vol. 4, p. 063105, 2012.

[20] P. K. Jha, E. P. N. Duque, J. L. Bashioum, and S. Schmitz, "Unraveling the mysteries of turbulence transport in a wind farm," *Energies*, vol. 8, pp. 6468–649, 2015.

[21] L. P. Chamorro, R. E. A. Arndt, and F. Sotiropoulos, "Turbulent flow properties around a staggered wind farm," *Boundary-Layer Meteorol.*, vol. 141, pp. 349–367, 2011.

[22] L. P. Chamorro, S. J. Lee, D. Olsen, C. Miliren, J. Marr, R. Arndt, and F. Sotiropoulos, "Turbulence effects on a full-scale 2.5mw horizontal-axis wind turbine under neutrally stratified conditions," *Wind Energy*, vol. 18, pp. 339–349, 2015.

[23] J. Meyers and C. Meneveau, "Flow visualization using momentum and energy transport tubes and applications to turbulent flow in wind farms," *J. Fluid. Mech.*, vol. 715, pp. 335–358, 2013.

[24] C. VerHulst and C. Meneveau, "Altering kinetic energy entrainment in large eddy simulations of large wind farms using unconventional wind turbine actuator forcing," *Energies*, vol. 8, pp. 370–386, 2015.

[25] S. Xie, C. L. Archer, N. Ghaisas, and C. Meneveau, "Benefits of collocating vertical-axis and horizontal-axis wind turbines in large wind farms," *Wind Energy*, vol. 17, 2016.

[26] P. Fischer, J. Lottes, D. Pointer, and A. Siegel, "Petascale algorithms for reactor hydrodynamics," *J. Phys. Conf. Series*, vol. 125, p. 012076, 2008.

[27] A. T. Patera, "A spectral element method for fluid dynamics: Laminar flow in a channel expansion," *J. Comput. Phys.*, vol. 54, pp. 468–488, 1984.

[28] Y. Maday and A. T. Patera, "Spectral element methods for incompressible Navier-Stokes equations," in *State-of-the-Art Surveys on Computational Mechanics*, ser. A.K. Noor, J.T. Oden (Eds.). ASME, New York, 1989, pp. 71–143 (Chapter 3).

[29] P. Fischer, "An overlapping Schwarz method for spectral element solution of the incompressible Navier-Stokes equations," *J. Comp. Phys.*, vol. 133, pp. 84–101, 1997.

[30] M. O. Deville, P. F. Fischer, and E. H. Mund, *High-Order Methods for Incompressible Fluid Flow*. Cambridge University Press, Cambridge, UK, 2002.

[31] H. Chen and B. Shizgal, "A spectral solution of Sturm-Liouville equation: comparison of classical and non-classical basis sets," *J. of Comp. Appl. Math.*, vol. 136, pp. 17–35, 2001.

[32] R. E. Lynch and J. R. Rice, "Direct solution of partial difference equations by tensor product methods," *Numer. Math.*, vol. 6, pp. 185–199, 1964.

[33] S. A. Orszag, "Spectral methods for problems in complex geometry," *J. Comput. Phys.*, vol. 37, pp. 70–92, 1980.

[34] E. Boström, "Investigation of outflow boundary conditions for convection-dominated incompressible fluid flows in a spectral element framework," 2015.

[35] P. F. Fischer, J. W. Lottes, and S. G. Kerkemeier, "Nek5000: an open source CFD solver," 2008, http://nek5000.mcs.anl.gov.

[36] S. A. Orszag, "Transform method for calculations of vector coupled sums: Application to the spectral form of vorticity equation," *J. Atmos. Sci.*, vol. 27, pp. 890–895, 1970.

[37] C. M. Canuto, Y. Hussaini, A. Quarteroni, and T. A. Zhang, *Spectral Methods in Fluid Dynamics*, 8th ed. Springer-Verlag, New-York, 1988.

[38] P. Sagaut, *Large Eddy Simulations for Incompressible Flows*. Springer Verlag, Berlin, 2006.

[39] L. C. Berselli, T. Iliescu, and W. J. Layton, *Mathematics of Large Eddy Simulation of Turbulent Flows*. Springer Verlag, Berlin, 2006.

[40] P. J. Mason and N. S. Callen, "On the magnitude of the subgrid-scale eddy coefficient in large-eddy simulations of turbulent channel flow," *J. Fluid. Mech.*, vol. 162, pp. 439–462, 1986.

[41] J. W. Deardorff, "A numerical study of three-dimensional turbulent channel flow at large Reynolds number," *J. Fluid. Mech.*, vol. 41, pp. 453–480, 1970.

[42] P. J. Mason and D. J. Thompson, "Stochastic backscatter in large-eddy simulations of boundary layers," *J. Fluid. Mech.*, vol. 242, pp. 51–78, 1992.

[43] J. A. Businger, J. C. Wyngaard, Y. Izulmi, and E. Bradley, "Flux profile relationships in the atmospheric surface layer," *J Atmos Sci.*, vol. 28, pp. 181–189, 1971.

[44] F. Porté-Agel, C. Meneveau, and M. B. Parlange, "A scale-dependant dynamics model for large eddy simulation: application to a neutral atmospheric boundary layer," *J. Fluid. Mech.*, vol. 415, pp. 261–284, 2000.

[45] J. G. Brasseur and T. Wei, "Designing large eddy simulation of turbulent boundary layer to capture law-of-wall scaling," *Phys. Fluids*, vol. 22, p. 021303, 2010.

[46] J. Meyers and P. Sagaut, "On the model coefficient for the standard and the variational multi-scale Smagorinsky model," *J. Fluid Mech.*, vol. 569, pp. 287–319, 2006.

[47] A. S. Monin and A. M. Obukhov, "Basic laws of turbulent mixing in the ground layer of the atmosphere," *Trans. Geophys. Inst. Akad. Nauk. USSR*, vol. 151, pp. 163–187, 1954.

[48] H. Schlichting, *Boundary-layer theory*, 8th ed. Berlin; New York: Springer, 2000.

[49] U. Schumann, "Subgrid scale model for finite difference simulations of turbulent flows in plane channels and annuli," *J. Comp. Phys.*, vol. 18, pp. 376–404, 1975.

[50] C. H. Moeng, "A large eddy simulation model for the study of planetary boundary-layer turbulence," *J. Atmos. Sci.*, vol. 46, pp. 2311–2330, 1984.

[51] R. Stoll and F. Porté-Agel, "Dynamic subgrid-scale models for momentum and scalar fluxes in large-eddy simulations of neutrally stratified atmospheric boundary layers over heterogeneous terrain," *Water Resources Research*, vol. 42, p. W01409, 2006.

[52] T. Chatterjee and Y. Peet, "Actuator line wind turbine simulations in atmospheric turbulent flows using spectral element method," AIAA paper 2015–0727, 2015, 05 - 9 January 2015, Kissimmmee, Florida.

[53] E. Bou-Zeid, C. Meneveau, and M. Parlange, "A scale-dependant Lagrangian dynamic model for large eddy simulation of complex turbulent flows," *Phys. Fluids*, vol. 415, p. 025125, 2005.

[54] P. Wu and J. Meyers, "A constraint for subgrid-scale stresses in the logarithmic region of high Reynolds number turbulent boundary layers: A solution to log-layer mismatch problem," *Phys. Fluids*, vol. 25, p. 015104, 2013.

[55] G. Grötzbach, "Direct numerical and large eddy simulations of turbulent channel flows," *Encyclopedia of Fluid Mechanics, ed. N. P. Cheremisinoff*, pp. 1337–1391, 1987.

[56] U. Piomelli, P. Moin, J. H. Freziger, and J. Kim, "New approximate boundary conditions for large-eddy simulations of wall-bounded flows," *Phys. Fluids A*, vol. 1, pp. 1061–68, 1989.

[57] T. Chatterjee, N. W. Cherukuru, Y. Peet, and R. Calhoun, "Incorporating realistic geophysical effects of mean wind from lidar measurements in large eddy simulation of wind turbine arrays," AIAA paper 2017–1165, 2017.

[58] J. Smagorinsky, "General circulation experiments with the primitive equations," *Journal of Monthly Weather Review*, vol. 91, no. 3, pp. 99–164, 1963.

[59] S. Dong, G. Karniadakis, , and C. Chryssostomidis, "A robust and accurate outflow boundary condition for incompressible flow simulations on severely-truncated unbounded domains," *J. Comput. Physics.*, vol. 261, pp. 83–105, 2014.

[60] A. A. Townsend, "Equilibrium layers and wall turbulence," *J. Fluid. Mech.*, vol. 11, pp. 97–120, 1961.

[61] R. Mittal and P. Moin, "Suitability of upwind-biased finite difference schemes for large-eddy simulation of turbulent flows," *AIAA J.*, vol. 35, pp. 1415–1417, 1997.

[62] M. Germano, U. Piomelli, P. Moin, and W. L. Cabot, "A dynamic subgrid-scale eddy viscosity model," *Phys. Fluids A*, vol. 3, pp. 1760–1765, 1991.

[63] C. Meneveau, T. Lund, and W. Cabot, "A Lagrangian dynamic sub-grid scale model of turbulence," *J. Fluid. Mech.*, vol. 319, pp. 353–385, 1996.

[64] J. Bardina, J. Ferziger, and W. Reynolds, "Improved subgrid scale models for large eddy simulation," AIAA Paper, 1980.

[65] S. Stolz and N. A. Adams, "An approximate deconvolution procedure for large-eddy simulations," *Phys. Fluids*, vol. 11, pp. 1699–1701, 1999.

[66] A. Andrén, A. R. Brown, J. Graf, P. J. Mason, C. H. Moeng, F. T. M. Nieuwstadt, and U. Schumann, "Large-eddy simulation of the neutrally stratified boundary layer: A comparison of four computer codes," *Q. J. R. Metl. Soc.*, vol. 120, pp. 1457–1484, 1994.

[67] P. P. Sullivan, J. C. McWilliams, and C. H. Moeng, "A subgrid-scale model for large-eddy simulation of planetary boundary-layer flows," *Boundary-Layer Met.*, vol. 71, pp. 247–276, 1997.

[68] S. Khanna and J. G. Brasseur, "Analysis of Monin-Obukhov similarity from large-eddy simulation," *J. Fluid Mech.*, vol. 345, pp. 251–286, 1997.

[69] F. T. M. Nieuwstadt and R. A. Brost, "The decay of convective turbulence," *J. Atmos Sci.*, vol. 43, pp. 532–546, 1986.

[70] F. K. Chow, R. Street, M. Xue, and J. H. Ferziger, "Explicit filtering and reconstruction turbulence modeling for large-eddy simulation of neutral boundary layer flow," *J. Atmos. Sci.*, vol. 62, p. 2058, 2005.

[71] S. Kawai and J. Larsson, "Wall-modeling in large eddy simulation: length scales, grid resolution and accuracy," *Phys. Fluids*, vol. 24, p. 015105, 2012.

[72] J. Meyers, "Error-landscape assessment of large eddy simulation: A review of methodology," *J. Sci. Comp.*, vol. 49, pp. 65–77, 2011.

[73] J. A. Templeton, G. Medic, and G. Kalitzin, "An eddy-viscosity based near-wall treatment for coarse grid large-eddy simulation," *Phys. Fluids*, vol. 17, p. 105101, 2005.

[74] N. Hutchins, T. B. Nickels, I. Marusic, and M. S. Chong, "Hot-wire spatial resolution issues in wall-bounded turbulence," *J. Fluid. Mech.*, vol. 635, pp. 103–136, 2009.

[75] A. J. Smits, B. J. Mckeon, and I. Marusic, "High-Reynolds number wall turbulence," *Annu. Rev. Fluid. Mech.*, vol. 43, pp. 353–375, 2011.

[76] J. Jiménez, J. D. Álamo, and O. Flores, "The large-scale dynamics of near-wall turbulence," *J. Fluid. Mech.*, vol. 505, pp. 179–199, 2004.

[77] J. D. Álamo, J. Jiménez, P. Zandonade, and R. Moser, "Scaling of the energy spectra of turbulent channels," *J. Fluid. Mech.*, vol. 500, pp. 135–144, 2004.

[78] Y. Hwang, "Statistical structure of self-sustaining attached eddies in turbulent channel flow," *J. Fluid. Mech.*, vol. 767, pp. 254–289, 2015.

[79] A. E. Perry, S. Henbest, and M. S. Chong, "Theoretical and experimental studies of wall turbulence," *J. Fluid. Mech.*, vol. 165, pp. 163–199, 1986.

[80] H. O. Kreiss and J. Oliger, "Comparison of accurate methods for the integration of hyperbolic equation," *Tellus.*, vol. 24, pp. 199–215, 1972.

[81] D. Gottileb and S. Orszag, "Numerical analysis of spectral methods: Theory and applications," SIAM, 1977.

[82] A. Kravchenko and P. Moin, "On the effect of numerical errors in large eddy simulation," *J. Comput. Phys.*, vol. 131, pp. 310–322, 1997.

[83] W. Cabot and P. Moin, "Approximate wall boundary conditions in the large-eddy simulation of high Reynolds number flow," *Flow, Turbul. Combust.*, vol. 63, pp. 263–291, 1999.

[84] J. Larsson, S. Kawai, J. Bodart, and I. Bermejo-Moreno, "Large eddy simulation with modeled wall-stress: recent progress and future directions," *Mechanical Engineering Reviews*, vol. 3, no. 1, pp. 1–23, 2016.

[85] J. Jiménez, "Cascades in wall bounded turbulence," *Annu. Rev. Fluid. Mech.*, vol. 44, pp. 27–45, 2012.

[86] H. M. Blackburn and S. Schmidt, "Spectral element filtering techniques for large eddy simulation with dynamic estimation," *J. Comput. Phys.*, vol. 186, pp. 610–629, 2003.

[87] R. Bouffanais, M. O. Deville, and E. Leriche, "Large-eddy simulation of the flow in a lid-driven cubical cavity," *Phys. Fluids.*, vol. 19, pp. 01–20, 2007.

[88] G. Lodato, P. Castonguay, and A. Jameson, "Structural wall-modeled les using a high-order spectral difference scheme for unstructured meshes," *Flow Turbulence Combust.*, vol. 92, pp. 579–606, 2014.

[89] J. B. Chapelier and G. Lodato, "A spectral-element dynamic model for the large-eddy simulation of turbulent flows," *J. Comput. Phys.*, vol. 321, pp. 279–302, 2016.

[90] J. Kim, P. Moin, and R. Moser, "Turbulence statistics in fully developed channel flow at low Reynolds number," *J. Fluid Mech.*, vol. 177, pp. 133–166, 1987.

[91] S. Hoyas and J. Jiménez, "Scaling of velocity fluctuations in turbulent channels up to $Re_\tau = 2003$," *Phys. Fluids*, vol. 18, p. 011702, 2006.

[92] M. Lee and R. D. Moser, "Direct numerical simulation of turbulent channel flow up to $Re_\tau = 5200$," *J. Fluid. Mech.*, vol. 774, pp. 395–415, 2015.

[93] A. E. Perry and I. Marusic, "A wall-wake model for the turbulence structure of boundary layers. Part 1. Extension of the attached eddy hypothesis," *J. Fluid. Mech.*, vol. 298, pp. 361–388, 1995.

[94] R. J. Adrian, "Hairpin vortex organization in wall turbulence," *Phys. Fluids*, vol. 19, p. 041301, 2007.

[95] B. J. Balakumar and R. J. Adrian, "Large and very-large-scale motions in channel and boundary-layer flows," *Phil. Trans. R. Soc.*, vol. 365, pp. 665–681, 2007.

[96] M. Guala, S. E. Hommema, and R. J. Adrian, "Large-scale and very-large-scale motions in turbulent pipe flow," *J. Fluid. Mech.*, vol. 554, pp. 521–642, 2006.

[97] J. H. Lee and H. J. Suang, "Comparison of very-large-scale motions of turbulent pipe and boundary layer simulations," *Phys. Fluids*, vol. 25, p. 045103, 2013.

[98] R. J. Adrian, C. D. Meinhart, and C. D. Tomkins, "Vortex organization in the outer region of the turbulent boundary layer," *J. Fluid. Mech.*, vol. 422, pp. 1–54, 2000.

[99] J. Laufer, "The structure of turbulence in fully developed pipe flow," 1994.

[100] J. F. Morrison, W. Jiang, B. J. Mckeon, and A. J. Smits, "Reynolds number dependence of streamwise velocity spectra in turbulent pipe flow," *Physical Review Letters*, vol. 88, pp. 214 501–1–4, 2002.

[101] M. Hites, "Scaling of high-Reynolds number turbulent boundary layers in the National Diagnostic Facility," Ph.D. dissertation, Illinois Institute of Technology, Chicago, 1997.

[102] I. Marusic and A. E. Perry, "A wall-wake model for the turbulence structure of boundary layers. Part 2. Further experimental support," *J. Fluid. Mech.*, vol. 298, pp. 385–407, 1995.

[103] T. B. Nickels, I. Marusic, S. Hafez, and M. S. Chong, "Evidence of the k^{-1} law in a high-Reynolds-number turbulent boundary layer," *Phys. Rev. Letters*, vol. 95, p. 074501, 2005.

[104] T. B. Nickels, I. Marusic, S. Hafez, N. Hutchins, and M. S. Chong, "Some predictions of the attached eddy model for a high Reynolds number boundary layer," *Phil. Trans. R. Soc.*, vol. 365, pp. 807–822, 2007.

[105] B. A. Kader and A. M. Yaglom, "Spectra and correlation functions of surface layer atmospheric turbulence in unstable thermal stratification," *In Turbulence and Coherent Structures (eds. O. Métais and M. Lesieur), Kluwer*, 1991.

[106] G. G. Katul, C. R. Chu, M. B. Parlange, J. D. Albertson, and T. A. Ortenburger, "Low-wavenumber spectral characteristics of velocity and temperature in the atmospheric boundary layer." *J. Geophys. Res.*, vol. 100, pp. 14 243–14 255, 1995.

[107] K. G. Mcnaughton, "Attached eddies and production spectra in atmospheric logarithmic layer," *J. Fluid. Mech.*, vol. 111, pp. 1–18, 2004.

[108] G. J. Kunkel and I. Marusic, "Study of the near-wall-turbulent region of the high-Reynolds- number boundary layer using an atmospheric flow," *J. Fluid. Mech.*, vol. 548, pp. 375–402, 2006.

[109] G. G. Katul, J. D. Albertson, C. I. Hsie, P. S. Konklin, J. T. Sigmon, M. B. Parlange, and K. R. Knoerr, "The "inactive" eddy motion and the large scale turbulent pressure fluctuations in the dynamic sublayer," *J. Atmos. Sci.*, vol. 53, pp. 2512–2524, 1996.

[110] J. F. Morrison, "The interaction between inner and outer regions of turbulent wall-bounded flow," *Phil. Trans. R. Soc. A.*, vol. 365, pp. 683–698, 2007.

[111] A. E. Perry and J. D. Li, "Experimental support for the attached eddy hypothesis in zero- pressure-gradient turbulent boundary layers," *J. Fluid. Mech.*, vol. 218, pp. 405–438, 1990.

[112] K. A. Flack, M. P. Schultz, and T. A. Shapiro, "Experimental support for Townsend's Reynolds number similarity hypothesis on rough walls," *Phys. Fluids*, vol. 19, p. 035102, 2005.

[113] J. Jiménez, "Turbulent flow over rough walls," *Annu. Rev. Fluid. Mech.*, vol. 36, pp. 173–196, 2004.

[114] G. G. Katul, A. Porporato, S. Shah, and E. Bou-Zeid, "Two phenomenological constants explain similarity laws in stably stratified turbulence," *Physical Review E.*, vol. 89, p. 023007, 2014.

[115] S. G. Saddaoughi and S. V. Veeravalli, "Local isotropy in turbulent boundary layers at high Reynolds number," *J. Fluid. Mech.*, vol. 268, pp. 333–372, 1994.

[116] G. G. Katul, A. Porporato, C. Manes, and C. Meneveau, "Co-spectrum and mean velocity in turbulent boundary layers," *Phys. Fluids*, vol. 25, p. 091702, 2013.

[117] S. Hoyas and J. Jiménez, "Reynolds number effects on the Reynolds-stress budgets in turbulent channels." *Phys. Fluids*, vol. 20, p. 101511, 2008.

[118] K. J. Bullock, R. E. Cooper, and F. H. Aberanthy, "Structural similarity in radial correlations and spectra of longitudinal velocity fluctuations in pipe flow," *J. Fluid. Mech.*, vol. 88, pp. 585–608, 1978.

[119] A. Bershadskii, E. Kit, A. Tsinober, and H. Vaisburd, "Strongly localized events of energy, dissipation, enstrophy and enstrophy generation in turbulent flows," *Fluid Dynamics Research*, vol. 14, p. 71, 1994.

[120] S. Chen, K. R. Sreenivasan, and M. Nelkin, "Inertial range scalings of dissipation and enstrophy in isotropic turbulence," *Physical Review Letters*, vol. 79, pp. 1253–1256, 1997.

[121] C. L. Archer, S. Mirzaeisefat, and S. Lee, "Quantifying the sensitivity of wind farm performance to array layout options using large-eddy simulation," *Geophysical Research Letter*, vol. 40, pp. 4963–4970, 2013.

[122] G. Mosetti, C. Poloni, and B. Diviacco, "Optimization of wind turbine positioning in large windfarms by means of a genetic algorithm," *Journal of Wind Engineering and Industrial Aerodynamics*, vol. 54, pp. 105–116, 1994.

[123] J. Meyers and C. Meneveau, "Optimal turbine spacing in fully developed windfarm boundary layers," *Wind Energy*, vol. 15, pp. 305–317, 2012.

[124] Y.-T. Wu and F. Porté-Agel, "Simulation of turbulent flow inside and above wind farms: Model validation and layout effects," *Boundary Layer Metereol.*, vol. 5, pp. 5340–5362, 2013.

[125] L. P. Chamorro, N. Tobin, R. E. A. Arndt, and F. Sotiropoulos, "Variable-sized wind turbines are a possibility for wind farm optimization," *Wind Energy*, vol. 17, pp. 1483–1494, 2014.

[126] R. J. Stevens, D. F. Gayme, and C. Meneveau, "Effects of turbine spacing on the power output of extended wind-farms," *Wind Energy*, vol. 19, pp. 359–370, 2016.

[127] T. Chatterjee and Y. Peet, "Spectra and large eddy structures in the double log-layer in a high Re wind turbine array boundary layer," ASME Turbo Expo GT2016-56359, 2016.

[128] J. Jiménez and J. del Álamo, "Very large anisotropic scales in turbulent wall-bounded flows," in *Statistical Theories and Computational Approaches to Turbulence*, Y. Kaneda and T. Gotoh, Eds. Springer Japan, 2003, pp. 105–112.

[129] J. Lee, J. Ahn, and H. J. Suang, "Comparison of large- and very-large-scale motions in turbulent pipe and channel flows," *Phys. Fluids*, vol. 27, p. 025101, 2015.

[130] E. Bou-Zeid, C. Meneveau, and M. Parlange, "A scale-dependant lagrangian dynamic model for large eddy simulation of complex turbulent flows," *Phys. Fluids*, vol. 415, p. 025125, 2005.

[131] S. Frandsen, R. Barthelmie, S. Pryor, O. Rathmann, S. Larsen, J. Hojstrup, and M. Thogersen, "Analytical modelling of wind speed decit in large offshore wind farms," *Wind Energy*, vol. 9, 2006.

[132] R. B. Cal, J. Lebrón, L. Castillo, H. S. Kang, and C. Meneaveau, "Experimental study of the horizontally averaged flow structure in a model wind-turbine array boundary layer." *J. Renewable Sustainable Energy*, vol. 2, p. 013106, 2010.

[133] J. Lébron, R. B. Cal, H. Kand, L. Castillo, and C. Meneveau, "Interaction between wind turbine array and turbulent boundary layer," Tech. Rep., 2009, 11th Americas Conference on Wind Engineering, San Juan, Puerto Rico, 22-26 June, 2009.

[134] C. VerHulst and C. Meneveau, "Large eddy simulation study of the kinetic energy entrainment by energetic turbulent flow structures in large wind farms," *Phys. Fluids*, vol. 8, p. 025113, 2014.

[135] H. Lettau, "Note on aerodynamic roughness-parameter estimation on the basis of roughness-element description," *J. Appl. Meteor*, vol. 8, p. 828, 1969.

[136] T. Chatterjee and Y. T. Peet, "Effect of artificial length scales in large eddy simulation of a neutral atmospheric boundary layer flow: A simple solution to log-layer mismatch," *Physics of Fluids*, vol. 29, p. 075175, 2017.

[137] Y. T. Peet and T. Chatterjee, "The contribution of large scale structures in the power generation of finite scale wind farms using large eddy simulation," TSFP10, 2017, 10th International Symposium on Turbulence and Shear Flow Phenomena (TSFP10), Chicago, USA, July, 2017.

[138] L. P. Chamorro and F. Porté-Agel, "Turbulent flow inside and above a wind farm: A wind-tunnel study," *Energies*, vol. 4, pp. 1916–1936, 2011.

[139] T. Ackermann and L. Söder, "Wind energy technology and current status: a review," *Renewable and Sustainable Energy Reviews*, vol. 4, pp. 315–374, 2000.

[140] C. L. Archer and M. Jacobson, "Evaluation of global wind power," *Journal of Geophysical Research: Atmosphere*, vol. 110, pp. 905–921, 2005.

[141] F. C. ., B. Leitl., and M. Schatzmann, *Wind Turbines in ABL-Flow: A Review on Wind Tunnel Studies*. Berlin, Heidelberg: Springer Berlin Heidelberg, 2012, pp. 239–242.

[142] R. J. A. M. Stevens and C. Meneveau, "Flow structure and turbulence in wind farms," *Annu. Rev. Fluid. Mech.*, vol. 49, pp. 311–339, 2017.

[143] M. H. Vested, N. Hamilton, J. N. Sørensen, and R. B. Cal, "Wake interaction and power production of variable height model wind farms," Journal of Physics: Conference Series 524, 2014, the Science of Making Torque from Wind 2014 (TORQUE 2014).

[144] Y. Chen, H. Li, K. Jin, and Q. Song, "Wind farm layout optimization using genetic algorithm with different hub height wind turbines." *Renew. Energy*, vol. 70, pp. 56–65, 2013.

[145] K. Chen, M. Song, X. Zhang, and S. Wang, "Wind turbine layout optimization with multiple hub height wind turbines using greedy algorithm." *Renew. Energy*, vol. 96, pp. 676–686, 2016.

[146] L. Wang, A. C. Tan, M. Cholette, and Y. Gu, "Comparison of the effectiveness of analytical wake models for wind farm with constant and variable hub heights," *Energy Convers Manage*, vol. 124, pp. 189–202, 2016.

[147] N. O. Jensen, "A note on wind generator interaction," Roskilde, Denmark: Riso National Laboratory, 1983.

[148] A. Vasel-Be-Hagh and C. L. Archer, "Wind farm hub-height optimization," *Applied Energy*, vol. 195, pp. 905–921, 2017.

[149] B. Dupont, J. Cagan, and P. Moriarty, "An advanced modeling system for optimization of wind farm layout and wind turbine sizing using a multi-level extended pattern search algorithm," *Energy*, vol. 106, pp. 802–814, 2016.

[150] T. Chatterjee and Y. Peet, "Contribution of large scale coherence to wind turbine power in a large eddy simulation model of periodic wind farms," *Physical Review Fluids*, vol. 3, p. 034601, 2018.

[151] "Tjæreborg wind turbine (Esbjerg): Geometric and operational data," Department of Fluid Mechanics, DTH, DK 2800, Lyngby VK-184, 1990.

[152] B. Cushman-Roisin, *Environmental Fluid Mechanics*. John Wiley & Sons, 2013.

[153] R. Gasch and J. Twele, *Scaling wind turbines and rules of similarity*. Berlin, Heidelberg: Springer Berlin Heidelberg, 2012, pp. 257–271. [Online]. Available: https://doi.org/10.1007/978-3-642-22938-1_7

[154] N. Troldborg, J. N. Sørensen, and R. Mikkelsen, "Numerical simulations of wake characteristics of a wind turbine in uniform inflow," *Wind Energy*, vol. 13, pp. 86–99, 2010.

[155] P. Weihing, C. Schulz, T. Lutz, and E. Krǎmer, "Comparison of the actuator line model with fully resolved simulations in complex environmental conditions," *J. Physics: Conf. Series*, vol. 854, p. 012049, 2017.

[156] J. Apt, "The spectrum of power from wind turbines," *Journal of Power Sources*, vol. 169, pp. 369–374, 2007.

[157] T. Chatterjee and Y. Peet, "Effect of artificial length scales in large eddy simulation of a neutral atmospheric boundary layer flow: A simple solution to log-layer mismatch," *Physics of Fluids*, vol. 29, p. 075105, 2017.

[158] P. Goupillaud, A. Grossmann, and J. Morlet, "Cycle-octave and related transforms in seismic signal analysis," *Geoexploration*, vol. 23, pp. 85–102, 1984.

[159] C. Torrence and G. P. Compo, "A practical guide to wavelet analysis," *Bulletin of American Metereological Society*, vol. 79, 1998.

[160] S. Mallat, *A Wavelet Tour of Signal Processing: The Sparse Way*. Academic Press, 2009.

[161] L. Debnath, *Wavelet Transforms and Their application*. Boston, U.S.A.: Birkhäuser, 2002.

[162] J. M. Lily and S. C. Olhede, "Generalized morse wavelets as a superfamily of analytic wavelets," *IEEE Transactions on Signal Processing*, vol. 60, pp. 6036–6041, 2012.

[163] B. Mandelbrot, "Intermittent turbulence in self-similar cascades: divergence of high moments and dimension of carrier," *J. Fluid. Mech.*, vol. 62, pp. 331–358, 1974.

[164] F. Argoul, A. Arneodo, G. Grasseau, Y. Gagne, E. J. Hopfinger, and U. Frisch, "Wavelet analysis of turbulence reveals the multifractal nature of the richardson cascade," *Nature*, vol. 338, pp. 51–53, 1989.

[165] M. Farge, G. Pellengrino, and K. Scheider, "Coherent vortex extraction in 3d turbulent flows using orthogonal wavelets," *Physical Review Letters*, vol. 87, p. 054501, 2001.

[166] J. Liandrat and F. Moret-Bailey, "The wavelet transform: some applications to fluid dynamics and turbulence," *Eur. J. Mech. B. Fluids*, vol. 9, pp. 1–19, 1990.

[167] M. Yamada and K. Ohkitani, "Orthonormal wavelet analysis of turbulence," *Fluid Dynamics Research*, vol. 8, pp. 101–115, 1991.

[168] C. Meneveau, "Analysis of turbulence in orthonormal wavelet transform representation," *J. Fluid. Mech.*, vol. 232, pp. 469–520, 1991.

[169] M. Farge, K. Schneider, G. Pellengrino, A. A. Ray, and R. S. Rogallo, "Coherent vortex extraction in three-dimensional homogeneous turbulence: Comparison between cvs-wavelet and pod-fourier decompositions," *Physics of Fluids*, vol. 15, p. 02886, 2003.

[170] G. G. Katul and M. B. Parlange, "Wavelet transforms and their applications to turbulence," *Boundary Layer Metereol.*, vol. 75, pp. 81–108, 1995.

[171] A. Ghate and S. Lele, "Subfilter-scale enrichment of planetary boundary layer large eddy simulation using discrete fourier-gabor modes," *J. Fluid. Mech.*, vol. 819, pp. 494–539, 2017.

[172] P. S. Westbury, N. D. Sandham, and J. F. Morrison, "Bursts and subgrid-scale energy transfer in turbulent wall-bounded flow," in *Advances in Turbulence VII*, U. Frisch, Ed. Dordrecht: Springer Netherlands, 1998, pp. 23–26.

[173] D. C. Dunn and J. F. Morrisson, "Analysis of the energy budget in turbulent channel flow using orthogonal wavelets," *Computers and Fluids*, vol. 34, pp. 199–224, 2005.

[174] W. J. Baars, K. M. Talluru, N. Hutchins, and I. Marusic, "Wavelet analysis of wall turbulence to study large-scale modulation of small scales," *Experiments in Fluids*, vol. 56, p. 188, 2015.

[175] M. Bassenne, H. J. Bae, and A. Lozano-Durán, "Mandala-inspired representation of the turbulent energy cascade," *Physical Review Fluids*, vol. 2, 2018. [Online]. Available: https://doi.org/10.1103/APS.DFD.2017.GFM.P0026

[176] M. Wilczek, B. Kadoch2, K. Schneider, R. Friedrich, and M. Farge, "Conditional vorticity budget of coherent and incoherent flow contributions in fully developed homogeneous isotropic turbulence," *Physics of Fluids*, vol. 24, p. 035108, 2012.

[177] M. Bassenne, J. Urzay, K. Schneider, and P. Moin, "Extraction of coherent clusters and grid adaptation in particle-laden turbulence using wavelet filters," *Journal of Computational Physics*, vol. 2, p. 054301, 2017.

[178] M. Farge, "Wavelet transforms and their applications to turbulence," *Annu. Rev. Fluid. Mech.*, vol. 24, pp. 395–457, 1992.

[179] N. D. Kelley, R. M. Osgood, J. T. Bialasiewicz, and A. Jakubowski, "Using wavelet analysis to assess turbulence/rotor interactions," *Wind Energy*, vol. 75, pp. 121–134, 2000.

[180] L. Chamorro, J. Hong, and C. Gangodagamage, "On the scale-to-scale coupling between a full- scale wind turbine and turbulence," *J. Turbul.*, vol. 16, pp. 617–632, 2015.

[181] T. Chatterjee and Y. Peet, "Large eddy simulation of a 3 × 3 wind turbine array using actuator line model with spectral elements," AIAA paper 2016–1988, 2016, 04 - 8 January 2016, San Diego, California.

[182] T. Kaushik, T. Chatterjee, , Y. Peet, and R. Calhoun, "Large eddy simulation analysis of wake characteristics of a wind turbine operating in yaw," AIAA paper 2017–1615, 2017.

[183] B. E. Merrill, Y. T. Peet, P. F. Fischer, and J. W. Lottes, "A spectrally accurate method for overlapping grid solution of incompressible navierstokes equations," *Journal of Computational Physics*, vol. 307, pp. 60–93, 2016.

[184] J. L. ón, R. B. Cal, H. S. Kang, L. Castillo, and C. Meneaveau, "Spacing dependence on wind turbine array boundary layers," 11th Americas Conference of Wind Engineering, 2009, san Juan, Puerto Rico, June 22-26, 2009.

[185] L. Sirovich, "Turbulence and dynamics of coherent structures. part i: Coherent structures," *Q. J. Appl. Math.*, vol. XLV, pp. 561–571, 1987.

[186] G. Berkooz, P. Holmes, and J. L. Lumley, "The proper orthogonal decomposition in the analysis of turbulent flows," *Annual Review of Fluid Mechanics*, vol. 25, no. 1, pp. 539–575, 1993.

[187] D. Gabor, "Theory of communication," *Journal of I. E. E. (London)*, vol. 93, pp. 429–441, 1946.

[188] J. M. Lily, "Element analysis: a wavelet based method for analysing time-localized events in noisy time series," *Proc. R. Soc. A*, vol. 473, p. 20160776, 2017.

[189] V. Perier, T. Philipovitch, and C. Basdevant, "Wavelet spectra compared to fourier spectra," *J. Maths. Phys.*, vol. 36, pp. 1506–1519, 1995.

[190] I. Daubechies, J. Lu, and H.-T. Wu, "Synchrosqueezed wavelet transforms: An empirical model decomposition-like tool," *Appl. Comput. Harmon. Anal.*, vol. 30, pp. 243–261, 2011.

[191] GauravThakur, EugeneBrevdo, and N. S.FučkarcHau-TiengWud, "The synchrosqueezing algorithm for time-varying spectral analysis: Robustness properties and new paleoclimate applications," *Signal Processing*, vol. 93, pp. 1079–1094, 2013.

[192] H.-T. Wu, P. Flandrin, and I. Daubechies, "One or two frequencies? the synchrosqueezing answers," *Adv. Adapt. Data Anal.*, vol. 03, pp. 29–39, 2011.

[193] A. J. Grinstead, C. Moore, and S. Jevrejeva, "Application of the cross wavelet transform and wavelet coherence to geophysical time series," *Nonlinear processes in Geophysics*, vol. 11, pp. 561–566, 2004.

[194] D. Maraun, J. Kurths, and M. Holschneider, "Nonstationary gaussian processes in wavelet domain: Synthesis, estimation and significance testing," *Physical Review E*, vol. 75, pp. 016 707–1–016 707–14, 2007.

[195] F. Porté-Agel, Y.-T. Wu, and C. H. Chen, "A numerical study of the effects of wind direction on turbine wakes and power losses in a large wind farm," *Energies*, vol. 6, pp. 5297–5313, 2013.

[196] A. Choukulkar *et al.*, "Evaluation of single and multiple doppler lidar techniques to measure complex flow during the xpia field campaign," *Atmos. Meas. Tech.*, vol. 10, pp. 247–264, 2017.

[197] G. V. Lungo, "Experimental characterization of wind turbine wakes: Wind tunnel tests and wind lidar measurements," *Journal of Wind Engineering and Industrial Aerodynamics*, vol. 149, pp. 35–39, 2016.

[198] L. D. Monache, L. Glascoe, J. Lundquist, J. Mirocha, M. Simpson, and M. Singer, "Ensemble-based data assimilation for wind energy predictions," The Fifth International Symposium on Computational Wind Engineering (CWE2010), 2010, chapel Hill, North Carolina, USA May 23-27, 2010.

[199] W. Y.Y.Cheng, Y. Liu, A. J.Bourgeois, Y. Wu, and S. EllenHaupt, "Short-term wind forecast of a data assimilation/weather forecasting system with wind turbine anemometer measurement assimilation," *Phys. Fluids.*, vol. 107, pp. 340–351, 2017.

[200] F. A. Castro, C. S. Santos, and J. C. L. da Costa, "One-way mesoscalemicroscale coupling for the simulation of atmospheric flows over complex terrain," *Wind Energ.*, vol. 18, pp. 1251 – 1272, 2015.

[201] J. D. Mirocha, D. Rajewski, N. Marjanovic, J. K. Lundquist, B. Kosovic, C. Draxi, and M. J. Churchfield, "Investigating wind turbine impacts on near-wake flow using profiling lidar data and large-eddy simulations with an actuator disk model," *Journal of Renewable and Sustainable Energy*, vol. 7, p. 043143, 2015.

[202] A. Risan, J. A. Lund, C.-Y. Chang, and L. Saetran, "Wind in complex terrain - lidar measurements for evaluation of cfd simulations," *Remote Sens.*, vol. 10, p. 59, 2018.

[203] W. Munters, C. Meneveau, and J. Meyers, "Shifted periodic boundary conditions for simulations of wall-bounded flows," *Phys. Fluids.*, vol. 25, p. 025112, 2016.

[204] N. W. Cherukuru, R. J. Calhoun, R. Krishnamurthy, S. Benny, J. Reuder, and M. Flugge, "2d var single doppler lidar retrieval and its application in offshore wind energy," *Energy Procedia*, vol. 137, pp. 497–504, 2017.

[205] Y.-T. Wu and F. Porté-Agel, "Simulation of turbulent flow inside and above wind farms: Model validation and layout effects," *Boundary-Layer Meteorology*, vol. 146, no. 2, pp. 181–205, 2013.

[206] M. Akbar and F. Porté-Agel, "Mean and turbulent kinetic energy budgets inside and above very large wind farms under conventionally-neutral condition," *Renewable Energy*, vol. 70, pp. 142–152, 2014.

[207] D. Allaerts and J. Meyers, "Large eddy simulation of a large wind-turbine array in a conventionally neutral atmospheric boundary layer," *Phys. Fluids.*, vol. 27, p. 065108, 2015.

[208] M. Akbar and F. Porté-Agel, "Influence of the coriolis force on the structure and evolution of wind turbine wakes," *Physical Review Fluids*, vol. 1, p. 063701, 2016.

[209] D. Allaerts and J. Meyers, "Boundary-layer development and gravity waves in conventionally neutral wind farms," *J. Fluid. Mech.*, vol. 814, pp. 95–130, 2017.

[210] W. T. M. Verkley, "On the beta plane approximation," *Journal of Atmospheric Sciences*, vol. 47, pp. 2453–2460, 1990.

[211] K. S. Mitraszeweski, "Study of the wall effect at offshore wind farms," Master's thesis, Technical University, Denmark, 2012.

[212] M. P. van der Laan and N. N. Sørensen, "Why the coriolis force turns a wind farm wake to the right in the northern hemisphere," *Journal of Physics: Conference Series*, vol. 753, p. 032031, 2016.

[213] J. Ducrée, S. Haeberle, T. Brenner, T. Glatzel, and R. Zengerle, "Pattern of flow and mixing in rotating radial microchannels," *Microfluid Nanofluid*, vol. 2, pp. 97–105, 2006.

[214] H. I. Andersson, "Flows dominated by centrifeugal and coriolis forces – a survey of euromech 336," *Fluid Dynamics Research*, vol. 18, pp. 53–64, 1996.

[215] Y. Peet, P. Sagaut, and Y. Charron, "Towards large eddy simulations of turbulent drag reduction using sinusoidal riblets," WSEAS Paper 565-355, 2007, presented at the 5th IASME/WSEAS International Conference on Fluid Mechanics and Aerodynamics, Vouliagmeni, Greece, August 25-27, 2007.

[216] N. V. Nikitin, F. Nicoud, B. Wasistho, K. D. Squires, and P. R. Spalart, "An approach to wall modeling in large-eddy simulations," *Phys. Fluids*, vol. 12, p. 1629, 2000.

[217] P. L. Houtekamer and F. Zhang, "Review of the ensemble kalman filter for atmospheric data assimilation," *Monthly Weather Review*, vol. 144, pp. 4489–4532, 2016.

[218] D. D. Kuhl, T. E. Rosmond, C. H. Bishop, J. McLay, and N. L. Baker, "Comparison of hybrid ensemble/4dvar and 4dvar within the navdas-ar data assimilation framework," *Monthly Weather Review*, vol. 141, pp. 2740–2758, 2013.

[219] D. Auroux and J. Blum, "Back and forth nudging algorithm for data assimilation problems," *C. R. Acad. Sci. Ser*, vol. 340, pp. 873–878, 2005.

[220] D. Auroux and J. Blum, "Diffusive back and forth nudging algorithm for data assimilation," *C. R. Acad. Sci. Ser*, vol. 349, pp. 849–854, 2011.

[221] G. E. Karniadakis, M. Israeli, and S. Orszag, "High-order splitting methods for the incompressible navier-stokes equations," *J. Comput. Phys.*, vol. 97, pp. 414–443, 1991.

[222] J. P. Boyd, "Two comments on filtering (artificial viscosity) for Chebyshev and Legendre spectral and spectral element methods: Preserving boundary conditions and interpretation of the filter as diffusion," *J. Comput. Phys.*, vol. 143, pp. 283–288, 1998.

APPENDIX A

WEAK FORMULATION IN SPECTRAL ELEMENT METHODS

A.1 Weak Formulation of NS: Galerkin projection

3D Navier-Stokes equation solving for velocity field $\mathbf{u}(\mathbf{x},t)$, scalar pressure field $p(\mathbf{x},t)$ with input volume force function $\mathbf{f}(\mathbf{x},t)$ (momentum and continuity equations).

$$\begin{aligned}
\frac{\partial \mathbf{u}}{\partial t} + \mathbf{u}.\nabla\mathbf{u} &= -\frac{1}{\rho}\nabla p + \nu\nabla^2\mathbf{u} + \mathbf{f} \qquad \text{in} \quad \Omega \times (0,T), \\
\nabla.\mathbf{u} &= 0 \quad \text{in} \quad \Omega \times (0,T), \\
\mathbf{u}(\mathbf{x},0) &= \mathbf{u}^0(\mathbf{x}) \quad \text{for} \quad \mathbf{x} \in \Omega, \\
\mathcal{B}(\mathbf{u}_b) &= 0 \qquad\quad \text{in} \quad \partial\Omega.
\end{aligned} \tag{A.1}$$

Here, $\Omega \subset \mathbb{R}^3$ is the three-dimensional domain in Equation (A.1), $\mathbf{u}^0(\mathbf{x})$ represents the initial condition of the PDE and $\partial\Omega$ represents the external surface of Ω on which the boundary conditions $\mathbf{u}_b$ are defined.

Sobolev spaces for velocity and pressure $X := H_0^1(\Omega)^3$ and $Z := L_0^2(\Omega)$ respectively

$$L_0^2(\Omega) = \left\{ q \in L^2(\Omega) \;\middle|\; \int_\Omega q d^3\mathbf{x} = 0 \right\} \tag{A.2}$$

$$H^1(\Omega) = \left\{ q \in L^2(\Omega) \; |\alpha| \leq 1, \; \middle| D^\alpha q \in L^2(\Omega) \right\} \tag{A.3}$$

$$H_0^1(\Omega) = \left\{ q \in H^1(\Omega) \;\middle|\; q\Big|_{\partial\Omega} = 0 \right\} \tag{A.4}$$

where $D^\alpha = \partial^\alpha / \partial x_1^{\alpha_1} \partial x_2^{\alpha_2} \partial x_3^{\alpha_3}$, with $|\alpha| = \alpha_1 + \alpha_2 + \alpha_3$, is the distributional derivative operator.

The weighted residual technique for the Navier Stokes equations requires

$$\int_\Omega \mathfrak{R}(\mathbf{u}) \mathbf{v} d^3\mathbf{x} = 0 \qquad \forall \mathbf{v} \in X, \tag{A.5}$$

where the residual $\mathfrak{R}$ in Equation(A.5)

$$\mathfrak{R}(\mathbf{u}) = \frac{\partial \mathbf{u}}{\partial t} + \mathbf{u}.\nabla\mathbf{u} + \frac{1}{\rho}\nabla p + \mathbf{f} - \nu\nabla^2\mathbf{u} \tag{A.6}$$

is orthogonally projected to the test space (same as trial space in Galerkin projection: we use the notation (,) for complete integration for projection for brevity). Similar procedure is performed for the continuity equation,

$$\left(\frac{\partial \mathbf{u}}{\partial t}, \mathbf{v}\right) + (\mathbf{u}\nabla\mathbf{u}, \mathbf{v}) = -(\nabla p, \mathbf{v}) + (\mathbf{f}, \mathbf{v}) \left(\nu\nabla^2\mathbf{u}, \mathbf{v}\right) \qquad \forall \mathbf{v} \in X, \tag{A.7}$$

$$(q, \nabla.\mathbf{u}) = 0 \qquad \forall q \in Z. \tag{A.8}$$

In discrete space, the trial and and test spaces for 3-dimensional velocity field is $X^N \subset X$ and scalar pressure field is $Z^N \subset Z$ where X^N, Z^N are finite polynomial function subspaces with N being the degree of the polynomial.

If E is the total number of non-overlapping elements in SEM, with the non-overlapping domains as $\cup_{e=1}^{E}\Omega_e$, the discrete subspaces for velocity and pressure can be represented as $X_N = X \cap \mathbb{P}^3_{N,E}$ and $Z_N = Z \cap \mathbb{P}^3_{N,E}$ for $\mathbb{P}_N - \mathbb{P}_N$ formulation, where $\mathbb{P}_{N,E}$ can be given by

$$\mathbb{P}_{N,E} = \left\{ \psi \;\middle|\; \psi \in L^2(\Omega);\ \psi|_{\Omega_e} \text{Lagrange-Legendre polynomial of degree} \leq N \right\}. \tag{A.9}$$

A.1.1 Legendre Polynomials

Legendre polynomials are finite series polynomial solutions to a special class of differential equations with parameter n.

$$(1 - x^2)\frac{d^2y}{dx^2} - 2x\frac{dy}{dx} + n(n+1)y = 0 \tag{A.10}$$

The polynomials are denoted by $L_N(x)$. The polynomials are even or odd functions of x depending on even or odd orders of n. A first few Legendre polynomials are

$$L_0(x) = 1 \qquad L_1(x) = x$$
$$L_2(x) = \frac{1}{2}(3x^2 - 1) \qquad L_4(x) = \frac{1}{2}(5x^3 - 3x)$$

with $L_k(\pm 1) = (-1)^k$ representing the bounds of the polynomial.

Important *recursion relations* to find the Legendre polynomials of higher order

$$\frac{x^2 - 1}{n}\frac{d}{dx}L_n(x) = xL_n(x) - L_{n-1}(x) \tag{A.11}$$

$$(n+1)L_{n+1}(x) = (2n+1)xL_n(x) - nL_{n-1}(x) \tag{A.12}$$

$$(2n+1)L_n(x) = \frac{d}{dx}\left[L_{n+1}(x) - L_{n-1}(x)\right] \tag{A.13}$$

The orthogonality of Legendre polynomials over L^2 inner product space ($-1 \leq x \leq 1$) can be given as

$$\int_{-1}^{1} L_p(x)L_q(x)\,dx = \frac{2}{2q+1}\delta_{pq} \tag{A.14}$$

where δ_{pq} is the Kronecker delta function. Similarly orthogonality of the derivatives and some modification Legendre polynomial (See Appendix A.1.2) can also be established in a straightforward manner.

A.1.2 Lagrange Interpolants

Roots of Lagrange Legendre polynomial for the velocity & pressure interpolants

$$(1 - \xi_j^2)L'_N(\xi_j) = 0, \quad \forall \xi_j \in [-1, 1]. \tag{A.15}$$

Equation (A.15) is solved using Newton-Raphson technique with initial condition of $\xi_j = \cos(j\pi/N), \quad j = 0, \ldots, N$, for obtaining a fast convergence. L'_N is the first derivative of N^{th} order Legendre polynomial and all the roots lie between ± 1 with a

clustering near -1 and 1. These nodes are commonly referred to as Gauss-Lobatto-Legendre (GLL) quadrature points, with the quadrature weights

$$\rho_j = \frac{2}{N(N+1)} \frac{1}{[L_N(\xi_j)]^2}, \quad 0 \leq j \leq N, \quad \forall \xi_j \in [-1, 1]. \tag{A.16}$$

The quadrature weights in Equation (A.16) are computed as a function of N^{th} order Legendre polynomials at GLL quadrature points. The discrete inner product in 3D thus reduces to

$$(f, g)_N = \sum_{i,j,k=0}^{N} \rho_{ijk} f_{ijk} g_{ijk}. \tag{A.17}$$

Here (f_{ijk}, g_{ijk}) are defined on 3D GLL quadrature nodes on a reference cube and quadrature weights are $\rho_{ijk} = \rho_i \rho_j \rho_k$.

The basis functions for expansion of the velocity variables correspond to Lagrange-Legendre interpolating polynomials,

$$\pi_{N,j}(\xi) = \prod_{i \neq j} \frac{\xi - \xi_j}{\xi_i - \xi_j} = \frac{-1}{N(N+1)} \frac{(1-\xi^2) L'_N(\xi)}{(\xi - \xi_j) L_N(\xi_j)}, \quad 0 \leq j \leq N, \quad \xi \in [-1, 1], \tag{A.18}$$

where ξ_j are GLL quadrature nodes. Figure A.1 shows the Lagrange-Legendre basis functions (Equation (A.18)) displaying the cardinality property, and they all have the common intersection point at the GLL quadrature nodes (roots of numerator of basis functions in Equation (A.18)) while $\pi_j(\xi)$ and $\pi_{N-j}(\xi)$ basis functions have reflective symmetry about $\xi = 0$.

A.2 BDFk-EXTk Scheme

The implicit Backward difference scheme of $k - th$ order (BDFk) using Taylor expansion of an ODE $u_t = g(u)$ can be given as

$$\frac{1}{\Delta t} \sum_{i=0}^{k} \beta_i u^{n+1-i} \approx g(u^{n+1}) \tag{A.19}$$

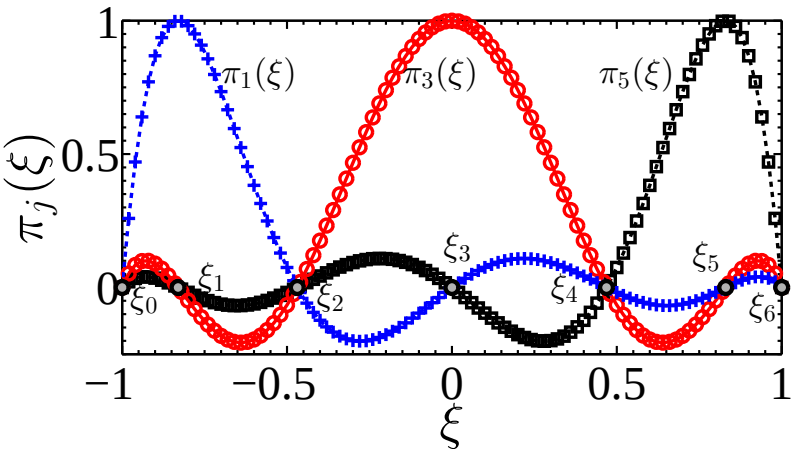

(a)

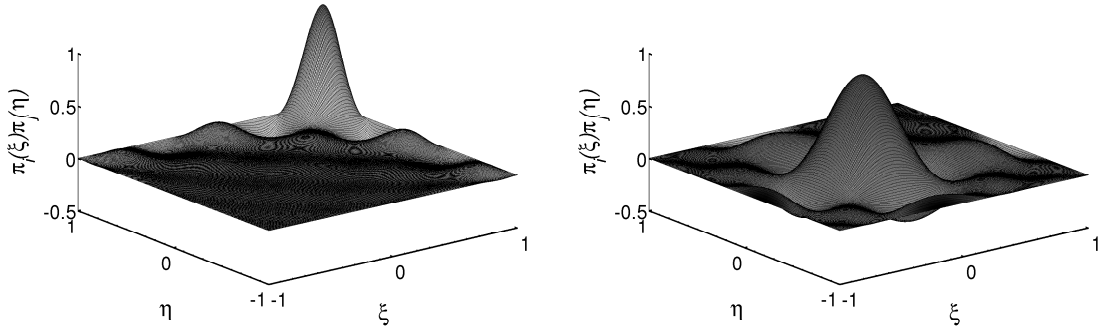

(b) (c)

Figure A.1: (a) Lagrange-Legendre polynomial interpolant $\pi_{j}{}_{j=0}^{N}$ with $N = 7$ (polynomial degree) in current SEM formulation. Blue $-+$, $\pi_1(\xi)$; Red $-\circ$, $\pi_5(\xi)$; Black $--\square$, $\pi_7(\xi)$; (b) $\pi_{1,1}(\xi,\eta)$ (c) $\pi_{4,4}(\xi,\eta)$. Figures (b), (c) obtained as Kronecker products of $\pi_i(\xi) \otimes \pi_j(\eta)$ for 2D case.

with Δt being the time step and βi are the BDF coefficients. To avoid the iterative form of non-linear non-symmetric system for implicit schemes of advection term, Karniadakis et. al [221] proposed a higher order extrapolation scheme on the non-linear terms (e.g. adevtion and other non-linear forcing). The $k' - th$ order extrapolation of a general non-linear term $g(u)$

$$g(u^{n+1}) \approx \sum_{i=1}^{k'} \alpha_i g(u^{n+1-i}) \tag{A.20}$$

with α_i being the extrapolation coefficients. Combining the two schemes together generates BDFk/EXTk scheme

$$\frac{1}{\Delta t}\sum_{i=0}^{k}\beta_i u^{n+1-i} \approx \sum_{i=1}^{k'}\alpha_i g(u^{n+1-i}) \tag{A.21}$$

with $k = k' \approx 2$ or 3

k	β_0	β_1	β_2	β_3	β_4	β_5
1	1	-1				
2	3/2	-2	1/2			
3	11/6	-3	3/2	$-1/3$		
4	25/12	-4	3	$-4/3$	1/4	
5	137/60	-5	5	$-10/3$	5/4	$-1/5$

Table A.1: BDF coefficients $\beta_{i=0}^{k}$ for orders $k = 1-5$

k	α_1	α_2	α_3
1	1		
2	2	-1	
3	3	-3	1

Table A.2: EXT coefficients $\alpha_{i=1}^{k}$ for orders $k = 1-3$

A.3 Tensor Products: Derivatives

The spectral element structure of the u velocity field is $u^e_{i,j,k}$, where $i,\ j,\ k = 0, N$, where N is the order of the polynomial and $e = 1, N_e$, where N_e is the number of elements. In lexicographical ordering (column manjor for FORTRAN), the complete

unwrapped u velocity field for each element can be given as $[u^e_{000}\ u^e_{100}\ u^e_{200}\ u^e_{300}$ $\ldots u^e_{N00}\ u^e_{010}\ u^e_{110} \ldots u^e_{N10}\ \ldots\ldots u^e_{NNN}]^T$. The grids in the r direction varies the quickest, followed by s and then t. Note, similar arguments hold for $v,\ w$ velocities which maintain the same data-structures as u. Further, the differentiation is just an operation involving matrix multiplication involving the Lagrange interpolant based differentiation matrix of size $(N+1)\times(N+1)$. Similar arguments (discussed below) can be shown to hold for filtering operations where a multiplication by a Filtering matrix ($\mathbf{F}$) is invoved. Additionally all these matrix manipulations have been perfformed within the GLL points at each element.

A.3.1 Gradient in the r irection

For computing the gradient in the r direction, we can contruct the u velocity field at each element, as a $(N+1)\times(N+1)^2$ matrix.

$$\tilde{\mathbf{u}} = \begin{bmatrix} u^e_{000} & u^e_{010} & \ldots & u^e_{0N0} & u^e_{001} & u^e_{011}\ldots \\ u^e_{100} & u^e_{110} & \ldots & u^e_{1N0} & u^e_{101} & u^e_{111}\ldots \\ u^e_{200} & u^e_{210} & \ldots & u^e_{2N0} & u^e_{201} & u^e_{211}\ldots \\ \vdots & \vdots & \vdots & \vdots & \vdots & \vdots \\ u^e_{N00} & u^e_{N10} & \ldots & u^e_{NN0} & u^e_{N01} & u^e_{N11}\ldots \end{bmatrix} \tag{A.22}$$

We would premultiply $\tilde{\mathbf{u}}$ by the differentiation matrix $\mathbf{D}$ which is a $(N+1)\times(N+1)$ matrix, such that each columns in the $\tilde{\mathbf{u}}$ matrix is multiplied by $\mathbf{D}$, to generate the $\mathbf{u_r}$ matrix of size $(N+1)\times(N+1)^2$,

$$\mathbf{u_r}_{(N+1)\times(N+1)^2} = \mathbf{D}_{(N+1)\times(N+1)}\tilde{\mathbf{u}}_{(N+1)\times(N+1)^2}$$

where differentiated vector values are obtained at each column, with different columns representing the differentiated values of u_r at different j,k indices.

A.3.2 Graient in the s Direction

For computing the gradient in the s direction, we would need to multiply the differentiation matrix in the direction of varying j, i.e. reshape and reconstruct $[u^e_{000}\ u^e_{100}\ u^e_{200}\ u^e_{300}\ \dots u^e_{N00}\ u^e_{010}\ u^e_{110}\dots u^e_{N10}\ \dots\dots u^e_{NNN}]^T$ such that the a fastest varying j direction can be identified.

We construct chunks of the $\tilde{\mathbf{u}}$ such that we construct a matrix $\widehat{\mathbf{u}}_\mathbf{k}$ of size $(N+1)\times(N+1)$. Hence, matrix $\widehat{\mathbf{u}}_\mathbf{0}$ can be written as

$$\widehat{\mathbf{u}}_\mathbf{0} = \begin{bmatrix} u^e_{000} & u^e_{010} & \dots & u^e_{0N0} \\ u^e_{100} & u^e_{110} & \dots & u^e_{1N0} \\ u^e_{200} & u^e_{210} & \dots & u^e_{2N0} \\ \vdots & \vdots & \vdots & \vdots \\ u^e_{N00} & u^e_{N10} & \dots & u^e_{NN0} \end{bmatrix} \tag{A.23}$$

In general matrix $\widehat{\mathbf{u}}_\mathbf{k}$ would have a structure as follows $(k = 0,\dots N)$

$$\widehat{\mathbf{u}}_\mathbf{k} = \begin{bmatrix} u^e_{00k} & u^e_{01k} & \dots & u^e_{0Nk} \\ u^e_{10k} & u^e_{11k} & \dots & u^e_{1Nk} \\ u^e_{20k} & u^e_{21k} & \dots & u^e_{2Nk} \\ \vdots & \vdots & \vdots & \vdots \\ u^e_{N00} & u^e_{N10} & \dots & u^e_{NNk} \end{bmatrix} \tag{A.24}$$

Now, for $\widehat{\mathbf{u}}_\mathbf{k}\ \ \forall k = 0,\dots N$, the fastest varying direction of s (j indices) is in the column direction, unlike, the row direction for computing u_r. Hence, to contruct u_s, we can premultiply the $\mathbf{D}$ matrix by the transpose of $\widehat{\mathbf{u}}^T_\mathbf{k}$, and then take the transpose again to retain the original orientation of data structure.

$$\mathbf{u}_{\mathbf{k},\mathbf{s}(N+1)\times(N+1)} = [\mathbf{D}_{(N+1)\times(N+1)}\widehat{\mathbf{u}_\mathbf{k}}^T_{(N+1)\times(N+1)}]^T$$

for $k = 0, N$. This is essentially post-multiplying $\mathbf{D}^T$ to each of $\mathbf{u_{k,s}}_{(N+1)\times(N+1)}$ for different k. Concatinating the matrix $\mathbf{u_{k,s}}$ for different k, we can generate the $\mathbf{u_s}_{(N+1)\times(N+1)^2}$ easily.

A.3.3 Graient in the t Direction

For computing the gradient in the s direction, we would need to multiply the differentiation matrix in the direction of varying k, i.e. reshape and reconstruct $[u^e_{000}\ u^e_{100}\ u^e_{200}\ u^e_{300}\ \dots u^e_{N00}\ u^e_{010}\ u^e_{110} \dots u^e_{N10}\ \dots\dots u^e_{NNN}]^T$ such that the a fastest varying k direction can be identified.

For that we construct a matrix $\overline{\mathbf{u}}$ of size $(N+1)^2 \times (N+1)$ which restructured from $[u^e_{000}\ u^e_{100}\ u^e_{200}\ u^e_{300}\ \dots u^e_{N00}\ u^e_{010}\ u^e_{110} \dots u^e_{N10}\ \dots\dots u^e_{NNN}]^T$ as follows.

$$\overline{\mathbf{u}} = \begin{bmatrix} u^e_{000} & u^e_{001} & \dots & u^e_{00N} \\ u^e_{100} & u^e_{110} & \dots & u^e_{10N} \\ u^e_{200} & u^e_{210} & \dots & u^e_{20N} \\ \vdots & \vdots & \vdots & \vdots \\ u^e_{NN0} & u^e_{NN1} & \dots & u^e_{NNN} \end{bmatrix} \tag{A.25}$$

Here, the fastest varying direction of k (for gradient in t) direction could be obtained in the direction of column. Following a similar analogy with Section A.3.2, we can see that $\mathbf{u}_t$ could be obtained by post-multiplying matrix $\overline{\mathbf{u}}$ by $\mathbf{D}^T$.

$$\mathbf{u_t}_{(N+1)^2\times(N+1)} = \tilde{\mathbf{u}}_{(N+1)^2\times(N+1)} \mathbf{D}^T_{(N+1)\times(N+1)}$$

It must be noted, that for a matrix multiplication, the order of operations involved here should be $\sim O((N+1)^4)$. In particular the number of operations is $(2N+1)(N+$

$1)^3$, since inside the row-column loop involving $(N+1)^2$ operations ,there are (N+1) multiplications and N additions that are being performed.

A snippet of the local gradients in the r,s,t direction using tensor products is given below for reference.

```
subroutine local_grad3(ur,us,ut,u,N,e,D,Dt)
c     Output: ur,us,ut         Input:u,N,e,D,Dt
      real ur(0:N,0:N,0:N),us(0:N,0:N,0:N),ut(0:N,0:N,0:N)
      real u (0:N,0:N,0:N,1)
      real D (0:N,0:N),Dt(0:N,0:N)
      integer e
      m1 = N+1
      m2 = m1*m1
      call mxm(D ,m1,u(0,0,0,e),m1,ur,m2)
      do k=0,N
         call mxm(u(0,0,k,e),m1,Dt,m1,us(0,0,k),m1)
      enddo
      call mxm(u(0,0,0,e),m2,Dt,m1,ut,m1)
      return
      end
```

A.4 Elemental Level Filtering

For the explicit filtering approach in near-wall modelling we use the modal approach of Boyd [222], see also 86, 87. With the modal filtering technique, decomposition of the variable u into the modal basis is sought,

$$u(\xi_i) = \sum_{k=0}^{N} \hat{u}_k \phi_k(\xi_i), \tag{A.26}$$

where $\xi_i, i = 0, \cdots, N$ represent the Gauss-Lobatto-Legendre (GLL) [30] clustering of the nodes inside each element, and the modal basis $\{\phi\}$,

$$\phi_0 = L_0(\xi), \quad \phi_1 = L_1(\xi) \quad \text{and} \quad \phi_k = L_k(\xi) - L_{k-2}(\xi), \quad 2 \leq k \leq N, \tag{A.27}$$

forms the hierarchical set of functions constructed from the Legendre polynomials $L_k(\xi)$. The bubble functions ϕ_k are designed to preserve homogeneous Dirichlet boundary conditions, since $\phi_k(\pm 1) = 0$ for $k \geq 2$ (Refer to 222). The inhomogeneous Dirichlet boundary conditions are satisfied by the low order polynomials ϕ_0, ϕ_1. The mapping between the nodal Lagrangian basis and the modal representation, defined by Equation (A.26), can be cast into the matrix form

$$\mathbf{u} = \Phi \hat{\mathbf{u}}. \tag{A.28}$$

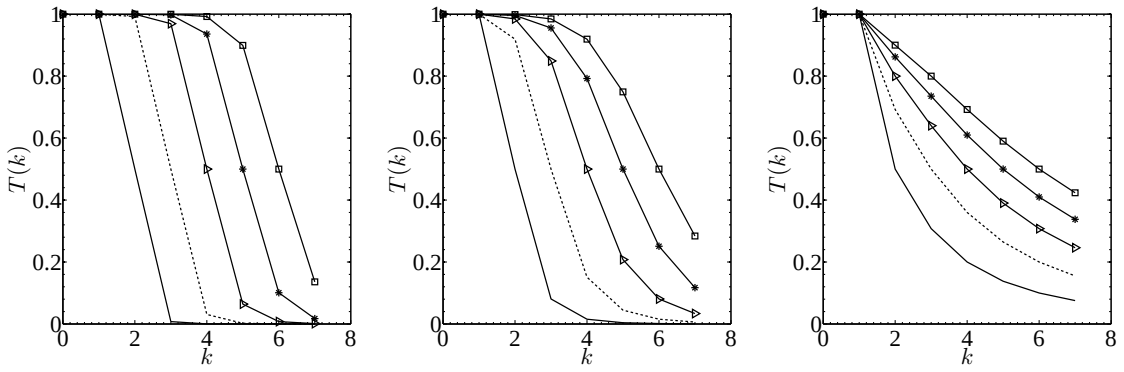

Figure A.2: Filter transfer function $T(k) = (1 + (k/\bar{k})^{\gamma})^{-1}$ (a) $\gamma = 12$ (b) $\gamma = 6$ (c) $\gamma = 2$. $-$, $\bar{k} = 2$; $--$, $\bar{k} = 3$; $-.-\triangle$ $\bar{k} = 4$; $-\star$, $\bar{k} = 5$; $-\square$ $\bar{k} = 6$ | $T(\bar{k}) = \frac{1}{2}$. The total number of modes $k_{max} = N = 7$, corresponding to GLL nodes = 8 (used in our simulation)

The low-pass filtering is performed in the modal space through a diagonal matrix $\mathbb{T}$ whose components are $T_0 = T_1 = 1$ (satisfying C_0 inter-element continuity) and $T_k = f(k; \bar{k}) = 1/(1 + (k/\bar{k})^{\gamma}), \quad 2 \leq k \leq N$. The function $f(k; \bar{k})$ is an attenuation

function, and $\bar{k}$ is the threshold value such that $T_k|_{k=\bar{k}} = 1/2$ (see Figure A.2). Parameters $\bar{k}$ and γ determine the precise shape of the filter transfer function. Decreasing $\bar{k}$ attenuates the large scale contents of the filtered velocity $\widetilde{u}_i$, while decreasing γ smoothens the transfer function more towards a non-projective filtering as seen in Figures A.2a, A.2b, A.2c. The filtering process in one dimension is given by

$$\widetilde{\mathbf{u}} = \mathcal{G} * \mathbf{u} = \Phi \mathbb{T} \Phi^{-1} \mathbf{u}. \tag{A.29}$$

Extrapolation to a 3D field can be achieved from 1D filter by a fast tensor product application [32]. In the current calculations, we define $k_c = N - \bar{k}$ as the number of modes being cut-off, and use $\gamma = 12$ (sharp spectral filter).

A.5 Stress Boundary Conditions in Weak Formulation

The viscous term in the weak form of the Navier-Stokes equations can be expanded using an integration by parts as follows

$$\left(\nu \nabla^2 \mathbf{u}, \mathbf{v}\right) = (2\nu \nabla \nabla^s \mathbf{u}, \mathbf{v}) = 2\nu \int_\Omega \nabla \nabla^s \mathbf{u} \cdot \mathbf{v} \mathrm{d}^3\mathbf{x} = -2\nu \int_\Omega \nabla^s \mathbf{u} \cdot \nabla^s \mathbf{v} \mathrm{d}^3\mathbf{x} + \int_\Omega 2\nu \nabla \left(\nabla^s \mathbf{u} \cdot \mathbf{v}\right) \mathrm{d}^3\mathbf{x}, \tag{A.30}$$

where $\mathbf{u}$ is the velocity vector and $\mathbf{v}$ is a vector in the test space used for Galerkin projection. Here, ∇^s is the symmetric part of the gradient tensor given as $\frac{1}{2}\left(\nabla() + \nabla()^T\right)$, and fluid stress in Ω is $\sigma_{ij} - \frac{1}{3}\sigma_{kk}\delta_{ij} = -2\nu\nabla^s\mathbf{u}$ (Newton's linear stress-strain rate relation). In the derivation of Eq. (A.30), we have used the fact that, from the divergence constraint $\nabla \cdot \mathbf{u} = 0$, one has

$$\nabla^2 \mathbf{u} = 2\nabla\nabla^s \mathbf{u}.$$

From the Gauss divergence theorem, volume integral in Ω can be replaced by a surface integral in $\partial\Omega$,

$$\int_\Omega 2\nu \nabla \left(\nabla^s \mathbf{u} \cdot \mathbf{v}\right) \mathrm{d}^3\mathbf{x} = \oint_{\partial\Omega} 2\nu \nabla^s \mathbf{u} \cdot \mathbf{n} \mathbf{v} \mathrm{d}S, \tag{A.31}$$

where $\mathbf{n}$ is the outward unit normal on the surface $\partial\Omega$. With SGS modelling, the molecular kinematic viscosity ν in Equation A.31 will be replaced by the total viscosity ν_{total} which is the sum of molecular and turbulent viscosities, $\nu_{tot} = \nu + \nu_t$. The closure of the integral of the $2\nu_{tot}\nabla^s\mathbf{u}$ term in $\partial\Omega$ is then related to the wall shear stress,

$$\oint_{\partial\Omega} 2\nu_{tot}\nabla^s\mathbf{u}\cdot\mathbf{n}\mathbf{v}\mathrm{d}S = \oint_{\partial\Omega} \tau_w^{model}\cdot\mathbf{n}\mathbf{v}\mathrm{d}S, \tag{A.32}$$

provided by the near-wall model. For stress-free boundary conditions, the obvious outcome is $\nabla^s\mathbf{u} = 0$.

APPENDIX B

MATHEMATICAL DETAILS OF OUTFLOW BOUNDARY CONDITION

B.1 Outflow Boundary Conditions

The weak formulation of Navier-Stokes equation can be written as

$$\int_\Omega \boldsymbol{v}\cdot\frac{\partial \boldsymbol{u}}{\partial t}\mathrm{d}\Omega+\int_\Omega \boldsymbol{v}\cdot\boldsymbol{u}\cdot\nabla\boldsymbol{u}\mathrm{d}\Omega=-\int_\Omega \boldsymbol{v}\cdot\nabla p\mathrm{d}\Omega+\frac{1}{Re}\int_\Omega \boldsymbol{v}\cdot\nabla^2\boldsymbol{u}\mathrm{d}\Omega+\int_\Omega \boldsymbol{v}\cdot\boldsymbol{f}\mathrm{d}\Omega \quad \text{(B.1)}$$

By the choice of test function v, and simple *Integration by Parts* of the pressure and viscous terms

$$\int_\Omega \boldsymbol{v}\cdot\nabla p\mathrm{d}\Omega=\oint_{\partial\Omega}(p\cdot\boldsymbol{n})\,\mathrm{d}S-\int_\Omega p\nabla\cdot\boldsymbol{v}\mathrm{d}\Omega \quad \text{(B.2)}$$

$$\nu\int_\Omega \nabla^2\boldsymbol{u}\cdot\boldsymbol{v}\mathrm{d}\Omega=\nu\int_\Omega \nabla\cdot\nabla\boldsymbol{u}\cdot\boldsymbol{v}\mathrm{d}\Omega=-\nu\int_\Omega \nabla\boldsymbol{u}\cdot\nabla^s\boldsymbol{v}\mathrm{d}\Omega+\int_{\partial\Omega}\nabla\boldsymbol{u}\cdot\boldsymbol{n}\mathrm{d}S \quad \text{(B.3)}$$

where $\boldsymbol{n}$ is the outward unit normal on the surface $\partial\Omega$. In the non-dimensional framework,

$$\begin{aligned}\int_\Omega \boldsymbol{v}\cdot(\frac{\partial\boldsymbol{u}}{\partial t}+\boldsymbol{u}\cdot\nabla\boldsymbol{u}-f)\mathrm{d}\Omega=&\int_\Omega p\nabla\cdot\boldsymbol{v}\mathrm{d}\Omega-\frac{1}{Re}\int_\Omega\nabla\boldsymbol{u}\cdot\nabla\boldsymbol{v}\mathrm{d}\Omega\\&+\oint_{\Gamma_1}(-p+\frac{1}{Re}\nabla\boldsymbol{u})\cdot\boldsymbol{n}\boldsymbol{v}\mathrm{d}S+\oint_{\Gamma_2}\nabla\boldsymbol{u}\cdot\boldsymbol{n}\boldsymbol{v}\mathrm{d}S\end{aligned} \quad \text{(B.4)}$$

The surface integrals Γ_1 correspond to the natural outflow boundary conditions ("do nothing" BC)

$$(-p+\frac{1}{Re}\nabla\boldsymbol{u})\cdot\boldsymbol{n})=0 \quad \text{(B.5)}$$

and the surface integral involving Γ_2 is the stress boundary condition A.5.

B.2 Energy Analysis

A stability analysis of the Navier-Stokes equation in the weak form (suitable for SEM framework) can be performed by projecting within the trial space $\boldsymbol{u}$.

$$\begin{aligned}\frac{d}{dt}(\boldsymbol{u},\ \boldsymbol{u})+(\boldsymbol{u},\ \boldsymbol{u}\nabla\boldsymbol{u})=&(\nabla\cdot\boldsymbol{u},p)-\frac{1}{Re}(\nabla\boldsymbol{u},\nabla\boldsymbol{u})\\&+\quad\oint_{\Gamma_1}\boldsymbol{u}\left(-p+\frac{1}{Re}\nabla\boldsymbol{u})\cdot\boldsymbol{n}\right)\mathrm{d}S+\frac{1}{Re}\oint_{\Gamma_2}\boldsymbol{u}\nabla\boldsymbol{u}\cdot\boldsymbol{n}\mathrm{d}S\end{aligned} \quad \text{(B.6)}$$

The non-linear term

$$(\boldsymbol{u},\ \boldsymbol{u}\nabla\boldsymbol{u}) = \int_\Omega \boldsymbol{u}\cdot\boldsymbol{u}\nabla\boldsymbol{u}\mathrm{d}\Omega = \int_\Omega \boldsymbol{u}\cdot\frac{1}{2}\nabla|\boldsymbol{u}|^2\mathrm{d}\Omega \tag{B.7}$$

Integration by Parts reveal that

$$\int_\Omega \boldsymbol{u}\cdot\frac{1}{2}\nabla|\boldsymbol{u}|^2\mathrm{d}\Omega = -\int_\Omega \underbrace{\nabla\cdot\boldsymbol{u}}_{=0}\frac{1}{2}|\boldsymbol{u}|^2\mathrm{d}\Omega + \oint_{\partial\Omega}\boldsymbol{u}\frac{1}{2}|\boldsymbol{u}|^2\cdot\boldsymbol{n}\mathrm{d}S \tag{B.8}$$

The surface integral in the non-linear term will vanish only for homogeneous Dirichlet / Periodic boundary conditions. Also the pressure projection term $(\nabla\cdot\boldsymbol{u}, p)$ is zero due to the divergence free constraint.

$$\begin{aligned}\frac{d}{dt}||\boldsymbol{u}||^2_{L^2(\Omega)} = -\frac{1}{Re}||\nabla\boldsymbol{u}||^2_{L^2(\Omega)} + \oint_{\Gamma_1}\boldsymbol{u}\left(-p+\frac{1}{Re}\nabla\boldsymbol{u}-\frac{1}{2}|\boldsymbol{u}|^2)\cdot\boldsymbol{n}\right)\mathrm{d}S \\ + \oint_{\Gamma_2}(\frac{1}{Re}\boldsymbol{u}\nabla\boldsymbol{u}-\frac{1}{2}\boldsymbol{u}|\boldsymbol{u}|^2)\cdot\boldsymbol{n}\mathrm{d}S\end{aligned} \tag{B.9}$$

For stabilized solution of NS equation, $\frac{d}{dt}||\boldsymbol{u}||^2_{L^2(\Omega)} \leq 0$. For simulations with $Re\to\infty$, the L^2 norm of energy equation

$$\frac{d}{dt}||\boldsymbol{u}||^2_{L^2(\Omega)} = \oint_{\Gamma_1\oplus\Gamma_2}\boldsymbol{u}(-\frac{1}{2}|\boldsymbol{u}|^2)\cdot\boldsymbol{n}\mathrm{d}S \tag{B.10}$$

The terms bearing the coefficient $1/Re$ going to zero and from the natural outflow boundary conditions

$$\oint_{\Gamma_1}\left(-p+\frac{1}{Re}\nabla\boldsymbol{u}\right)\cdot\boldsymbol{n}\mathrm{d}S = 0$$

the stability of NS equation (energy analysis) is guided by terms from the nontrivial boundary conditions at $\Gamma_1,\ \Gamma_2$.

Condition of stability

$$\boldsymbol{u}\cdot\boldsymbol{n}\geq 0 \quad \text{for} \quad \Gamma_1\oplus\Gamma_2$$

. At the bottom "wall" stress boundary condition no-penetration of large eddies ensure $\boldsymbol{u}\cdot\boldsymbol{n} = 0 \quad$ for $\quad\Gamma_2,\ \Rightarrow$ condition of stability only guided by the outflow boundary condition $\boldsymbol{u}\cdot\boldsymbol{n}\geq 0 \quad$ for $\quad\Gamma_1$

B.2.1 Sponge Layer

In a sponge region the idea is to damp out all unwanted reflections by adding extra forcing to the flow. The sponge layer can be developed in various ways. One such way is close to the outflow, there is a small artificial region of high viscosity to slow down the high speed flow realistically without triggering spurious reflected waves due to the change of medium.

From the perspective of stability analysis (Equation(B.9)) the L^2 norm of energy equation can be controlled since $-\frac{1}{Re}||\nabla \boldsymbol{u}||^2_{L^2(\Omega)}$ starts dominating the flow near the outflow boundary condition ($\frac{d}{dt}||\boldsymbol{u}||^2_{L^2(\Omega)} \leq 0$)

B.2.2 Stabilized Natural Boundary Condition

Adding the condition $\boldsymbol{u}\left(-p + \frac{1}{Re}\nabla \boldsymbol{u} - \frac{1}{2}|\boldsymbol{u}|^2) \cdot \boldsymbol{n}\right)$ if an energy influx on Γ_1 is present, the growth of L^2 energy norm as $Re \to \infty$ is eliminated. To remove the discontinuity that appears when fluxes turn from negative to positive from one time step to another a smooth step function was used. This methodology is along the lines of Dong et al. [59].

$$-p \cdot \boldsymbol{n} + \frac{1}{Re}\nabla \boldsymbol{u} \cdot \boldsymbol{n} - \frac{1}{2}|\boldsymbol{u}|^2 \Theta(\boldsymbol{n}, \boldsymbol{u}) = 0 \quad \text{on} \quad \Gamma \tag{B.11}$$

where

$$\Theta(\boldsymbol{n}, \boldsymbol{u}) = \left(1 - \frac{\tanh(\boldsymbol{n} \cdot \boldsymbol{u})}{U\delta}\right)$$

is smooth Heaviside step function to remove sudden discontinuity of the outflow fluxes with U, δ being some chosen velocity and length scale in the flow and $\boldsymbol{n}$ is the unit normal vector at the outflow boundary.

APPENDIX C

GRID SENSITIVITY RESULTS OF NEUTRAL ATMOSPHERIC BOUNDARY LAYER

The behaviour of the wall-damped Smagorinsky model is documented for different grids (refer to Table C.1) in the current section. Two methods of grid refinement or coarsening have been considered with respect to the baseline grid: (*i*) vertical, where the element sizes in the horizontal directions are unaltered; (*ii*) global, where element sizes in all directions are altered while preserving the aspect ratio of the elements. In both cases, the polynomial order of the basis functions, that is the number of collocation points per element, is left unchanged. While the vertical grid variation has been applied to all parametric variations of the wall-damped models, the additional global variation of the grid has been tested only for the overdissipative model $C_0^{16}n^2k_c^{4/7}$ and our best performing optimally-dissipative model $C_0^{19}n^{05}k_c^{4/7}$. The variation of the filter length scale C_s for different wall-damped Smagorinsky models with grid refinement is shown in Figure C.1. The figure clearly demonstrates that the behaviour and the near-wall growth of the coefficient is still preserved for different grids. The slow growth of C_s versus z/Δ in $C_0 = 0.19, n = 0.5$ model results in a correct scaling of the filter scales with the grid size Δ showing similar dependence as in a scale-dependant model [44], while the sharp saturation towards the constant value in the models with $n \geq 1$ makes the variation of C_s with the grid in the near-wall region erroneously less sensitive.

Figure C.2 illustrates the variation of normalized streamwise velocity gradient $\Phi(z)$ and streamwise variance $\widetilde{\overline{u'^2}}/u_\tau^2$ with wall distance z/H on different grids. The plot illustrates that the physics imposed by the subgrid scale model in wall-damped Smagorinsky model is more dominant than that imposed by the grid itself. As expected, for cases $C_0^{16}n^2k_c^{4/7}, C_0^{09}n^2k_c^{4/7}, C_0^{17}n^1k_c^{4/7}$, where the *artificial viscous sub-layer* is present, we do observe that refining or coarsening the grids compared to the baseline grid does shift the location of the viscous sub-layer towards or away from the "wall", which is more prominent in the cases of global grid variation, without attenuating or

amplifying the peak of the LLM in $\Phi(z)$. This is consistent with the presence of the LES diffusion imposed by the grid size and confirms that the location of "log-layer mismatch" is indeed tied to the grid [45,68]. However, in Case $C_0^{19}n^{05}k_c^{4/7}$, where the log-layer mismatch has been eliminated, the near-wall region is fairly unaffected by the grid variation. In this respect, Case $C_0^{19}n^{05}k_c^{4/7}$ is least sensitive to the grids even for second order moments $(\widetilde{u'^2})$.

To complete the process of performing grid-sensitivity tests, we further plot the energy spectra at different grids in order to illustrate how the variation of physics at multiple scales of motion is affected by the grid sizes. For the normalized 1D u, w energy spectra and uw cospectra (Figure C.3), the scaling laws of the wavenumbers for different parametric models $C_0^{16}n^2k_c^{4/7}$, $C_0^{17}n^1k_c^{4/7}$, $C_0^{09}n^2k_c^{4/7}$, $C_0^{19}n^{05}k_c^{4/7}$ remain reasonably invariant with the grid coarsening or refinement with respect to the baseline grid. Similarly, in the 2D premultiplied streamwise energy spectra reported for Cases $C_0^{16}n^2k_c^{4/7}$, $C_0^{19}n^{05}k_c^{4/7}$ in Figure C.4, it is illustrated that the spectral shape (sizes of eddies) at various locations from the wall is preserved for different grids as well. Our best performing model $C_0^{19}n^{05}k_c^{4/7}$ demonstrates the least sensitivity in the scaling and shape of the spectra, even for the global variation of the grids g1, g2 compared to the baseline grid. Furthermore, it is worth noting that overdissipative models like $C_0^{16}n^2k_c^{4/7}$, where the "artificial viscous sublayer" is present, are affected stronger by the global grid variation and consistently manifest a larger variation in spectra, while preserving the shape and the scaling laws.

Case	$N_x^e \times N_y^e \times N_z^e$	N_{xyz}	Δ_x/Δ_z	Δ_x/Δ_y	$\Delta z/z_0$
v1	$30 \times 20 \times 20$	4.19×10^6	4.188	1.33	23
bs	$30 \times 20 \times 24$	5.02×10^6	5.0265	1.33	27
v2	$30 \times 20 \times 30$	6.27×10^6	5.8543	1.33	32
g1	$20 \times 13 \times 16$	1.47×10^6	5.0265	1.33	18
bs	$30 \times 20 \times 24$	5.02×10^6	5.0265	1.33	27
g2	$45 \times 30 \times 36$	16.87×10^6	5.0265	1.33	40

Table C.1: The grid parameters for LES of atmospheric boundary layer. bs is the baseline grid. { v1,bs,v2 } – grid sensitivity test in the vertical direction. { g1,bs,g2 } – grid sensitivity test in the global domain. Computational domain: $2\pi H \times \pi H \times H$

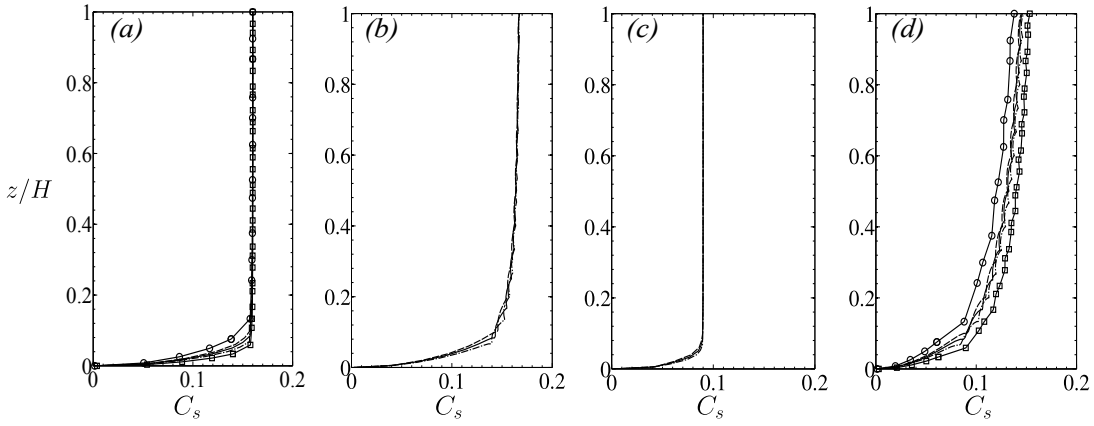

Figure C.1: Filter length scale coefficient C_s of various Smagorinsky models on different grids: (a) Case $C_0^{16} n^2 k_c^{4/7}$, (b) Case $C_0^{17} n^1 k_c^{4/7}$, (c) Case $C_0^{09} n^2 k_c^{4/7}$, (d) Case $C_0^{19} n^{05} k_c^{4/7}$. Vertical grid variation: Dashed – v1 , Solid – bs, Chain dotted – v2. Global grid variation (for (a), (d)): $\circ$ – g1, $\square$ – g2. See Table C.1 for grid details.

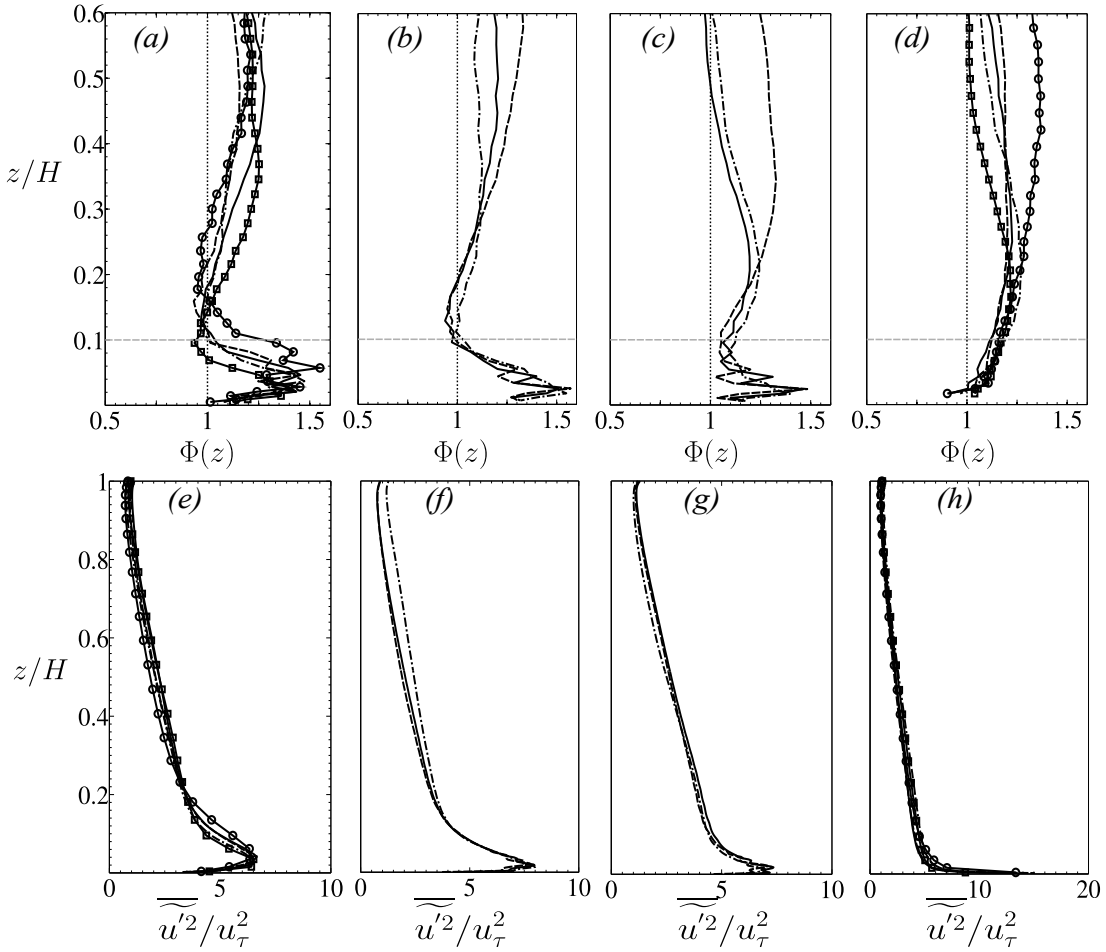

Figure C.2: Normalized streamwise velocity gradient $\Phi(z) = \kappa z/u_\tau dU/dz$ (Figures (a) – (d)) and resolved streamwise variance $\widetilde{u'^2}/u_\tau^2$ (Figures (e) – (h)) for various Smagorinsky models on different grids (a),(e) Case $C_0^{16}n^2k_c^{4/7}$ (b),(f) Case $C_0^{17}n^1k_c^{4/7}$ (c),(g) Case $C_0^{09}n^2k_c^{4/7}$ (d),(h) Case $C_0^{19}n^{05}k_c^{4/7}$. Vertical grid variation (spectral elements): Dashed – v1 , Solid – bs, Chain dotted – v2. Global grid variation (for (a), (d)): ∘ – g1, □ – g2. See Table C.1 for grid details.

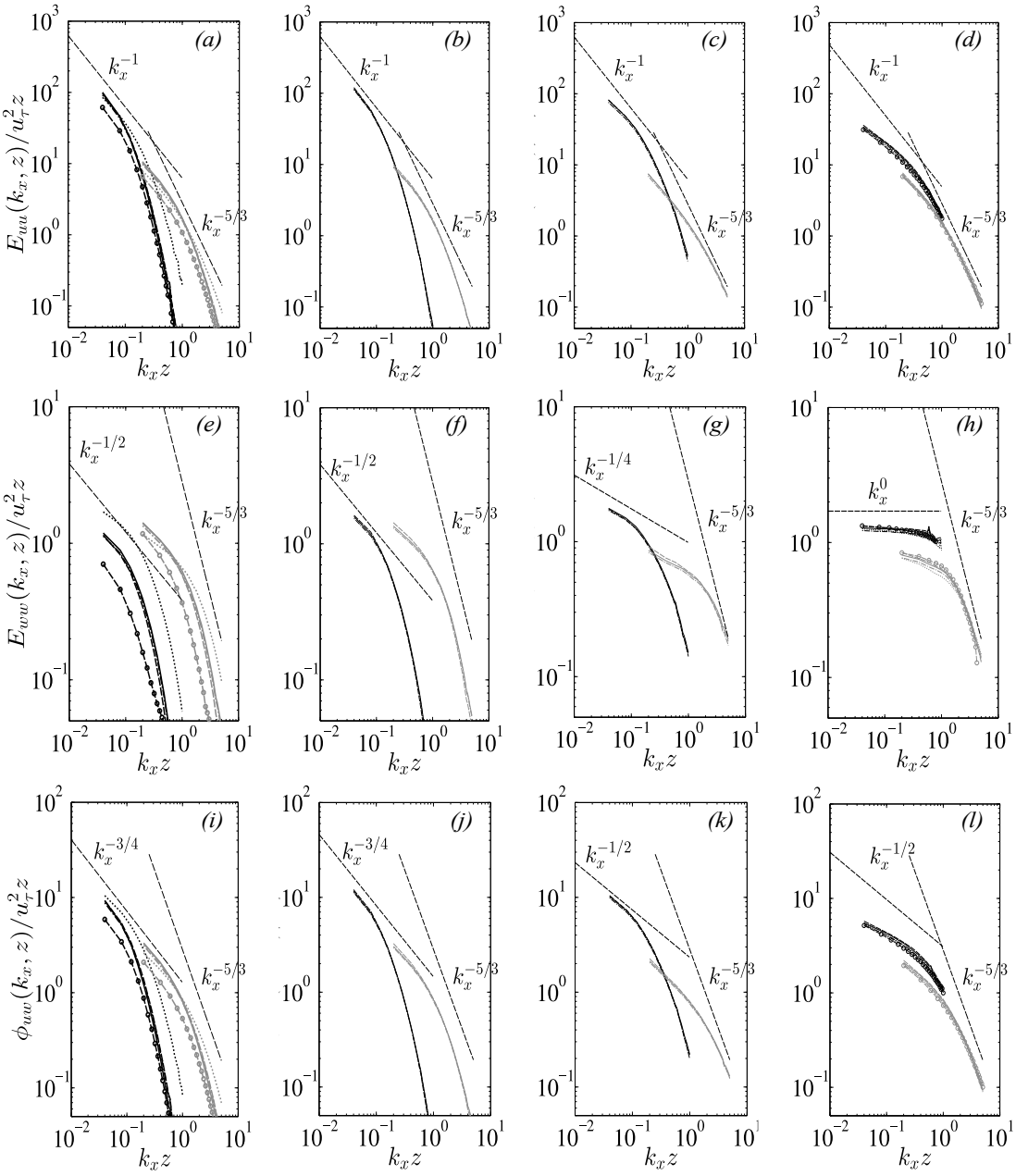

Figure C.3: Normalized streamwise energy spectra, E_{uu} (Figures (a) – (d)), wall-normal energy spectra, E_{ww} (Figures (e) – (h)) and cospectra ϕ_{uw} (Figures (i) – (l)) vs $k_x z$ for various parameters of wall-damped Smagorinsky model on different grids. (a),(e),(i) Case $C_0^{16} n^2 k_c^{4/7}$; (b),(f),(j) Case $C_0^{17} n^1 k_c^{4/7}$; (c),(g), (k) Case $C_0^{09} n^2 k_c^{4/7}$; (d),(h), (l) Case $C_0^{19} n^{05} k_c^{4/7}$. Vertical grid variation: Dashed – v1 , Solid – bs, Chain dotted – v2. Global grid variation (for (a), (d)): ∘ – g1, Dotted – g2. See Table C.1 for grid details.

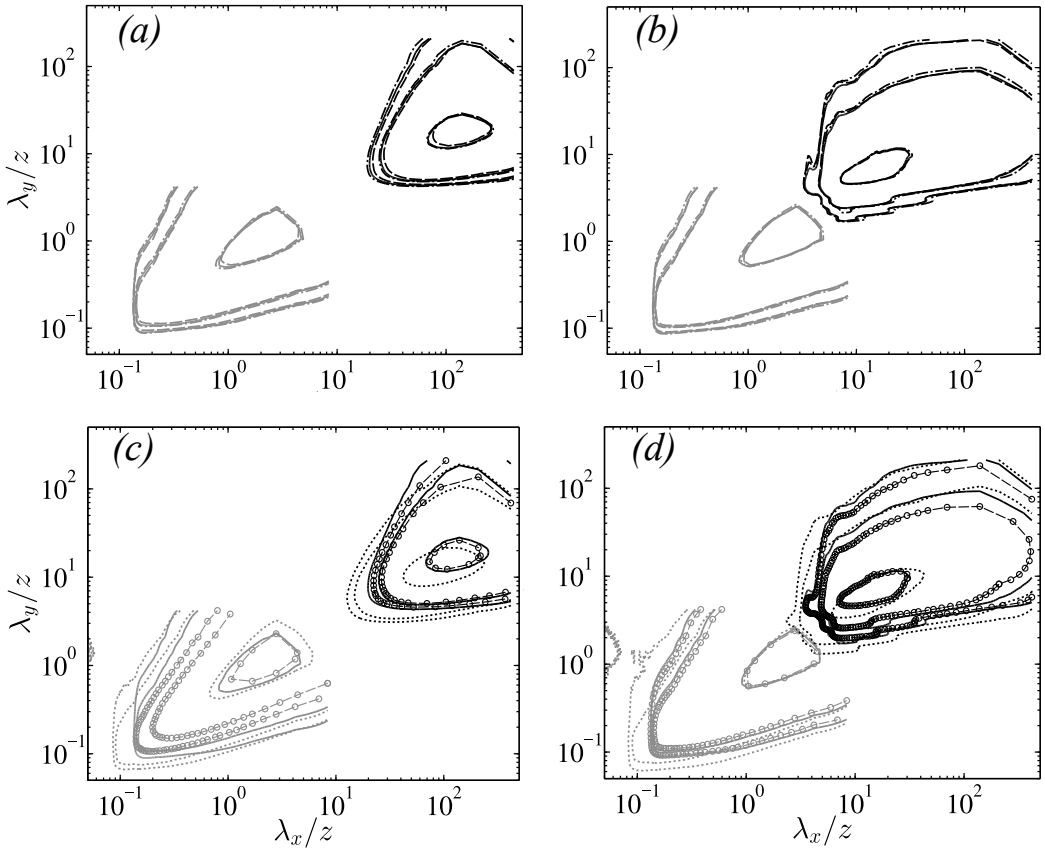

Figure C.4: Premultiplied 2D energy spectra contours $k_x k_y E_{uu}(k_x, k_y, z)/u_\tau^2$ in λ_x, λ_y plane for two different parametric variations of the wall-damped Smagorinsky model on different grids. $z/H = 0.02$ (black), $z/H = 0.875$ (gray). (a),(c) – Case $C_0^{16} n^2 k_c^{4/7}$; (b), (d) – Case $C_0^{09} n^{05} k_c^{4/7}$. Contours at $6.25\%, 12.5\%, 80\%$ of maximum. Vertical grid variation: Dashed – v1 , Solid – bs, Chain dotted – v2. Global grid variation (for (a), (d)): $\circ$ – g1, Dotted – g2. See Table C.1 for grid details.

APPENDIX D

NUMERICAL GRID DESIGN AND CORRELATION IN PERIODIC WIND FARMS

D.1 Details of Numerical Grids and Resolution

Numerical grids and grid refinement

This section presents the details of the numerical grids, their structure and the resolution, used for the simulations discussed in the current work. Tables D.1, D.2 show a comparison of the grids used in the simulations of the neutral atmospheric boundary layer and wind farms, respectively, with that of the previous literature. While most of the previously reported numerical studies relevant to the subject used a uniform grid spacing in the context of Fourier spectral finite difference or staggered finite difference schemes, the current spectral-element based method (SEM) uses Gauss-Lobato-Legendre (GLL) quadrature point distribution which is non-uniform within the element and clusters the points towards the element boundaries. Thus, while comparing our grids to the previous studies, $\Delta_x,\ \Delta_y,\ \Delta_z$ for the SEM is reported in the mean sense, by dividing *spectral element size* $\Delta^e_{x,y,z}$ in the x, y, z direction (which is invariant in each direction in the present ABL simulations) by the order of the Legendre polynomial p. While the grid resolution of previous neutral ABL simulations displays a considerable amount of scatter, our spectral element grid parameters appear to be consistently within the range of this scatter. Furthermore, our previous work [136] has revealed that our spectral element grid sizes were within the requirements of *High-Accuracy-Zone* of Brasseur and Wei [45], as was manifested by the proper logarithmic trends of the mean velocity profile and correct spectral scaling laws in ABL for our best-performing subgrid-scale model [136] utilized in the current work.

Along the similar lines, Table D.2 manifests the grid resolution of periodic wind farms from the previous literature as compared against the spectral element simulations. The current wind turbine array boundary layer (WTABL) grids for all the

cases were obtained by refinement of the base spectral-element ABL grid discussed above. It was thus ensured that the WTABL grids are first of all adequately resolved for correctly capturing the atmospheric boundary layer trends with LES. While most of the previous periodic wind farm simulations relied on the actuator disc models for the turbines and had uniform grid spacing, our spectral element simulations with the *actuator line model* for wind turbine blades manifests grid non-uniformity. In addition to a non-uniform clustering of GLL quadrature points within each element discussed previously, the actuator line model also requires non-uniform size of the elements in order to properly capture the helical vortices propagating downstream of the turbines [12, 52]. The grid parameters $\Delta_x,\ \Delta_y,\ \Delta_z$ in Table D.2 for the SEM cases are thus defined in the *global mean* sense and represent the ratio of the domain size in a given direction to the total number of collocation points in this direction, $\Delta_\eta = L_\eta/(N_\eta^e\, p)$.

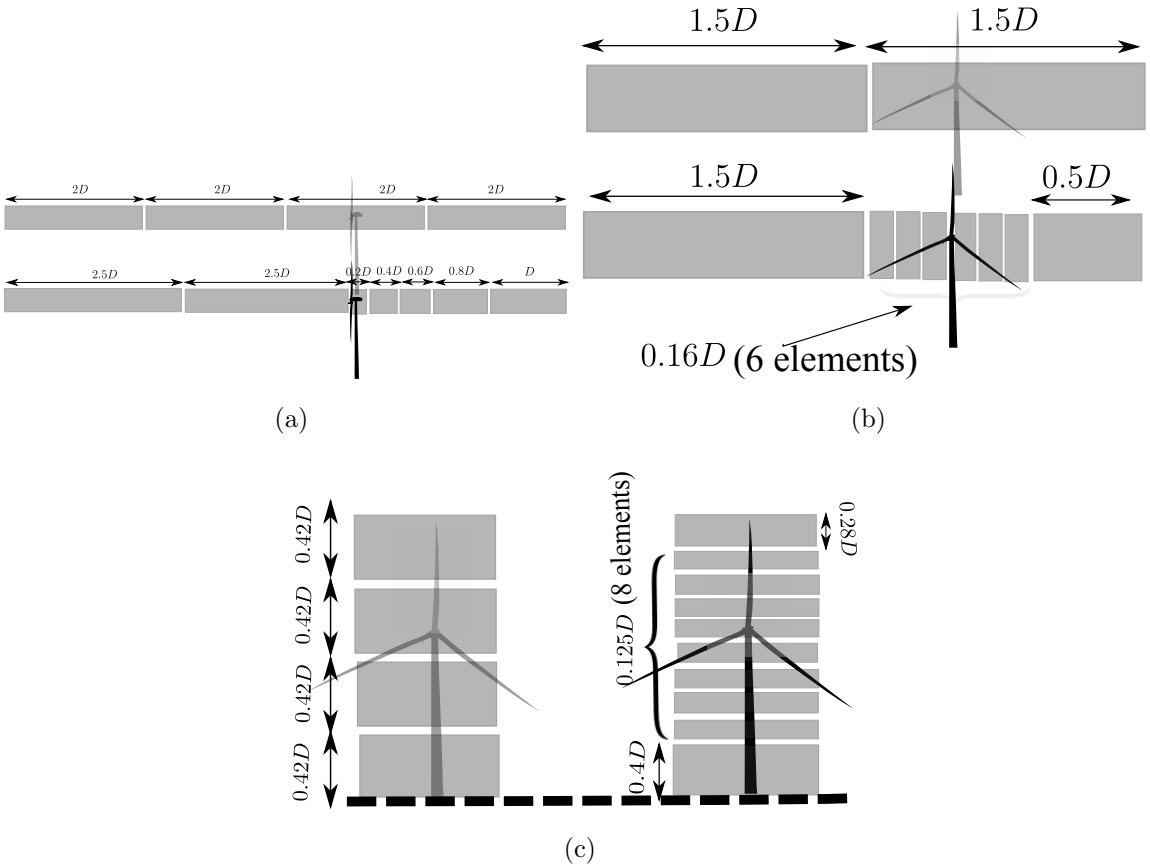

Figure D.1: Schematic of grid refinements of Case I compared to neutral ABL in the region near the WT rotors in (a) streamwise (b) spanwise and (c) vertical direction. Location of a hypothetical turbine (in gray) shown in the neutral ABL grid. $D = 0.1H$ is the rotor diameter. Thick dashed black line – location of the bottom rough wall surface.

Resolved scales in LES simulation

The refinement of the ABL grid to correspond to the periodic wind farm cases was done according to the rules described below. A schematic of the refinement of grids near the wind turbine rotors is also provided in Figure D.1. The description below follows the example of grid for Case I, while the grids for the other Cases IIa,IIb and III are designed based on a similar logic. It must be noted that even though the neutral ABL grid has the elements of a uniform size in x, y, z directions, the location of the wind turbines is not necessarily at the *element boundaries*. Thus in Figure D.1,

the streamwise and spanwise element refinements shown are representative of all the turbine rotors in the 4^{th} row and the 1^{st} column, respectively. Even though the elements stretched in the streamwise and spanwise direction during the refinements of WT grids for differently located turbines may be slightly different in size, the essential idea behind the refinement remains the same as illustrated in Figure D.1a, D.1b. The wall-normal refinement shown in Figure D.1c holds for all the turbine rotors.

(a) A baseline ABL grid documented in Tables C.1, D.1 is used, which utilizes $30 \times 20 \times 24$ elements with a polynomial order $p = 7$.

(b) Horizontal (streamwise) refinement of grids near WT rotor: 3 elements in the streamwise direction are added downstream of each of the 8 turbines, while subsequently stretching only the neighbouring elements as required. Total number of streamwise elements in the WT array is $30 + 8 \times 3 = 54$

(c) Horizontal (spanwise) refinement of grids near WT rotor: 6 elements in the spanwise direction are added in the rotor region that uniformly span the rotor-swept area of diameter D for 6 turbines in each of 6 rows, while subsequently stretching only the neighbouring elements as required. Total number of spanwise elements in the WT array is $20 + 6 \times 6 = 56$

(d) Vertical (wall-normal) refinement of grids near WT rotor: 8 elements in the vertical direction are added in the rotor region that uniformly span the rotor-swept area of diameter D for 6 turbines in each of 6 rows. While grids in the near wall region are thus substantially refined, grids in the outer layer region are stretched proportionately (while still being in the *High-Accuracy-Zone* [45] of vertical grids) to maintain the same number of spectral elements ($N_z^e = 24$) in the vertical direction.

Case	Geometry	N_{xyz}	Δ_x/H	Δ_y/H	Δ_z/H	Δ_x/Δ_z	Δ_y/Δ_z	Δ_x/Δ_y
Sullivan et al.(1994)^a [67]	$2.6H \times 2.6H \times H$	$192 \times 192 \times 75$	0.014	0.014	0.013	1.02	1.02	1.0
Sullivan et al. (1994)^b [67]	$3H \times 3H \times H$	$96 \times 96 \times 96$	0.031	0.031	0.013	2.3	2.3	1.0
Porte-Agel et al. (2000) [44]	$2\pi H \times 2\pi H \times H$	$54 \times 54 \times 54$	0.116	0.116	0.019	6.5	6.5	1.0
Brasseur et al. (2010) [45]	$3H \times 3H \times H$	$360 \times 360 \times 128$	0.008	0.008	0.008	1	1	1.0
Xie et al. (2013) [25]	$2H \times 2H \times H$	$96 \times 96 \times 96$	0.021	0.021	0.01	2	2	1
Meyers et al. (2013) [54]	$2\pi H \times \pi H \times H$	$128 \times 128 \times 96$	0.049	0.025	0.01	4.7	2.4	2.1
Verhulst et al. (2014) [134]	$\pi H \times \pi H \times H$	$128 \times 128 \times 61$	0.025	0.025	0.016	1.5	1.5	1
Stevens et al. (2015) [14]	$4\pi H \times 2\pi H \times H$	$1024 \times 512 \times 256$	0.012	0.012	0.004	3	3	1
Current ABL (PoF, 2017) [136]	$2\pi H \times \pi H \times H$	$211 \times 141 \times 169$	0.029	0.022	0.006	4.8	3.7	1.3

Table D.1: Comparison of various resolution parameters of spectral element neutral ABL simulations [136] with the previous literature. Sullivan et al.(1994)^a – weakly convective ABL, Sullivan et al.(1994)^b – neutral ABL.

Case	Geometry	N_{xyz}	Δ_x/H	Δ_y/H	Δ_z/H	Δ_x/Δ_z	Δ_y/Δ_z	Δ_x/Δ_y
Calaf et al. (2010) [5]	$2\pi H \times \pi H \times H$	$128 \times 192 \times 61$	0.049	0.016	0.016	2.9	2.9	3
Verhulst et al. (2014) [134]	$2\pi H \times \pi H \times H$	$256 \times 128 \times 61$	0.025	0.025	0.016	1.5	1.5	1
Stevens et al. (2015) [126]	$6\pi H \times \pi H/2 \times H$	$1024 \times 128 \times 256$	0.019	0.012	0.004	4.7	3	1.6
I	$2\pi H \times \pi H \times H$	$379 \times 393 \times 169$	0.016	0.008	0.006	2.6	1.3	2.0
IIa	$2\pi H \times \pi H \times H$	$316 \times 393 \times 169$	0.019	0.008	0.006	3.2	1.3	2.3
IIb	$2\pi H \times \pi H \times H$	$379 \times 309 \times 169$	0.016	0.01	0.006	2.6	1.6	1.3
III	$2\pi H \times \pi H \times H$	$379 \times 393 \times 169$	0.016	0.008	0.006	2.6	1.3	2.0

Table D.2: Comparison of the various resolution parameters of current periodic wind farm simulations (Cases I, IIa, IIb, III) with the previous literature. Grid parameters of I, IIa, IIb, III are defined in the global mean sense. All simulations in wind farms are performed in neutral ABL framework.

Table D.3 shows the minimum and maximum grid resolution of the current spectral element wind farm simulations, averaged over the GLL points within the element. This demonstrates that spectral elements of size that are an order of magnitude smaller are present near the "actuator lines" than in the region far away from the turbines. Note that the minimum and maximum element sizes do not depend on a case, since the element refinement and stretching is local to the turbines and does not depend on the number of turbines.

Tables D.2, D.3 illustrate that the grid sizes chosen for the current wind farm

spectral element simulations are on par with the finer resolution simulations from the previous literature. Furthermore, the current exponentially accurate spectral element methodology provides non-dissipative and low-dispersive numerical schemes beneficial for Large Eddy Simulations [136], which conforms to the ideas of utilizing highly-accurate numerical schemes for a proper description of turbulent interactions in WT arrays [5]. The smallest resolved length scale of the neutral ABL simulations

Case	$\Delta_x/H\Big\vert_{min}$	$\Delta_x/H\Big\vert_{max}$	$\Delta_y/H\Big\vert_{min}$	$\Delta_y/H\Big\vert_{max}$	$\Delta_z/H\Big\vert_{min}$	$\Delta_z/H\Big\vert_{max}$
I	0.003	0.037	0.0024	0.023	0.0014	0.013
IIa	0.003	0.037	0.0024	0.023	0.0014	0.013
IIb	0.003	0.037	0.0024	0.023	0.0014	0.013
III	0.003	0.037	0.0024	0.023	0.0014	0.013

Table D.3: Maximum and minimum grid sizes for current wind farm simulations – Cases I, IIa, IIb, III.

can be defined using the Nyquist criterion as

$$\lambda_{\eta,resABL} = 2\,\Delta^e_\eta/p = 2\,\Delta_\eta, \tag{D.1}$$

where Δ^e_η is the element size in the η direction, p is the order of the polynomial approximation, and Δ_η is the "mean" grid size presented in Table D.1. This definition aims to reconcile the high-order approximation defined on spatially-varying GLL points, and the classical Fourier approximation of the same resolution. It is thus seen from Table D.1 that the smallest resolved length scale corresponds to $\lambda_{x,resABL} = 0.058H = 0.58D$, and $\lambda_{y,resABL} = 0.044H = 0.44D$.

For WTABL grids, the element resolution is nonuniform, and, while the largest element sizes are on par with these of the ABL grid, the resolution near the wind turbine rotors is about ten times finer, which means that the length scales that are on the order of magnitude smaller, are captured by the grid around the location of

wind turbines. However, during Fourier analysis, the scale contribution is defined in a sense of a global averaging, and the spatial information is lost. In this sense, the contribution to the Fourier spectra at a particular wavenumber comes from the spatial regions where this wavenumber might be resolved, and where it might be unresolved. As a result, different physics captured in different regions of the grid is manifested as a combined effect in the spectra at wavelengths $\lambda_{x,y} < \lambda_{\eta,resABL}$. Therefore, only the length scales that are adequately resolved everywhere in the computational domain can be considered reliable in the context of Fourier spectral analysis, and we thus restrict our analysis to the length scales $\lambda_x > \lambda_{x,resABL} \sim 0.6D$, and $\lambda_y > \lambda_{y,resABL} \sim 0.5D$ in this paper. Multiresolution features of the grid and the ability to capture different scales of motion at different spatial locations can potentially be explored with multiresoluton analysis techniques such as wavelets, and is left for the future work. Practically, the spectral analysis in the current study is accomplished by spectrally interpolating the results of the LES simulations onto a uniform grid for Fourier analysis, with 1024×512 gridpoints, which gives an effective Fourier grid resolution of $\Delta_\eta^F = 0.006H$, or wavelength resolution $\lambda_\eta^F = 0.012H$, that does not interfere with the resolved length scales of $\lambda > 0.05H$ as defined above. Although the scales below $\lambda < D$ are resolved by the grid, they are also affected by the SGS dissipation, as discussed in Section 4.4.1.

D.2 Integral Length Scales

The integral length scales can be calculated from the correlation coefficients

$$\rho_{u_i' u_j'}(\boldsymbol{r}; z) = \frac{\mathfrak{R}_{u_i' u_j'}(\boldsymbol{r}; z)}{[\mathfrak{R}_{u_i' u_i'}(0, z)]^{1/2} [\mathfrak{R}_{u_j' u_j'}(0; z)]^{1/2}} \tag{D.2}$$

constructed from the two-point correlations discussed in the previous section. In the current paper, for the neutral ABL and the WTABL arrays, we consider the integral

length scales calculated from the correlations of the streamwise velocity fluctuations, $\rho_{u'u'}(\boldsymbol{r}; z)$, which play a dominant role in the turbulence statistics.

Figures D.2, D.3 reflect the 2D correlation coefficient $\rho_{u'u'}(\boldsymbol{r}; z)$ for the wind farm cases I, IIa, IIb, III and the neutral ABL (without wind turbines) at two different wall-normal locations. While at the outer layer, $z = 8.75D$ (Figure D.3) all the wind farm layouts and neutral ABL display similar features of the gradual decay of the correlation coefficient $\rho_{u'u'}$ with increasing separations Δ_x, Δ_y, the correlation coefficient at hub-height locations of wind farms ($z = D$ for Cases I, IIa, IIb; $z = 3.3D$ for Case III) and the neutral ABL at $z = D$, manifests remarkably different behaviour. At $z = D$, the correlation coefficient of neutral ABL illustrates a single peak, while $\rho_{u'u'}$ at the hub-heights of different wind farm layouts manifests multiple peaks in line with the matrix arrangement of the wind turbines. It must be noted that similar peaks in the spectral picture were also observable in Figures 4.6a, 4.8,and 4.10.

Integral length scales in the current paper plotted in Figure 4.12 are defined as

$$\mathfrak{L}_{uu}(z) = \int_{r_x \in \mathbb{R}} \rho_{u'u'}(\Delta_x, 0; z) d\Delta_x \tag{D.3}$$

by utilizing the correlation coefficient $\rho_{u'u'}(\Delta_x, 0; z)$ between the two points separated only at the streamwise direction, at the same spanwise location y. As can be seen from Figures D.2, D.3, this definition of length scales, from choosing two points $\boldsymbol{x}_r = (x, y), \boldsymbol{x}_r + \boldsymbol{r} = (x + \Delta_x, y)$ at a fixed spanwise location in the construction of the two point correlation in Equation (4.5), and subsequently the correlation coefficient, while averaging in the spanwise direction, yields the upper bound on length scales owing to highly correlated motions in the presence of streamwise dynamics. The contours of $\rho_{u'u'}$ further help us understand the reason for the modulation of integral length scales in the wind farms compared to the neutral ABL (without turbines).

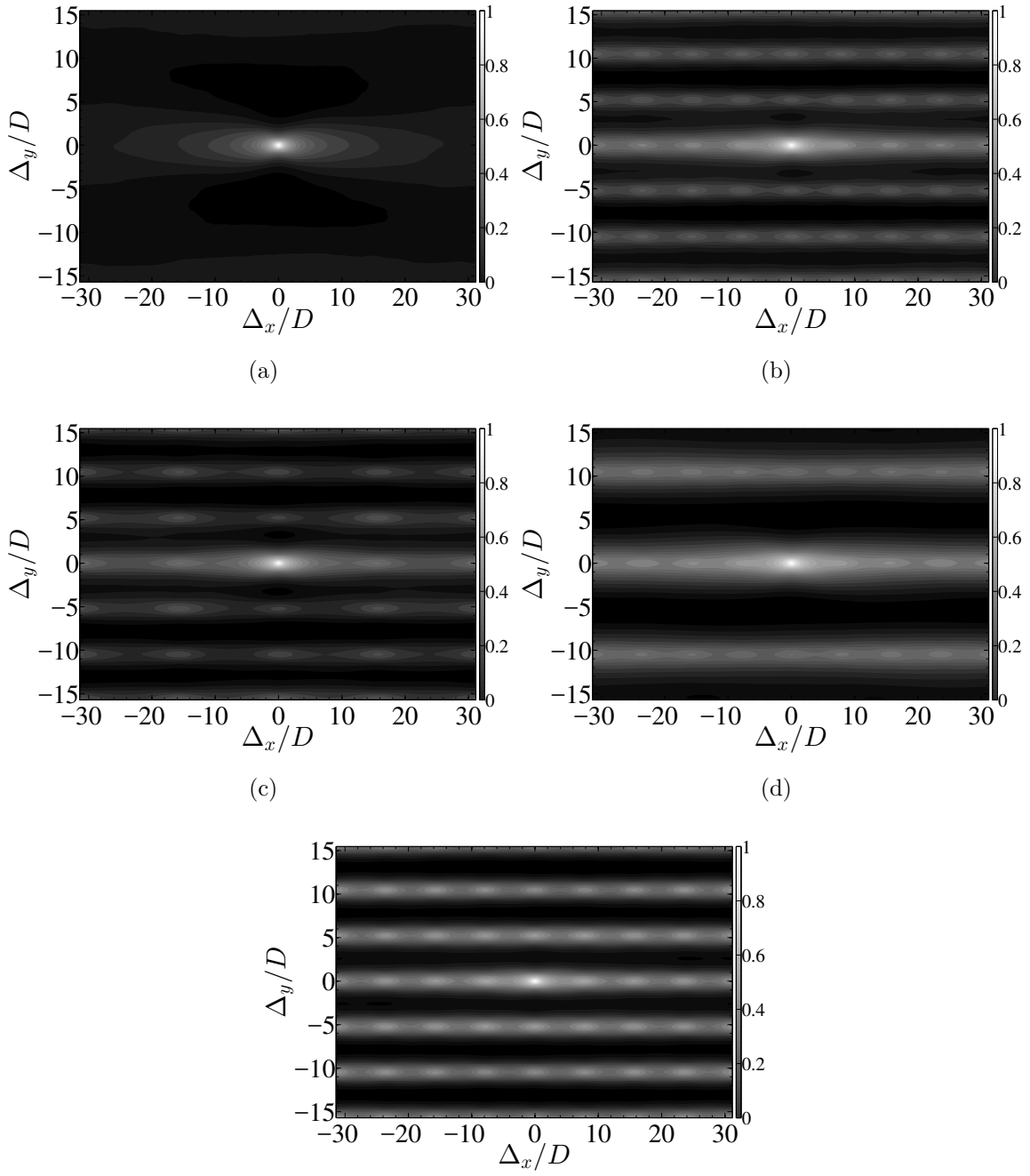

Figure D.2: Streamwise 2D correlation coefficient $\rho_{u'u'}(\boldsymbol{r}; z = \xi)$ for flows with and without wind turbines. Figures (a)–(e) correspond to the Cases neutral ABL at $\xi = D$ and I,IIa,IIb,III at $\xi = z_h$ (hub-height) respectively.

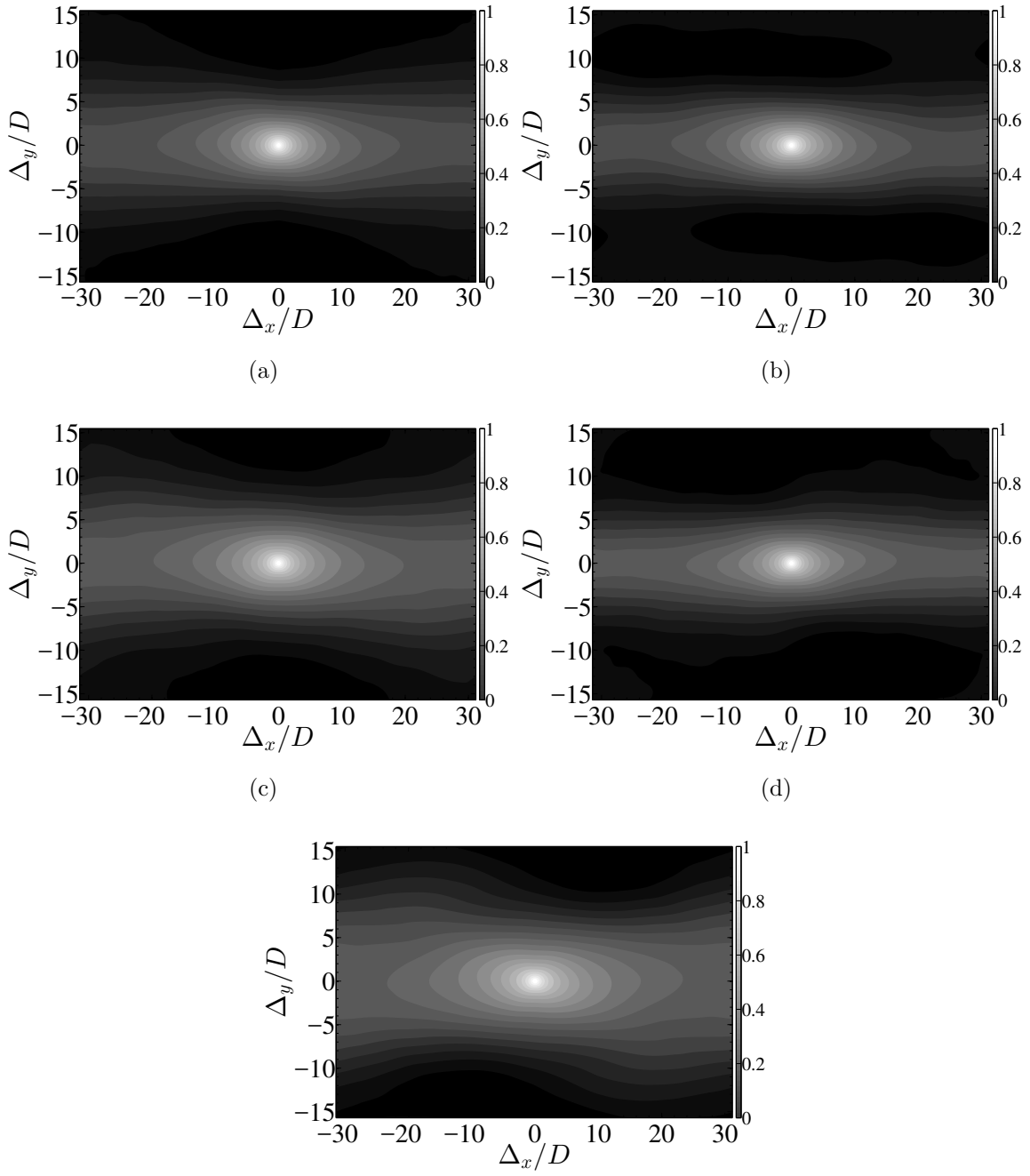

Figure D.3: Streamwise 2D correlation coefficient $\rho_{u'u'}(\boldsymbol{r}; z = 8.75D)$ for flows with and without wind turbines. Figures (a)–(e) correspond to the Cases neutral ABL, I,IIa,IIb, and III, respectively.

D.3 Uncertainty of the Large Scales

The larger-scale structures also have the larger coherence times, and therefore fewer decorrelated snapshots available throughout the duration of the simulations. Although there can be many different sources of uncertainty in the simulations, here we have attempted to estimate the uncertainty in the averaging time on the large scale end off the spectra. Since the major question is on the influence of uncertainty on the conclusions made about the contribution of length scales to the wind turbine power, through the MKE flux difference, we have decided to estimate the uncertainty in the spectra of the MKE flux difference specifically. In addition, since it would be useful to associate each value of the uncertainty parameter with a single quantitative output, we consider an output as the integral value of the MKE flux difference over the large scales of motion, i.e. $\delta_L = \int_{10\pi D}^{20\pi D} \Delta\hat{\Phi}_p(\lambda_x)\mathrm{d}\lambda_x$ for the streamwise spectra, and $\delta_M = \int_{5\pi D}^{10\pi D} \Delta\hat{\Phi}_p(\lambda_y)\mathrm{d}\lambda_y$ for the spanwise spectra. The analysis proceeds as follows. We work with the data originally collected over the duration of 25 T_e, where T_e is the flow through time. We vary the averaging times T_{av} as 1, 2, 3, 4, 5, 6, 7, 8, 9, 10, 15, 25 T_e. For every averaging time, we obtain $N_{av} = 25\,T_e/T_{av}$ values of the observable output, i.e. δ_L and δ_M. For example, we obtain 25 independent values of δ_L, δ_M for $T_{av} = T_e$, 12 values for $T_{av} = 2\,T_e$ etc., all the way down to one value for $T_{av} = 25\,T_e$. An example of comparison of two typical samples of the premultiplied MKE flux difference spectra $k_x\Delta\hat{\Phi}_p(\lambda_x)/U_\infty^3$, $k_y\Delta\hat{\Phi}_p(\lambda_y)/U_\infty^3$ obtained for some selected averaging times is shown in Figures D.4, D.5. It can be seen that the differences indeed drastically decrease as the averaging time increases. It is the integral of these one-dimensional curves over the large-scale end of the spectra which is considered as the quantitative output δ_L, δ_M in the current uncertainty analysis. We can then compute statistical values of the outputs, such as their mean and the standard variation, for each T_{av}. The value of

the coefficient of variation C_v (standard deviation divided by the mean) versus T_{av} for δ_L, δ_M, are plotted in Figures D.6a, D.6b. It can be seen that the coefficient of variation C_v decreases with T_{av} more or less exponentially. A least-squares exponential model was fitted to the data and is also plotted in Figures D.6a, D.6b. Although the reliability of uncertainty analysis itself decreases with the decrease in the number of available samples, this analysis nonetheless can serve as a useful guideline while judging on the effect of the averaging time on the uncertainty in spectra. One can extrapolate the fitted least-squares models to the averaging time of $T_{av} = 25\,T_e$, where only one snapshot is available, making statistical analysis impossible, and further to $T_{av} = 50\,T_e$. The analysis shows that as the averaging time is increased from $T_{av} = 25\,T_e$ to $T_{av} = 50\,T_e$, the coefficient of variation C_v decreases from 0.25% to 0.003% for the streamwise spectra, and from 0.22% to 0.01% for the spanwise spectra. To keep a low bound on uncertainty values as reflected in the current analysis, and to increase the credibility of the results, the decision has been made to increase the averaging time from 25 to 50 flow through times for all the data presented in the revised manuscript. As the presented uncertainty values of less than 0.01% are significantly smaller than the reported differences in spectra in the large-scale region between the different cases (up to 20% for the difference between Case III and the other cases in the cumulative spanwise spectra values), we conclude that these differences are due to the physical modulation of the flow by wind farms and are above the uncertainty values.

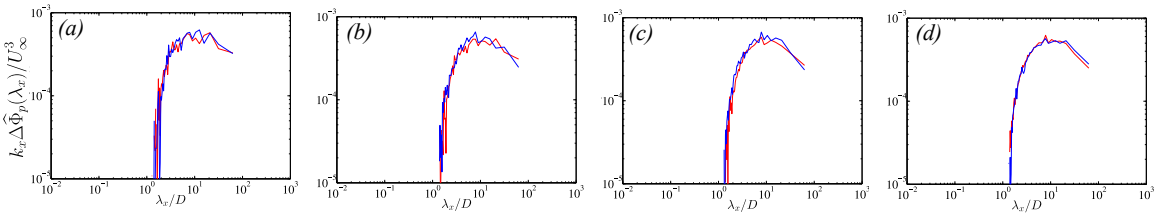

Figure D.4: Two typical samples of premultiplied MKE flux difference $k_x\Delta\hat{\Phi}_p(\lambda_x)/U_\infty^3$ averaged over (a) T_e (b) $2T_e$ (c) $5T_e$ (d) $10T_e$. All plots are from Case I simulation.

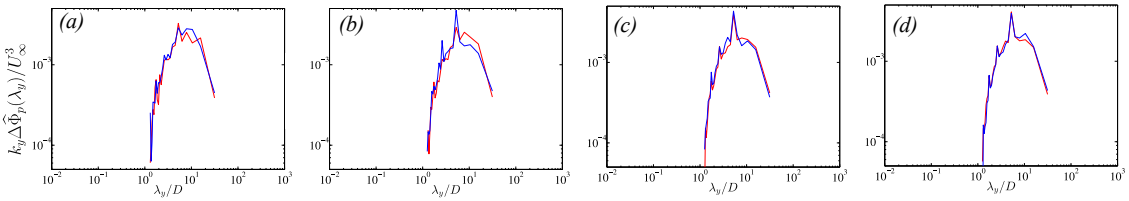

Figure D.5: Two typical samples of premultiplied MKE flux difference $k_y\Delta\hat{\Phi}_p(\lambda_y)/U_\infty^3$ averaged over (a) T_e (b) $2T_e$ (c) $5T_e$ (d) $10T_e$. All plots are from Case I simulation.

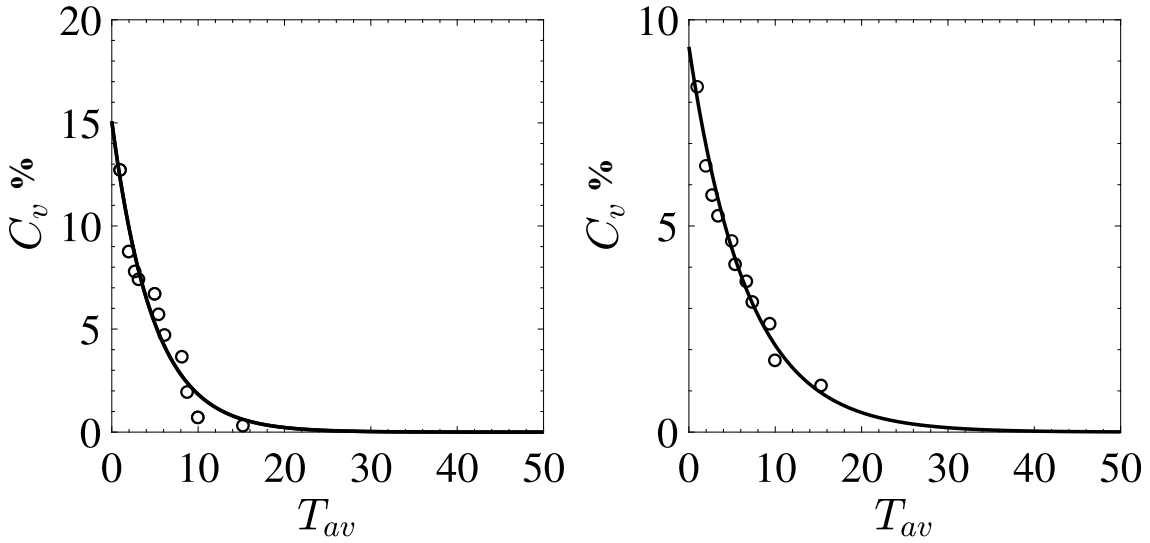

Figure D.6: Coefficient of variation C_v (in %) measuring the uncertainty of large scales for various averaging times T_{av} of the snapshots. Open circles: LES data. Solid black line: exponential fit with 95% confidence bounds (a) Uncertainty in δ_L corresponding to largest streamwise scales, fit – $C_v = 14.04\exp(-0.1677T_{av})$ (b) Uncertainty in δ_M corresponding to the largest spanwise scales, fit – $C_v = 9.346\exp(-0.149T_{av})$

APPENDIX E

FOURIER AND WAVELET ENERGY SPECTRA

E.0.1 Fourier Transform

For the turbulent fluctuating velocity field $u_i'(x,y,z,t) \in \Omega(\mathbb{R}^3, [0,\infty) \cap L_2(\mathbb{R}))$, the Fourier transform in the streamwise direction can be written as

$$\hat{u}_i'(k_x|y,z,t) = \int_{-\infty}^{\infty} u_i'(x,y,z,t) e^{-ik_x x} \mathrm{d}x \tag{E.1}$$

where $\hat{u}_i'(k_x,k_y|z,t) \in \Omega(\mathbb{C}^3, [0,\infty) \cap L_2(\mathbb{R}))$. The backward transform, thus follows as $u_i'(x,y,z,t) = \mathcal{F}^{-1}\{\hat{u}_i'(k_x|y,z,t)\} = \dfrac{1}{2\pi}\displaystyle\int_{\infty}^{\infty} \hat{u}_i'(k_x|y,z,t) e^{ik_x x} \mathrm{d}k_x$. The convolution in physical space of the velocity variable is the product of the Fourier variables which gives rise to Parseval's theorem for the energy.

$$\int_{-\infty}^{\infty} u_i^{'*}(x,y,z,t) u_i'(x+r_x,y,z,t) \mathrm{d}x = \frac{1}{2\pi} \int_{\infty}^{\infty} \hat{u}_i^{'*}(k_x|y,z,t) \hat{u}_i'(k_x|y,z,t) e^{ik_x r_x} \mathrm{d}k_x \tag{E.2}$$

For, $r_x \to 0$, we arrive at Parseval's theorem, i.e. the equality of energy in the physical and Fourier space. Here $*$ denotes complex conjugate.

$$\int_{-\infty}^{\infty} u_i'(x,y,z,t) u_i'(x,y,z,t) \mathrm{d}x\mathrm{d}y = \frac{1}{2\pi} \int_{\infty}^{\infty} \hat{u}_i^{'*}(k_x|y,z,t) \hat{u}_i'(k_x|y,z,t) \mathrm{d}k_x \tag{E.3}$$

since, for $u_i \in \Omega(\mathbb{R}^3, [0,\infty) \cap L_2(\mathbb{R}))$, $u_i^* = u_i$. In the sense of L_2 norm, we can also write

$$||u_i'(x,y,z,t)||_2 = ||\hat{u}_i'(k_x,k_y|z,t)||_2 \tag{E.4}$$

if we subsume the factor 2π insde Fourier coefficient $\hat{u}_i'(k_x,k_y|z,t)$.

Further invoking the linearity of the integration operator, we can invoke a time average operator on Equation E.10 owing to the statistical stationarity of the signal.

$$\int_{-\infty}^{\infty} \langle u_i'(x,y,z,t)^2 \rangle_T \mathrm{d}x = \frac{1}{(2\pi)^2} \int_{\infty}^{\infty} \langle |\hat{u}_i'(k_x|y,z,t)|^2 \rangle_T \mathrm{d}k_x \tag{E.5}$$

where $\langle\rangle_T$ is the time average operator of the form $\displaystyle\lim_{T\to\infty} \int_0^T ()\mathrm{d}t$.

For 1D energy spectra $E_{u_i'}(k_x;z)$ at different z locations can be obtained as

$$E_{u_i'}(k_x;z) = \int_{-\infty}^{\infty} \langle |\hat{u}_i(k_x|y,z,t)|^2 \rangle_T \mathrm{d}y \tag{E.6}$$

The calculation of $E_{u_i'}(k_x;z)$ can also be calculated from the 2D Fourier spectra $\hat{u}_i(k_x,k_y|y,z,t)$ as

$$E_{u_i'}(k_x;z) = \int_{-\infty}^{\infty} \langle |\hat{u}_i'(k_x,k_y|z,t)|^2 \rangle_T \mathrm{d}k_y \quad \forall i = 1 \tag{E.7}$$

where the 2D Fourier spectra can be calculated as

$$\hat{u}_i(k_x,k_y|z,t) = \int_{-\infty}^{\infty} u_i(x,y,z,t) e^{-i(k_x x + k_y y)} \mathrm{d}x\mathrm{d}y \tag{E.8}$$

For the turbulent fluctuating velocity field $u_i'(x,y,z,t) \in \Omega(\mathbb{R}^3, [0,\infty) \cap L_2(\mathbb{R}))$ the Fourier transform in the streamwise direction can be written as

$$\hat{u}_i'(k_x|y,z,t) = \int_{-\infty}^{\infty} u_i'(x,y,z,t) e^{-ik_x x} \mathrm{d}x \tag{E.9}$$

where $\hat{u}_i'(k_x,k_y|z,t) \in \Omega(\mathbb{C}^3, [0,\infty) \cap L_2(\mathbb{R}))$.

Invoking the temporal average of Parseval's identity, i.e., the equivalence of energy in the physical and spectral space for stationary signals,

$$\int_{-\infty}^{\infty} \langle u_i'(x,y,z,t)^2 \rangle_T \mathrm{d}x = \frac{1}{(2\pi)^2} \int_{\infty}^{\infty} \langle |\hat{u}_i'(k_x|y,z,t)|^2 \rangle_T \mathrm{d}k_x \tag{E.10}$$

For 1D energy spectra $E_{u_i'}(k_x;z)$ at different z locations can be obtained as

$$E_{u_i'}(k_x;z) = \int_{-\infty}^{\infty} \langle |\hat{u}_i(k_x|y,z,t)|^2 \rangle_T \mathrm{d}y \tag{E.11}$$

where $\langle \rangle_T$ is the time average operator of the form $\lim_{T\to\infty} \int_0^T () \mathrm{d}t$.

E.0.2 Wavelet Transform

The wavelet transform, like the Fourier integral transform, can be analogously defined. The basis function of the wavelet transform, is $\psi \in L_2(\mathbb{R})$ which satisfies the

admissibility condition as

$$C_\psi = \int_\infty^\infty \frac{|\hat{\psi}(k_x)|^2}{|k_x|} \mathrm{d}k_x < \infty \tag{E.12}$$

where $\hat{\psi}(k_x)$ is the 1D Fourier transform of ψ. The wavelet transform of u_i, i.e., $\mathcal{W}_\psi[u_i](a,b) \in \Omega(\mathbb{C}^3, [0,\infty) \cap L_2(\mathbb{R}))$ can be given as

$$\mathcal{W}_\psi[u_i](a,b)|_{y,z} = \int_{-\infty}^\infty u_i'(x,y,z,t)\psi_{a,b}^*(x)\mathrm{d}x \tag{E.13}$$

where $\psi_{a,b}(x) = \dfrac{1}{\sqrt{|a|}}\psi\Big(\dfrac{x-b}{a}\Big)$ is obtained by translating and dilating the mother wavelet.

$$\mathcal{F}\{\mathcal{W}_\psi[u_i'](a,b)|_{y,z}\} = \sqrt{|a|}\hat{u}_i'(k_x|y,z,t)\hat{\psi}^*(ak_x) \tag{E.14}$$

where $*$ denotes the complex conjugate. We can arrive at the temporally averaged Parseval's identity of wavelet transform analogous to the Fourier space.

$$\int_\infty^\infty \langle |u_i'(x,y,z,t)|^2\rangle_T \mathrm{d}x = \frac{1}{C_\psi}\int_{-\infty}^\infty\int_{-\infty}^\infty \langle \Big|\mathcal{W}_\psi[u_i'](a,b)|_{y,z}\Big|^2\rangle_T \frac{\mathrm{d}b\mathrm{d}a}{a^2} \tag{E.15}$$

A further simplification of the RHS of Equation E.15 can be obtained as follows.

$$\frac{1}{C_\psi}\int_{-\infty}^\infty \Big\langle \frac{\Big|\{\mathcal{W}_\psi[u_i'](a,b)|_{y,z}\}\Big|^2}{|a|}\Big\rangle_T \frac{\mathrm{d}b\mathrm{d}a}{|a|} = \frac{1}{2\pi}\int_{-\infty}^\infty \frac{\mathrm{d}a}{|a|}\int_\infty^\infty \langle|\hat{u}_i'(k_x|y,z,t)\rangle_T|\hat{\psi}(ak_x)|^2\rangle_T \mathrm{d}k_x \tag{E.16}$$

We can define the wavelet energy spectra as function of scale and translation a, b at different wall-normal locations as

$$\widetilde{E}_{u_i'}(a,b;z) = \frac{1}{C_\psi}\int_{-\infty}^\infty \Big\langle \frac{\Big|\{\mathcal{W}_\psi[u_i'](a,b)|_{y,z,t}\}\Big|^2}{|a|}\Big\rangle_T \mathrm{d}y \tag{E.17}$$

We now replace a (scale) , b (translation) by wavenumbers $\widetilde{k}_x$, $\widetilde{x}$, to distinguish it from the variables without the tilde (k_x, x) used in the physical and Fourier space respectively. Please note, $a = k_\psi/\widetilde{k}_x$, where k_ψ is the centroid wave-number of the mother wavelet. However, to avoid confusion, we have dropped the tilde in the wavelet

formulae used in the main document.

Along the lines of [166], and using Equation E.15 we can define a space dependent energy spectra as a function of $(\widetilde{x}, \widetilde{k}_x)$

$$\widetilde{E}_{u_i'}(\widetilde{k}_x, \widetilde{x}; z) = \frac{1}{k_\psi C_\psi} \int_0^\infty \left\langle \frac{\left| \{\mathcal{W}_\psi[u_i'](k_\psi/\widetilde{k}_x, \widetilde{x})|_{y,z,t}\} \right|^2}{|a|} \right\rangle_T \mathrm{d}y \quad \widetilde{k}_x > 0 \tag{E.18}$$

with $\widetilde{E}_{u_i'}(\widetilde{k}_x; z) = \int_{-\infty}^{\infty} \widetilde{E}_{u_i'}(\widetilde{k}_x, \widetilde{x}; z)\mathrm{d}\widetilde{x} = \frac{1}{k_\psi} \int_0^\infty E_{u_i'}(k_x; z)|\hat{\psi}(\frac{k_\psi}{\widetilde{k}_x} k_x)|^2 \mathrm{d}k_x.$

$\widetilde{E}_{u_i'}(\widetilde{k}_x; z)$, the global streamwise energy spectrum is the streamwise Fourier spectrum smoothed by the wavelet spectrum at each scale. $E_{u_i'}(k_x; z)$ is defined in Equation E.11.

Also note, that the spatial variation of the global energy is calculated as $C_\psi^{-1} \int_{-\infty}^{\infty} \widetilde{E}_{u_i'}(\widetilde{k}_x, \widetilde{x}; z)\mathrm{d}\widetilde{k}_x/\widetilde{k}_x = \widetilde{E}_{u_i'}(\widetilde{x}; z)$. The details of the derivation can be found in [161]. In the main document, we would interchangably use wavenumbers $k_{x,y}$ and the wavelength $\lambda_{x,y}$ for the coefficients of wavelet transforms.

E.0.3 Morse, Morlet and Syncrosqueezed Morlet wavelet

The wavelet used in all the energy spectral analysis is an analytical morse wavelet [162], morlet wavelet [158] and the syncrosqueezed transform of the morlet wavelet [191].

The Fourier transform of the analytical Morse wavelet is defined as

$$\hat{\psi}(k_x|\beta, \gamma) = H(k_x) a_{\beta,\gamma} k_x^\beta e^{-k_x^\gamma} \tag{E.19}$$

which ensures that the wavelet is well-localized in physical and Fourier space. $H(k_x)$ is the Heaviside step function and $a_{\beta,\gamma} = 2(e\gamma/\beta)^{\beta/\gamma}$ a normalization constant. The parameters β, γ decides the shape of the wavelet. For example, β, decides the spread of the wavelet in the physical space (decay or compactness parameter), and γ manifests symmetry of the mother wavelet with zero skewness. $\gamma = 3$, for symmetric wavelet

and it also ensures minimum Heisenberg area, i.e. the product of the uncertainties in the space and wavelength resolution. The peak wavenumber, $(\beta/\gamma)^{1/gamma}$ is chosen to be ≈ 2 for the current work. For more details about morse wavelet, please refer to the works of [162, 188].

The analytical Morlet wavelet (a complex exponential with a real gaussian window) and its Fourier transform can be defined as

$$\psi_\sigma(x) = \exp(ik_0x - x^2/2) \tag{E.20}$$

$$\hat{\psi}_\sigma(k_x) = \sqrt{2\pi}\exp(-\frac{1}{2}(k_x - k_0)^2) \tag{E.21}$$

The central wavenumber $k_0 \approx 5$ along the lines of previous literature [159, 178].

A desirable property of the wavelets is their "localization" property, i.e. ψ should be well-localized in both space and wavenumber. In other words, ψ and its derivatives must decay very rapidly. For frequency localization, its Fourier transform $\hat{\psi}$ must decay rapidly as the wavenumber $k_x \to \infty$, and $\hat{\psi}$ should be flat in the neighbourhood of $k_x = 0$. The flatness at $k_x = 0$ is associated with the number of vanishing moments of ψ. The k^{th} moment of ψ is defined by

$$M_k = \int_\infty^\infty x^k \psi(x)\mathrm{d}x \tag{E.22}$$

A wavelet of n vanishing moments would require $M_k = 0 \forall k = 1, \ldots n$, or equivalently, $d^k\hat{\psi}(k_x)/dk_x^k = 0, \quad \forall k = 0, 1 \ldots n$. Both Morse and Morlet wavelets satisfy the property of vanishing moments approximately. It is straightforward to observe that for Morse wavelets, the n^{th} order moments are proportional to $\exp(-k_x^\gamma)$, while for Morlet wavelets, the moments are proportional to $\exp(-\frac{1}{2}(k_x - k_0)^2)$, and both decay rapidly as $k_x \to \infty$. For the Morlet wavelet, the choice of $k_0 = 5$, ensures that the first 6 moments are approximately zero for the wavelet.

Synchrosqueezed transform

For brevity, we bring back the symbols a, b (scale and translation parameters) that we have previously used for the definition of continous wavelet transforms. Using the defintion of wavelet transform of a variable f $\mathcal{W}_\psi[f](a,b)$ as in Equation E.13, we can define the phase transform $\|(a,b)$ by

$$\mathcal{K}_f(a,b) = \frac{\partial_t \mathcal{W}_\psi[f](a,b)}{2\pi i \mathcal{W}_\psi[f](a,b)} \tag{E.23}$$

where $\mathcal{K}_f(a,b)$ can be thought of as an "FM demodulated" wavelength estimate that cancels out the influence of wavelet ψ on $\mathcal{W}_\psi[f](a,b)$ and results in a modified wavelength scale representation of the function f.

The wavelet synchrosqueezing transform of f, for a smooth function $h \in C_0^\infty$, $||h||_{L^1} = 1$ with accuracy δ and thresholds $\widetilde{\epsilon}$ and M is given as

$$S_{f,\widetilde{\epsilon}}^{\delta,M}(b,\eta) = \int_{\Gamma_{f,\widetilde{\epsilon}}^M} \frac{\mathcal{W}_\psi[f](a,b)}{a^{3/2}} \frac{1}{\delta} h(\frac{\eta - \mathcal{K}_f(a,b)}{\delta}) da \tag{E.24}$$

$\Gamma_{f,\widetilde{\epsilon}}^M = \{(a,b) : a \in [M^-1, M], |\mathcal{W}_\psi[f](a,b)| > \widetilde{\epsilon}\}$, Also for $S_{f,\widetilde{\epsilon}}^{\delta,M\to\infty}(b,\eta)$ with use $a > 0$. The syncrosqueezing transform essentially maps the wavelet transform from $(b,a) \to (b, \mathcal{K}(a,b))$ or squeezes the wavelet transform over regions where the phase transform is constant. The resulting instantaneous frequency value is reassigned to a single value at the centroid of the continous wavelet transform space wavenumber region. This reassignment results in sharpened output from the synchrosqueezed transform (potentially can detect singularities) when compared to the CWT. For more details related to the algorithm, see [190, 191].

Notation: Due to the finiteness of the domain, the wave numbers from $(-\infty, \infty)$ are projected to $(-k_{max}, k_{max})$, where k_{max} is the largest wave number in the computational domain. Similar analogy can be drawn from the finite size of the domain. For brevity of analysis, the 1D forward and backward transform in the main document

have been written as $\int_{k\in\mathbb{R}}$ and $\int_{x\in\mathbb{R}}$ respectively.

APPENDIX F

PROPER ORTHOGONAL DECOMPOSITION

F.1 3D POD – Method of Snapshots

The POD analysis was carried out using the *method of snapshots* [185]. The 3D velocity vector field is represented as $\boldsymbol{u}(\boldsymbol{x},t) \equiv u_i(x,y,z,t) \quad \forall i = 1,\ldots,3$. Here, $u_i(x,y,z,t) \in \Omega(\mathbb{R}^3,[0,\infty) \cap L_2(\mathbb{R}^3))$. The velocity field can be decomposed into a set of orthonormal basis functions $\boldsymbol{\varphi} \in V \equiv \Omega(\mathbb{R}^3 \cap L_2(\mathbb{R}^3))$.

$$\boldsymbol{u}'(\boldsymbol{x},t) = \sum_{j=0}^{\infty} a_j(t)\boldsymbol{\varphi}_j(\boldsymbol{x}) \tag{F.1}$$

where the turbulent velocity fluctuation field $\boldsymbol{u}'(\boldsymbol{x},t) = \boldsymbol{u}(\boldsymbol{x},t) - \overline{\boldsymbol{u}}(\boldsymbol{x})$, and $\overline{\boldsymbol{u}}(\boldsymbol{x})$ is the time average of the velocity field. $(\varphi_i,\varphi_j) = \delta_{ij} \quad \forall i,j$. The POD problem can be cast as a contrained variational problem, with the minimization of the objective function $\mathfrak{J}(\boldsymbol{\varphi}) = \langle|(\boldsymbol{u}',\boldsymbol{\varphi})|^2\rangle_T - \Lambda(||\boldsymbol{\varphi}||^2-1)$, $\langle\rangle_T$ is a temporal averaging procedure. A necessary condition of the extrema dictates that the functional derivative vanish for all variations $\boldsymbol{\varphi}+\varepsilon\boldsymbol{\psi} \in V$, $\varepsilon \in \mathbb{R}$, .i.e.,$\dfrac{d}{d\varepsilon}\mathfrak{J}(\boldsymbol{\varphi}+\varepsilon\boldsymbol{\psi})|_{\boldsymbol{\varepsilon}=0} = 0$. The method of snapshot is an approximation to the solution of $\dfrac{d}{d\varepsilon}\mathfrak{J}(\boldsymbol{\varphi}+\varepsilon\boldsymbol{\psi})|_{\boldsymbol{\varepsilon}=0} = 0$ [186] using temporal correlation intead of spatial correlation. Mathematically, the POD method of snapshots [185] of the velocity field dataset arises when solving for the projection of the dataset $\mathbf{P}_r : V \mapsto V_r$ of fixed rank r, minimizing the error $\displaystyle\sum_{j=0}^{N_t-1} ||\boldsymbol{u}'_j - \mathbf{P}_r\boldsymbol{u}'_j||^2$ in the least-square sense with the contraint $||\varphi|| = 1$ ($||.||$ is the norm corresponding to the inner product $(,) \in V$). The temporal snapshots of the velocity field $\boldsymbol{u}(\boldsymbol{x},t_j) \ \forall j = 1,\ldots,N_t$ have been written as $\boldsymbol{u}_j$ in the error expression for brevity. The projection $\mathbf{P}_r$ can be written as

$$\mathbf{P}_r\boldsymbol{u}'_m = \sum_{j=0}^{r-1}(\boldsymbol{\varphi}_j,\boldsymbol{u}'_m)\boldsymbol{\varphi}_j = \sum_{j=0}^{r-1} a_j(t_m)\boldsymbol{\varphi}_j(\boldsymbol{x}), \quad r \leq N_t \tag{F.2}$$

The correlation matrix in indicial notation is given as

$$C_{mn} = \frac{1}{N_t}(\boldsymbol{u}'(\boldsymbol{x},t_m),(\boldsymbol{u}'(\boldsymbol{x},t_n)) \tag{F.3}$$

This method ensures that the eigenvalue problem arising is independant of the size of V which is equal to $\Omega(\mathbb{R}^{3k})$ (k: number of coordinates in $\boldsymbol{u}(\boldsymbol{x},t)$ at discrete grid points). In the eigenvalue problem in Equation F.4 below, Λ is the eigenvalue correponding to the turbulent kinetic energy and $\boldsymbol{v}$ is the eigenvector.

$$[\boldsymbol{C}]\boldsymbol{v} = \Lambda\boldsymbol{v} \tag{F.4}$$

The POD eigenmode can be contructed from the eigenvalues and eigenvectors as

$$\boldsymbol{\varphi}_k(\boldsymbol{x}) = \sum_{j=0}^{N_t-1} b_k(t_j)\boldsymbol{u'}(\boldsymbol{x},t_j) \tag{F.5}$$

for some coefficients b. Using equation F.2 for $\boldsymbol{u'}(\boldsymbol{x},t_j)$, equation F.5 can be expanded as

$$\begin{aligned}\boldsymbol{\varphi}_k(\boldsymbol{x}) &= \sum_{j=0}^{N_t-1} b_k(t_j) \sum_{l=0}^{N_t-1} a_l(t_j)\boldsymbol{\varphi}_l(\boldsymbol{x}) \\ &= \sum_{j=0}^{N_t-1}\sum_{l=0}^{N_t-1} b_k(t_j)a_l(t_j)\boldsymbol{\varphi}_l(\boldsymbol{x})\end{aligned} \tag{F.6}$$

Since, $(\boldsymbol{\varphi}_k,\boldsymbol{\varphi}_l) = \delta_{kl}$, it is straightforward to see from equation F.6 that $b_k(t_j)a_l(t_j) = \delta_{kl}/N_t \quad \forall j$. It is important to note, that Parseval's identity can be applied in POD (orthonormal basis functions) as well (See Appendix E), which from the inner product (taken in spatial domain, defined in V) gives rise to $||\boldsymbol{u'}(\boldsymbol{x},t)||^2 = \sum_{j=0}^{N_t-1} a_j(t)^2$, and hence $\langle a_j(t)a_k(t)\rangle_T = \Lambda_j\delta_{jk} \quad \forall j = 0,\ldots,N_t-1$. Thus, since $b_k a_l = \delta_{kl}/N_t$, the coefficient b_k can be defined as $b_k = \dfrac{a_k}{\Lambda_k N_t}$. Also the eigenvector $v_k = \dfrac{a_k}{\sqrt{\Lambda_k N_t}}$ is consistent with the orthonormality of $\boldsymbol{\varphi}$.

F.1.1 2D Fourier POD modes

The spanwise Fourier transform of the turbulent fluctuating velocity, $\hat{\boldsymbol{u}}'(k_y|x,z,t) = \int_{k_y\in\mathbb{R}} \boldsymbol{u'}e^{-ik_y y}\mathrm{d}y \ \in \Omega(\mathbb{C}^3,[0,\infty)\cap L_2(\mathbb{R}))$

The complex Fourier POD (FPOD) basis function expansion can be given as

$$\hat{\boldsymbol{u}}'(k_y|x,z,t) = \sum_{j=0}^{\infty} \tilde{a}_j(t)\widetilde{\boldsymbol{\varphi}}_j(k_y|x,z), \quad \widetilde{\boldsymbol{\varphi}} \in \Omega(\mathbb{C}^2, [0,\infty) \cap L_2(\mathbb{R}^3)) \tag{F.7}$$

The orthonormality of the FPOD modes are defined as $(\widetilde{\boldsymbol{\varphi}}_i, \widetilde{\boldsymbol{\varphi}}_j^*) = \delta_{ij}$ with respect to the inner product space $L_2(\mathbb{R})$.

The magnitude and the argument of the complex modes, are expressed as $|\widetilde{\boldsymbol{\varphi}}_j| = \sqrt{\widetilde{\varphi}_j^l \widetilde{\varphi}_j^{*l}}$, $\arg[\widetilde{\boldsymbol{\varphi}}_j] = \tan^{-1} \dfrac{(\widetilde{\varphi}_j^l - \widetilde{\varphi}_j^{*l})}{i(\widetilde{\varphi}_j^l + \widetilde{\varphi}_j^{*l})}$ respectively, where summation is performed over the superscript l indicial notation. The turbulent kinetic energy of the complex velocity field at each wave-numbers is the sum of eigenvalues of the POD problem, $||\langle \hat{\boldsymbol{u}}'(k_y|x,z,t)||_2 \rangle_T = \sum_{k=0}^{N_t-1} \Lambda_k(k_y)$.

APPENDIX G

CONSENT TO USE PUBLISHED MATERIAL

I, Tanmoy Chatterjee, declare that the consent has been obtained from co-author Dr. Yulia Peet to use the published work in chapter 3 and 4 of this document. Chapter 3 was published in the Physics of Fluids in 2017 with the title *Effect of artificial length scales in large eddy simulation of a neutral atmospheric boundary layer flow: A simple solution to log-layer mismatch.* Chapter 4 was published in Physical Review Fluids in 2018 with the title *Contribution of large scale coherence to wind turbine power: A large eddy simulation study in periodic wind farms.*